Evidence for the Higgs boson in the $\tau^+\tau^-$ final state and its CP measurement in proton-proton collisions with the ATLAS detector

陽子-陽子衝突におけるアトラス検出器を用いた
$\tau^+\tau^-$ 終状態によるヒッグス粒子の実験的証拠と **CP** 測定

October 2015

Yuki SAKURAI

Evidence for the Higgs boson in the $\tau^+\tau^-$ final state and its CP measurement in proton-proton collisions with the ATLAS detector

陽子-陽子衝突におけるアトラス検出器を用いた
$\tau^+\tau^-$ 終状態によるヒッグス粒子の実験的証拠と **CP** 測定

October 2015

Waseda University
Graduate School of Advanced Science and Engineering
Department of Pure and Applied Physics
Research on Particle Physics Experiment

Yuki SAKURAI

Abstract

The discovery of a Higgs boson in di-boson final state by ATLAS and CMS experiments was reported in July 2012, and then, from now it is important to measure properties of the discovered Higgs boson for understanding the nature of electroweak symmetry breaking predicted by the Standard Model (SM) of particle physics. This thesis presents a search for the Higgs boson in the $\tau\tau$ final state using the data recorded by the ATLAS detector at the LHC, corresponding to an integrated luminosity of up to 4.5 fb^{-1} of $\sqrt{s} = 7$ TeV in 2011 and 20.3 fb^{-1} of $\sqrt{s} = 8$ TeV in 2012. In addition, a study of CP measurement in the $\tau\tau$ final state is also presented assuming an environment of $\sqrt{s} = 8$ TeV in 2012 with an integrated luminosity of 20.3 fb^{-1}.

The first part of this thesis is a search for the Higgs boson in the $\tau\tau$ final state. The $H \to \tau\tau$ decay mode mainly from gluon-gluon fusion (ggF) and vector boson fusion (VBF) production processes is the most sensitive channel in fermionic final states. Event selections and categorizations are optimized corresponding to the ggF and the VBF. Several background processes contributes to the selected signal region, mainly from $Z \to \tau\tau$, W+jets and QCD processes. The $Z \to \tau\tau$ background contributes due to the same final state as the $H \to \tau\tau$ signal. The W+jets and the QCD backgrounds contrubute by that jets are mis-identified as τ leptons with their large production cross sections. Data driven techniques are applied for their estimations and validations. A multi-variate technique, Boosted Decision Tree (BDT) as classifier, is applied to maximize the sensitivity. Input variables of the BDT are separately optimized to the ggF and the VBF processes using their characteristic topologies. A maximum likelihood fit is performed to the data with the expected signal and background on the BDT output distribution in order to measure the signal strength μ, which is defined as the ratio of cross section times branching ratio in the data to that in theoretical prediction. The measured signal strength is:

$$\mu = 1.43^{+0.27}_{-0.26}(\text{stat.})\ ^{+0.32}_{-0.25}(\text{syst.})\ \pm 0.09(\text{theory syst.}).$$

The observed (expected) significance is 4.5 (3.4) standard deviation. The result presents "evidence for the decay of the Higgs boson into leptons" and "first evidence for the Yukawa coupling to down-type fermions".

The another main part of this thesis is a study of the CP measurement in the $H \to \tau\tau$ final state. The SM predicts the Higgs boson has a CP-even state, while a CP-odd Higgs boson predicted in several Beyond the Standard Model (BSM) theories. The CP state of the Higgs boson reflects the transverse spin correlation of τ leptons in the final state. Dedicated angle variable, so-called acoplanarity angle, is reconstructed to distinguish the CP-even and CP-odd Higgs boson. The measurement is performed in the signal region based on the same analysis strategy as the $H \to \tau\tau$ search, while some additional selections are applied to enhance a signal over background ratio. A maximum likelihood fit on the acoplanarity angle distribution is performed, in order to obtain an expected exclusion sensitivity of the

CP-odd Higgs boson. The result of the expected limit is 56% confidence level assuming the data of 20.3 fb^{-1} at $\sqrt{s} = 8$ TeV.

Acknowledgments

This thesis would not have been materialized without the help from many people who involved my research.

I would like to express the deepest appreciation to my supervisor Assoc. Prof. Kohei Yorita for providing great opportunities to contribute to particle physics and for encouraging advice to my research. By chasing his back, I learned a lot about physics and furthermore about life. I am sincerely looking forward to collaborative experiment with him in the near future that I have grown as a scientist.

I would like to offer my special thanks to Prof. Masakazu Washio, Prof. Hiroyuki Abe and Prof. Junichi Tanaka for their proof-reading of this thesis. The quality of this thesis is clearly improved by their meaningful surggestions.

I would like to express my gratitude to staff in the Kohei Yorita laboratory, Dr. Koji Ebina, Dr. Naoki Kimura and Dr. Masashi Tanaka. I received many technical advice and continuous support from Dr. Koji Ebina and Dr. Naoki Kimura, and I had a lot of good time with them for six years. I learned many things from Dr. Masashi Tanaka through physics discussions. I respect him as a scientist. Also I would like to thank every student in the laboratory. I shared a lot of fun time with Mr. Takashi Mitani and Mr. Tomoya Iizawa for three years at CERN. I hope that we can continue to study physics as a fellow in the future. I would also like to thank all other laboratory members including graduates, for their encouragements.

I would like to thank to members involved in ATLAS Tau and Tau Trigger working groups. Special thanks to Dr. Soshi Tsuno for his continuous support and encouragement to my research for three years, also thanks to the group conveners, Dr. Stan Lei, Dr. Stefania Xella, Dr. Will Davey, Dr. Pier Olivier and Dr. Matthew Beckingham, for their tolerant and supportive convener-ship.

I am deeply grateful to ATLAS $H \to \tau\tau$ analysis members. Special thanks to Dr. Koji Nakamura and Dr. Keita Hanawa. I worked closely with them, and their suggestions and advice helped me in several situations. Also thanks to Dr. Alex Tuna, Dr. Nils Ruthman, Dr. Quentin Buat, Dr. Thomas Schwindt, Dr. Michel Trottier-McDonald, Dr. Elias Coniavitis, Dr. Daniela Zanzi, Dr. Sasha Pranko, Dr. Romain Madar, Dr. Lidia Dell'Asta, Dr. Katy Grimm, Dr. Sinead Farrington, Dr. Luca Fiorini. They gave me meaningful suggestions and ideas for my research trough many discussions. I was lucky to have such an excellent collaboration.

I would also like to thank Japanese students and scientists who met at CERN, especially Mr. Ryosuke Fuchi (and his wife), Mr. Masahiro Morinaga, Dr. Kenji Kiuchi, Mr. Kazuki Nagata. Discussions, travels and dinner with them were wonderful time during my stay at CERN.

Finally, I would like to express my gratitude to my family: father, mother and sister, for their moral support and warm encouragements.

Contents

CHAPTER 1

Introduction

1.1 The Standard Model and the Higgs Boson

Current particle physics is described by the quantum field theory, so-called the Standard Model (SM). The SM consists of six leptons and six quarks as elementary particles, and gauge fields are introduced to describe interactions between the particles. The gauge fields in the SM are required in order the symmetries $SU(3)_C \otimes SU(2)_L \otimes U(1)_Y$ of the SM to be gauge symmetries, where interactions are mediated by mass-less bosons. The $SU(3)$ gauge symmetry describes the strong interaction between quarks and the gluon, while the $SU(2)_L \otimes U(1)_Y$ gauge symmetry [1] describes the electroweak interaction propagated by the photon and the W and Z bosons, respectively. The Higgs mechanism [2–4] is introduced in order to provide particle masses without discarding the gauge-symmetry. The Higgs mechanism is based on the Higgs field that has a non-vanishing vacuum expectation value triggering spontaneous symmetry breaking. The W and Z boson masses are given by an interaction between the gauge field and the Higgs field, and the particle created by the Higgs field after the Higgs mechanism is called the Higgs boson. The W and Z boson masses are predicted by this mechanism, and their expected values are consistent with measured values. The Higgs mechanism also provides lepton and quark (fermion) masses by introducing a coupling between the Higgs boson and fermions, while their absolute values are determined by a measurement of the coupling constant, referred to as Yukawa coupling. In this section, an overview of the Higgs mechanism and the Yukawa coupling is given [5].

1.1.1 The Higgs Mechanism

The Higgs mechanism leads to the mass generation via spontaneous symmetry breaking. Spontaneous symmetry breaking is a process that a full symmetric system moves to a lower symmetry system, where the potential of the system settles into the energetically stable vacuum. In the Higgs mechanism, spontaneous symmetry breaking is caused by a complex scalar doublet Φ, described as

$$\Phi = \begin{pmatrix} \phi^+ \\ \phi^0 \end{pmatrix} = \frac{1}{\sqrt{2}} \begin{pmatrix} \phi_0 + i\phi_2 \\ \phi_3 + i\phi_4 \end{pmatrix}. \tag{1.1}$$

The Lagrangian of the Higgs field is expressed by

$$\begin{aligned} L_{\text{Higgs}} &= (D_\mu \Phi)^\dagger (D_\mu \Phi) - V(\Phi), \\ V(\Phi) &= \mu^2 (\Phi^\dagger \Phi) + \frac{\lambda}{4} (\Phi^\dagger \Phi)^2, \end{aligned} \tag{1.2}$$

where D_μ is the covariant derivative and $V(\Phi)$ is the Higgs potential, which is parameterized by the the mass parameter μ and self-coupling constant λ. The Lagrangian 1.2 is invariant under the transformation of $SU(2)_L \otimes U(1)_Y$ symmetry. While the coupling constant λ is required to be $\lambda > 0$ for a stable vacuum, μ^2 can be considered in two scenarios. In case of $\mu^2 > 0$, the potential $V(\Phi)$ is stable at the ground state of $|\Phi| = 0$. On the other hand, in case of $\mu^2 < 0$, the potential has a local maximum at

$$|\Phi|^2 = \frac{-\mu^2}{2\lambda} = \frac{1}{2}\nu^2, \tag{1.3}$$

where ν is the vacuum expectation value. If the Φ takes finite minimum value, the $SU(2)_L \otimes U(1)_Y$ symmetry is spontaneously broken. The ϕ^+ and the imaginary part of ϕ^0 are absorbed into massive $W^\pm$ and Z bosons as their longitudinal modes. Such an absorption process is referred to as the Higgs mechanism. After the Higgs mechanism occurs, the complex scalar field Φ can be expressed by

$$\Phi = \frac{1}{\sqrt{2}} \begin{pmatrix} 0 \\ \nu + h \end{pmatrix}, \tag{1.4}$$

where h represents the field that creates the Higgs boson. Using this equation, the Lagrangian can be expanded as

$$\begin{aligned} L_{Higgs} &= \frac{1}{2}(\partial_\mu h)^2 + \frac{1}{4}g^2 W_\mu W^\mu (\nu + h)^2 \\ &+ \frac{1}{8}(\nu\sqrt{g^2 + g'^2})(\nu + h)^2 Z_\mu Z^\mu \\ &+ \frac{\mu^2}{2}(\nu + h)^2 - \frac{\lambda}{16}(\nu + h)^4, \end{aligned} \tag{1.5}$$

where the W and Z represents the physical W and Z fields, and g and g' represents $SU(2)_L$ and $U(1)_Y$ gauge coupling constants, respectively. The Higgs mechanism generates mass terms of W, Z and the Higgs bosons leaving the photon and gluon mass-less in the SM Lagrangian including 1.5. The masses of the W and Z bosons are extracted from equation (1.5) as:

$$m_H = \sqrt{2\lambda\nu^2}, \quad m_W = \frac{g\nu}{2}, \quad m_Z = \frac{\nu}{2}\sqrt{g^2 + g'^2}. \tag{1.6}$$

The W and Z boson masses (m_W and m_Z) can be predicted by the SM as shown in equation (1.6), those are consistent with the experimental results. However, the Higgs boson mass (m_H) contains a free parameter λ, that is the Higgs self-coupling constant.

1.1.2 Yukawa Couplings

The Higgs field in the SM also generates fermion masses by introducing interactions between the same complex scalar $SU(2)$ doublet Φ, a left-handed fermion SU(2) doublet Ψ_L and a right-handed fermion singlet Ψ_R, referred to as Yukawa couplings. The general Lagrangian for such interactions can be de-

scribed as

$$L_{Yukawa} = -Y_f(\bar{\Psi}_L \Psi_R)\Phi + h.c., \tag{1.7}$$

where Y_f is the Yukawa coupling constant between the Higgs boson and fermions, and $h.c.$ represents the Hermitian conjugate. By introducing the spontaneous symmetry breaking with the Higgs field of equation (1.4), the Lagrangian is expanded as

$$L_{Yukawa} = -\frac{\nu Y_f}{\sqrt{2}}(\bar{\Psi}_L \Psi_R + \bar{\Psi}_R \Psi_L)(1 + \frac{h}{\nu}). \tag{1.8}$$

Thus, the fermion mass is provided as

$$m_f = \frac{\nu Y_f}{\sqrt{2}}. \tag{1.9}$$

In case of quarks, the field provides a mass term also for up side of the $SU(2)$ quark doublet by converting the Higgs doublet Φ to Φ'. The general Lagrangian for quark Yukawa couplings is described as:

$$\begin{aligned} L_{Yukawa} &= -Y_d(\bar{\Psi}_{d,L}\Psi_{d,R})\Phi - Y_u(\bar{\Psi}_{u,L}\Psi_{u,R})\Phi^{'} + h.c. \\ &= -\frac{\nu Y_d}{\sqrt{2}}(\bar{\Psi}_{d,L}\Psi_{d,R} + \bar{\Psi}_{d,R}\Psi_{d,L})(1 + \frac{h}{\nu}) - \frac{\nu Y_u}{\sqrt{2}}(\bar{\Psi}_{u,L}\Psi_{u,R} + \bar{\Psi}_{u,R}\Psi_{u,L})(1 + \frac{h}{\nu}), \\ \Phi^{'} &= \begin{pmatrix} -\phi_0 \\ \phi^- \end{pmatrix} = \frac{1}{\sqrt{2}} \begin{pmatrix} \nu + h \\ 0 \end{pmatrix}, \end{aligned} \tag{1.10}$$

.

In both cases, the fermion mass can be described by the equation (1.9). While the Higgs mechanism is an excellent theory that explains generation mechanism of both boson and fermion masses, it has an uncertain aspect that cannot predict absolute values of masses since the Yukawa coupling constants Y_f are free parameters. These values must be experimentally measured for the verification of the Higgs mechanism, which is one of main scopes of this thesis.

1.2 Phenomenology of the Higgs Boson at the LHC

1.2.1 Production Processes

The Higgs boson production at the LHC is dominated by four processes: gluon fusion (ggF), vector boson fusion (VBF), vector boson associated (VH) and top quark associated ($t\bar{t}H$) processes. Leading-order (LO) level Feynman diagrams of signal production processes considered in this analysis are shown in Fig. 1.1.

The ggF process has the largest cross section in the four processes. The Higgs boson produced via a heavy quark loop from gluons, where a heavy quark is dominated by a top quark loop due to a large Yukawa coupling. Thus, the discovery of the ggF indicates an indirect confirmation of Yukawa coupling.

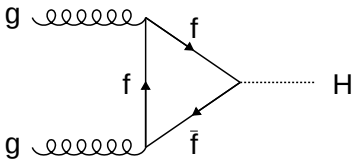

(a) Gluon fusion (ggF)

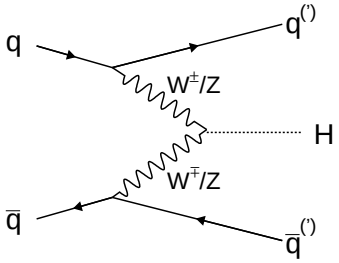

(b) Vector boson fusion (VBF)

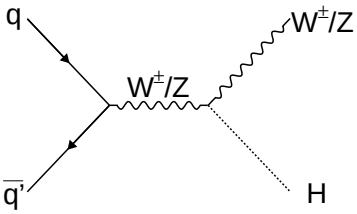

(c) Vector boson associated (VH)

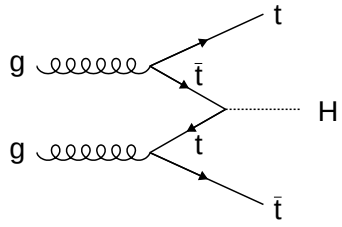

(d) top pair associated ($t\bar{t}H$)

Fig. 1.1: Leading-order Feynman diagrams of the Higgs boson production processes at the LHC.

The final state of the process is only the Higgs boson, and therefore the process is relatively hard to separate from background events in the analysis. The VBF process has the second largest cross section. In this process, typically two jets in the forward and backward regions of the detector are associated. The characteristic signature is useful to suppress background events in the analysis. The VBF process provides the information of the direct coupling of the Higgs boson and weak gauge bosons. In the VH process, the Higgs boson is produced associated with the vector boson (Z or W boson). In this process, there are several final states depending on decay products of the vector boson. Especially, the final state contains leptons is effective to suppress background, such as multi-jet events. The $t\bar{t}H$ process has the Higgs boson is produces associated with top quark pair. This process provides the information of the top Yukawa coupling. However, this process does not contribute significantly to signal regions in this thesis due to the smallest cross section. The production cross section for each process and inclusive cross sections at $\sqrt{s} = 7, 8$ and 14 TeV are shown in Fig. 1.2.

1.2.2 Decay Modes and Experimental Search Channels

The branching ratio of the Higgs boson depends on masses of the decay products as shown in Fig. 1.3 (a) because the Higgs boson coupling is proportional to the masses. In the interested region around the measured Higgs boson mass of $m_H \sim 125$ GeV, the dominant decay mode is the $H \to b\bar{b}$ decay with the branching ratio of $\sim 57.7\%$. The second largest decay mode is the $H \to WW$ decay with the branching ratio of $\sim 21.5\%$. This decay mode is suppressed in the region since one of W bosons can be produced with on-shell. The third largest decay mode is the $H \to \tau\tau$ decay with the branching ratio of $\sim 6.3\%$.

Although the Higgs boson decays into several particles, certain combinations of production processes and decay modes can be used taken into account trigger limitations and background contributions. The

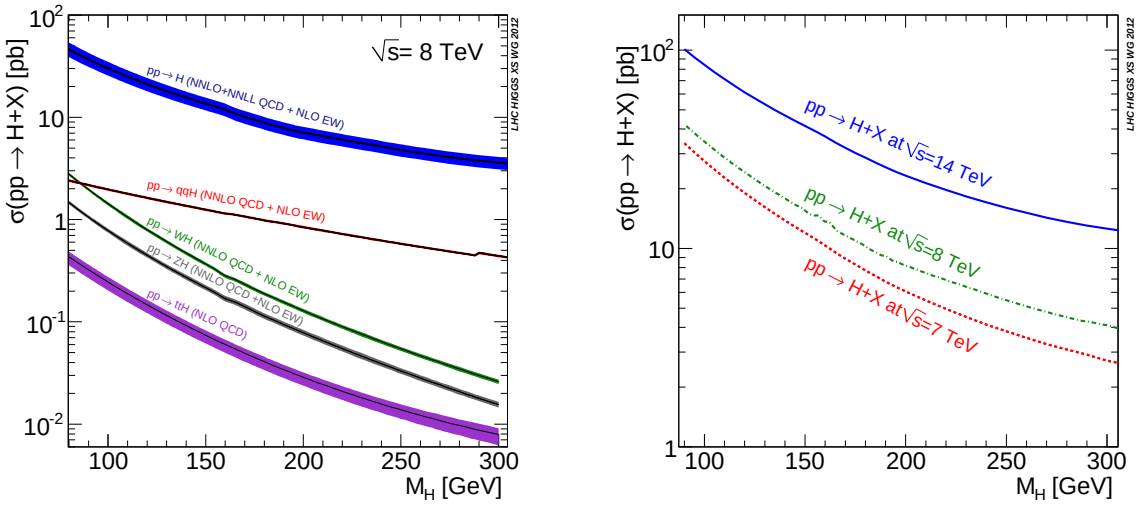

(a) (b)

Fig. 1.2: (a) Production cross sections of the SM Higgs boson of main production processes at $\sqrt{s} = 8$ TeV and (b) inclusive cross sections at $\sqrt{s} = 7, 8$ and 14 TeV as a function of m_H.

product of production cross section times branching ratio (event rate) for each important experimental search channel at the LHC is shown in Fig. 1.3 (b). The $H \to \tau\tau$ channel has the largest event rate around the region of $m_H \sim 125$ GeV.

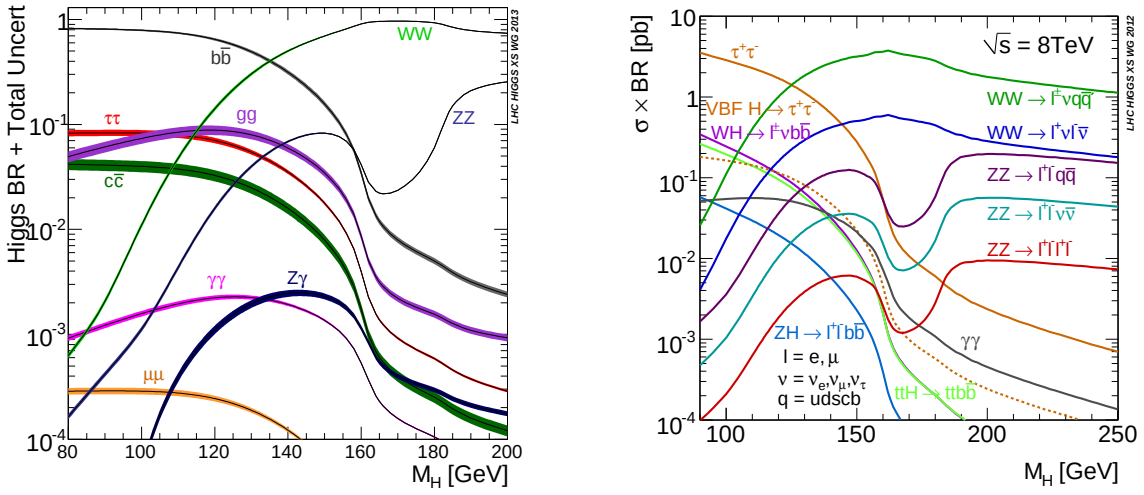

(a) (b)

Fig. 1.3: (a) Branching ratios of the SM Higgs boson and (b) production cross sections at $\sqrt{s} = 8$ TeV times branching ratio for experimentally important processes (b) as a function of m_H.

1.2.3 Experimental Status of the Higgs Boson Searches

The Higgs boson has been searched experimentally for a long time since the Higgs mechanism was proposed. While the Higgs boson mass is a free parameter in the SM as mentioned in Section 1.1.1, the mass range can be constrained by mass measurements of W boson and top quark because the W boson mass depends on the top quark and the Higgs boson masses through radiative effects [6]. the Higgs boson is predicted to contribute their measured masses through loop corrections. The first Higgs boson search was indirectly performed based on two dimensional mass fit of W boson and top quark by the LEP experiments [7], where the top quark mass was estimated by electroweak measurements. This indirect search was updated with the precisely measured W boson mass from the LEP2 and the Tevatron, and the directly measured top quark mass from the Tevatron [8]. The Higgs boson mass is favoured in a lower mass range ($30\,\text{GeV} < m_H < 300\,\text{GeV}$) by the indirect search.

Based on the result, the direct Higgs boson searches were performed at the LEP/LEP2 and the Tevatron experiments. The LEP2 experiments finally set a lower exclusion limit of the Higgs boson mass of $m_H > 114\,\text{GeV}$ at 95% confidence level using the vector boson associated production (VH), where a main contribution from the $(H \to b\bar{b})(Z \to q\bar{q})$ final state [9]. The Tevatron experiments (CDF and DØ experiments) are also performed the direct search with several experimental search channels. These channels are combined, and the Tevatron set an exclusion limit of the Higgs boson mass of two regions: $90\,\text{GeV} < m_H < 109\,\text{GeV}$ and $149\,\text{GeV} < m_H < 182\,\text{GeV}$ at 95% confidence level [10]. Main contributions of lower and higher limits are from the $VH \to b\bar{b}$ and the $H \to WW^* \to \ell^+\nu\ell^-\bar{\nu}$ channels, respectively. The $H \to \tau\tau$ search was performed in the CDF experiment, the upper limit of the SM cross section times branching ratio ($\sigma_{\text{SM}} \times \text{B}(H \to \tau\tau)$) is 16.4 at $m_H = 125\,\text{GeV}$ [11].

The LHC started the operation in 2010, and the ATLAS and CMS experiments collected data with the center-of-mass energy of 7 TeV in 2010-2011 and 8 TeV in 2012. In July 2012, both experiments reported the discovery of a new particle, that is most likely the Higgs boson, with a mass of about $125\,\text{GeV}$, the integrated luminosities are $4.8(5.1)\,\text{fb}^{-1}$1 at $\sqrt{s} = 7\,\text{TeV}$ and $5.8(5.3)\,\text{fb}^{-1}$ at $\sqrt{s} = 8\,\text{TeV}$ for the ATLAS (CMS) experiment [12, 13]. The discovery was mainly provided from diboson decay channels, i.e., the $H \to \gamma\gamma$, $H \to ZZ$ and $H \to WW$ channels. Figure 1.4 shows the p-value of the background-only hypothesis as a function of m_H, which is obtained from the combination of results from the $H \to \gamma\gamma$ and $H \to ZZ$ and $H \to WW$ searches. With full dataset in 2011-2012, corresponding to an integrated luminosity of up to $25\,\text{fb}^{-1}$, the measurement of spin and parity quantum numbers of the discovered Higgs boson was performed by both experiments. The results are consistent with the SM prediction of the Higgs boson with $J^P = 0^+$ [14] (see Section 1.3.2).

The discovery of the Higgs boson was made by the $H \to \gamma\gamma$, $H \to ZZ$ and $H \to WW$ channels. Therefore, it is important to measure properties of the discovered Higgs boson for understanding the nature of electroweak symmetry breaking. The current main topics of the Higgs analysis are an observation of the coupling between the Higgs boson and ferimons, and its property measurements.

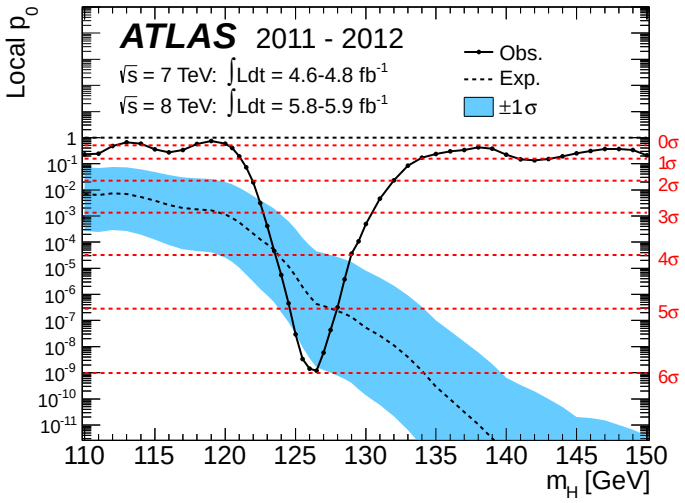

Fig. 1.4: Observed local p_0 (solid line) as a function of m_H. The dashed curve shows the expected local p_0 under the hypothesis of the SM Higgs boson signal at that mass with its plus/minus one sigma band. The horizontal dashed lines indicate the p-values corresponding to significances of 1 to 6 σ [12].

1.2.4 Phenomenology of the $H \to \tau\tau$

The $H \to \tau\tau$ channel plays an important role in the Higgs boson search as fermion channels due to its high event rate and relatively clean signature in the final state. This section introduces properties and decay modes of a τ lepton, and an experimental signature of the $H \to \tau\tau$ final state.

Tau Lepton Decays

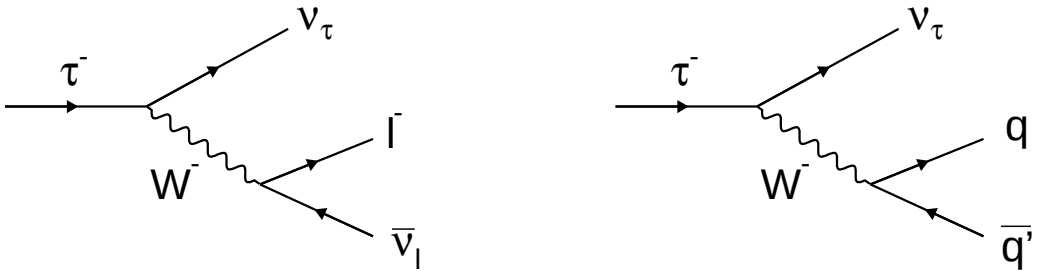

Fig. 1.5: Feynman diagrams of τ lepton decay for (a) leptonically and (b) hadronically.

The tau lepton [15] is the heaviest lepton with a mass of 1.78 GeV, a mean life time of $(290.6 \pm 1.0) \times 10^{-15}$s and an average decay length of 87.11 μm. The tau lepton typically decays before reaching the active region of the ATLAS detector. The decay is classified into leptonically $\tau \to \ell\nu_\ell\nu_\tau$ ($\ell = e/\mu$) and hadronically $\tau \to$ hadrons ν_τ, as shown in Fig. 1.5. The leptonic decay is further classified into electron

and muon decays, and the total branching ratio is $\sim 35\%$. The lepton from the leptonic decay is referred to as τ_ℓ in this thesis. The hadronic decay has several decay modes corresponding to the number and kind of hadrons, and the total branching ratio is $\sim 65\%$. Decay products of the hadrinic decay are referred to as τ_{had} in this thesis. One and three charged hadrons from the hadronic decay are referred to as 1-prong and 3-prong decay, respectively. The hadronic decay is further classified corresponding to the number of neutral hadrons, mainly neutral pions. A typical process of the decay into 1-prong τ_{had} associated with one neutral pion is $\tau^\pm \to \rho^\pm \left(\to \pi^\pm\pi^0\right)\nu_\tau$ process, and associated with two neutral pions is $\tau^\pm \to a_1^\pm \left(\to \pi^\mp\pi^0\pi^0\right)\nu_\tau$ process, where ρ and a_1 are short-lived mesons with a mass of $\sim$ 770 MeV and $\sim$ 1260 MeV, respectively. A typical process of the 3-prong decay is $\tau^\pm \to a_1^\pm \left(\to \pi^\pm\pi^\mp\pi^\pm\right)\nu_\tau$ process. Dominant decay modes of a tau lepton are listed in Table 1.1 with their branching ratios.

Decay modes	Branching ratio [%]
leptonic decay	35.24 ± 0.08
$\tau^- \to e^-\nu_e\nu_\tau$	17.83 ± 0.04
$\tau^- \to \mu^-\nu_\mu\nu_\tau$	17.41 ± 0.04
hadronic decay	64.76 ± 0.21
$\tau^- \to \pi^-\nu_\tau$	10.83 ± 0.06
$\tau^- \to \pi^-\pi^0\nu_\tau$	25.52 ± 0.09
$\tau^- \to \pi^-\pi^0\pi^0\nu_\tau$	9.30 ± 0.11
$\tau^- \to \pi^-\pi^0\pi^0\pi^0\nu_\tau$	1.05 ± 0.07
$\tau^- \to K^-\nu_\tau$	0.700 ± 0.010
$\tau^- \to K^-\pi^0\nu_\tau$	0.429 ± 0.015
$\tau^- \to \pi^-\pi^-\pi^+\nu_\tau$	8.99 ± 0.06
$\tau^- \to \pi^-\pi^-\pi^+\pi^0\nu_\tau$	2.70 ± 0.08

Table 1.1: Summary of tau lepton decay modes and corresponding branching ratios [15].

$H \to \tau\tau$ channel

Corresponding to the tau lepton decay, the $H \to \tau\tau$ channel can be classified into three channels: the fully leptonic channel $H \to \tau_\ell\tau_\ell$, the fully hadronic channel $H \to \tau_{\text{had}}\tau_{\text{had}}$, and the lepton-hadron channel $H \to \tau_\ell\tau_{\text{had}}$, with branching ratios of 12.4%, 42% and 45.6%, respectively. Experimental search sensitivity of each channel is determined corresponding to the branching ratio and the number of neutrinos from τ lepton decays (see Section 4.1). The lepton-hadron channel has the largest event rate and a clean final state due to the presence of the lepton, and they leads this channel to have the highest sensitivity in the $H \to \tau\tau$ search. While the fully hadronic channel has the same degree of the branching

ratio with the lepton-hadron channel, this channel suffers from large multi-jet backgrounds. This channel is the second channel in the $H \to \tau\tau$ search. As a feature of this channel, this channel is able to precisely reconstruct kinematic distributions than other two channels due to a less number of neutrinos in the final state, and it is useful in both the search and property measurements of the Higgs boson. While the fully leptonic channel has the cleanest final state because of two leptons, its branching ratio is the smallest and the resolution of reconstructed kinematic distributions is lower than other channels due to the presence of four neutrinos in the final state. This channel is the third channel in the $H \to \tau\tau$ search. The three channels are independently analyzed, and then the $H \to \tau\tau$ search result are obtained by a combination of three channels.

1.3 CP Measurement of the Higgs Boson

1.3.1 Two Higgs Doublet Model

After the observation of the coupling between the Higgs boson and τ leptons, one of the most important remaining question is whether the observed Higgs boson is the SM Higgs boson or a part of an extended Higgs sector predicted by BSM theory models. The SM predicts the Higgs boson has a CP-even state, while a CP-odd Higgs boson appears in several BSM theories based on the two Higgs doublet model (2HDM) [16, 17], which is a minimal extension from the SM Higgs sector. In the 2HDM, two complex scalar doublets Φ_1 and Φ_2 are introduced as:

$$\Phi_i = \begin{pmatrix} \phi^+ \\ \frac{1}{\sqrt{2}}(\nu_i + h_i + iz_i) \end{pmatrix}, \ (i = 1, 2). \tag{1.11}$$

Introducing the two doublets, the general potential of the Higgs field $V(\Phi_1, \Phi_2)$ can be expressed by:

$$\begin{aligned} V(\Phi_1, \Phi_2) &= m_{11}^2 \Phi_1^\dagger \Phi_1 + m_{22}^2 \Phi_2^\dagger \Phi_2 - (m_{12} \Phi_1^\dagger \Phi_2 + h.c) + \frac{\lambda_1}{2}(\Phi_1^\dagger \Phi_1)^2 + \frac{\lambda_2}{2}(\Phi_2^\dagger \Phi_2)^2 \\ &+ \lambda_3 (\Phi_1^\dagger \Phi_1)(\Phi_2^\dagger \Phi_2) + \lambda_4 (\Phi_1^\dagger \Phi_2)(\Phi_2^\dagger \Phi_1) + \frac{\lambda_5}{2}\left[(\Phi_1^\dagger \Phi_2)^2 + h.c.\right], \end{aligned} \tag{1.12}$$

where λ_{1-5} represents coupling constants, and m_{11},m_{22} and m_{12} are mass parameters. The Higgs doublets 1.11 have eight degrees of freedom in total. After spontaneous symmetry breaking, three of them are absorbed to give mass to the W and Z bosons. Assuming a CP-symmetry conservation, the remaining five degrees of freedom correspond to five physical Higgs bosons: two neutral CP-even bosons (h and H), one neutral CP-odd boson (A) and a pair of charged bosons ($H^\pm$). After all, the parameters in the above Higgs potential are converted into the masses of five bosons, the ratio of the vacuum expectation values of two doublets ($\tan\beta \equiv \nu_2/\nu_1$), the mixing angle between two CP-even bosons (α) and the potential parameter (m_{12}^2). In addition, this model can be classified into two types, referred to as type I and type II 2HDM, those are distinguished by the structure of Yukawa coupling. All fermions couple to only Φ_2 in type I 2HDM, while up-type fermions couple to Φ_2 and down-type fermions couple to Φ_1 in type II. Although the choice of two types depends on theory models, the CP-even and CP-odd Higgs bosons

are included in both types. The typical examples of the theory including two Higgs doublets are followings: the minimal super-symmetric SM (MSSM) [18–21], the axion model [22] and the baryogenesis model [23]. The measurement of the CP state of the discovered Higgs boson is of primary importance to determine whether it is the SM (CP-even) Higgs boson or the BSM (CP-odd) Higgs boson.

1.3.2 Experimental Status of the CP Measurements of the Higgs Boson

With the discovery of the Higgs boson, the measurement of the spin and CP quantum numbers were performed by the ATLAS and the CMS experiments based on di-boson decay channels: the $H \to \gamma\gamma$, the $H \to ZZ^* \to 4\ell$ and the $H \to WW^* \to \ell\nu\ell\nu$ channels [14,24]. The analysis dataset corresponding to an integrated luminosity of $4.6(5.1)$ fb^{-1} collected at $\sqrt{s} = 7$ TeV and $20.3(19.7)$ fb^{-1} collected at $\sqrt{s} = 8$ TeV. In order to test the SM prediction of the Higgs boson with $J^P = 0^+$, alternative hypotheses of $J^P = 0^-$, 1^+, 1^- and 2^+ are studied. Focusing on the $H \to ZZ^* \to 4\ell$ as a typical example, the measurement was performed with total eight discriminant variables, five angle variables in the four-body decay, and invariant masses of lepton pairs and four leptons. Multivariate analysis was used to discriminate the $J^P = 0^+$ hypothesis from each alternative hypothesis. The results exclude all of the alternative models in favour of the SM Higgs boson hypothesis at more than 97.8% confidence level. Figure 1.6 shows an example distribution of the test statistics of the Higgs boson with $J^P = 0^+$ (SM), and with $J^P = 0^-$ (BSM) hypotheses in the ATLAS experiment, where the exclusion limit is 97.8% confidence level. Although the result indicates that the Higgs boson in di-boson channels is consistent with the SM, it is important to test the consistency with the fermion final states. Moreover, the CP-odd Higgs boson must decay into di-boson via a fermion loop, so that the direct CP measurement can be performed by only fermion final states. This is the primary motivation of the CP measurement in the $\tau\tau$ final state.

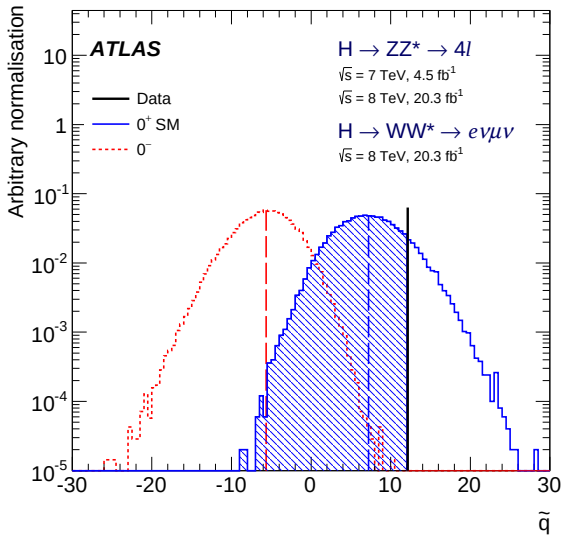

Fig. 1.6: An example distribution of the test statistic q for the combination of the $H \rightarrow$ZZ$^* \rightarrow 4\ell$ and the $H \rightarrow WW^* \rightarrow \ell\nu\ell\nu$ channels in the ATLAS experiment. The solid black line represents observed data, while the solid blue line and the dashed red line represent the Higgs boson with $J^P = 0^+$ (SM), and with $J^P = 0^-$ (BSM) hypotheses, respectively [14].

CHAPTER 2

LHC and ATLAS detector

The analysis in this thesis uses the data collected by the ATLAS (A Toroidal Lhc ApparatuS) detector in collisions of proton-proton delivered by the Large Hadron Collider (LHC). In this chapter, the LHC accelerator complex and the ATLAS detector configurations are summarized.

2.1 Large Hadron Collider

The LHC [25] is proton-proton circular collider located at European Organization for Nuclear Research (CERN) in Geneva, Switzerland. The collider is arranged in an underground circular tunnel at a depth of ranging from 50m to 175m with a circumference of 27km, which was initially constructed for the Large Electron Positron Collider (LEP) experiment. The LHC is designed to provide center of mass energies up to $\sqrt{s} = 14$ TeV with instantaneous luminosity of over 10^{34} cm^{-2} s^{-1}. The accelerator chain located at CERN increases the energy of proton beams in stages and the chain is enable to be achieved such performance finally at the LHC main ring.

2.1.1 Accelerator Chain

The protons, obtained from ionizing hydrogen gas, are injected to a linear accelerator (LINAC2) at first, and they are accelerated to 50 MeV. The protons are then grouped into bunches by Radio-Frequency (RF) cavities, and the proton bunches are injected into a series of accelerators : Proton Synchrotron Booster (PSB), Proton Synchrotron (PS), Super Proton Synchrotron (SPS). The proton beam is accelerated and the energy is increased to 1.4 GeV, 25 GeV and 450 GeV, respectively. Finally, the proton beam is injected into the LHC main ring and they are accelerated to the designed energy. The proton accelerator chain is summarized in Fig. 2.1.

2.1.2 LHC Run-1 Data Taking

The first run of the LHC, referred to as "LHC Run-1", was successfully finished in 2013. The initial design of the LHC is to collide proton beams at $\sqrt{s} = 14$ TeV with instantaneous luminosity of over 10^{34} cm^{-2} s^{-1}. During initial operation in 2008, a large section of the superconducting magnets in the LHC are quenched. It was decided to reduce the energy of the LHC for the initial run during a repair of these magnets and an addition of quench protections. After the repairing, in 2010 and 2011, the LHC was operated with the energy of proton beams of 3.5 TeV, producing center-of-mass energy

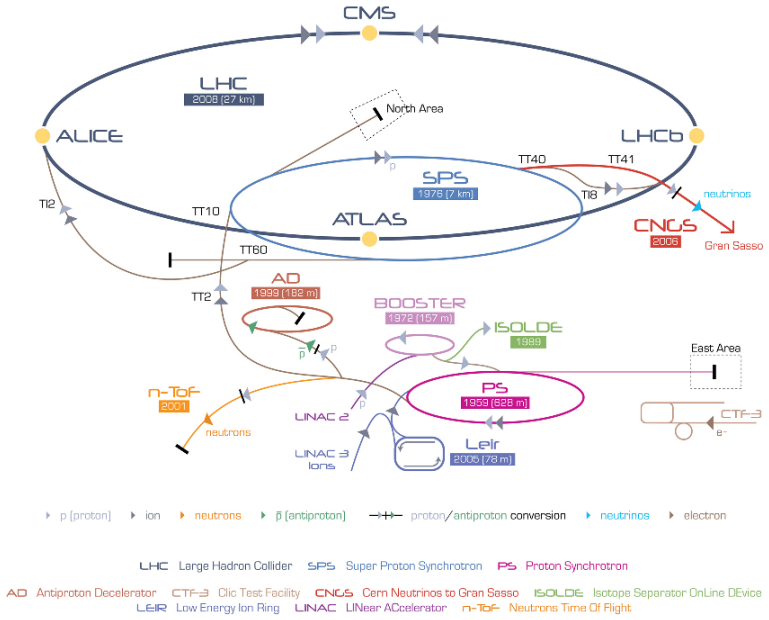

Fig. 2.1: A overview of the CERN accelerator chain [26]

$\sqrt{s}$ = 7 TeV. In 2010, proton-proton collisions corresponding to an integrated luminosity of 48.1 pb^{-1} were delivered to the ATLAS experiment with a recording efficiency of 93.6%. The beam intensity was increased after that, and the collision data was collected corresponding to an integrated luminosity of 5.46 fb^{-1} during the 2011 data taking, with a recording efficiency of 93.5%. In 2012, the energy of proton beams increased to 4 TeV, producing $\sqrt{s} = 8$ TeV. The collision data was collected corresponding to an integrated luminosity of 23.3 fb^{-1} with a recording efficiency of 93.5%. LHC operation parameters are summarized in Table 2.1, compared to design parameters. The analysis presented in this thesis is performed with the data taken in 2011 and 2012.

Parameters	Design	2011	2012
Center-of-mass energy [TeV]	14TeV	7TeV	8TeV
Beam energy [TeV]	7TeV	3.5TeV	4TeV
Bunch spacing [ns]	25	50	50
Number of bunches	2808	1318	1318
Number of protons per Bunch	1.15×10^{11}	1.15×10^{11}	1.15×10^{11}
Peak Luminosity [cm^{-2} s^{-1}]	1.0×10^{34}	3.7×10^{33}	7.7×10^{33}

Table 2.1: LHC beam parameters of 2011, 2012 and original design

Data Quality

The recorded data of the ATLAS detector in 2011 and 2012 correspond to an integrated luminosity of 5.08 fb^{-1} and 21.3 fb^{-1}, respectively. However, the data must be satisfied a data quality criteria. The ATLAS data taking is operated in each period defined by the ATLAS data acquisition system, referred

to as “Run”. The Run is subdivided into “luminosity block”, which holds each integrated luminosity information. The ATLAS monitoring systems of each sub-detector and dedicated data quality shifters check qualities of the recorded data for each luminosity block. The quality information of luminosity block is listed run by run, so-called “Good Run List”, and it is used in physics analyses to ensure that the analyzed data is not affected by detector failures. The integrated luminosity of the good quality data in 2011 and 2012 is 4.25 fb^{-1} and 20.3 fb^{-1}, respectively. Figure 2.2 (a) shows the integrated luminosity with respect to operation times for delivered, recorded and good quality data.

Pileups

Due to a high instantaneous luminosity, single bunch crossing produces multiple proton-proton interactions, so-called “pileup”. The number of interactions per bunch crossing depends on run conditions, while typical events have the average number of 20.7 (9.1) in 2012 (2011) data. Figure 2.2 (b) shows distributions of the mean number interactions per crossing $< \mu >$ in 2011 and 2012. The pile-up events affects adversely to physics analyses because additional tracks and energy deposits of particles from the pileup events give ambiguity of physics object reconstructions and identifications. In order to model pileup events in simulation samples, a dedicated $< \mu >$ rescaling is performed (see Section 4.3.2).

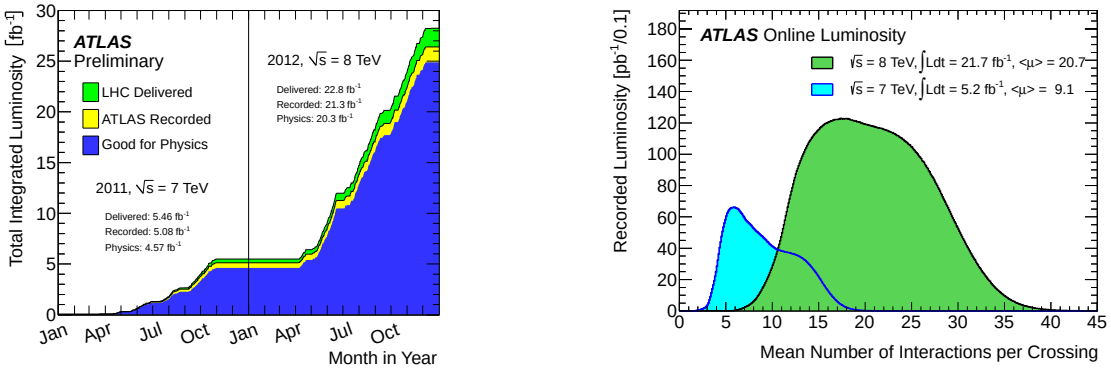

(a) (b)

Fig. 2.2: (a) The integrated luminosity with respect to operation time for delivered (green), recorded (yellow) and good quality data (blue). (b) The $< \mu >$ distributions in 2011 (blue) and 2012 (green) [27].

2.2 ATLAS Detector

The ATLAS [28–30] detector is a general purpose detector located at one of the proton-proton collision point of the LHC, and it is designed to verify the wide range of the interests of the SM (e.g. Higgs boson, top quark and so on) and search for the BSM physics at the LHC energy scale. To study these physics interests, the ATLAS detector reconstructs and identifies a wide range of objects, i.e. electrons, photons, muons, τ_{had}s, jets and the missing transverse energy ($E_{\text{T}}^{\text{miss}}$).

The ATLAS detector consists of a barrel region and two endcap region with several sub-detector systems, Tracking Detectors, Magnetic Systems, EM (Electromagnetic) Calorimeter, Hadron Calorimeter and Muon Spectrometer, in order from inner to outer. Schematic view of the ATLAS detector is shown in Fig. 2.3.

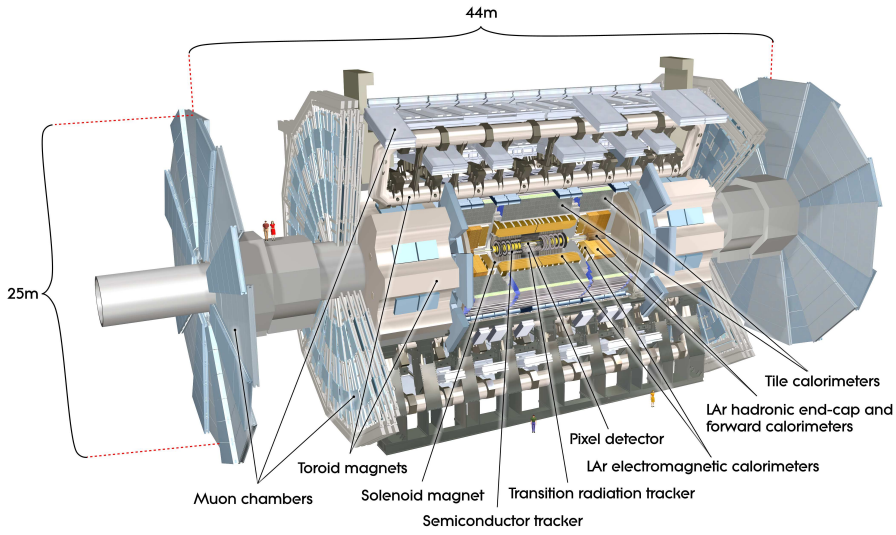

Fig. 2.3: Schematic view of the ATLAS Detector Systems. The dimensions are 25 m in height and 44 m in length. The overall weight of the detector is approximately 7 kilotons [28].

In the ATLAS coordinate system, the z axis is defined as the beam direction, and the x and y axis are defined as horizontal and vertical axes towards the center of the LHC ring, respectively. The azimuthal angle ϕ is defined with respect to the x axis between $-\pi$ and π, where $\phi = 0$ represents the positive x axis. The polar angle θ is defined with respect to the z axis between 0 and π, where $\theta = 0$ represents the positive z axis. The pseudo rapidity $\eta = 1/2 \ln \tan(\theta/2)$ is often used instead of the polar angle. The distance between objects in $\eta - \phi$ plane is defined as $\Delta R = \sqrt{\Delta\eta^2 + \Delta\phi^2}$. The transverse momentum and energy are defined as $p_{\mathrm{T}} = p \times \sin\theta$ and $E_{\mathrm{T}} = E \sin\theta$ in the x-y plane, respectively.

2.2.1 Inner Detector

The tracking system [31, 32], referred to as the Inner Detector (ID), is located at innermost part of the ATLAS detector in order to measure the momentum of charged particles and to determine the location of vertices. The ID consists of three sub-detectors, silicon pixel tracker (Pixel) [33, 34] ,semiconducting silicon micro-strip tracker (SCT) [35–37] and transition radiation tracker (TRT) [38–40]. The solenoid magnet system surrounds of the ID, which generates a 2 Tesla magnetic field. The layout and the coverage of the ID are summarized in Fig. 2.4 and Figure 2.5, respectively.

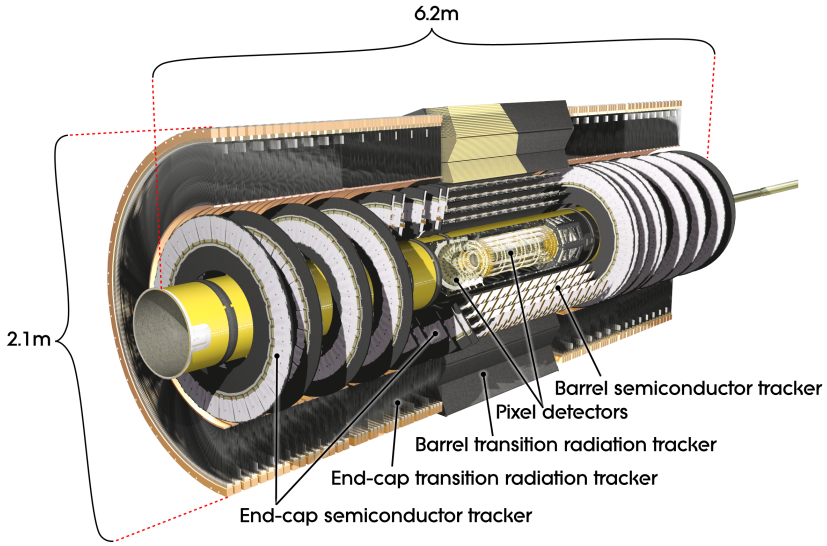

Fig. 2.4: Cut-away view of the ATLAS tracking detectors [28].

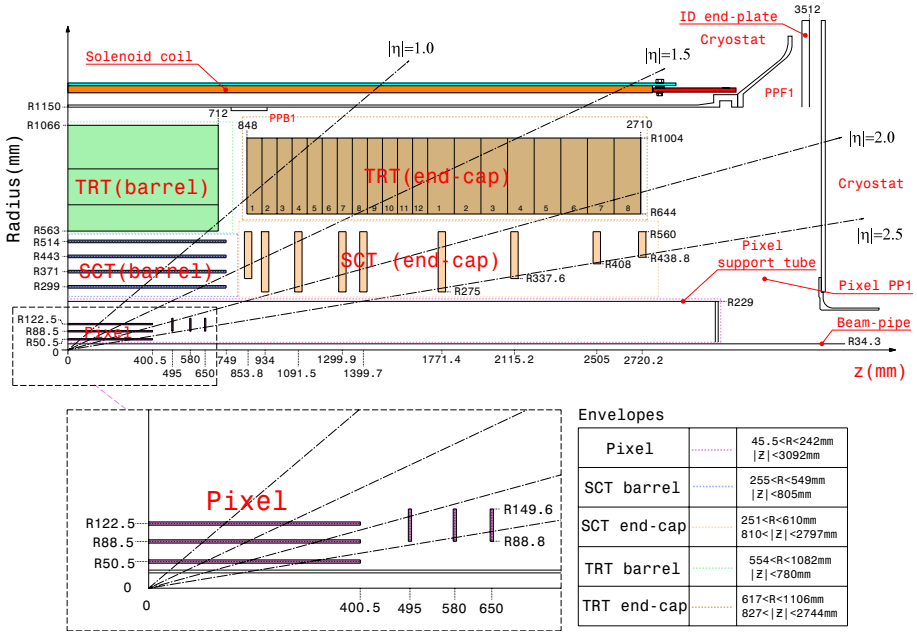

Fig. 2.5: Plan view of a quarter-section of the ATLAS tracking detectors with active dimensions and envelopes [28].

Pixel Detector

The Pixel detector is the innermost detector consisting of semiconduction silicon sensors with the pixel size $50 \times 400 \mu m^2$, with a coverage up to $|\eta| = 2.5$. The space point measurements of charged particle are performed with high resolution due to such small pixel size of the sensors. The innermost layer of this detector is located at the radius of 51 mm from the LHC beam pipe. The typical resolutions are $(\sigma_\phi, \sigma_z) = (10\ \mu\text{m}, 115\ \mu\text{m})$ in the barrel region, and $(\sigma_\phi, \sigma_r) = (10\ \mu\text{m}, 580\ \mu\text{m})$ in the endcap region.

The total number of readout channels is ~ 80.4 million.

Semi-Conductor Tracker (SCT)

The SCT is the second innermost detector consisting of eight strip layers, with a coverage up to $|\eta| = 2.5$, The unit of the SCT module consists of two layers of semiconducting silicon strip sensors with a pitch of 80 μm. The two layers are mounted in each module with a small stereo angle of 40mrad to measure the coordinates of ϕ and z. The typical resolutions of each module is $(\sigma_\phi, \sigma_z) = (17\ \mu\text{m}, 580\ \mu\text{m})$ in the barrel region, and $(\sigma_\phi, \sigma_r) = (17\ \mu\text{m}, 580\ \mu\text{m})$ in the endcap region. In total, the number of readout channels is ~ 6.3 million.

Transition Radiation Tracker (TRT)

The TRT is the outermost detector with a coverage up to $|\eta| < 2.0$. The TRT consists of straw tubes filled with a xenon based mixture gas with a gold plated tungsten wire. The length of each tube is 144 cm and 37 cm in the barrel and endcap region, respectively. Average 30 hits (maximum 36 hits) per track are provided by the TRT, and it allows to perform precision tracking. The TRT uses the transition radiation, which is emitted by charged particles when it passes a boundary of two dielectric materials. The intensity of the transition radiation is proportional to the Lorentz factor γ of the particle, which enables to the particle identification and the separation between electron and charged pion.

2.2.2 Calorimeters

The calorimeter system is located on the outside of the ID to measure the particle energy, with a coverage up to $|\eta| < 4.9$. The system consists of the electromagnetic (EM) and hadron calorimeters. The EM calorimeters are designed to be sensitive to the electromagnetic interactions in order to measure the energy of electrons and photons, while the hadron calorimeters are sensitive to hadronic interaction to measure the hadron energy. A cut-away view of the calorimeter system is shown in Fig. 2.6.

Electromagnetic Calorimeter

The EM calorimeter consists of ~ 1.5 mm accordion-shaped lead plates as absorbers and 2.1 mm gaps filled with the liquid argon as active layers. The energy of charged particles are measured by detecting ionization of charged particles inside the liquid argon. The maximum drift time is $450ns$ by applying a high voltage of $\sim 2,000$ V. This calorimeter separately consists of one cylindrical barrel calorimeter ($|\eta| < 1.475$) with a small gap of 4 mm at $|z| = 0$ and two wheel endcap calorimeters ($1.375 < |\eta| < 3.2$). Each calorimeter contains three different layers for high angular resolution and to detect full shower shapes. The first layer is mounted with a granularity of $\Delta\eta \times \Delta\phi = 0.0031 \times 0.098$ and $4.3\ X_0$ radiation length, referred to as strip layer. It allows to identify $\pi^0 \to \gamma\gamma$ decays, which is one of main background to photons [41] and is used in the identification of hadronically decaying τ lepton (see Section 3.4). The

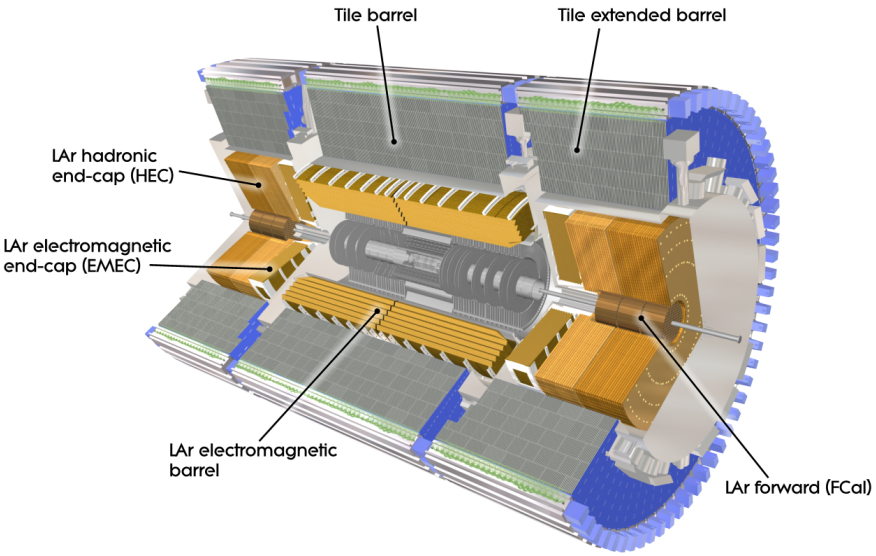

Fig. 2.6: Cut-away view of the ATLAS calorimeter system [28].

second layer has a granularity of $\Delta\eta \times \Delta\phi = 0.025 \times 0.0245$ with 16 X_0 radiation length, and the most of energy from EM shower is measured by this layer. The third layer measures the tails of EM shower, and it enables to distinguish EM showers from hadronic showers. The granularity of this layer is $\Delta\eta \times \Delta\phi = 0.050 \times 0.025$. In addition to three layers, one 11 mm thin layer, referred to as pre-sampler, is mounted in front of the strip layer, with a granularity of $\Delta\eta \times \Delta\phi = 0.025 \times 0.1$. The pre-sampler covers the range of $|\eta| < 1.8$ to correct the energy loss in materials before the EM calorimeter. A schematic view of the barrel module of the EM calorimeter is shown in Fig. 2.7.

Hadron Calorimeter

The hadron calorimeter is mounted surrounding the EM calorimeter, and it consists of one barrel calorimeter ($|\eta| < 1.7$), two endcap hadron calorimeters ($1.5 < |\eta| < 3.2$). The barrel calorimeter uses steel plates as absorber and scintillation tiles as active material, with a granularity of $\Delta\eta \times \Delta\phi = 0.1 \times 0.1$. The scintillation photons are guided by wavelength shifter fibers, and they are read out by photo-multiplier tubes. The endcap calorimeters use coppers and liquid argon gas as absorber and active media, respectively. Each calorimeter has the total thickness of 10 interaction lengths, it is sufficient to decrease punch-trough hadrons.

Additionally, the forward calorimeter is mounted to cover higher pseudo-rapidity region of $3.1 < |\eta| < 4.9$. This calorimeter is combined with EM and hadron calorimeters. The EM calorimeter uses copper, which length is optimized for EM interaction, as absorber, while the hadron calorimeter uses tungsten as absorber. Both calorimeters are filled with liquid argon gas as active media.

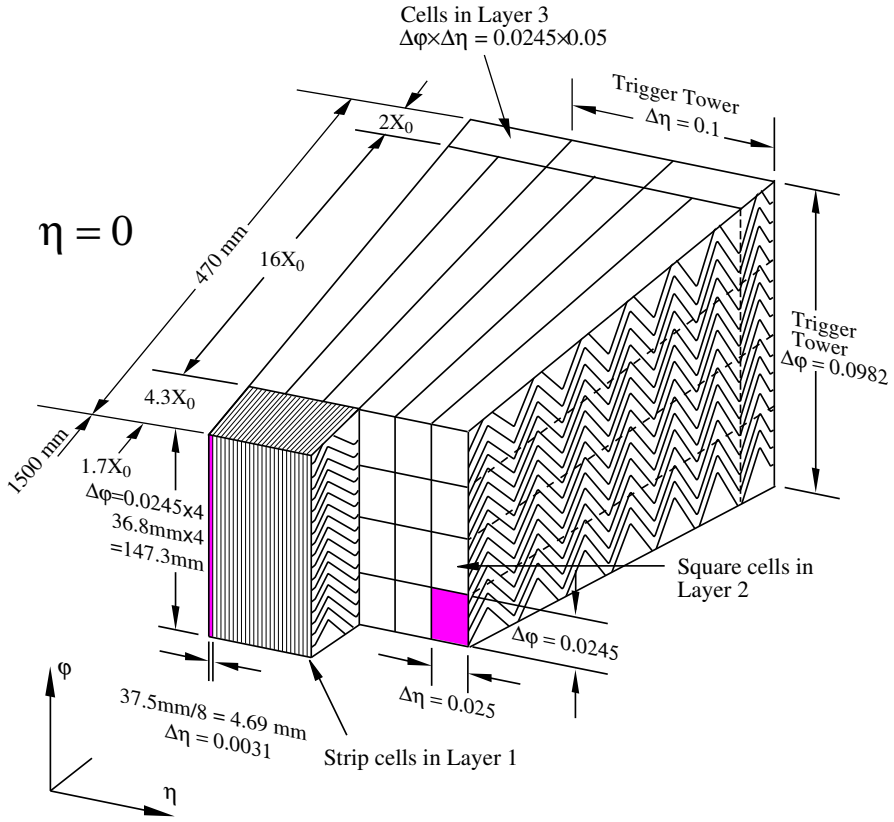

Fig. 2.7: Schematic view of the barrel module of the EM calorimeter [28].

2.2.3 Muon Spectrometer

The outermost detector in the ATLAS detector is the Muon Spectrometer (MS) with a coverage up to $|\eta| = 2.7$. The cut-away view of the MS is shown in Fig. 2.8. The MS consists of two precision tracking chambers and two trigger chambers, with air-core toroid magnet system. The muon momentum is measured from the deflection of the muon trajectory in the magnetic field. The two precision chambers consist of three layers of the Monitored Drift Tubes (MDT) for the pseudo-rapidity range of $|\eta| < 2.0$ and two layers of the Cathode Strip Chambers (CSC) for $2.2 < |\eta| < 2.7$. The MDT are made from multi-layers of tubes, while the CSC is multi-wire proportional chambers. Both chambers are filled with Ar/CO_2 mixture gas. Since the MDT and the CSC chambers require a wide time window of ~ 700 μs, two dedicated trigger chambers are equipped to provide fast responses, which satisfies the ATLAS level 1 trigger requirement of selecting events in every $25ns$. The Resistive Plate Chambers (RPC) consists of three layers for the barrel region ($|\eta| < 1.05$) and the Thin Gap Chambers (TGC) consists of three layers for the endcap region ($1.05 < |\eta| < 2.4$).

2.2.4 Trigger and Data Acquisition System

An average bunch crossing rate during data taking in 2011 and 2012 is $\sim$ 20 MHz, and it does not allow to continuously read out all information from the ATLAS detector due to limitations of the ATLAS

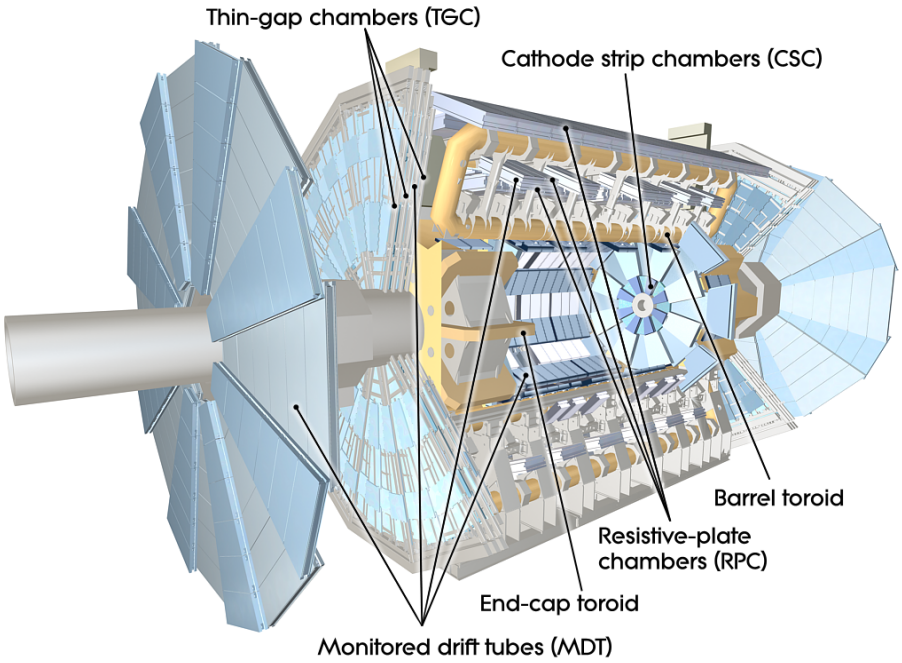

Fig. 2.8: Cut-away view of the ATLAS muon spectrometer [28].

storage and computing systems. Therefore, a trigger system is necessary to efficiently select interesting events. The ATLAS trigger system consists of three levels: the hard-ware based level 1 (L1) trigger, and the soft-ware based Level 2 (L2) and Event Filter (EF) triggers.

The L1 trigger makes trigger decisions within an average processing time of 2.5 μs using the limited information form the calorimeter and the MS, reducing the event rate to 75 kHz from initial $\sim$ 20 MHz. Coincidence information from the RPC and the TGC is used to trigger high p_{T} muons, while the calorimeter information with a low granularity of $\Delta\eta \times \Delta\phi = 0.1 \times 0.1$ is used to trigger electrons/photons, jets, τ_{had} and large transverse missing energy ($E_{\mathrm{T}}^{\mathrm{miss}}$). The L1 system sends information about signatures of triggered objects with their η and ϕ coordinates to the L2 trigger system. Figure 2.9 shows the block diagram of the L1 trigger and a schematic view of the electron/photon and τ_{had} trigger algorithms at the L1. The coordinate information is referred to as Region-Of-Interest (ROI).

The L2 trigger is a software-based system and can use the full detector information within the ROIs. The tracking information from the ID is available from the L2 and the energy information is more sophisticated with higher granularity than the L1. The event rate is reduced to 3.5 kHz within an average processing time of $\sim$ 49 ms.

The EF is the final stage trigger system to further select events from those passing the L2, and the event rate is reduced to $\sim$ 200 Hz within an average processing time of $\sim$ 4 sec. During data taking in 2012, the availability of storage and computing resources are increased, so that the output rate of the EF is increased to $\sim$ 400 Hz. the EF performs a full event reconstruction using the full detector granularity, and thereby the trigger objects at the EF are reconstructed with similar definitions of offline objects. Finally, the information of events passing the trigger system is recorded to the ATLAS storage system.

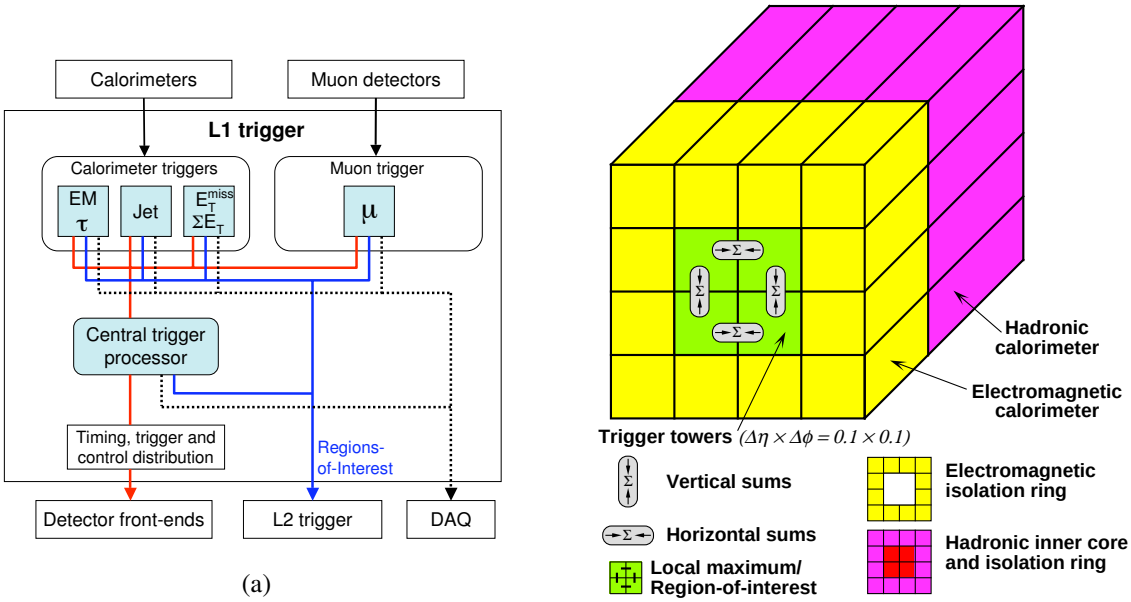

Fig. 2.9: (a) A block diagram of the ATLAS L1 trigger, and (b) a schematic view of electron/photon and τ_{had} trigger algorithms at L1 [28].

CHAPTER 3

Object Definition

This chapter describes online trigger algorithms and offline particle reconstruction algorithms. As discussed in Section 1.2.4, the $H \rightarrow \tau\tau$ analysis can be divided into three channels depending on τ decays. The analysis presented in this thesis focuses on the lepton-hadron and the fully hadronic channels. For online trigger algorithms, a single electron/muon trigger and a di-τ_{had} trigger are used in the lepton-hadron channel and in the fully hadronic channel, respectively. Physics objects used in this thesis are electrons, muons, τ_{had}s, jets and missing transverse energy. Reconstruction, identification and energy/momentum calibration algorithms are detailed for those objects in this Chapter. At First, track and vertex reconstruction algorithms are introduced in Section 3.1 as common inputs of particle reconstructions. Then, reconstruction algorithms of each physics object are detailed in Section 3.2, 3.3, 3.4, 3.5 and 3.6. A calorimeter cluster is also one of common inputs, and its reconstruction algorithm is described in Section 3.5

3.1 Tracks and Vertices

Track Reconstruction

Tracks originated from charged particle are one of common input of physics object reconstruction. Moreover, they are used to identify a primary vertex and other vertices. The track reconstruction is based on two algorithms, "inside-out" and "outside-in".

In the inside-out algorithm, the track reconstruction starts from track seeds constructed by all of the Pixel layers and a first layer of the SCT detectors. The seed tracks provide track candidates with their directional information, and then track candidates are defined in the ID by performing a fit with tracks segments and hits from the Pixel and SCT, where the fit includes global χ^2 and Kalman filter algorithms. Finally, the track candidate is extended to the TRT by refitting with additional hit in the TRT. The reconstructed track from the inside-out algorithm is required to have $p_{\text{T}} > 400$ MeV and $|\eta| < 2.5$.

The outside-in algorithm is performed after the track reconstruction using inside-out algorithm. In the algorithm, the track reconstruction starts from track segments of the TRT, and then they are extrapolated towards the ID. Finally, tracks are defined by performing the fit with tracks segments and hits from the Pixel and SCT, This algorithm aims to reconstruct tracks by charged particles from the secondary vertices, such as heavy flavor quarks/τ lepton decays and photon conversions. Both algorithms provide reconstructed tracks with their track parameters at a point of the closest approach (pca) from a reference point. The parameters consist of following five parameters (as illustrated in Fig. 3.1):

- κ: $\frac{1}{p_{\mathrm{T}}} \times \frac{q}{|q|}$ (q represents a charge)
- ϕ_0: the azimuthal angle between x axis and track direction at the pca in the transverse (x-y) plane
- θ: the polar angle between z axis and track direction in the longitudinal (r-z) plane ($r = \sqrt{\mathrm{x}^2 + \mathrm{y}^2}$)
- d_0: the distance between the pca and the reference point (impact parameter)
- z_0: the z axis coordinate of the pca.

The reference point is defined as the coordinate center of (x,y,z)=(0,0,0) in the track reconstruction, while the point is moved to a primary vertex position after a vertex reconstruction. The pca and track parameters are also propagated considering the track radius calculated using the field map of the ATLAS magnetic field. Physics objects that include charged particles are reconstructed based on these parameters.

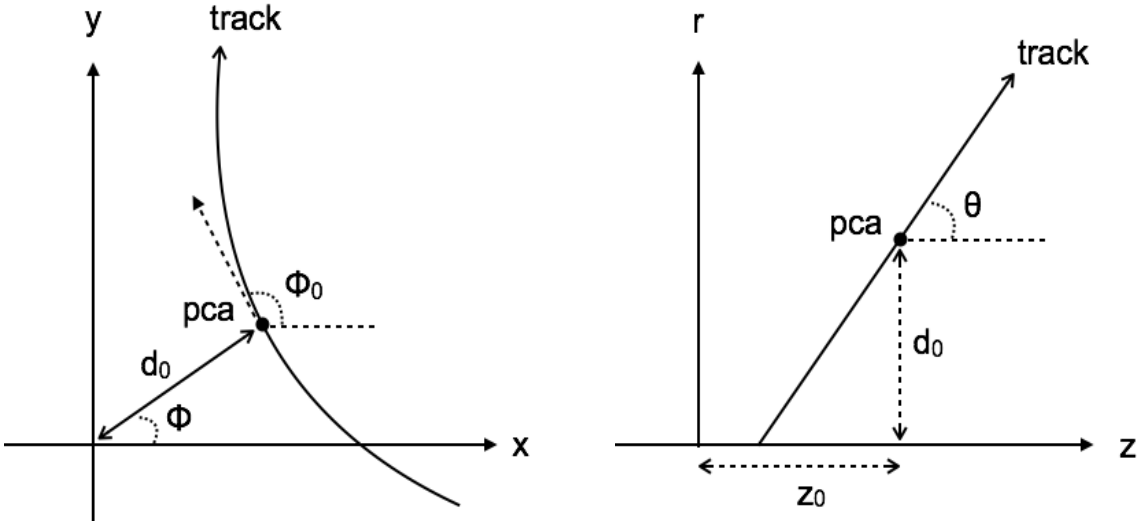

(a) (b)

Fig. 3.1: Illustration of track parameters in the (a) transverse and (b) longitudinal planes.

Vertex Reconstruction

Vertices are reconstructed using an "iterative vertex finding" algorithm [42,43]. Vertex seeds are obtained from the z position at the beam-line of the reconstructed tracks. An iterative χ^2 fit is performed to the vertex seed and neighboring tracks. Displaced tracks with $\chi^2 > 7\sigma$ are used as a new vertex seed, and this procedure is repeated until no additional vertices can be found. After the vertex finding, vertices are required to have more than two associated tracks. A primary vertex is defined as the vertex with the largest sum of squared transverse momenta of the associated tracks ($\sum p_{\mathrm{T}}^2$).

3.2 Electrons

Electrons have an important role on many physics analyses because of their clean signature and a precision measurement of four-momentum. For the $H \to \tau\tau$ analysis, the electron from a leptonically decaying tau is used as a final state object. The electron has clean signature even at a trigger level, and therefore the data collected by a single electron trigger is used in the $H \to \tau_{\mathrm{e}}\tau_{\mathrm{had}}$ channel.

Single Electron Trigger

At the L1, electron trigger objects are identified using a sliding window algorithm [44] on a 4×4 group of EM calorimeter towers with a granularity of $\Delta\eta \times \Delta\phi = 0.1 \times 0.1$. The L1 trigger is fired if the transverse energy of the electron object exceeds the L1 trigger threshold. The transverse energy of the electron object is measured from horizontal or vertical tower pair within the central 2×2 towers. The electron object which passes the L1 trigger is provided to the L2 trigger with the position of the candidate, referred to as Region Of Interest (ROI). At the L2, fast energy and tracking reconstructions of electron objects are performed within their ROIs. The step-by-step cut-based selections, which are almost the same as the identification method described in the next section, are applied to electron objects, and the L2 trigger is fired if the object passes all selection criteria. At the EF, full energy and track reconstructions, and identification criteria described in Ref. [45] are applied to electron objects. The trigger menus used in Section 4 are referred to as `e24vhi_medium1` and `e60_medium1` for 8 TeV, and `e20_medium`, `e22_medium` and `e22vh_medium1` for 7 TeV. The numbers in their names represent transverse energy thresholds at EF of each trigger, and `medium` represents a *medium* working point of the electron identification, where additional shower shape cuts are applied to `medium1` menus. In order to cope with the increase of the pile-up events, an additional veto cut on the energy deposit in the hadron calorimeter (hadron veto) is applied, referred to as `vh`. Finally, `i` represents a requirement that a track of the trigger object is isolated from other tracks. For 7 TeV, three menus are used in turn to cope with the increase of the trigger rate due to the enhancement of the instantaneous luminosity of the LHC in 2011. For 8 TeV, the data is combined by taking a logical "OR" of `e24vhi_medium1` and `e60_medium1` triggers to keep the trigger efficiency even in a high transverse momentum region. The single electron trigger efficiency is measured using $Z \to$ ee events in the data using a so-called tag-and-probe method [46]. The method requires two electrons, referred to as tag-electron and probe electron, respectively. Both electrons are required to have $E_{\mathrm{T}} > 25$ GeV and $|\eta| < 2.47$. The tag-electron is required to be triggered by the single electron trigger and to pass *tight* identification. while the probe-electron is required to pass *medium* identification, while it is not required to be triggered by the single electron trigger. In addition, window cut of the invariant mass calculated from two electrons is required to be consistent with the Z boson mass, and therefore the event is ensured to be generated from the $Z \to$ ee process. The single electron trigger efficiency can be measured using the probe electron because the probe electron is unbiased from triggers, and its purity is high. The combined trigger efficiencies of `e24vhi_medium1` and `e60_medium1` for the L1, L2 and EF are shown in Fig. 3.2. The bump of the efficiency around $E_{\mathrm{T}} \approx 60$ GeV is clearly visible due to the combination of two triggers, and the efficiency is dropped in the crack region of the EM calorimeter ($1.37 < |\eta| < 1.52$). The measurement

is also performed to simulated $Z \rightarrow$ ee events, and scale factors are obtained by taking the ratio of efficiencies from data and simulated events. The scale factors are used to correct a normalization and kinematic distributions of simulation samples. Systematic uncertainty on the scale factors are $1 \sim 2\%$ depending on the transverse energy and pseudo-rapidity of the reconstructed electron.

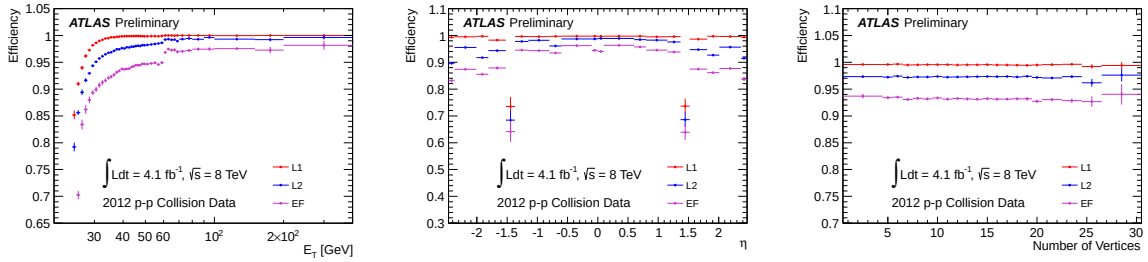

(a) (b) (c)

Fig. 3.2: Single electron trigger efficiencies at L1,L2 and EF as a function of (a) the transverse energy, (b) pseudo-rapidity of the probe electron and (c) the number of vertices. The probe electron is required to have $E_{\mathrm{T}} > 25$ GeV, $|\eta| < 2.47$ and to pass the *medium* identification, while it is not required to be triggered the single electron trigger. Two different single electron triggers with transverse energy thresholds at 24 and 60 GeV are combined in the plots. The trigger efficiencies are measured by the $Z \rightarrow$ ee tag-and-probe method with data [46].

Reconstruction and Identification

An electron reconstruction starts from finding seed clusters with $E_{\mathrm{T}} > 2.5$ GeV. The seed clusters are searched by a sliding window algorithm [44] using a cluster size of $\Delta\eta \times \Delta\phi = 0.075 \times 0.125$. Then, reconstructed tracks are matched to the seed clusters with a requirement of $p_{\mathrm{T}} > 1$ GeV and $\Delta\eta(\text{seed cluster,track}) < 0.05$, where one track which has minimum $\Delta\mathrm{R}(\text{seed cluster,track})$ is chosen in case that multiple tracks are matched. In order to precisely determine track parameters, the matched track is refitted with a Gaussian Sum Fitter algorithm [47] which includes the non-linear bremsstrahlung effects. After the track matching and refitting, the electron cluster is rebuilt from the seed cluster and matched track, considering additional energy contributions that are energy deposit in materials outside the EM calorimeter, lateral and longitudinal energy leakage outside the seed cluster. The four-momentum of the electron candidate is determined from the electron cluster and matched track information.

The electron candidates after the reconstruction contains a number of hadrons, photon conversions, and semi-leptonic decays of heavy flavors. The electron identification is necessary to increase the purity of the electron candidates. Several discriminating variables are used for the identification, and they are grouped into shower shape, strip layer, track quality and cluster-track matching variables [45]. The three working points are defined as *loose*, *medium* and *tight*, corresponding identification efficiencies of 95%, 85% and 75%, respectively. Shower shape variables are especially sensitive to pile-up effect, and therefore an additional correction is applied in order to make signal efficiencies almost constant against the number of vertices.

The identification efficiencies for each working point are shown in Fig. 3.3. The efficiencies are measured using tag-and-probe method in $Z \rightarrow$ ee and $J/\psi \rightarrow$ ee events. Both electrons are required to have $|\eta| < 2.47$. The tag-electron is required to be triggered by the single electron trigger, to have $E_{\mathrm{T}} > 20$ GeV and to passe *tight* identification. The probe-electron is required to have $E_{\mathrm{T}} > 7$ GeV, while it is not applied both trigger and identification requirements. The tag-and-probe method is described above and more detail is explained in Ref. [45]. Scale factors of the efficiencies are measured in parallel using tag-and-probe method, and they are used to correct simulation samples.

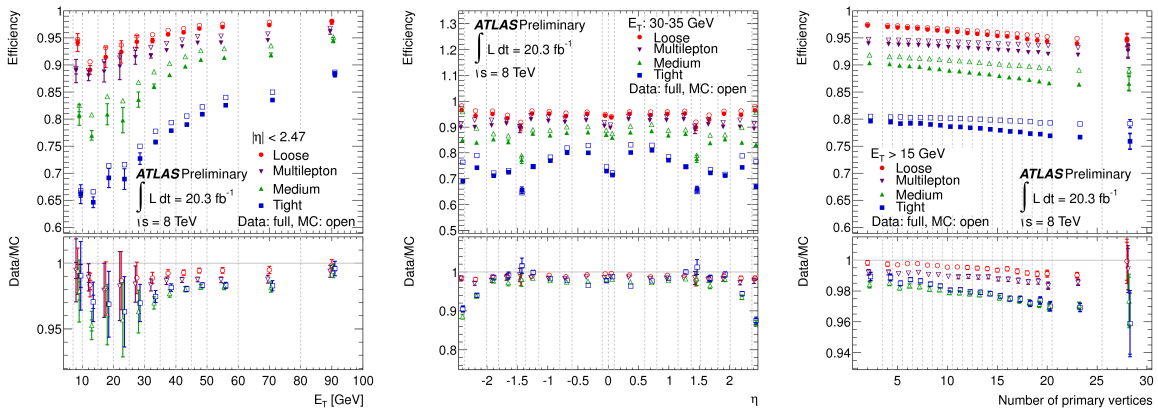

(a) (b) (c)

Fig. 3.3: Electron identification efficiencies for each working point as a function of (a) the transverse energy , (b) pseudo-rapidity of the probe-electron and (c) number of vertices. The probe-electron is required to have $p_{\mathrm{T}} > 7$ GeV and $|\eta| < 2.47$, while it is not applied trigger and identification requirements. The identification efficiencies are measured by the $Z \rightarrow$ ee tag-and-probe method in the data, and the scale factors shown at the bottom panels are used to correct simulation samples [45].

Energy Scale and Resolution

The electron energy is reconstructed based on the seed cluster, and the energy is calibrated considering energy loss in the material in front of the calorimeter from simulation based method. The electron energy scale and resolution are necessary to correct the difference between data and simulation samples, which can be expressed by:

$$E^{data} = E^{sim.}(1 + \alpha_i), \tag{3.1}$$

where E^{data} and $E^{sim.}$ are the electron energy in the data and the simulation, α_i represents their fractional difference at a given electron pseudo-rapidity region i. The correction factors α_i are determined by a resonance fitting of $Z \rightarrow$ ee and $J/\psi \rightarrow$ ee events. Figure 3.4 shows the di-electron mass distribution and the correction factors as a function of the transverse energy of the reconstructed electron with $|\eta| < 0.6$. The correction factors are applied to simulation samples to correct the electron energy. Systematic uncertainties on the correction factors are less than 0.5%.

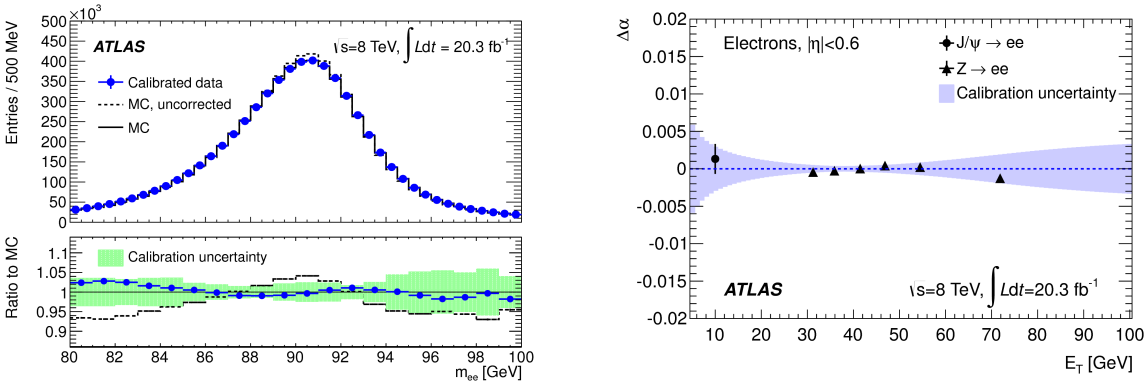

(a) (b)

Fig. 3.4: (a) The di-electron mass distribution and (b) the correction factor as a function of the transverse energy of the reconstructed electron with $|\eta| < 0.6$. Before and after corrected distribution from simulated $Z \rightarrow$ ee events are also shown in (a). The band in (b) represents the systematic uncertainty on the correction factor [48].

3.3 Muons

Muons are also important physics object for physics analyses because of following experimental signatures: The muon is a minimum ionizing particle (MIP), which weakly interacts to the calorimeter, and track parameters are precisely measured using combined information of the ID and MS. This signature allows to distinguish muons from jets and electrons efficiently, at both the online trigger and offline analysis level. In the $H \rightarrow \tau\tau$ analysis, muons from leptonic decaying τs are used as the final state object, and a single muon trigger is used in the $H \rightarrow \tau_\mu \tau_{\text{had}}$ channel.

Single Muon Trigger

At the L1, muon trigger objects are defined by coincident signals from the Muon Spectrometer (MS), which consists of the Resistive Plate Chambers (RPC) for the barrel region ($|\eta| < 1.05$) and Thin Gap Chambers (TGC) for endcap region ($1.05 < |\eta| < 2.4$). They are classified into six estimated transverse momentum categories, and trigger is fired if at least one of the category exceeds the L1 trigger transverse momentum threshold. The muon trigger object including its position (ROI) is provided to the L2 trigger. At the L2, the muon trigger object is refined using the trigger and precision chambers. A fast track fitting is performed within the ROI, and the transverse momentum is estimated using Look-Up-Table (LUT) based on the result of the fast track fitting. Then, the reconstructed tracks from the ID are combined with the tracks from MS. At the EF, full muon reconstruction and identification described in the next section are applied to the muon trigger object.

The trigger menus used in Section 4 are referred to as `mu24i_tight` for 8 TeV, and `mu18` and `mu18_medium` for 7 TeV. The numbers in their names represent transverse momentum thresholds at EF. `tight` and `medium` corresponds to L1 threshold values, which are 15 GeV and 11 GeV, respectively. In 2012, an additional track isolation requirement represented by `i` is applied to deal with the higher instantaneous

luminosity. The single muon trigger efficiency is measured using the tag-and-probe method of $Z \to \mu\mu$ events in the data. The method requires two opposite charged muons, referred to as tag-muon and probe-muon, respectively. Both muons are required to have $p_{\mathrm{T}} > 25$ GeV, $|\eta| < 2.5$ and to be CB muon (see the next section). The tag-muon is required to be triggered by the single muon trigger, while the probe-muon is not. The measurement method is almost the same as Section 3.2, and more detail is described in Ref. [49–51]. The trigger efficiencies of `mu24i_tight` as a function of the transverse momentum of the reconstructed muon are shown in Fig. 3.5 for the barrel ($|\eta| < 1.05$) and endcap ($|\eta| > 1.05$) regions. While the efficiencies show sharp turn-on curves, absolute values in plateau regions are around 70% and 85% due to the crack regions of the MS, detailed in the next section. The scale factors are extracted by this measurement, and they are used to correct simulation samples.

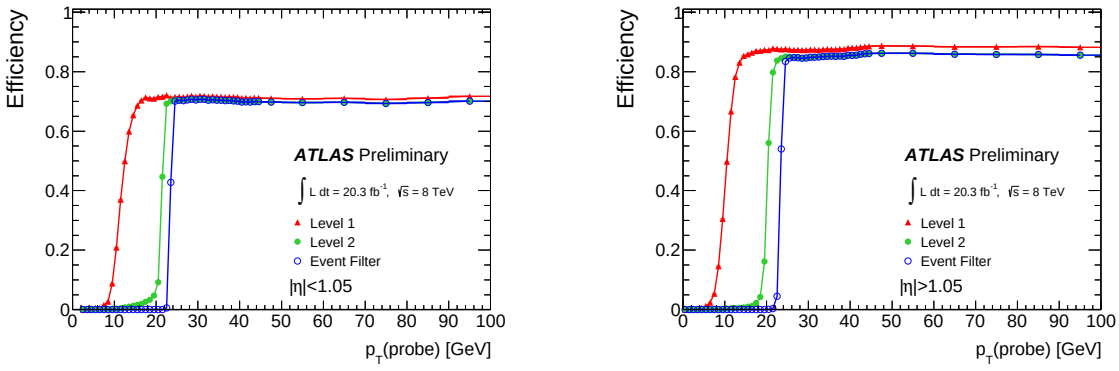

(a) (b)

Fig. 3.5: Single muon trigger efficiencies for L1,L2 and EF for (a) the barrel ($|\eta| < 1.05$) and (b) the endcap ($|\eta| > 1.05$) regions as a function of the transverse momentum of the probe muon. The probe-muon is required to have $p_{\mathrm{T}} > 25$ GeV, $|\eta| < 2.5$ and to be CB muon, while it is not required to pass single muon. The trigger efficiencies are measured by the $Z \to \mu\mu$ tag-and-probe method in the data [52].

Reconstruction and Identification

The muon reconstruction is performed using the combined information provided by the Muon Spectrometer (MS) and the Inner Detector (ID). Three different reconstruction algorithms are defined corresponding to different combination method of their information [50]:

- **Stand-Alone (SA) muon**: the muon track is reconstructed by only using the MS information. The parameters related to the vertex are determined by the extrapolating the track to interaction point, considering the effect of an expected energy loss in calorimeters.
- **Combined (CB) muon**: the muon track reconstruction is independently performed by the MS and the ID, and track parameters are determined by combining two tracks using the covariance matrices. The combination improves the resolution of track parameters, and therefore the combined muon has the highest purity compared with other algorithms.

- **Segment-tagged (ST) muon** : the muon track is reconstructed by the ID information with a requirement that at least one track segment in the MS has to be associated with the reconstructed track.

In the analysis presented in this thesis, muons from mainly the CB muon algorithm are used, while the ST muon algorithm is used for the object overlap removal.

The reconstruction and identification efficiencies are measured using tag-and-probe method of $Z \to \mu\mu$ events in the data. The tag-muon is required to be triggered by the single muon trigger, to have $p_{\mathrm{T}} > 25$ GeV and to be CB muon. The probe-muon is required to have $p_{\mathrm{T}} > 20$ GeV, while it is not applied both trigger and identification requirements. Both muons are required to have $|\eta| < 2.5$. The efficiencies are shown in Fig. 3.6 as a function of the transverse momentum and pseudo-rapidity of the CB muon. The efficiency drop is clearly visible at $\eta \approx 0$ and $1.1 < \eta < 1.3$ where are the crack regions of the MS. The MS is partially installed at $\eta \approx 0$ to provide the service for the ID and calorimeters. At $1.1 < \eta < 1.3$, the MS was not yet installed in 2012[1)]. The scale factors shown in the plots are used to correct simulation samples, and their systematic uncertainties are summarized in Section 4.8.2.

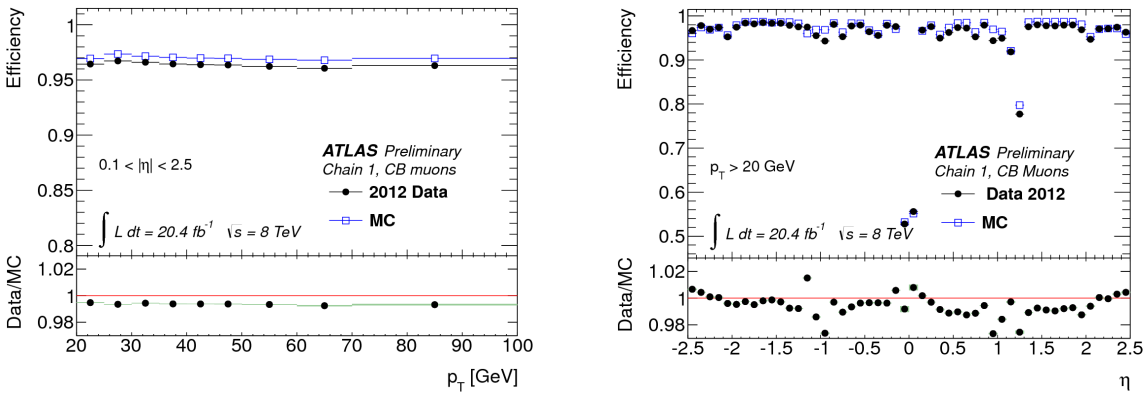

(a) (b)

Fig. 3.6: (a) Muon identification efficiencies as a function of the transverse momentum of the reconstructed muon with $0.1 < |\eta| < 2.5$ and (b) pseudo-rapidity of the probe-muon with $p_{\mathrm{T}} > 20$ GeV. The probe-muon is required to have $p_{\mathrm{T}} > 20$ GeV and $|\eta| < 2.5$, while it is not applied both trigger and identification requirements. The efficiencies are measured by the $Z \to \mu\mu$ tag-and-probe method in the data. The scale factors shown at the bottom panels are used to correct simulation samples [51].

Momentum Scale and Resolution

The muon momentum scale and resolution [50, 51] are determined by a resonance fitting in $Z \to \mu\mu$, $J/\psi \to \mu\mu$ and $\Upsilon \to \mu\mu$ events. The fractional momentum resolution can be parameterized with the

[1)]The installation in this region was finished during the LHC shutdown in 2013-2014.

quadratic sum of two terms:

$$\frac{\sigma_{p_{\mathrm{T}}}}{p_{\mathrm{T}}} = a \oplus (b \times p_{\mathrm{T}}) \,, \tag{3.2}$$

where a is the constant term of the effect from multiple scattering and b is the p_{T} dependence term of the intrinsic resolution due to the spatial resolution of detector components. The momentum correction parameters are obtained by fitting the di-muon mass spectrum distribution using the template derived from simulated $Z \to \mu\mu$ events. The fitting is performed in pseudo-rapidity bins of the reconstructed muon. The di-muon mass distribution and di-muon mass resolution as a function of the pseudo-rapidity of the leading muon are shown in Fig. 3.7. The correction factors are applied to correct simulation samples, and their systematic uncertainties are around $0.1 \sim 0.2\%$ depending on the muon pseudo-rapidity.

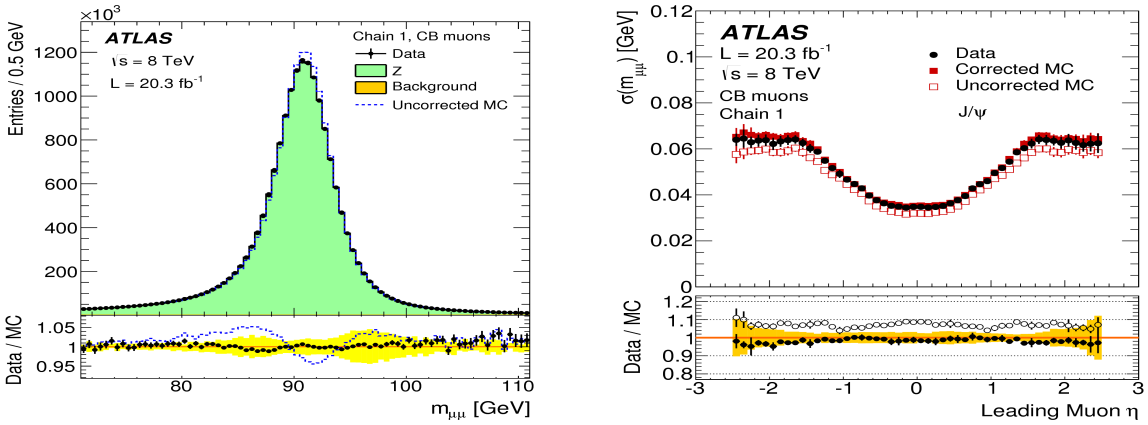

(a) (b)

Fig. 3.7: (a) The di-muon mass distribution and (b) the mass resolution as a function of the pseudo-rapidity of the leading muon. Distribution from simulated $Z \to \mu\mu$ events before and after correction are also shown.

3.4 Hadronic Taus

The reconstruction and identification of the τ lepton and its decay products are crucial role in the $H \to \tau\tau$ analysis. As described in Section 1.2.4, a tau lepton has two decay categories, referred to as leptonically and hadronically decaying tau. The leptonically decaying tau decays into a lepton (electron or muon) and two neutrinos in the final state. The two neutrinos are not directly detectable in the ATLAS detector, and it is difficult to distinguish from a prompt electron or muon. The lepton from the leptonically decaying tau is reconstructed and identified by the procedure described in Section 3.2 and 3.3. On the other hand, the hadronically decaying tau decays into an odd number of charged hadrons with or without a few neutral pions and one neutrino. The decay products are detectable except for the neutrino, and therefore

[2)]The muon with higher transverse momentum in di-muon

dedicated reconstruction and identification algorithms are applied. The detectable decay products τ_{had} are classified into 1-prong and 3-prong, according to the number of charged hadrons. The branching ratio of five charged hadrons is negligible contribution, a total of $\sim 0.08\%$. The main background of τ_{had} is hadronic jets produced from the fragmentation of quarks and gluons. In addition, electrons can be background because they have similar signature as 1-prong τ_{had}s. The discrimination from jets and electrons are performed in the τ_{had} identification using experimental signature of τ_{had} characteristics, such that the decay products are highly collimated than jets due to the fact that most of the tau lepton has a high momentum compared to the tau lepton mass. The τ_{had} reconstruction, identification, energy scale and τ_{had} trigger algorithm are described in this section.

τ_{had} Trigger

A τ_{had} trigger is used to collect data analyzed in $H \to \tau_{\text{had}}\tau_{\text{had}}$ channel. At the L1, a seed of a τ_{had} trigger object is defined as the L1 electron trigger object (see Section 3.2). While the energy of the electron object is defined by two EM calorimeter towers, the energy of the tau object is obtained by adding four Hadron calorimeter towers, which are associated with the central 2×2 EM calorimeter towers used in search of the electron object. Thus, the energy of the τ_{had} trigger object is defined by two EM calorimeter and four Hadron calorimeter towers. As an additional option, an isolation requirement is prepared in the L1 τ_{had} trigger to reduce the trigger rate. The isolation is defined by providing an energy threshold on isolation towers, where are twelve EM calorimeter towers surrounding the central 2×2 EM calorimeter towers. This requirement is based on the fact that τ_{had} energy deposition is more collimated than jets. The L1 τ_{had} trigger is fired if the transverse energy of the tau object exceeds the L1 trigger threshold with or without passing isolation requirement. Information of the L1 τ_{had} trigger object including its ROI is provided to the L2. At the L2, a fast tracking is performed within the ROI to calculate discriminant variables. The L2 τ_{had} trigger object is classified into 1-prong and multi-prong corresponding to the number of tracks counted within the region of $\Delta\text{R} < 0.3$ from a center of the object position. A L2 trigger selection on discriminant variables is applied separately for 1-prong and multi-prong objects. At the EF, the similar algorithm to the offline reconstruction and identification (see the next section) are applied separately for 1-prong and multi-prong, which is based on the the Boosted Decision Tree (BDT) algorithm [53].

The single τ_{had} trigger efficiencies are measured using the tag-and-probe method of $Z \to \tau\tau \to \ell\tau_{\text{had}}$ events in the data collected by the single electron or muon trigger. The tag-electron (tag-muon) is required to have $E_{\text{T}}(p_{\text{T}}) > 20$ GeV, $|\eta| < 2.47(2.5)$ and to pass the *tight* identification (to be the CB muon). The probe-τ_{had} is required as follows: $p_{\text{T}} > 20$ GeV, $|\eta| < 2.5$, one or three charged tracks, opposite charge from the tag-lepton, and to pass the *medium* identification (see the next section). Several event selections are applied to suppress background events, and a dedicated background estimation is performed, which are detailed in Ref. [54]. The trigger efficiencies as a function of the transverse momentum of the probe-τ_{had} and the number of vertices are shown in Fig. 3.8. The scale factors are extracted by this measurement, and they are used to correct simulation samples. The systematic uncertainties on the scale factors are $\sim 2\%$ for 20 GeV $< p_{\text{T}} <$ 50 GeV, while the uncertainties are $\sim 8\%$ for $p_{\text{T}} = 100$ GeV.

The τ_{had} misidentification probability is relatively higher than electrons and muons. In order to suppress trigger rate, the p_{T} threshold of the single tau trigger set to a higher value, such as 100 GeV in 7 TeV and 125 GeV in 8 TeV. The threshold is not effective to the $H \to \tau_{\text{had}}\tau_{\text{had}}$ analysis, and therefore a di-τ_{had} trigger requiring two single τ_{had} is used for the $H \to \tau_{\text{had}}\tau_{\text{had}}$ channel. The scale factors for di-τ_{had} trigger efficiencies are obtained by the product of the scale factors of two single τ_{had} triggers.

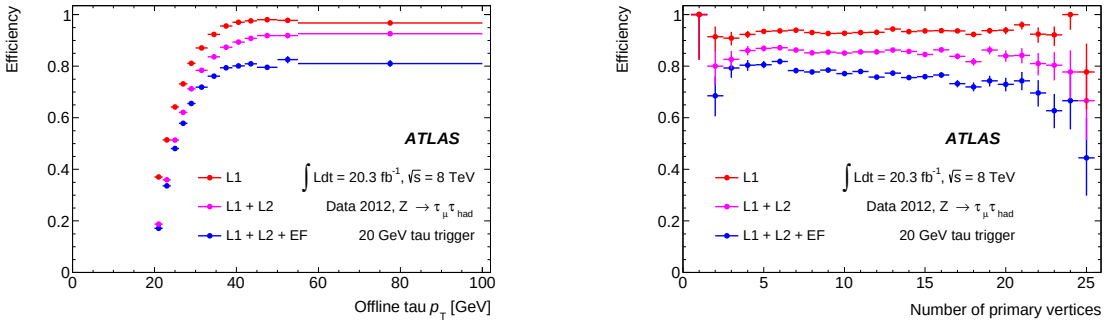

(a) (b)

Fig. 3.8: Tau trigger efficiencies as a function of (a) the transverse momentum of the reconstructed τ_{had} with $|\eta| < 2.5$ and (b) the number of vertices. The efficiencies are measured by the $Z \to \tau\tau \to \mu\tau_{\text{had}}$ tag-and-probe method in the data [54].

Reconstruction and Identification

A seed of the τ_{had} reconstruction is defined using the same algorithm as the jet reconstruction (see Section 3.5), with requirements of $p_{\text{T}} > 10$ GeV and $|\eta| < 2.5$. Then, the seed is associated with the vertex chosen by a dedicated vertex association method. The method is based on jet vertex fraction algorithm [55], and it is referred to as Tau Jet Vertex Association (TJVA) method [54]. The TJVA provides the vertex which has the highest vertex fraction. The vertex is more precise than the primary vertex defined as the highest $\sum(p_{\text{T}}^{\text{track}})^2$ because the TJVA method is robust to pile-up conditions. The direction of calorimeter variables are calculated by coordinated with the origin of this vertex. While the τ_{had} angles η and ϕ are determined by the seed direction, the transverse energy is calculated by a dedicated energy calibration from the seed energy, which is described in the next section. The τ_{had} invariant mass is defined to zero, and therefore the transverse momentum is identical with the transverse energy. Then, reconstructed tracks are matched with the τ_{had} seed in the core region defined as a region within $\Delta\text{R}(\text{seed,track}) < 0.2$ from a center of the τ_{had} direction, where tracks are required to pass selection criteria: $p_{\text{T}}^{\text{track}} > 1$ GeV, quality cut using the number of tracking detector hits and impact parameters. The reconstructed τ_{had} is classified into 1-prong, 3-prong or multi-prong according to the number of tracks in the core region. The track association is also performed in the isolation region defined as a region within $0.2 < \Delta\text{R}(\text{seed,track}) < 0.4$ to calculate discriminant variables.

A neutral pion (π^0) reconstruction is performed in 8 TeV to increase the performance of the τ_{had} identification. The first step of the reconstruction is to determine the number of neutral pions (N_{π^0}) by using

the BDT. The concept and the discrimination algorithm of the BDT are detailed in Section 4.7. Two different BDTs are defined to classified into $N_{\pi^0} = 0$ and $N_{\pi^0} > 0$, and to classified into $N_{\pi^0} = 1$ and $N_{\pi^0} > 1$. The same discriminant variables are input to BDTs, which are related to measured information of the strip layer and combined information of calorimeter and tracking detector. For a training procedure, simulated $Z/Z' \to \tau\tau$ and $W \to \tau\nu_\tau$ events are used as the signal sample, while large collision data samples collected by jet triggers are used as the background sample. Simulated $Z' \to \tau\tau$ events with masses of 500 GeV, 750 GeV, 1000 GeV and 1250 GeV are used to enhance the performance of the BDT in a higher p_{T} region, where the Z' boson is a new gauge boson with a high mass predicted by several BSM theories [56–61]. By applying cut on the two BDT outputs, N_{π^0} are classified into $N_{\pi^0} = 0$, $N_{\pi^0} = 1$ and $N_{\pi^0} > 1$, corresponding to the purity of $\sim 81.8\%$, $\sim 47.5\%$ and $\sim 68.9\%$, respectively. The second step is to determine four-momenta of neutral pions in case of $N_{\pi^0} = 1$ and $N_{\pi^0} > 1$. The clusters in the core region of the reconstructed τ_{had} is corrected by subtracting the contributions from pile-up and electric noise effects, which are estimated from the isolation region. Then, one cluster or the pair of clusters is selected as π^0 cluster(s) using combined information of energy deposition in the strip layer, the EM and Hadron calorimeters. Finally, the four-momenta of neutral pions are obtained from the energy and position of the π^0 cluster(s). The N_{π^0} and variables using π^0 four-momenta are used in the τ_{had} identification for 8 TeV.

Since jets and electrons can be reconstructed as τ_{had}s, the τ_{had} identification is performed to reject them. The identification is based on the BDT algorithm using the τ_{had} characteristic signature. The two BDTs are separately trained for 1-prong and 3-prong reconstructed τ_{had}. The same training samples are used as the π^0 reconstruction, simulated $Z/Z' \to \tau\tau$ and $W \to \tau\nu_\tau$ events for signal, and data samples collected by jet triggers for background. Input variables are based on calorimeter shower shapes, tracking information and calorimeter and tracking combined information using following features:

- The energy deposition from a τ_{had} are more collimated than jets.
- The cone size of a τ_{had}, the distance between a τ_{had} and associated tracks, is narrow compared to jets.
- The τ_{had} total energy is almost carried by the highest p_{T} track.
- The τ_{had} has more significant impact parameters than jets due to the relatively long decay length of the τ lepton.
- The number of neutral pion in τ_{had} is almost zero or one, while jets can contain more.

Several input variables corresponding to 1-prong and 3-prong τ_{had}s are defined and used as input to the BDTs, detailed in Ref. [54]. Typical two input variable distributions for τ_{had}s and jets are shown in Fig. 3.9, where f_{cent} is is a fraction of transverse energy deposited in the region within $\Delta\mathrm{R} < 0.1$ and $\Delta\mathrm{R} < 0.2$ from a center of the τ_{had} direction, and $N_{\mathrm{iso}}^{\mathrm{track}}$ is the number of tracks associated with a τ_{had} in the region of $0.2 < \Delta\mathrm{R} < 0.4$. The variables related to π^0 are included only for 8 TeV to increase the identification performance.

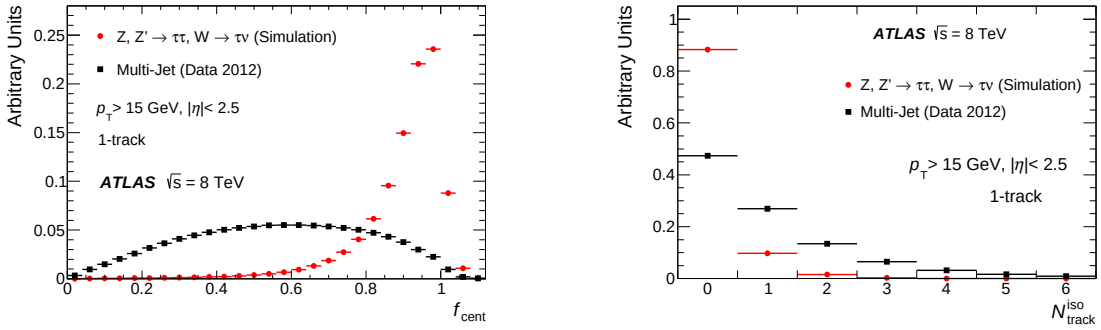

(a) (b)

Fig. 3.9: (a) f_{cent} and (b) $N_{\text{iso}}^{\text{track}}$ distributions of the reconstructed 1-prong τ_{had} for signal and background samples. In the signal samples, only τ_{had} matched to generator-level τ_{had}s are used [54].

Three working points of the identification are defined as *loose*, *medium* and *tight* by varying cut points on the BDT outputs, corresponding to signal efficiencies of $\sim 70\%$, $\sim 60\%$ and $\sim 40\%$ for 1-prong and $\sim 45\%$, $\sim 40\%$ and $\sim 30\%$ for 3-prong, respectively. The corresponding background efficiencies are $1\% \sim 10\%$ for 1-prong and $0.1\% \sim 2\%$ for 3-prong depending on the τ_{had} transverse momentum. The signal efficiencies of three working points as a function of the number of vertices are shown in Fig. 3.10 for 1-prong and 3-prong. The efficiencies are successfully kept even in a high pile-up condition.

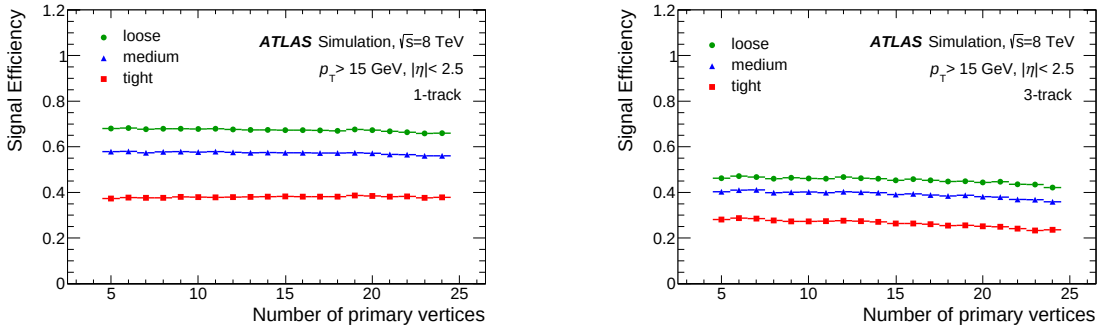

(a) (b)

Fig. 3.10: τ_{had} identification efficiencies of three working points for the reconstructed τ_{had} with $p_{\text{T}} > 15$ GeV and $|\eta| < 2.5$ for (a) 1-prong and (b) 3-prong as a function of the number of vertices, where the reconstructed τ_{had} is required to match with the generator-level τ_{had}. The efficiencies are obtained from simulation samples, and they are stable up to the large number of vertices [54].

The τ_{had} identification efficiency is measured using the tag-and-probe method of $Z \to \tau\tau \to \ell\tau_{\text{had}}$ events in the data collected by the single electron or muon trigger. The tag-electron (tag-muon) is required to have $E_{\text{T}}(p_{\text{T}}) > 20$ GeV, $|\eta| < 2.47(2.5)$ and to pass the *tight* identification (the CB muon). The probe-τ_{had} is required as follows: $p_{\text{T}} > 20$ GeV, $|\eta| < 2.5$, to have one or three charged tracks and opposite charge from the tag-lepton. In addition, several event selection criteria are applied to increase the τ_{had} purity, detailed in Ref. [54]. The probe-τ_{had}s are almost jets even applying the event selections because

the probe-τ_{had} is not applied the τ_{had} identification. A dedicated background estimation is necessary, which is performed by a template fitting on the number of tracks in the region of $\Delta\text{R} < 0.6$ from a center of the probe-τ_{had}. The wider cone size increases a discrimination ability between τ_{had}s and jets, while the ability is reduced in case of the large number of vertices due to pile-up. A p_{T}-weighted track counting algorithm is applied to improve the discrimination, expressed by:

$$D = \max\left[\frac{p_{\text{T}}^{\text{core}}}{p_{\text{T}}^{\text{outer}}} \times \Delta\text{R}(\text{core}, \text{outer}) \right] < 4, \tag{3.3}$$

where $p_{\text{T}}^{\text{core}}$ is the transverse momentum of any tracks in the core region of $\Delta\text{R} < 0.2$ and $p_{\text{T}}^{\text{outer}}$ is the transverse momentum of a candidate track in the outer region of $0.2 < \Delta\text{R} < 0.6$. $\Delta\text{R}(\text{core}, \text{outer})$ represents a distance between these tracks. The candidate tracks in the outer region are only counted if the tracks pass the requirement $D < 4$. The algorithm is based on the fact that pile-up tracks have large distance and relatively lower momentum than tracks from τ_{had}. hence the $D < 4$ cut leads to reduce pile-up tracks. The template of the number tracks for τ_{had} is obtained from simulated $Z \to \tau\tau$ events for separately 1-prong and 3-prong, while the template for jets are obtained from a same sign control region in the data. The control region is defined by inverting a charge requirement between the tag-lepton and probe-τ_{had}, where the region is dominated by multi-jet and W+jets events. The template for electrons is obtained from simulated $Z \to$ ee events. The number of track distributions for τ_{had}s and jets after the template fitting are shown in Fig. 3.11. The identification efficiency is measured by taking the ratio of the number of τ_{had} events estimated by the fitting before and after applying τ_{had} identification. The fitting is separately performed to each transverse momentum and pseudo-rapidity region. The scale factors of the efficiencies from data and simulation are close to one for all regions, and their systematic uncertainties are around $2\% \sim 5\%$ depending on the τ_{had} transverse momentum and pseudo-rapidity.

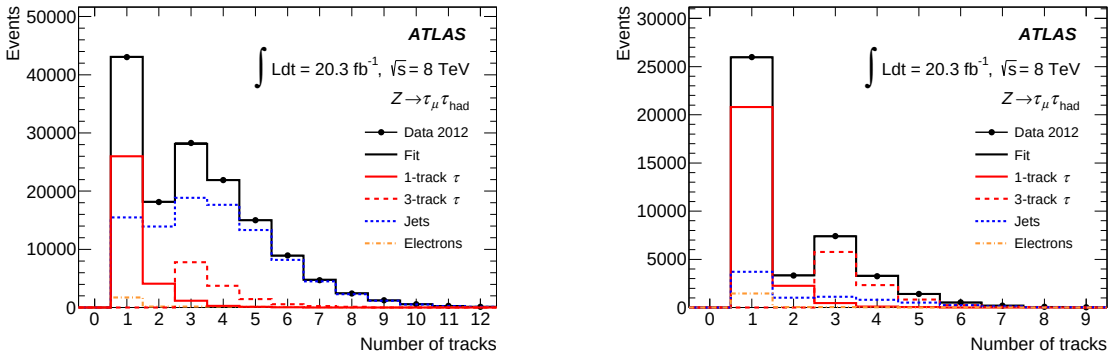

Fig. 3.11: The number of tracks distribution of τ_{had}s and jets with $p_{\text{T}} > 25$ GeV and $|\eta| < 2.5$ for (a) before and (b) after applying the *medium* τ_{had} identification [54].

The identification is also performed to discriminate τ_{had}s from electrons using an additional electron BDT. The electron BDT is trained by simulated $Z/Z' \to \tau\tau$ events and $Z \to$ ee events as signal and background samples, respectively. Input variables are related to the shower shape in the EM calorimeter

and information about the high and low threshold TRT hits because electron shower shape is more narrow than a 1-prong τ_{had}, and a transition radiation is emitted in the TRT by electrons. Three working points are defined as *loose*, *medium* and *tight*, corresponding to the signal efficiencies of $\sim 75\%$, $\sim 85\%$ and $\sim 95\%$. The selection efficiency of electrons is measured using $Z \rightarrow \text{ee}\,(\text{e} \rightarrow \tau_{\text{had}})$ tag-and-probe method. While one isolated and *tight* identified electron is used as the tag-electron, and second electron is used as the probe-τ_{had} misidentified from an electron. The measurement is separately performed for six τ_{had} pseudo-rapidity bins, and data/simulation scale factors are obtained from each region. Systematic uncertainties are around $8\% \sim 30\%$ which are mainly driven by statistical uncertainties.

Tau Energy Scale

The reconstructed τ_{had} energy is calibrated with the Tau Energy Scale (TES). The fraction of the τ_{had} energy deposition in the EM calorimeter is larger, and also a cone size of energy reconstruction is smaller than jets, and therefore a dedicated energy calibration for the τ_{had} is necessary instead of the Jet Energy Scale (JES) (see Section 3.5). The TES is firstly estimated based on simulation-base method by taking difference between the measured τ_{had} energy and generator-level τ_{had} energy. Then, the estimated TES is further corrected by a data-driven method.

The simulation-based TES is computed as a function of the τ_{had} transverse energy using $Z/Z' \rightarrow \tau\tau$ and $W \rightarrow \tau\nu_{\tau}$ events, referred to as a response curve. The τ_{had} is required to pass following selection: $E_{\text{T}} > 15$ GeV, $|\eta| < 2.4$, pass *medium* identification, $\Delta\text{R}\,(\tau_{\text{had}}, \text{jets}) > 0.5$, matching with generator-level τ_{had} with $E_{\text{T}} > 10$ GeV. The response curve is evaluated in intervals of generator-level energy at each τ_{had} pseudo-rapidity region separately for 1-prong and multi-prong. Absolute values for each intervals are determined by taking mean values of fitted Gaussian function. The result of response curves for 1-prong and multi-prong is shown in Fig. 3.12. While the variation of the response curves due to a pile-up condition is a few percent level, a pile-up correction is applied with respect to the number of vertices. The correction factor is obtained from simulated events for each pseudo-rapidity region, and the variation of the correction is in the range of $90 \sim 410$ MeV.

The simulation-based TES is calibrated using data, referred to as an *in-situ* calibration method. The calibration is performed by fitting on the m_{vis} distribution, where the m_{vis} is the invariant mass of the μ and the τ_{had}. The event selection criteria are applied to increase the τ_{had} purity, detailed in Ref. [54]. The TES is parameterized by the calibration factor α with the following equation:

$$E^{data} = E^{sim.}(1 + \alpha), \tag{3.4}$$

where E^{data} and $E^{sim.}$ are the τ_{had} energy in the data and the simulation. A fifth-order polynomial fit on the m_{vis} distribution is performed to match the m_{vis} peak position between data and the simulation. Then, the α is extracted by the result. The measured calibration factors are $\alpha = 0.8\%$ for 1-prong and $\alpha = 1.1\%$ for 3-prong in 2012, and they are applied to simulation samples. Combined systematic uncertainties are considered for the TES measurement of simulation-based and *in-situ* based method, detailed in Section 4.8.2.

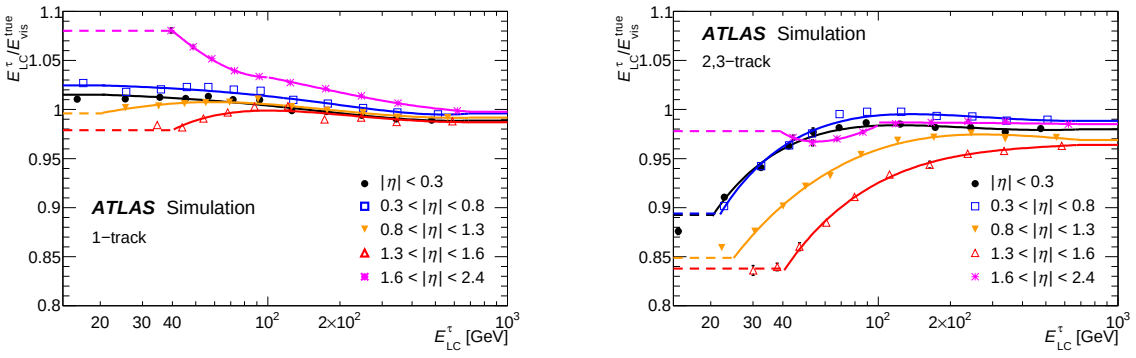

(a) (b)

Fig. 3.12: The response curve of the tau energy scale for (a) 1-prong and (b) multi-prong as a function of the reconstructed energy. For low transverse regions, the TES is assumed to be constant [54].

3.5 Jets

Reconstruction

Jets used in the analysis are reconstructed using the anti-k_t algorithm with distance parameter $R = 0.4$ [62]. The reconstruction starts from finding seed cells. The seed cells are required to have larger energy than $4\sigma_{\text{noise}}$. The σ_{noise} is the electronic noise from the calorimeter and the noise from pile-up. The topo-clusters are built from the seed cells by the following algorithm: The neighbour cells from the seed cell, which have larger energy than $2\sigma_{\text{noise}}$, are added to the seed cell. Then cells surrounding neighbours are also added. This procedure is repeated until the energy of cells surrounding neighbours exceed 2σ. The cluster merging and splitting algorithms are detailed in Ref. [55]. The topo-cluster energy is calibrated by LCW method (see the next section), and then the anti-k_t algorithm is applied to the calibrated topo-clusters to reconstruct jets. In this algorithm, two arbitrary topo-clusters which have a smallest d_{ij} parameter value are combined. This combination is iterated until the combined topo-cluster B becomes the smallest d_{iB} value. These parameters are expressed by:

$$\begin{aligned} d_{ij} &= \min(p_{\mathrm{T}i}^{-2}, p_{\mathrm{T}j}^{-2}) \frac{\Delta \mathrm{R}_{ij}^2}{R^2}, \\ d_{iB} &= p_{\mathrm{T},i}^{-2}, \end{aligned} \tag{3.5}$$

where i and j are two arbitrary topo-clusters, and $\Delta \mathrm{R}_{ij}$ represents the distance between them and R is the distance parameter corresponds to the size of the reconstructed jet. The advantage of the anti-k_t algorithm is that the shape of the reconstructed jet to be more cone-like compared to other reconstruction algorithms [63], and it is useful for the energy calibration and a subtraction of underlying events and pile-up. This is caused by the reconstruction procedure: beginning from high p_{T} topo-clusters and ending with low p_{T} clusters.

Energy Scale

The reconstructed topo-cluster energy should be corrected in order to cope with energies deposited outside the topo-cluster and in materials outside the calorimeter. In addition, the electronic noise and the noise from pile-up should be removed, so that a local cluster weighting (LCW) [55] method is applied for the calibration. The LCW method classifies topo-clusters into EM and hadron clusters by the measured energy density and the longitudinal shower depth. The topo-clusters are separately calibrated for EM and hadron clusters. The calibration factors are derived from simulated events of single charged pion or single neutral pion. The jet reconstruction is performed using calibrated topo-clusters.

The reconstructed jets are further corrected by the simulation-based calibration and the data-driven calibration. For the simulation-based calibration, the calibration factors are derived from simulated di-jet events, comparing energies of reconstructed and generator-level jets. The factors are parameterized by the transverse energy and the pseudo-rapidity of the reconstructed jet. For the data-driven calibration, the calibration factors are derived using *in-situ* calibration method with di-jet, Z+jets and γ+jets events in the data. The method uses the transverse momentum balance between the reconstructed jet and referenced objects, i.e. γ, Z boson and jet system. The correction factors are parameterized by the transverse momentum and the pseudo-rapidity of the reconstructed jet. Several systematic uncertainties on the JES are considered for each calibration step, classified as follows:

- Uncertainty on the *in-situ* calibration method.
- Uncertainty on the η-intercalibration.
- Close-by jets uncertainty for the JES difference between isolated jets and widely spread jets.
- Flavour composition and response uncertainties for the JES difference between quark and gluon initiated jets.
- Uncertainty for the JES difference between b-jets and other jets.
- Uncertainty on the pileup correction.

The JES uncertainties for 8 TeV as a function of p_{T} ($|\eta| = 0$) and η (p_{T} = 40 GeV) are shown in the Figure 3.13. The uncertainty for central jets with high transverse momenta is around $\sim 2\%$, while the uncertainty for forward jets with low transverse momenta is around $\sim 7\%$.

Jet Vertex Fraction

The reconstructed jets contains a large amount of pile-up initiated jets. In order to reduce them, a dedicated pile-up suppression algorithm is applied, referred to as the Jet Vertex Fraction (JVF) algorithm [55]. The JVF is evaluated for each reconstructed jet using jet associated track p_{T} and the primary vertex information, defined as

$$\mathrm{JVF} = \frac{\sum p_{\mathrm{T}}^{\mathrm{track}}(\mathrm{PV})}{\sum p_{\mathrm{T}}^{\mathrm{track}}(\mathrm{PV}) + \sum_{0<i<\mathrm{N_{vtx}}}^{\mathrm{N_{vtx}}} \left(\sum p_{\mathrm{T}}^{\mathrm{track}}(\mathrm{vtx}_i)\right)}, \tag{3.6}$$

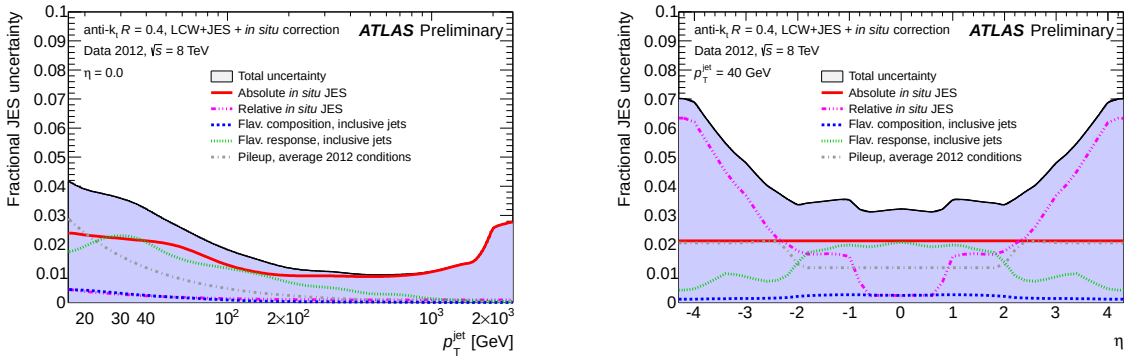

(a) (b)

Fig. 3.13: Fractional systematic uncertainties on the jet energy scale for each components (a) as a function of p_{T} for jets with $|\eta| = 0$, and (b) as a function of η for jets with $p_{\mathrm{T}} > 40$ GeV. The total uncertainty, the quadrature sum of all components, is shown as a blue band [64].

where PV is the primary vertex with the largest $\sum(p_{\mathrm{T}}^{\mathrm{track}})^2$, and vtx_i is a certain reconstructed vertex i except for the primary vertex, and N_{vtx} represents total number of vertex i. As described in the equation (3.6), the JVF represents the p_{T} fraction of tracks associated with the primary vertex. The JVF $= -1$ is assigned in case that the reconstructed jet does not have associated tracks. The JVF can be considered in the range of $|\eta| < 2.4$ due to the tracking detector acceptance. The selection efficiency of the JVF is measured for data and simulation using Z+jets events, and the scale factor is obtained around 1 within the systematic uncertainty of less than 1%.

b-Jets Identification

Based on the relatively long lifetime of the B hadrons, the b-jet tagging is performed using the MultiVariate tagging algorithm, referred to as MV1 algorithm [65, 66]. The MV1 algorithm uses several discriminant variables related to impact parameters [67] and secondary vertices [68]. The algorithm is only applied to jets within the region $|\eta| < 2.4$ due to the tracking detector acceptance. In this analysis, the b-tagging with the working point corresponding to 70% signal efficiency is used to suppress top background events, and to define the dedicated control region of top events. The b-tagging efficiency is measured using di-leptonic $t\bar{t}$ events classified into four channels depending on lepton flavors and the number of jets, and the scale factor between data and simulation is also derived from this measurement to correct simulation samples. Systematic uncertainties on the scale factor are the order of $(2\% \sim 8\%)$ depending on the transverse momentum and the pseudo-rapidity.

3.6 Missing Transverse Energy

In the $H \to \tau\tau$ analysis, the missing transverse energy $E_{\mathrm{T}}^{\mathrm{miss}}$ is an important observable due to the presence of neutrinos from the tau lepton decay and neutrinos cannot be detected by the ATLAS detector. The $E_{\mathrm{T}}^{\mathrm{miss}}$ reconstruction is based on energy depositions in the calorimeter and muons reconstructed from

the ID and the MS, described as

$$E^{\text{miss}}_{\text{x(y)}} = E^{\text{miss,calo}}_{x(y)} + E^{\text{miss},\mu}_{x(y)} = -(E^{\text{calo}}_{x(y)} + E^{\mu}_{x(y)}), \tag{3.7}$$

$$E^{\text{miss}}_{\text{T}} = \sqrt{(E^{\text{miss}}_{\text{T}_x})^2 + (E^{\text{miss}}_{\text{T}_y})^2}, \tag{3.8}$$

where $E^{\text{calo}}_{x(y)}$ represents reconstructed and calibrated energies from electrons, photons, τ_{had} and jets, and $E^{\mu}_{x(y)}$ is calculated energies of reconstructed muons after applying the momentum calibration. A requirement of $p_{\text{T}} > 20$ GeV is applied to the jet reconstruction. The calo term is also included energy depositions from particles that is not be reconstructed, referred to as soft term. For the energy reconstruction of the soft term, calibrated topo-clusters are used to reduce the effect of calorimeter noise. Tracks, which are not associated with any objects or topo-clusters, are also taken into account as soft term. The equation (3.7) can be expanded as

$$E^{\text{miss}}_{\text{x(y)}} = (E^{\text{miss,e}}_{x(y)} + E^{\text{miss},\gamma}_{x(y)} + E^{\text{miss},\tau_{\text{had}}}_{x(y)} + E^{\text{miss,jet}}_{x(y)} + E^{\text{miss,soft}}_{x(y)}) + E^{\text{miss},\mu}_{x(y)}. \tag{3.9}$$

The $E^{\text{miss}}_{\text{T}}$ resolution is reduced by pile-up events, mainly for the jet term and the soft term. In order to cope with this, a dedicated pile-up suppression is applied to these two terms. For jet term, a requirement of $|\text{JVF}| > 0$ for jets with $p_{\text{T}} < 50$ GeV and $|\eta| < 2.4$ is introduced in the jet reconstruction (see Section 3.5). For soft term, a dedicated scale factor is applied to $E^{\text{miss,soft}}_{x(y)}$, referred to as Soft Term Vertex Fraction (STVF). The STVF is defined as similar to JVF, expressed by

$$\text{STVF} = \frac{\sum p^{\text{soft track}}_{\text{T}}(\text{PV})}{\sum p^{\text{soft track}}_{\text{T}}(\text{PV}) + \sum^{\text{N}_{\text{vtx}}}_{0<i<\text{N}_{\text{vtx}}} \left(\sum p^{\text{soft track}}_{\text{T}}(\text{vtx}_i)\right)}. \tag{3.10}$$

Figure 3.14 (a) shows the $E^{\text{miss}}_{\text{T}}$ resolution as a function of the scalar sum of transverse energy of all objects used in the $E^{\text{miss}}_{\text{T}}$ reconstruction before (black) and after (red) applying the STVF correction in the VBF $H \to \tau\tau$ events. The $E^{\text{miss}}_{\text{T}}$ resolution is actually improved by using the STVF correction. Figure 3.14 (b) shows the linearity between reconstructed and generator-level $E^{\text{miss}}_{\text{T}}$ as a function of generator-level $E^{\text{miss}}_{\text{T}}$. A positive bias is clearly visible in the low $E^{\text{miss}}_{\text{T}}$ region due to resolutions of all objects. The STVF correction improves the $E^{\text{miss}}_{\text{T}}$ linearity at the region of $E^{\text{miss}}_{\text{T}} < 100$ GeV, while the $E^{\text{miss}}_{\text{T}}$ is slightly over-corrected at the region of $E^{\text{miss}}_{\text{T}} > 100$ GeV.

All objects are used in the $E^{\text{miss}}_{\text{T}}$ reconstruction, systematic uncertainties on the $E^{\text{miss}}_{\text{T}}$ depends on the systematic uncertainties on energy scales and resolutions for each object. The unique systematic uncertainty on the $E^{\text{miss}}_{\text{T}}$ is a part related to soft term scale and resolution, which is evaluated by $Z \to \mu\mu$ events. The systematic uncertainties on the soft term are $\sim 8\%$ for the scale and $\sim 5\%$ for the resolution.

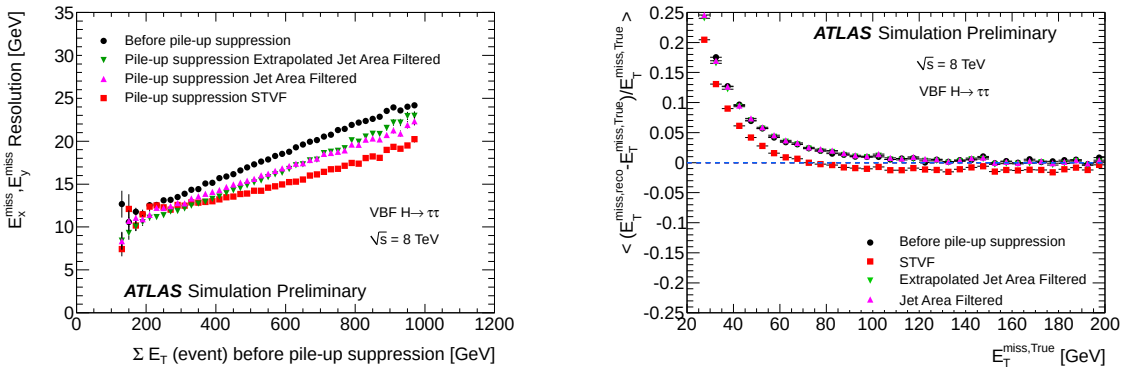

(a) (b)

Fig. 3.14: (a) $E_{\mathrm{T}}^{\mathrm{miss}}$ resolutions as a function of the total transverse energy $\sum E_{\mathrm{T}}$ and (b) $E_{\mathrm{T}}^{\mathrm{miss}}$ linearity between measured $E_{\mathrm{T}}^{\mathrm{miss}}$ and parton-level $E_{\mathrm{T}}^{\mathrm{miss}}$ in VBF $H \rightarrow \tau\tau$ events [69].

CHAPTER 4

Search for the Higgs Boson in $H \to \tau\tau$ Final State

This chapter describes the search for the Standard Model Higgs Boson in the $\tau\tau$ final state. The $H \to \tau\tau$ analysis can be divided into three channels depending on τ lepton decays as discussed in Section 1.2.4. This chapter focuses on the analysis of the $H \to \tau_\ell\tau_{\text{had}}$ channel, while the final result is obtained from the combination of results of three channels. First, the signature of the $H \to \tau\tau$ signal process and main background processes are described in Section 4.1 and Section 4.2. Then, the data and simulation samples are described in Section 4.3. Section 4.4 describes event selections and categories, with definitions of dedicated control regions for each background process. In order to confirm the excess from the $H \to \tau\tau$ signal events in data distribution, the development of reliable background modeling methods is essential in this analysis. The modeling is detailed in Section 4.6 with the comparison between data and expected background events. The remaining background events after the event selections are discriminated from signal events by a boosted decision tree (BDT), one of multivariate event classification algorithm. The BDTs are separately trained for two categories, and their output scores are used as final discriminant variables. A concept of the BDT algorithm and its implementation in this analysis are described in Section 4.7. In order to evaluate a significance of signal events and a signal strength in the observed data distribution, a maximum likelihood fit is performed to BDT output scores. The search results of the $H \to \tau_\ell\tau_{\text{had}}$ analysis (the significance and the signal strength) are summarized in Section 4.9 with the procedure of the maximum likelihood fit. As the final result of this analysis, the combination result of three channels is also described in Section 4.9.3.

4.1 Signature of $H \to \tau\tau$ Final State

The signature of $H \to \tau\tau$ process depends on both production processes and τ lepton decays. The ggF process has the largest cross section than other processes. This process doesn't have additional partons at leading-order (LO), while an additional parton contribution in this process is large due to initial state radiations from gluons. Reconstructed jets from the additional partons make a characteristic topology, that the Higgs boson is boosted against the jet system. The boosted topology is useful to construct discriminant variables between signal and background events, such as the invariant mass of di-τ system and the sum of transverse momentum of all objects. Therefore, events with the boosted topology are preferentially selected in this analysis. The VBF process has the second largest cross section, and it already includes two quarks in leading-order level. An additional parton contribution in this process is smaller than the ggF process because the VBF process occurs with purely electroweak interaction. Two out-going quarks are reconstructed as jets with relatively high p_{T} and a large pseudo-rapidity gap. This

characteristic topology is useful to reduce background events. The VH process is also considered in this analysis, but the contribution is not significant due to a small cross section and complex final states from vector boson decay. The $t\bar{t}H$ process has the smallest cross section and different final state objects (top quarks) from other signal processes, so that the contribution from the $t\bar{t}H$ process is negligible in this analysis.

The $H \to \tau\tau$ search is performed with three channels corresponding to τ lepton decays. The fully leptonic decay channel, $H \to \tau\tau \to \ell\ell + 4\nu$, is defined for the process that both τ leptons decay into leptons. This channel is the most clean signature in the final state because of the pure reconstruction of leptons (muons and electrons), while this channel has the lowest sensitivity due to the smallest branching ratio of 12.4%, and the worst resolution of the di-τ invariant mass due to four neutrinos in the final state. The fully hadronic decay channel, $H \to \tau\tau \to \tau_{\text{had}}\tau_{\text{had}} + 2\nu$, is defined for the process that both τ leptons decay hadronically. This channel has the second largest branching ratio of 42%, and the highest mass resolution because of less number of neutrinos. However, this channel has the second most sensitivity due to relatively large QCD backgrounds. The lepton-hadron decay channel, $H \to \tau\tau \to \ell\tau_{\text{had}} + 3\nu$, is defined for the process that one τ lepton decays leptonically and the other τ lepton decays hadronically. This channel has the highest sensitivity because of the following reasons: the largest branching ratio of 45.6%, the relatively clean signature due to one lepton, and the second highest mass resolution because less number of neutrinos than the fully leptonic channel. This channel is often called as "golden channel" in the $H \to \tau\tau$ search. The following sections describe the detail of analysis of the lepton-hadron channel. The combination result of three channels is described in Section 4.9.3.

4.2 Background Processes

Main background events in the lepton-hadron channel can be categorized into two processes: events with one real lepton and one real τ_{had} referred to as intrinsic background, events with one misidentified τ_{had} from a jet referred to as fake τ_{had} background. Background events with one misidentified τ_{had} from a lepton are counted as a minor background in this analysis.

The main process of the intrinsic background is $Z \to \tau\tau \to \ell\tau_{\text{had}}$ events, where the objects in the final state are completely the same as signal events. The typical Feynman diagram of the $Z \to \tau\tau$ with additional partons is shown in Fig. 4.1 (a). Two features can be considered to distinguish between signal and $Z \to \tau\tau \to \ell\tau_{\text{had}}$ background events. The first one is the invariant mass of the di-tau system because of the mass difference between the Higgs boson and the Z boson. The mass reconstruction method and its resolution is one of the crucial topics in this analysis. The other one is the kinematic properties related to additional jets in the final state. As discussed in Section 4.1, ggF and VBF production processes have different characteristic topologies: the boosted topology and two jets with a large pseudo-rapidity gap, respectively. The analysis strategy is optimized according to these characteristics.

Main contribution of the fake τ_{had} background are from W+jets, multi-jet, $t\bar{t}$, single top and $Z \to \ell\ell$ +jets processes. Especially, the W+jets and multi-jet process are dominant sources of the fake τ_{had} background. Typical Feynman diagrams of W+jets and multi-jet processes are shown in Fig. 4.1 (b) and

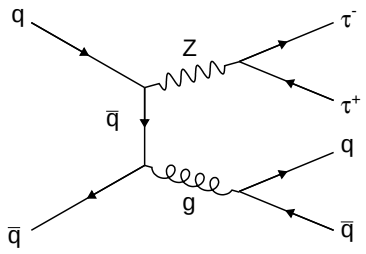

(a) $Z \to \tau\tau$ +jets

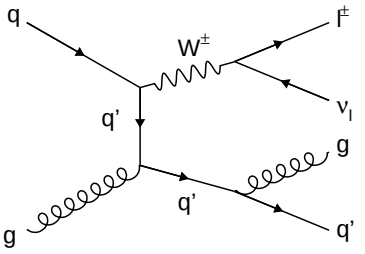

(b) W+jets

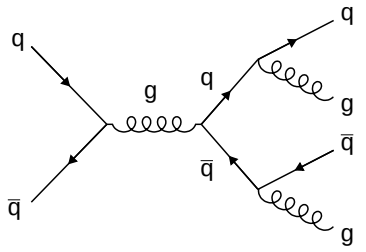

(c) multi-jet

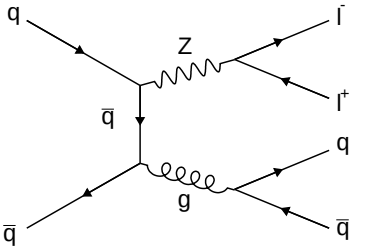

(d) $Z \to \ell\ell$ +jets

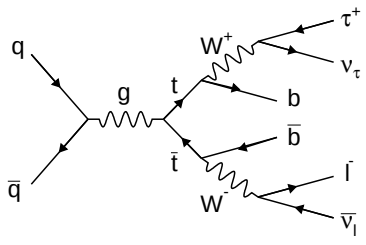

(e) top pair

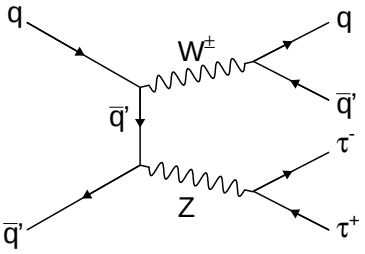

(f) di-boson

Fig. 4.1: Feynman diagrams of each typical background process with additional partons in the final state.

(c).

The W+jets events can be background in case that the W boson decays into one lepton and one neutrino, and a jet is misidentified as τ_{had}. The transverse mass of the lepton and the neutrino (m_{T}) is an useful variable to reject W+jets background events. The definition of the transverse mass is:

$$m_{\text{T}} = \sqrt{2p_{\text{T}}^{\ell} E_{\text{T}}^{\text{miss}} \left(1 - \cos\Delta\phi\left(\ell, E_{\text{T}}^{\text{miss}}\right)\right)}. \tag{4.1}$$

The W+jets background has the Jacobian peak around the W boson mass ($\sim$ 80 GeV) in the m_{T} distribution, as shown in Fig. 4.5 (b). In addition, transverse angular variables are also useful for further suppression (see Section 4.7.2). The multi-jet background from QCD process is another dominant process of the fake τ_{had} background, where two jets are misidentified as a lepton and a τ_{had}. Misidentification probabilities of the jet$\rightarrow \ell$ and the jet$\rightarrow \tau_{\text{had}}$ are $\leq 3\%$ and $\leq 10\%$, respectively. However, the cross section of the QCD process is huge ($\sigma_{\text{QCD}} \sim 10^8$ nb) compared with other processes. Both the W+jets and multi-jet events are estimated as the fake τ_{had} background (see Section 4.6.2).

The other SM processes, such as $Z \rightarrow \ell\ell$, $t\bar{t}$, single top and di-boson processes, also contribute as background. Typical Feynman diagrams of these processes are shown in Fig. 4.1 (d), (e) and (f).

The $Z \rightarrow \ell\ell$ events are selected as background events from two processes: The one process is that one lepton from the Z boson decay is not identified, and a jet is misidentified as τ_{had} This process is denoted by $Z \rightarrow \ell\ell$ (jet $\rightarrow \tau_{\text{had}}$), and it is estimated as a part of the fake τ_{had} background. The other process is that one lepton is misidentified as τ_{had}, denoted by $Z \rightarrow \ell\ell$ ($\ell \rightarrow \tau_{\text{had}}$). The contribution of this process is small because of the small misidentification probability of $\tau_{\text{had}} \rightarrow \ell$ thanks to the dedicated electron veto algorithm (see Section 3.4). The $Z \rightarrow \ell\ell$ ($\ell \rightarrow \tau_{\text{had}}$) process is estimated by simulation samples.

In $t\bar{t}$ and single top events, the branching ratio that top quark decays into the W boson and one bottom quark is $\sim 100\%$. These events are selected as background events from mainly three different processes: The first process is that one real lepton from the W boson decay is identified, and a jet is misidentified as τ_{had}. This process is denoted by Top (jet $\rightarrow \tau_{\text{had}}$), and is estimated as the fake τ_{had} background. The second one is that both one real lepton and one real τ_{had} are identified from W bosons decay, denoted by Top (τ_{had}). The last one is that one real lepton from the W boson decay, and an another lepton is misidentified as τ_{had}, denoted by Top ($\ell \rightarrow \tau_{\text{had}}$). Both the Top ($\tau_{\text{had}}$) and the Top ($\ell \rightarrow \tau_{\text{had}}$) are estimated by simulation samples. These backgrounds are suppressed using the b-jets tagging information (see Section 3.5).

The di-boson (WW, WZ, ZZ) events have several processes to select as background, according to the W and Z boson decay. However, the events are counted as a minor background due to their small cross sections compared with other backgrounds. The di-boson events are estimated by simulation samples for all decay processes.

4.3 Data and Simulation Samples

4.3.1 Data Sample

The data sample analyzed in this analysis is from proton-proton collision at the center-of-mass energy of 7 TeV in 2011 and 8 TeV in 2012, collected by the single electron or single muon trigger described in Section 3.2 and 3.3. Data quality criteria is applied to ensure that the data is recorded with all detector subsystems being operational. After applying the criteria, the integrated luminosity is 4.5 fb^{-1} at $\sqrt{s} =$ 7 TeV and 20.3 fb^{-1} at $\sqrt{s} = 8$ TeV. The 2011 and 2012 data samples are analyzed separately, and then the results of 2011 and 2012 are combined for the final result.

4.3.2 Simulation Samples

$H \to \tau\tau$ signal samples

For the $H \to \tau\tau$ signal simulation, samples with the different Higgs boson mass are generated between 100 GeV and 150 GeV in a 5 GeV step. Several event generators are used depending on the Higgs boson production process.

The ggF sample is generated using POWHEG [70–72] event generator at Next-to-Leading-Order (NLO) in QCD, interfaced to PYTHIA [73] for the parton shower, hadronization and underlying events, with the CT10 [74] parameterisation of the parton distribution functions (PDFs). The ggF cross section is taken from a higher-order calculation at a Next-to-Next-to-Leading-Order (NNLO) in QCD [75–80], including soft-gluon resummation up to Next-to-Next-to-Leading-Logarithmic (NNLL) [81] and NLO Electroweak (EW) corrections [82, 83]. The shape of the generated p_{T} distribution of the Higgs boson (p_{T}^{H}) is used to apply additional corrections separately for $H+ < 2$ jets and $H+ \geq 2$ jets events. In the $H+ < 2$ jets case, a reweighting is performed to match to the distribution from a NNLO calculation including NNLL terms obtained from the HRes2.1 program [84]. The HRes2.1 program calculates a differential cross section as a function of p_{T}^{H} ($\mathrm{d}\sigma/\mathrm{d}p_{\mathrm{T}}^{H}$) including the effect of top and bottom quark masses [85], and a dynamic renormalization and factorization scale, $\mu = \sqrt{(m_H)^2 + (p_T^H)^2}$, is used in the calculation. In the $H+ \geq 2$ jets case, a reweighting is performed to match to the distribution from MiNLO HJJ prediction [86]. Additional partons are not presence in the ggF process at LO so that final state jets are generated only from the initial state radiation. The sensitivity of ggF process is dominantly obtained from higher jet multiplicity case as discussed in Section 4.1. Therefore, $H+ \geq 2$jets is separately corrected by the dedicated program. The MiNLO HJJ program calculates the $H+ \geq 2$ jets process at NLO in QCD interfacing to parton shower programs.

The VBF sample is also generated using POWHEG [87] at NLO in QCD interfaced to PYTHIA with the CT10 PDFs. The VBF cross section is calculated at full NLO QCD and EW corrections with an approximate NNLO QCD correction. The NLO EW corrections for VBF production process depend on the p_{T}^{H}, varying from a few percent at low p_{T}^{H} to $\sim 20\%$ at $p_{\mathrm{T}}^{H} = 300$ GeV [88]. A reweighting is

performed based on the difference of p_{T}^{H} distributions between POWHEG+PYTHIA simulation without NLO EW corrections and HAWK [89, 90] generator with the corrections.

WH and ZH samples are simulated with PYTHIA generator, and CTEQ6L1 [91] parameterisation is used for PDFs. Cross sections of these samples are calculated at NNLO QCD with NLO EW radiative corrections [92].

Background Samples

For background processes, simulation samples of all dominant processes are prepared except for the multi-jet sample. The multi-jet final state generated from the QCD process is complicated, and the precise simulation is hard to match with a real data. In addition, a large amount of generation is required due to the large cross section of the QCD process ($\sim 10^8$ nb). The multi-jet events are estimated with fully data driven technique in this analysis instead of the simulation-based estimation (see Section 4.6.2).

The W+jets sample is generated using ALPGEN [93] event generator interfaced to PYTHIA for 8 TeV and HERWIG+JIMMY [94, 95] for 7 TeV, for the simulation of the parton shower, hadronization and underlying events with the CTEQ6L1 parameterisation of PDFs set. From LO matrix element calculation, ALPGEN provides events of a W boson production process with up to five additional partons, with the MLM matching scheme [96] between the matrix element and parton showers. The W+jets cross section is calculated at NNLO in QCD.

The simulation procedure and the cross section calculation of the Z/γ^*+jets sample are the same as the W+jets sample, while Z+jets samples are generated separately for low and high invariant mass of di-lepton ($m_{\ell\ell}$). The threshold of the $m_{\ell\ell}$ is 40 GeV and 60 GeV for 8 TeV and 7 TeV, respectively. The overall of Z/γ^*+jets simulation is a combination of low and high mass samples normalized by the inclusive cross section times corresponding event filter efficiency. The VBF production of Z/γ^* boson is additionally considered and generated using SHERPA [97] generator with LO cross section.

The $t\bar{t}$ sample with the top quark mass of 172.5 GeV is simulated with POWHEG interfaced to PYTHIA with the CTEQ6L1 parameterisation for PDF set. The single top sample is generated using POWHEG interfaced to PYTHIA for the s-channel and Wt process, while ACERMC+PYTHIA [98] interfaced to PYTHIA is used for the t-channel process. Cross sections of $t\bar{t}$ [99–104] and single top [105–107] sample are calculated at NNLO QCD including soft-gluon resummation up to NNLL.

For di-boson production process, WZ and ZZ samples are simulated with HERWIG generator, while the WW samples are generated separately for the $qq \to WW$ process and the loop included $gg \to WW$ process. The $qq \to WW$ process is generated using ALPGEN interfaced to HERWIG , and the $gg \to WW$ process is simulated with GG2WW [108] generator interfaced to HERWIG+JIMMY . Cross sections of each di-boson sample are calculated at NLO QCD [109].

All simulation samples used in this analysis are listed in Table 4.1 with generators and corresponding cross sections.

Process	Generator	$\sigma \times Br$ [pb]	
		8 TeV	7 TeV
ggF $H \to \tau\tau$ ($m_H = 125$ GeV)	POWHEG+PYTHIA	1.22	0.96
VBF $H \to \tau\tau$ ($m_H = 125$ GeV)	POWHEG+PYTHIA	0.10	0.08
WH $H \to \tau\tau$ ($m_H = 125$ GeV)	PYTHIA	0.045	0.037
ZH $H \to \tau\tau$ ($m_H = 125$ GeV)	PYTHIA	0.026	0.021
$W(\to \ell\nu)$+jets ($\ell = e, \mu, \tau$)	ALPGEN+PYTHIA (HERWIG)	$36.8 \cdot 10^3$	$31.5 \cdot 10^3$
$Z/\gamma^*(\to \ell\ell)$+jets (high mass)	ALPGEN+PYTHIA (HERWIG)	$34.5 \cdot 10^2$	$32.2 \cdot 10^2$
$Z/\gamma^*(\to \ell\ell)$+jets (low mass)	ALPGEN+HERWIG	$13.0 \cdot 10^3$	$11.7 \cdot 10^3$
VBF $Z/\gamma^*(\to \ell\ell)$+jets	SHERPA	1.1	-
$t\bar{t}$	POWHEG+PYTHIA	252.9	177.3
Single top Wt	POWHEG+PYTHIA	22.4	15.7
Single top s-channel leptonic	POWHEG+PYTHIA	1.8	1.5
Single top t-channel	ACERMC+PYTHIA	28.4	20.9
WZ, ZZ ($\geq 1\ell$)	ALPGEN+HERWIG	8.3	6.9
$qq \to WW \to 2\ell 2\nu$, $q\bar{q}\ell\nu$	GG2WW+HERWIG	29.2	17.4
$gg \to WW \to 2\ell 2\nu$	HERWIG	0.20	0.14

Table 4.1: Summary of simulation samples with their generators and corresponding cross section values for $\sqrt{s} = 8$ TeV and 7 TeV. For signal samples, the $H \to \tau\tau$ branching ratio is included in the quoted cross sections, and the Higgs boson mass is assumed as 125 GeV. For $t\bar{t}$, single top Wt and t-channel samples, inclusive cross sections are quoted. For all other background samples, the quoted cross section includes the branching ratio of the leptonic decay of W/Z bosons.

Simulation of Pileups

In order to model pileup events in simulation samples, an inclusive sample of proton-proton collision events is generated. The inclusive sample is overlaid to a simulation of hard scatter events. The number of overlaid events is varied according to a Poisson distribution with a given average of number of interaction $< \mu >$, and then a reweighting is performed to match a distribution of the number of interactions per bunch crossing in data events, referred to as $< \mu >$ rescale. For example, Figure 4.2 shows $< \mu >$ distributions for the simulation and data in 2012. In Fig. 4.2 (a), distributions with and without $< \mu >$ rescale are shown, demonstrating the $< \mu >$ rescale is correctly performed to match between simulation and data samples. The same rescale is also performed for 2011 samples.

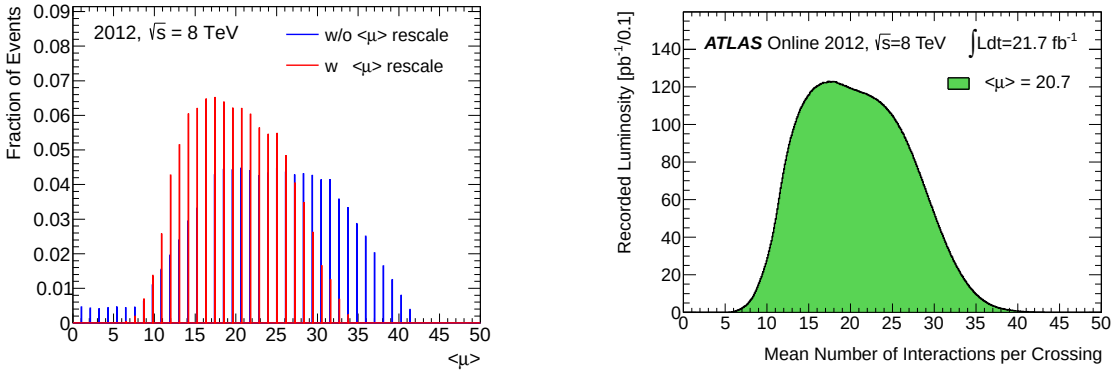

(a) (b)

Fig. 4.2: (a) $< \mu >$ distributions of the simulation in 2012 for with (red) and without $< \mu >$ rescale (blue), and (b) $< \mu >$ distributions of the data in 2012. The $< \mu >$ rescale is performed to match between the simulation and data.

Detector Simulation

In order to simulate the ATLAS detector response, a full detector simulation using the GEANT4 program [110] is applied for all simulation samples. The simulation is performed for particle interactions in materials of all sub-detectors including the effect of known detector defects, and provides the simulation result in the same format with data samples. It is allows to perform the same online trigger algorithms, object reconstructions, identifications and analysis procedures with data samples. The ATLAS simulation is detailed in Ref. [111].

4.4 Event Selection and Categorization

4.4.1 Object Definition

After applying basic data quality selections and trigger requirements, physics objects are defined to reconstruct event final states. During reconstruction and identification for each object, there is possibility to overlap between objects. Such overlaps are resolved by selecting objects in the order of priority, referred to as the overlap removal. The priority is muons, electrons, τ_{had}s and jets from highest to lowest, corresponding to their reconstruction and identification efficiencies (see Section 3). The object reconstruction and identification are performed in this order.

First, muons are identified because of the highest reconstruction purity. The muon identification has two criteria: The first one is a *loose* identification used in the overlap removal. In the *loose* identification, muon candidates are required to be combined or segmented-tagged muons with $p_{\text{T}} > 10$ GeV and $|\eta| < 2.5$ (see Section 3.3). The second criterion is a *tight* identification, which is used as the main object definition. In the *tight* identification, muon candidates are required to be combined muons with $p_{\text{T}} > 26$ GeV for 8 TeV or $p_{\text{T}} > 22$ GeV for 7 TeV, where p_{T} thresholds are in accordance with thresholds of

single muon triggers in 8 TeV and 7 TeV. Moreover, track and calorimeter isolation requirements are applied in the *tight* identification. The track isolation is defined as a transverse momentum ratio between the muon candidate track and the sum of tracks within a cone of $\Delta R < 0.4$ from the center of the direction of the muon candidate ($I(p_T, 0.4)$). The calorimeter isolation is defined as a transverse energy ratio between the muon candidate and the sum of calorimeter cells within a cone of $\Delta R < 0.2$ from the center of the direction of the muon candidate ($I(E_T, 0.2)$). $I(p_T, 0.4) < 0.06$ and $I(E_T, 0.2) < 0.06$ are required in the *tight* identification. Muon candidates which pass *loose* and *tight* selections are referred to as *loose* and *tight* muons, respectively.

Second, electrons are identified with the same procedure as muons, *loose* and *tight* identifications. In the *loose* identification, electron candidates are required to pass the *medium* electron identification described in Section 3.2, with $p_T > 15$ GeV and $|\eta| < 2.47$. The electron candidates within the crack (boundaries between barrel and endcap EM calorimeters) region of $1.37 < |\eta| < 1.52$ are rejected. Additionally, the overlap removal is performed between electron candidates and *loose* muons, where the electron candidates within a cone of $\Delta R < 0.2$ from the center of the *loose* muon are discarded. In the *tight* identification, electron candidates are required to pass the *tight* electron identification, with $p_T > 26$ GeV for 8 TeV or $p_T > 25$ GeV for 7 TeV. The p_T thresholds are in accordance with p_T thresholds of single electron trigger in 8 TeV and 7 TeV. Isolation requirements for electron candidates are also required, where the variable definitions are the same as muons, $I(p_T, 0.4) < 0.06$ and $I(E_T, 0.2) < 0.06$. Electron candidates which pass *loose* and *tight* selections are referred to as *loose* and *tight* electrons, respectively.

Next, τ_{had}s are identified by requiring to pass the *medium* identification with $p_T > 20$ GeV and $|\eta| < 2.5$. The number of tracks associated with τ_{had} candidates in a cone of $\Delta R < 0.2$ is required to be one or three, and an absolute charge value of each τ_{had} candidate must to be one. In addition, the *medium* electron veto is applied to only for the $H \to \tau_e \tau_{had}$ channel. The overlap removal is also performed with a cone size of ΔR ¡0.2, where τ_{had} candidates overlapped with *loose* muons or electrons are discarded. In the overlap removal with *loose* muons, the threshold of *loose* muon p_T is reduced to 2 GeV in order to reduce $\mu \to \tau_{had}$ fake background events (mainly from the $Z/\gamma^* \to \mu\mu$ process).

Finally, jet candidates are identified by requiring $p_T > 30$ GeV and $|\eta| < 4.5$. The overlap removal with a cone size of $\Delta R < 0.2$ is performed with *loose* muons, *loose* electrons and τ_{had}s. Additionally, jets with $p_T < 50$ GeV and $|\eta| < 2.4$ is required to pass the JVF selection of $|\text{JVF}| > 0.5$ for 8 TeV and $|\text{JVF}| > 0.75$ for 7 TeV (see Section 3.5).

The object definitions of muons, electrons, τ_{had}s and jets are summarized in Table 4.2, including the definitions used in the overlap removal.

4.4.2 Event Selection and Categorization

After the object definitions, event selections so-called "preselection" are applied to select events with the same final states as the $H \to \tau_\ell \tau_{had}$ signal events. At first, events are required to pass the single muon or electron trigger. Then, one primary vertex which has the largest $\sum (p_T^{track})^2$ is required to reject background from non-collision processes, where the vertex is reconstructed by requiring at least four

Object	Overlap Removal	Object Definition
Muons	Combined or segmented-tagged	Combined
	$p_{\mathrm{T}} > 10$ GeV	$p_{\mathrm{T}} > 26$ GeV (22 GeV for 7 TeV)
	$\lvert\eta\rvert < 2.5$	$I(p_{\mathrm{T}}, 0.4) < 0.06$
		$I(E_{\mathrm{T}}, 0.2) < 0.06$
Electrons	*Medium* Identification	*Tight* Identification
	$p_{\mathrm{T}} > 15$ GeV	$p_{\mathrm{T}} > 26$ GeV (25 GeV for 7 TeV)
	$\lvert\eta\rvert < 2.47$	$I(p_{\mathrm{T}}, 0.4) < 0.06$
	Not within $1.37 < \lvert\eta\rvert < 1.52$	$I(E_{\mathrm{T}}, 0.2) < 0.06$
	Overlap removal with muons	
	Overlap Removal & Object Definition	
τ_{had}	*Medium* Identification	
	Medium electron veto only for $H \to \tau_{\mathrm{e}}\tau_{\mathrm{had}}$ channel	
	$p_{\mathrm{T}} > 20$ GeV	
	$\lvert\eta\rvert < 2.47$	
	$\lvert\text{charge}\rvert = 1$	
	$\mathrm{N_{track}}$ = 1 or 3	
	Overlap removals with muons and electrons	
Jets	$p_{\mathrm{T}} > 30$ GeV	
	$\lvert\eta\rvert < 4.5$	
	JVF cut for jets with $\lvert\eta\rvert < 2.4$ and $p_{\mathrm{T}} < 50$ GeV	
	Overlap removals with muons, electrons and τ_{had}s	

Table 4.2: Summary of the object definitions. For muons and electrons, the definitions used in the overlap removal and the di-lepton veto are also listed. The same criteria are used in both 7 TeV and 8 TeV analysis.

associated tracks. Events with two or more *loose* leptons are discarded, referred to as the di-lepton veto. In addition, events are required to have exactly one *tight* lepton. Background events with two real leptons (mainly from $Z \to \ell\ell$ process) are reduced by these selections. At the last stage of the preselection, events with non physical MMC solution is discarded (see Section 4.5). This selection ensures that all events after the preselection have a valid $m_{\tau\tau}$ value. The preselection criteria is summarized in Table 4.3.

Preselection
Single lepton trigger
At least one primary vertex
Di-lepton veto
Exactly one muon or electron
Exactly one τ_{had}
Physical MMC solution

Table 4.3: Summary of the preselection criteria.

After applying the preselection, events are sorted into two categories to separate the VBF signal events and the ggF signal events with the boosted topology. These categories are analyzed separately due to different background compositions and event yields, and then results of these categories are combined for the final result. The definitions of two categories are based on different kinematic properties.

VBF Category

The VBF category is defined to select VBF signal events using the signature of the VBF process, which is the presence of two high p_{T} jets with a large pseudo-rapidity gap in the final state. The schematic diagram of the VBF topology is illustrated in Fig. 4.3 (a). The leading and sub-leading jets are required to have $p_{\text{T}} > 50$ GeV and 30 GeV, respectively. The pseudo-rapidity difference between two jets is required to be $\Delta\eta\left(\text{jet}_1, \text{jet}_2\right) > 3.0$, shown in Fig. 4.3 (b). In addition, events with low visible mass $m_{\text{vis}} < 40$ GeV are removed to suppress the fake τ_{had} background events. The definition of m_{vis} is described in Section 4.5.

Boosted Category

Target events of the Boosted category are events with the boosted Higgs boson, where the main contribution is from the ggF process. The selection is a requirement of the vector sum of transverse momenta of the lepton, τ_{had} and $E_{\text{T}}^{\text{miss}}$, denoted by p_{T}^{H}. This p_{T}^{H} variable corresponds to the transverse momentum of the Higgs boson, so that $p_{\text{T}}^{H} > 100$ GeV is required to enhance the signal events with the boosted topology. Figure 4.4 shows a schematic diagram of the boost topology and the p_{T}^{H} distributions for signal and

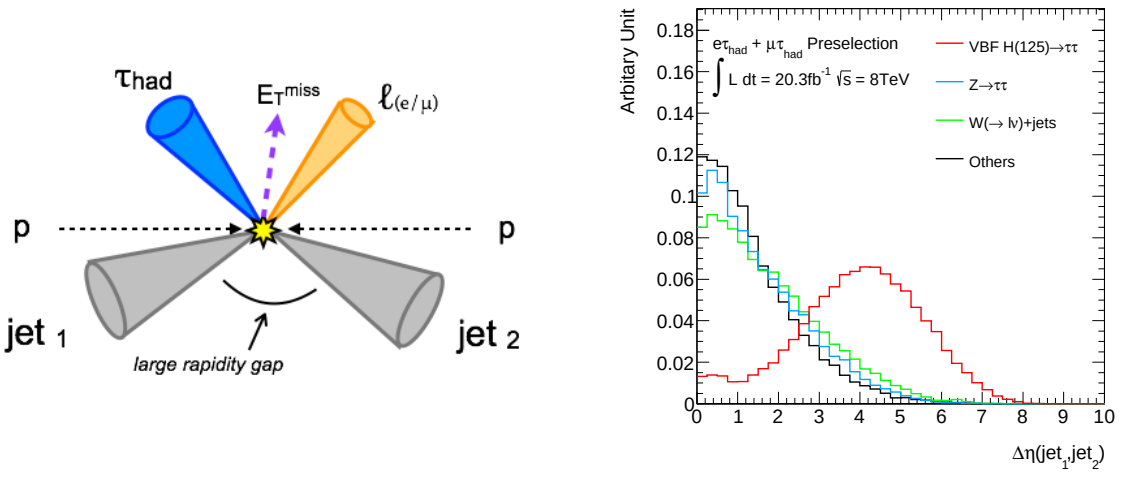

(a) VBF topology

(b) $\Delta\eta$ (jet1, jet2)

Fig. 4.3: (a) Schematic diagram of the VBF topology in the VBF $H \to \tau_\ell \tau_{\text{had}}$ process, and (b) the $\Delta\eta$ (jet1, jet2) distributions for VBF signal (red), $Z \to \tau\tau$ (blue), W+jets (green) and other (black) background events, where the Higgs boson mass is set to 125 GeV. The other background events represent the sum of the $Z \to \ell\ell$ +jets, $t\bar{t}$, single top and di-boson events. Events are required to pass the preselection and to have at least two jets with $p_{\text{T}} > 30$ GeV.

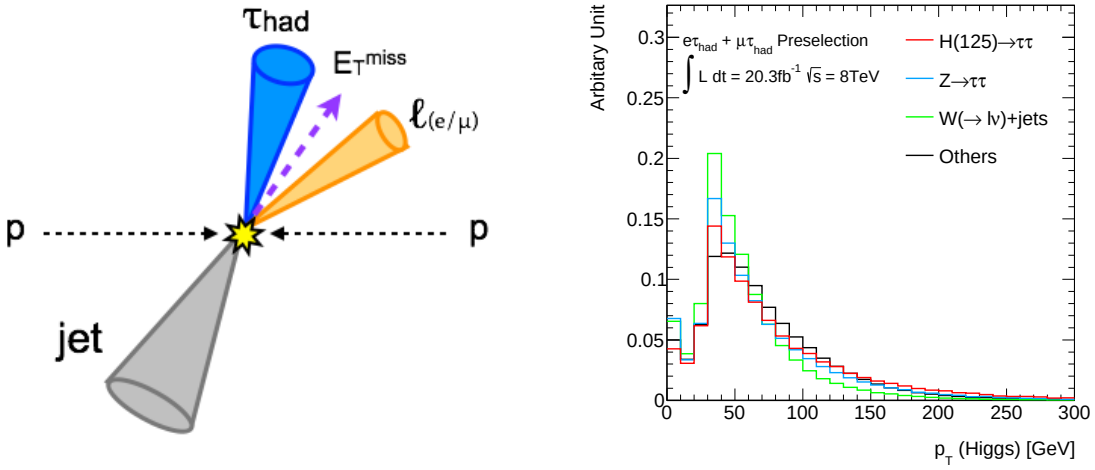

(a) Boosted topology

(b) p_{T}^{H}

Fig. 4.4: (a) Schematic diagram of the boosted topology in the $H \to \tau_\ell \tau_{\text{had}}$ process, and (b) the p_{T}^{H} distributions for signal (red), $Z \to \tau\tau$ (blue), W+jets (green) and other (black) background events. The signal is the sum of all signal processes where the Higgs boson mass is set to 125 GeV, and the other background events represent the sum of the $Z \to \ell\ell$ +jets, $t\bar{t}$, single top and di-boson events. Events are required to pass the preselection and to have at least 1 jet with $p_{\text{T}} > 30$ GeV.

background events. In addition, the Boosted category is required to be orthogonal to the VBF category, which means that events passed the VBF category selection are rejected from the Boosted category.

4.4.3 Signal and Control Regions

After the categorization, signal and control regions are defined for the VBF and Boosted categories. The signal region is used for the $H \to \tau_\ell \tau_{\text{had}}$ search, and in addition several dedicated control regions are defined to evaluate background estimations. The summary of definitions for the VBF and Boosted categories is shown in Table 4.4.

Signal Region

The signal region is defined by three different requirements: One is a requirement of opposite charge between lepton and τ_{had} based on the neutral Higgs boson charge. The others are a requirement of $m_{\text{T}} < 70$ GeV and b-jet veto to reduce background events from W+jets and $t\bar{t}$ /single top events, respectively.

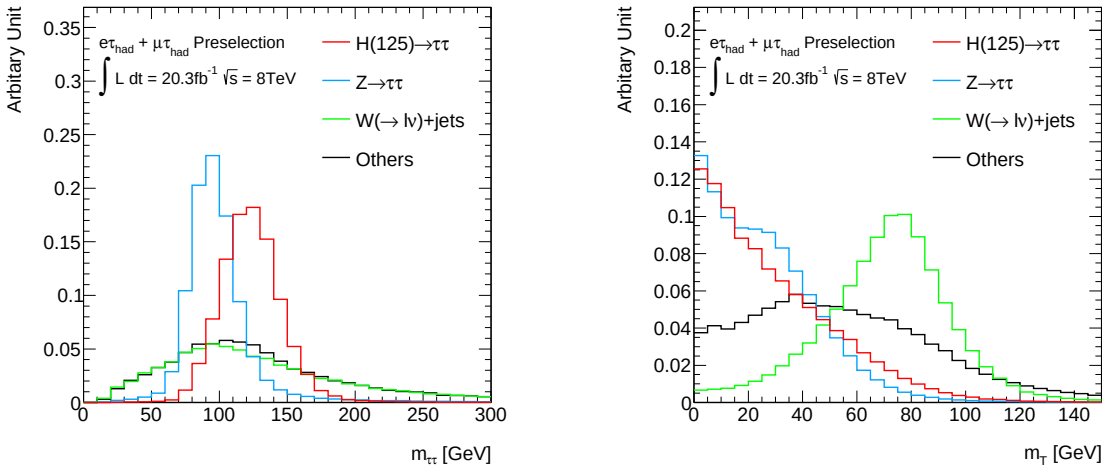

(a) $m_{\tau\tau}$ (b) m_{T}

Fig. 4.5: (a) The $m_{\tau\tau}$ and (b) the m_{T} distributions for signal (red), $Z \to \tau\tau$ (blue), W+jets (green) and other (black) background events. The signal is the sum of all signal processes where the Higgs boson mass is set to 125 GeV, and the other background events represent the sum of the $Z \to \ell\ell$ +jets, $t\bar{t}$, single top and di-boson events. Events are required to pass the preselection.

$Z \to \tau\tau$ Control Region

It is difficult to define a pure $Z \to \tau\tau$ control region due to the same final state as signal events. The $Z \to \tau\tau$ control region is defined as a part of signal region by requiring two additional requirements: One is $m_{\tau\tau} < 100$ GeV to reduce the signal contamination ($\sim 15\%$), where $m_{\tau\tau}$ is reconstructed by the MMC method (see Section 4.5). The other is $m_{\text{T}} < 40$ GeV to further suppress the W+jets background events.

W+jets Control Region

The transverse mass m_{T} is a powerful variable to reject (or enhance) W+jets background events. The selection of W+jets control region is the same as the signal region selection except for inverting the m_{T} cut, $m_{\text{T}} > 70$ GeV.

Multi-jet Control Region
In order to enhance the multi-jet events, the lepton track isolation requirement is inverted ($I(p_{\mathrm{T}}, 0.4) \leq 0.06$) and the calorimeter isolation is removed. There is non-negligible contamination from the $W(\rightarrow e\nu)$+jets events only changing the isolation requirement, and therefore the electron identification is relaxed to the *loose* working point in order to enhance the purity of multi-jet events.

Top Control Region
A top control region is defined to validate and correct the normalization of the Top (τ_{had}) and the Top ($\ell \rightarrow \tau_{\mathrm{had}}$) events. The events are required to have at least one b-jet in event and $m_{\mathrm{T}} > 70$ GeV, while other selections are the same as the signal region.

Top (jet $\rightarrow \tau_{\mathrm{had}}$) Control Region
An additional control region is defined for the Top (jet $\rightarrow \tau_{\mathrm{had}}$) events, which is used in a fake factor estimation method (see Section 4.6.2). This control region is defined by requiring at least one b-jet, and $m_{\mathrm{T}} < 70$ GeV. The selection must be an orthogonal to the selection of the Top (τ_{had}) and Top ($\ell \rightarrow \tau_{\mathrm{had}}$) control region in order to avoid duplicate use of control events.

$Z \rightarrow \ell\ell$ (jet $\rightarrow \tau_{\mathrm{had}}$) Control Region
The $Z \rightarrow \ell\ell$ (jet $\rightarrow \tau_{\mathrm{had}}$) events can be enhanced with following selections: a requirement of exactly two same flavor leptons with opposite sign, and the invariant mass of the two leptons is consistent with the Z boson mass window of 61 GeV $< m_{\ell\ell} <$ 121 GeV. This control region is used in the fake τ_{had} estimation.

Same Sign Control Region
This control region is used to validate a fake τ_{had} background estimation (see Section 4.6.2). While the opposite sign requirement enhances the $H \rightarrow \tau\tau$ and the $Z \rightarrow \tau\tau$ events based on a neutral boson charge, the same sign requirement enhances the fake τ_{had} background. The selection of this control region is only changed from an opposite sign to a same sign, while the other selections are the same as the signal region.

4.5 Mass Reconstruction

The invariant mass of di-τ ($m_{\tau\tau}$) is one of the most important variables in the $H \rightarrow \tau\tau$ search, but it cannot be directly reconstructed due to the presence of neutrinos from τ decays.

The most simplest reconstruction method is the invariant mass of detectable (visible) decay products, referred to as the visible mass (m_{vis}). However, this method completely ignores the effect of neutrinos, so that a peak of the m_{vis} distribution significantly differs from the original boson mass.

The collinear mass approximation [112] is one of the frequently used methods instead of the m_{vis}, based on two important assumptions. One is that neutrinos from τ decays are collinear with the visible τ decay products. The other is that the missing transverse energy in the event is only produced from neutrino energies. Two neutrinos from a leptonically decaying τ are treated as one neutrino system in this method. Thus, neutrino four-momenta are estimated by following equations:

Region	VBF	Boosted
Signal Region (SR)	Opposite Sign	Opposite Sign
	≥ 2 jets ($p_{\mathrm{T}} > 50/30$ GeV)	Not VBF
	$\Delta\eta\,(\mathrm{jet}_1, \mathrm{jet}_2) > 3.0$	$p_{\mathrm{T}}^{H} > 100$ GeV
	$m_{\mathrm{T}} < 70$ GeV	$m_{\mathrm{T}} < 70$ GeV
	b-jet veto	b-jet veto
	$m_{\mathrm{vis}} > 40$ GeV	$m_{\mathrm{vis}} > 40$ GeV
$Z \to \tau\tau$	SR cut and	SR cut and
Control Region	$m_{\mathrm{T}} < 40$ GeV	$m_{\mathrm{T}} < 40$ GeV
(CR)	$m_{\tau\tau} < 110$ GeV	$m_{\tau\tau} < 110$ GeV
W+jets CR	As SR, but	As SR, but
	$m_{\mathrm{T}} > 70$ GeV	$m_{\mathrm{T}} > 70$ GeV
multi-jet CR	As SR, but	As SR, but
	lepton $I(p_{\mathrm{T}}, 0.4) > 0.06$	lepton $I(p_{\mathrm{T}}, 0.4) > 0.06$
	remove lepton $I(E_{\mathrm{T}}, 0.2)$ cut	remove lepton $I(E_{\mathrm{T}}, 0.2)$ cut
	loose ID only for $H \to \tau_{\mathrm{e}}\tau_{\mathrm{had}}$	*loose* ID only for $H \to \tau_{\mathrm{e}}\tau_{\mathrm{had}}$
Top CR	As SR, but	As SR, but
	≥ 1 b-tagged jet and	≥ 1 b-tagged jet and
	$m_{\mathrm{T}} > 70$ GeV	$m_{\mathrm{T}} > 70$ GeV
Top (jet $\to \tau_{\mathrm{had}}$) CR	As SR, but	As SR, but
	≥ 1 b-tagged jet and	≥ 1 b-tagged jet and
	$m_{\mathrm{T}} < 70$ GeV	$m_{\mathrm{T}} < 70$ GeV
$Z/\gamma^* \to \ell\ell$	As SR, but	As SR, but
(jet $\to \tau_{\mathrm{had}}$) CR	2 OS same-flavor leptons	2 OS same-flavor leptons
	$61 < m_{\ell\ell} < 121$ GeV	$61 < m_{\ell\ell} < 121$ GeV
Fake τ_{had} CR	As SR, but	As SR, but
	Same sign	Same sign

Table 4.4: Summary of signal and control regions for VBF and Boosted categories.

$$
\begin{aligned}
E_{\mathrm{T}_x}^{\mathrm{miss}} &= p_{\mathrm{mis1}} \sin\theta_{\mathrm{vis1}} \cos\phi_{\mathrm{vis1}} + p_{\mathrm{mis2}} \sin\theta_{\mathrm{vis2}} \cos\phi_{\mathrm{vis2}}, \\
E_{\mathrm{T}_y}^{\mathrm{miss}} &= p_{\mathrm{mis1}} \sin\theta_{\mathrm{vis1}} \sin\phi_{\mathrm{vis1}} + p_{\mathrm{mis2}} \sin\theta_{\mathrm{vis2}} \sin\phi_{\mathrm{vis2}}, \\
\phi_{\mathrm{mis1}} &\approx \phi_{\mathrm{vis1}},\ \theta_{\mathrm{mis1}} \approx \theta_{\mathrm{vis1}}, \\
\phi_{\mathrm{mis2}} &\approx \phi_{\mathrm{vis2}},\ \theta_{\mathrm{mis2}} \approx \theta_{\mathrm{vis2}},
\end{aligned} \tag{4.2}
$$

where $E_{\mathrm{T}_{x(y)}}^{\mathrm{miss}}$ is the x(y) component of the missing transverse energy. ϕ and θ represents polar and azimuthal angles. Subscripts of mis1,2 and vis1,2 denote neutrino systems and visible products from τ decays, respectively. The di-τ invariant mass is then calculated as:

$$
\begin{aligned}
m_{\tau\tau} &= \frac{m_{\mathrm{vis}}}{\sqrt{x_1 x_2}}, \\
x_{1,2} &= \frac{p_{\mathrm{vis1,2}}}{p_{\mathrm{vis1.2}} + p_{\mathrm{mis1,2}}},
\end{aligned} \tag{4.3}
$$

where $x_{1,2}$ are momentum fractions of the visible τ decay products. Although the collinear method is possible to fully reconstruct the $m_{\tau\tau}$ including neutrino four-momenta, a reasonable mass resolution is given only in a small phase space: the di-τ system is highly boosted because of associated high p_{T} jets. Indeed, the equation (4.3) cannot be solved ($x_{1.2} < 0$ or $x_{1.2} > 1$)) in case that di-τ are emitted as back-to-back. Moreover, the method is sensitive to the $E_{\mathrm{T}}^{\mathrm{miss}}$ resolution, and it makes long tails of the reconstructed mass distribution due to the $E_{\mathrm{T}}^{\mathrm{miss}}$ worse resolution.

The missing mass calculator (MMC) [113] is an improved program to overcome weak points of the collinear method, such as no solution and long tails. The MMC is possible to reconstruct the di-τ invariant mass for any event topology. The MMC imposes an assumption that visible τ decay products are not affected from detector resolutions and an origin of neutrinos is only from τ decays. Under the assumptions, the reconstruction of neutrino four-momenta requires to solve 6 to 8 unknown parameters. The parameters are constrained by following equations:

$$
\begin{aligned}
E_{\mathrm{T}_x}^{\mathrm{miss}} &= p_{\mathrm{mis1}} \sin\theta_{\mathrm{mis1}} \cos\phi_{\mathrm{mis1}} + p_{\mathrm{mis2}} \sin\theta_{\mathrm{mis2}} \cos\phi_{\mathrm{mis2}}, \\
E_{\mathrm{T}_y}^{\mathrm{miss}} &= p_{\mathrm{mis1}} \sin\theta_{\mathrm{mis1}} \sin\phi_{\mathrm{mis1}} + p_{\mathrm{mis2}} \sin\theta_{\mathrm{mis2}} \sin\phi_{\mathrm{mis2}}, \\
m_{\tau_1}^2 &= m_{\mathrm{mis1}}^2 + m_{\mathrm{vis1}}^2 + 2\sqrt{p_{\mathrm{vis1}}^2 + m_{\mathrm{vis1}}^2}\sqrt{p_{\mathrm{mis1}}^2 + m_{\mathrm{mis1}}^2} \\
&\quad -2p_{\mathrm{vis1}}p_{\mathrm{mis1}} \cos\Delta\theta_{\mathrm{vis1,mis1}}, \\
m_{\tau_2}^2 &= m_{\mathrm{mis2}}^2 + m_{\mathrm{vis2}}^2 + 2\sqrt{p_{\mathrm{vis2}}^2 + m_{\mathrm{vis2}}^2}\sqrt{p_{\mathrm{mis2}}^2 + m_{\mathrm{mis2}}^2} \\
&\quad -2p_{\mathrm{vis2}}p_{\mathrm{mis2}} \cos\Delta\theta_{\mathrm{vis2,mis2}},
\end{aligned} \tag{4.4}
$$

where $m_{\tau_{1,2}}$ are the invariant mass of the τ ($m_\tau = 1.77$ GeV), $m_{\mathrm{mis1,2}}$ are the invariant mass of neutrino

systems ($m_{\text{mis1,2}} = 0$ in case that τ decays hadronically). $\Delta\theta_{vis,mis}$ is an polar angle difference between the visible product and the neutrino system. Although the equation (4.4) reduces unknown parameters, there are still 2 to 4 unknown parameters: $\phi_{\text{mis1,2}}$ ($m_{\text{mis1,2}}$). An additional knowledge of τ decay kinematics can be used to distinguish more likely solutions from less likely ones. These parameters are determined by global event likelihood using $\Delta\theta_{\text{3D}}$ as probability density functions (PDFs), where $\Delta\theta_{\text{3D}}$ is a three-dimensional angle between the visible product and the neutrino system. The PDFs are obtained from simulated $Z \to \tau\tau$ events with respect to the momentum of the original τ lepton ($p(\tau)$). Figure 4.6 shows PDFs, $P(\Delta\theta_{\text{3D}}, p(\tau))$, for the leptonic, 1-prong and 3-prong τ decays with $45 < p(\tau) \leq 50$ GeV.

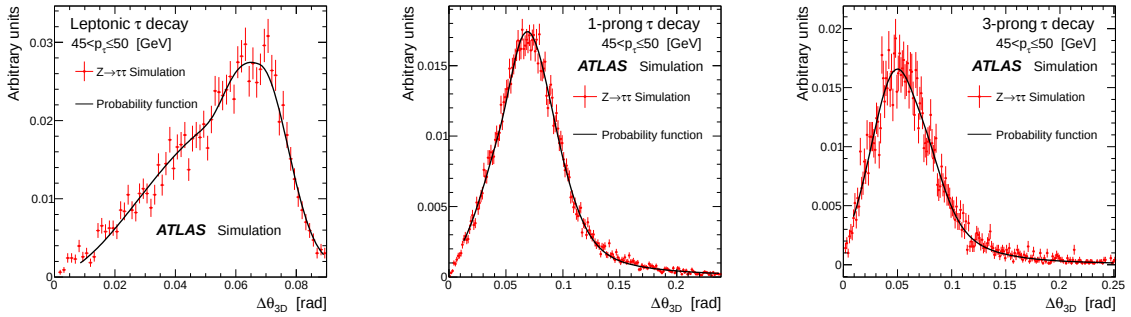

(a) (b) (c)

Fig. 4.6: Probability density functions $P(\Delta\theta_{\text{3D}}, p_{\text{T}})$ for (a) the leptonic, (b) 1-prong and (c) 3-prong τ decays with $45 < p(\tau) \leq 50$ GeV. Red dot shows the PDFs obtained from simulated $Z \to \tau\tau$ events, while black line shows a fit result with a Gaussian plus landau function.

The MMC includes an effect of finite resolution of the $E_{\text{T}}^{\text{miss}}$ measurement in order to improve the $m_{\tau\tau}$ resolution. The effect is taken into account by introducing two probability functions of the $E_{\text{T}}^{\text{miss}}$ resolution to the likelihood:

$$P(\Delta E_{\text{T}_{x,y}}^{\text{miss}}) = \exp\left(-\frac{\left(\Delta E_{\text{T}_{x,y}}^{\text{miss}}\right)^2}{2\sigma^2}\right), \tag{4.5}$$

where $\Delta E_{\text{T}_{x,y}}^{\text{miss}}$ are variations between a measured and true $E_{\text{T}}^{\text{miss}}$ for x and y components, and σ is the $E_{\text{T}}^{\text{miss}}$ resolution measured from calibration data samples. Thus, the likelihood is defined as:

$$L = P(\Delta\theta_{\text{3D,1}}, p_{\text{T,1}}) \times P(\Delta\theta_{\text{3D,2}}, p_{\text{T,2}}) \times P(\Delta E_{\text{T}_x}^{\text{miss}}) \times P(\Delta E_{\text{T}_y}^{\text{miss}}). \tag{4.6}$$

The MMC scans about 10^5 phase space of ($\phi_{\text{mis1,2}}, E_{\text{T}_x}^{\text{miss}}, E_{\text{T}_y}^{\text{miss}}$ ($, m_{\text{mis1,2}}$)), and then a number of $m_{\tau\tau}$ and L are produced at all scan points. The peak value of the $m_{\tau\tau} \times L$ histogram is used as the final estimated $m_{\tau\tau}$. The MMC is able to estimate physical $m_{\tau\tau}$ value with high reconstruction efficiency around $97\% \sim 99\%$.

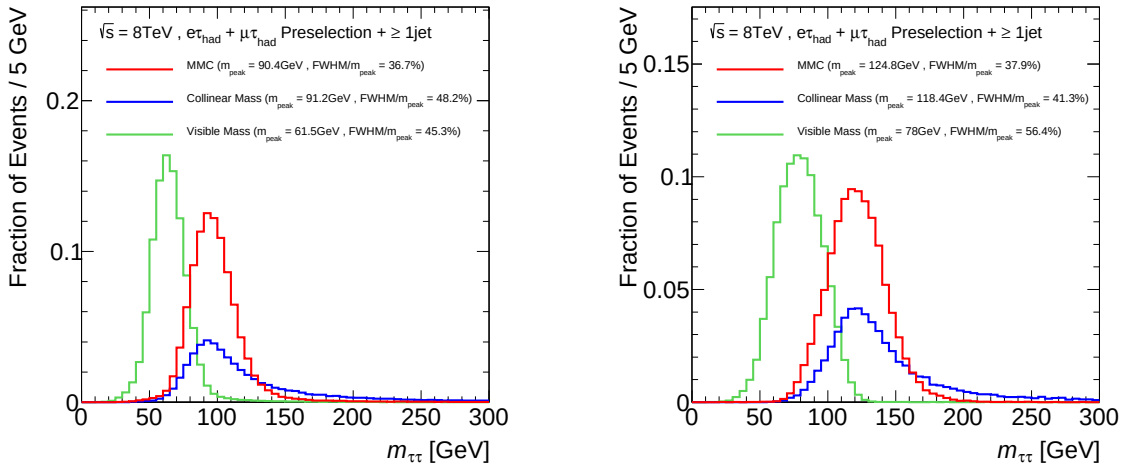

(a) (b)

Fig. 4.7: $m_{\tau\tau}$ distributions using the visible (green), the collinear (blue) and the MMC (red) methods for (a) the $Z \to \tau\tau \to \ell\tau_{\text{had}}$ and (b) the $H \to \tau_\ell\tau_{\text{had}}$ with the Higgs boson mass of 125 GeV. Events are required to pass the preselection and to have at least one jet with $p_{\text{T}} > 30$ GeV.

Figure 4.7 shows $m_{\tau\tau}$ distributions of different three methods, separately for $Z \to \tau\tau \to \ell\tau_{\text{had}}$ and $H \to \tau_\ell\tau_{\text{had}}$ with the Higgs boson mass of 125 GeV processes. Events are required to pass the preselection and to have at least one jet with $p_{\text{T}} > 30$ GeV. This jet requirement increases physical solutions of the collinear method from $25.2 \pm 0.3\%$ to $42.3 \pm 0.3\%$. On the other hand, the efficiency of the MMC is $\sim 99\%$ in spite of the jet requirement. Figure 4.8 shows the linearity of the $m_{\tau\tau}$ peak and the Root-Mean-Square (RMS) of the $m_{\tau\tau}$ histogram, as a function of the input Higgs boson mass from 100 GeV to 150 GeV in a 5 GeV step. The peaks can be almost correctly reconstructed by the MMC, while the peaks of collinear method are shifted under ~ 5 GeV, depending on the Higgs boson mass values. The RMSs of the MMC and the collinear method are $18\% \sim 27\%$ and $41\% \sim 52\%$, respectively. Although the RMSs of the visible mass are of the order of $14\% \sim 15\%$, the peaks of the visible mass are significantly smaller from the Higgs boson mass of the order of 40 GeV $\sim$ 50 GeV due to not considering neutrino four-momenta. This analysis uses the MMC method to reconstruct the $m_{\tau\tau}$ because of better mass peak reconstruction with the smaller RMS than the collinear method.

4.6 Background Model

In order to search for $H \to \tau_\ell\tau_{\text{had}}$ signal events, background contributions must be well understood and estimated as precise as possible. This section describes background estimation methods for each background component and comparisons between data and background modeling. The $Z \to \tau\tau$ and the fake τ_{had} background, which are main background components, are estimated by data-driven techniques, while other backgrounds are estimated by simulation samples normalized to cross sections predicted theoretically.

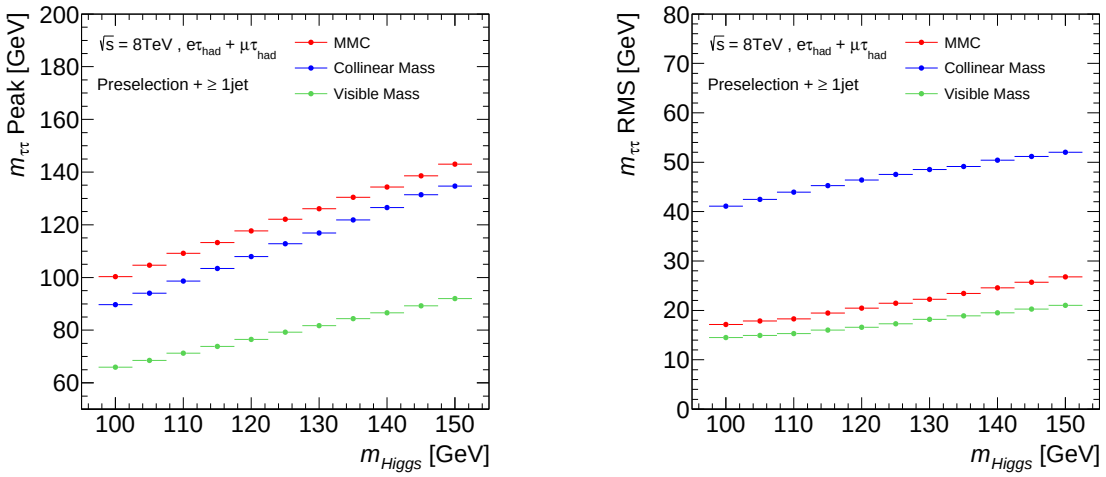

(a) (b)

Fig. 4.8: (a) The linearity of the di-τ mass peak and (b) the Root Mean Square (RMS) of the di-τ mass histogram for the visible mass (green), the collinear (blue) and the MMC (red), as a function of the Higgs boson mass. The mass peak is defined as a mean of Gaussian fit to the di-τ mass histogram, where a fit range is $\pm$RMS from a maximum entry bin. Events are required to pass the preselection and to have at least one jet with $p_{\mathrm{T}} > 30$ GeV.

4.6.1 $Z \to \tau\tau$ Background

The $Z \to \tau\tau$ process is a large intrinsic background to $H \to \tau\tau$ signal events, so that the modeling of the $Z \to \tau\tau$ background is one of the important points in this analysis. Ideally, this background would be estimated by completely data-driven technique. However, it is difficult to define its dedicated control region with high-purity and high-statistics because this background has the same objects and similar kinematics as the signal. The contribution of the $Z \to \tau\tau$ background is modeled by a data and simulation hybrid sample, so-called an embedding sample [114]. The embedding sample is generated from $Z \to \mu\mu$ events in data by replacing real muons to simulated τ leptons. The $Z \to \mu\mu$ events in data are used as a starting point of the sample generation because kinematics of the Z boson decay and additional jets are identical between $Z \to \mu\mu$ and $Z \to \tau\tau$ events. The difference between two processes is only effects of a mass difference between muons and τ leptons.

The $Z \to \mu\mu$ candidate events are collected using two muon triggers: the one is a di-muon trigger with p_{T} thresholds of $18/8$ GeV for leading/sub-leading muon, and the other is a single muon trigger with a p_{T} threshold of 24 GeV. The candidate events are required to have at least two muons, passing *tight* muon identification (see 4.4.1), where p_{T} and isolation requirements are modified as following: the leading (sub-leading) muon is required to fulfill $p_{\mathrm{T}} > 20(15)$ GeV, the track isolation is relaxed to $I(p_{\mathrm{T}}, 0.4) < 0.2$, and the calorimeter requirement is removed. In addition, two muons are selected by a requirement of opposite charge, and $m_{\mu\mu} > 40$ GeV. After above selections, the $Z \to \mu\mu$ events can be obtained from the data with high-purity and high-statistics.

Then, reconstructed two muons are removed from $Z \to \mu\mu$ events. Two track associated with recon-

structed muons is subtracted from data events. In order to determine calorimeter cells associated with reconstructed muons, simulated $Z \to \mu\mu$ events are generated with the same kinematics as the original data events without pile-up interactions. The calorimeter cell energies in the simulated events are subtracted from data events.

A simulation of the $Z \to \tau\tau$ decay is performed in order to add simulated τ leptons into muon subtracted data events. The four-momenta of two τ leptons are derived from reconstructed two muons, according to

$$p_\tau = \sqrt{E_\mu^2 - m_\tau^2}, \tag{4.7}$$

where the muon mass is replaced to the τ lepton mass keeping the original muon energy. The production vertex of τ lepton pair is set to the same as the reconstructed muon pair. The decay of two τ leptons and their radiation are simulated by the TAUOLA [115] and the PHOTOS [116] programs. The simulated $Z \to \tau\tau$ decays are then passed through the ATLAS detector simulation and reconstruction [117].

Then, a kinematic filter is applied to simulated τ leptons in order to increase the number of events which pass the preselection. The filter requires events to have one lepton with $p_{\mathrm{T}}(e/\mu) > 18/15$ GeV from a leptonically decaying tau and one τ_{had} with $p_{\mathrm{T}}(\tau_{\mathrm{had}}) > 15$ GeV from hadronically decaying tau. In case that events do not pass the selection, the simulation of the $Z \to \tau\tau$ decay is repeated until passing the filter selection. A kinematic bias from the filter is corrected by applying event-by-event weight corresponding to the filtering efficiency.

Finally tracks and cell energies from the simulated τ lepton decays are merged to muon subtracted data events. Figure 4.9 shows example displays of a $Z \to \mu\mu$ data event, the corresponding simulated $Z \to \tau\tau$ event and the hybrid event after the embedding, where one τ lepton decays into a muon and the other one decays into hadrons in the $Z \to \tau\tau$ simulation.

The main advantage of this method is direct use of data except for τ lepton decay products, and thereby systematic uncertainties related from jets, pile-up interactions and underlying events do not need to be considered. Especially not considering jet related uncertainties is beneficial because the kinematic properties of additional jets is used for the category definition and the background suppression, which are important parts of this analysis. Two uncorrelated sources of the systematic uncertainty are considered for this method. The one is related to the isolation requirement in the initial data selection. The uncertainty is evaluated by varying the isolation selection from the nominal ($I(p_{\mathrm{T}}, 0.4) < 0.2$) to a *tight* isolation requirement ($I(p_{\mathrm{T}}, 0.4) < 0.06$ and $I(E_{\mathrm{T}}, 0.2) < 0.04$) or no isolation selection. The second one is for the muon calorimeter cell subtraction procedure. The cell energies of the simulated muons are varied by $\pm 20\%(30\%)$ for the 8 TeV(7 TeV) analysis.

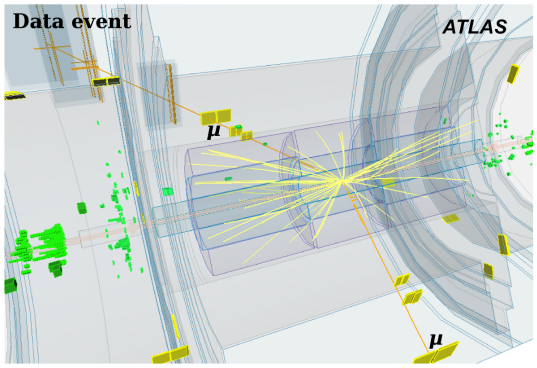

(a) $Z \to \mu\mu$ data event

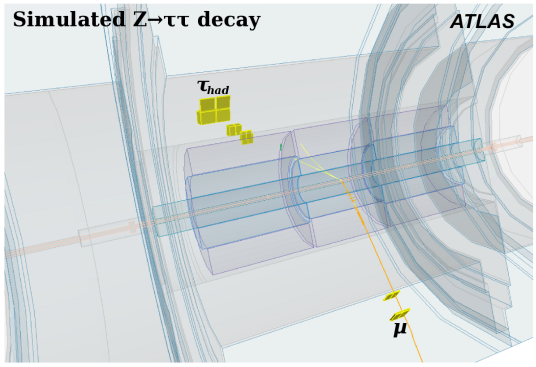

(b) simulated $Z \to \tau\tau$ event

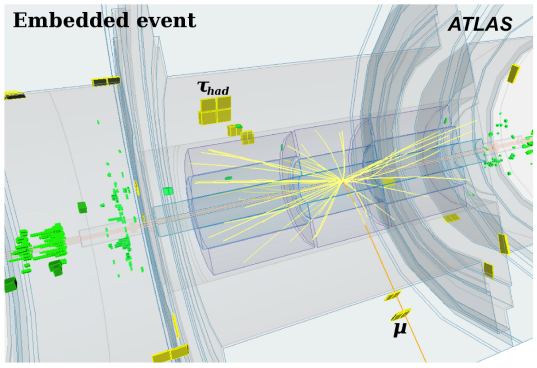

(c) embedded hybrid event

Fig. 4.9: Event display of (a) the $Z \to \mu\mu$ data event, (b) the corresponding simulated $Z \to \tau\tau$ event and (c) the embedded hybrid event. In the simulated $Z \to \tau\tau$ event, one τ lepton decays into a muon and the other one decays into hadrons. Lines and boxes shows reconstructed tracks and calorimeter cells, respectively.

4.6.2 Fake τ_{had} Background

The fake τ_{had} background consists of W+jets, multi-jet, $Z \to \ell\ell$ (jet $\to \tau_{\text{had}}$) and Top (jet $\to \tau_{\text{had}}$), which are events with one misidentified τ_{had} from a jet. It is hard to estimate this background from simulation samples due to a poor modeling of detector performance for the jet to τ_{had} misidentification, and therefore this background is estimated by data-driven technique, so-called "fake factor" method.

The fake factor (FF) method estimates the number of fake τ_{had} background events and their shapes, based on data events with "anti-τ_{had}" objects and "fake factor". The anti-τ_{had} object is defined as the same τ_{had} object selection except for the *medium* τ_{had} identification. Based on the BDT τ_{had} identification and its corresponding working points (see Section 3.4), the anti-τ_{had} is defined as the following requirement: 0.7 $\times$ *loose* working point $<$ BDT score $<$ *medium* working point. In order to minimize the difference between the anti-τ_{had} object and the misidentified τ_{had}, very low BDT scored τ_{had} candidates are discarded. Figure 4.10 shows a fraction of an origin of a τ_{had} candidate in the simulated W+jets background events as a function of the BDT score. Events are required to pass the preselection and the W+jets control region selection. The origin is identified by a parton-level information of simulation samples. As a reference, the 0.7 $\times$ *loose* working point corresponds to $0.36 \sim 0.40$ for the 1-prong and $0.35 \sim 0.39$ for 3-prong, while the *medium* working point corresponds to $0.57 \sim 0.65$ for 1-prong and $0.53 \sim 0.59$

for 3-prong, depending on τ_{had} p_{T} (20 GeV $\sim$ 100 GeV). Large pile-up and gluon contributions can be seen in the low BDT score region, while the high BDT score region is dominated by quark contributions. Thus, the lower BDT score cut of 0.7 $\times$ BDT *loose* working point is introduced, considering statistics of events with the anti-τ_{had} object.

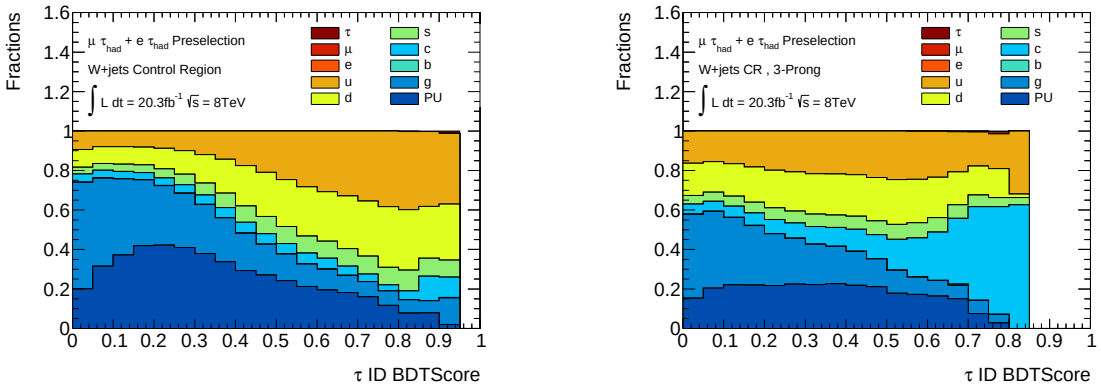

(a) 1-prong (b) 3-prong

Fig. 4.10: Fraction of an origin of τ_{had} candidates as a function of BDT score used in the τ_{had} identification for (a) 1-prong and (b) 3-prong in W+jets control region after the preselection.

Based on the anti-τ_{had} object, anti-τ_{had} control regions and the fake factor are defined. The anti-τ_{had} control regions are defined corresponding to the signal, W+jets, multi-jet, $Z \to \ell\ell$ (jet $\to \tau_{\text{had}}$) and Top (jet $\to \tau_{\text{had}}$) control regions. Definitions of each anti-τ_{had} control region are the same as described in Table 4.4 except for the exactly one identified τ_{had} requirement, which is replaced to a requirement of at least one anti-τ_{had} objects. The fake factor is defined as a transfer factor from a anti-τ_{had} region to an identified τ_{had} region, where the identified τ_{had} region denotes the signal or control region with exactly one τ_{had} object.

In the FF method, the fake τ_{had} background in the signal region is estimated by multiplying the fake factor into the anti-τ_{had} signal region. As the simplest case, if an anti-τ_{had} region contains exactly one anti-τ_{had} object for each event, and if the fake factor doesn't have any dependencies, the FF method is expressed by::

$$N_{\text{bkg.}}^{\text{id,SR}} = \left(N_{\text{data}}^{\text{anti,SR}} - N_{\text{others}}^{\text{anti,SR}} \right) \times \text{FF}, \tag{4.8}$$

$$\text{FF} = \frac{N_{\text{data}}^{\text{id,CR}}}{N_{\text{data}}^{\text{anti,CR}}}, \tag{4.9}$$

where $N_{\text{bkg.}}^{\text{id,SR}}$ is the estimated number of fake τ_{had} background events in the signal region, N^{data} and N^{data} are the number of data and non fake τ_{had} background events in the anti-τ_{had} signal region, respectively. The $N_{\text{others}}^{\text{anti,SR}}$ consists of Top (τ_{had}), Top ($\ell \to \tau_{\text{had}}$), $Z \to \ell\ell$ ($\ell \to \tau_{\text{had}}$) and diboson events, and they are

estimated by simulation samples. The fake factor is obtained by taking a ratio of $N_{\text{data}}^{\text{id,CR}}$ and $N_{\text{data}}^{\text{anti,CR}}$.

The anti-τ_{had} region contains more than one anti-τ_{had}, whose fraction is $3 \sim 5\%$ depending on categories and regions. All the anti-τ_{had} objects in data events are used to define anti-τ_{had} regions. The N^{anti} in the equation (4.8) is converted as:

$$N^{\text{anti}} = \sum_{i=1}^{N_{\text{evt.}}^{\text{anti}}} \sum_{j=1}^{\text{n}_i}, \tag{4.10}$$

where $N_{\text{evt.}}^{\text{anti}}$ represents the number of anti-τ_{had} events, n_i is the number of anti-τ_{had} objects in a event i, and j represents a j-th anti-τ_{had} object.

In addition, the fake factor depends on several factors related to the anti-τ_{had} object, and therefore the equation (4.8) is converted as:

$$N_{\text{bkg.}}^{\text{id,SR}} = \sum_{i=1}^{N_{\text{evt.,data}}^{\text{anti,SR}}} \sum_{j=1}^{\text{n}_i} \text{FF}_j - \sum_{i=1}^{N_{\text{evt.,others}}^{\text{anti,SR}}} \sum_{j=1}^{\text{n}_i} \text{FF}_j, \tag{4.11}$$

where FF_j represents the fake factor for a j-th anti-τ_{had} object. The main sources of the fake factor dependency are the number of tracks (n_{prong}), the transverse momentum (p_{T}), and the event category. The fake factor is separately measured as a function of τ_{had} p_{T} for 1-prong and 3-prong, and for the VBF and Boosted categories, In addition, the fake factor depends on an origin of the anti-τ_{had} object whether a quark or a gluon. The fraction of the origin (i.e., quark/gluon fraction) is different depending on physics processes, and the measurement of the fraction from data events is quite difficult. Thus, the fake factor is separately measured for each control region, and then they are combined for the signal region. Figure 4.11 shows measured fake factors for each fake τ_{had} background processes: W+jets, multi-jet, $Z \to \ell\ell$ (jet $\to \tau_{\text{had}}$) and Top (jet $\to \tau_{\text{had}}$) processes.

The combined procedure is expressed by:

$$\text{FF}(p_{\text{T}}, \text{n}_{\text{prong}}, \text{category}) = \sum_{i=bkg.} R_i \, \text{FF}_i(p_{\text{T}}, \text{n}_{\text{prong}}, \text{category}), \tag{4.12}$$

$$R_i = \frac{N_i^{\text{anti,SR}}}{N_{\text{fakes}}^{\text{anti,SR}}}, \tag{4.13}$$

where R_i represents an event fraction of a background i in the anti-τ_{had} signal region, and $N_{\text{fakes}}^{\text{anti,SR}}$ is the total number of fake τ_{had} events.

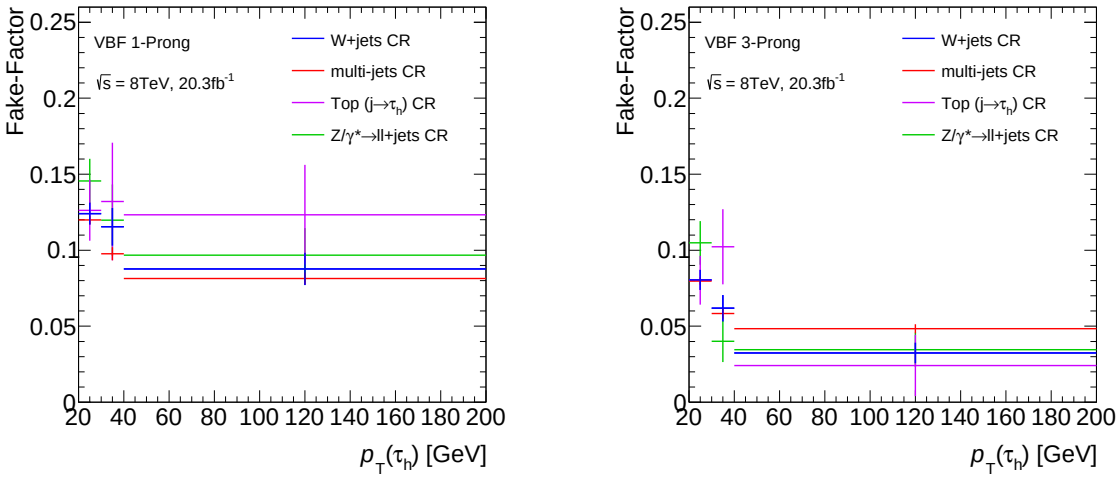

(a)

(b)

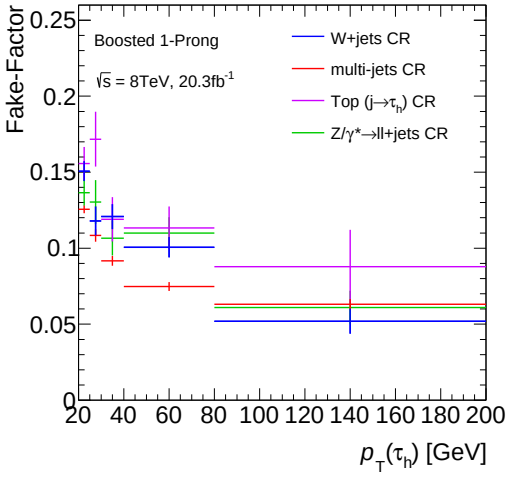

(c)

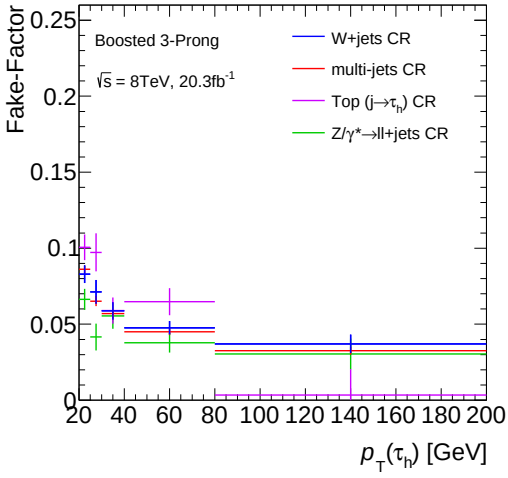

(d)

Fig. 4.11: Fake Factors obtained from each control region as a function of τ_{had} p_{T} for (a,c) 1-prong and (b,d) 3-prong, and for (a,b) VBF and (c,d) Boosted categories in 8TeV.

For the W+jets background, the fraction ($R_{\text{W+jets}}$) is derived from data events using a part of simulation term as the following:

$$
\begin{aligned}
R_{\text{W+jets}} &= \frac{N^{\text{anti-SR}}_{W\text{+jets}}}{N^{\text{anti-SR}}_{\text{fakes}}} = \frac{N^{\text{anti-SR}}_{W\text{+jets}}}{N^{\text{anti-SR}}_{\text{data}} - N^{\text{anti-SR}}_{\text{others MC}}}, \\
N^{\text{anti-SR}}_{W\text{+jets}} &= N^{\text{anti-WCR}}_{\text{data}} \times \frac{N^{\text{anti-SR}}_{W\text{+jets MC}}}{N^{\text{anti-WCR}}_{W\text{+jets MC}}}.
\end{aligned}
\tag{4.14}
$$

In order to estimate the $R_{\text{W+jets}}$, the total number of fake τ_{had} background events ($N^{\text{anti-SR}}_{\text{fakes}}$) and the number of W+jets events in the anti-τ_{had} signal region ($N^{\text{anti-SR}}_{W\text{+jets}}$) have to be estimated. The $N^{\text{anti-SR}}_{\text{fakes}}$

is obtained from the number of data events in the anti-τ_{had} signal region ($N_{\text{data}}^{\text{anti-SR}}$) by subtracting the number of non fake τ_{had} background events estimated by simulation samples ($N_{\text{others MC}}^{\text{anti-SR}}$). The $N_{W\text{+jets}}^{\text{anti-SR}}$ is obtained from the number of data events in the anti-τ_{had} W+jets control region by multiplying the transfer factor of anti-τ_{had} W+jets to anti-τ_{had} signal region, where the transfer factor is derived from simulation sample ($N_{W\text{+jets MC}}^{\text{anti-SR}}/N_{W\text{+jets MC}}^{\text{anti-WCR}}$).

For the Top (jet $\rightarrow$ τ_{had}) and $Z \rightarrow \ell\ell$ (jet $\rightarrow$ τ_{had}) backgrounds, the R_{Top} and the $R_{Z/\gamma^* \rightarrow \ell\ell}$ are estimated from simulation samples due to low statistics and non-negligible $\ell \rightarrow \tau_{\text{had}}$ contamination in each anti-τ_{had} control region. For multi-jet background, the $R_{\text{multi-jet}}$ is simply calculated by $1 - R_{\text{W+jets}} - R_{\text{Top}} - R_{Z/\gamma^* \rightarrow \ell\ell}$ because other fractions are determined as mentioned before and the simulation sample of the multi-jet process is not used in this analysis. Table 4.5 presents each R_i for the VBF and Boosted categories in the 8 TeV and 7 TeV analysis. Since the fractions are estimated by a part of simulation samples, its ambiguity is considered as one of the systematic uncertainty sources of the FF method.

	7TeV		8TeV	
	VBF	Boosted	VBF	Boosted
$R_{\text{W+jets}}$	0.60 ± 0.020	0.75 ± 0.014	0.46 ± 0.011	0.62 ± 0.008
$R_{\text{multi-jet}}$	0.24 ± 0.008	0.13 ± 0.003	0.40 ± 0.008	0.26 ± 0.003
R_{Top}	0.13 ± 0.005	0.06 ± 0.001	0.03 ± 0.001	0.07 ± 0.001
$R_{Z/\gamma^* \rightarrow \ell\ell}$	0.03 ± 0.001	0.06 ± 0.001	0.11 ± 0.003	0.05 ± 0.001

Table 4.5: Fractions of each fake τ_{had} background in the anti-τ_{had} signal region. The quoted uncertainties represent statistical uncertainties.

Then, the combined fake factor for signal region is derived from the equation (4.12). Figure 4.12 shows the combined fake factors for the VBF and Boosted categories in the 8 TeV analysis. Systematic uncertainties of the fake factor method is described in Section 4.8.3. Finally, the number of fake τ_{had} events in the signal region is estimated by the equation (4.11). Figure 4.13 shows a comparison between the observed data and the estimated fake τ_{had} background in the same sign control region: the $\Delta\eta$ (jet1, jet2) distribution for the VBF category, and the $\sum p_{\text{T}}$ distribution for the Boosted category, where the sum p_{T} is the transverse momentum sum of the lepton, τ_{had}, $E_{\text{T}}^{\text{miss}}$ and jets.

4.6.3 Top Background

The Top (jet $\rightarrow$ τ_{had}) background is estimated as a part of the fake τ_{had} background. The remaining contribution from the Top (τ_{had}) and Top ($\ell \rightarrow \tau_{\text{had}}$) events is estimated based on simulation samples, normalized to their predicted cross sections. The normalization is additionally corrected by applying scale factors derived from the top control region. The scale factors are obtained separately for the VBF and Boosted categories, by the following: $\text{SF} = (\text{N}_{\text{data}} - \text{N}_{\text{other}})/\text{N}_{\text{top}}$, where N_{data} represents the number of data events in the control region, N_{top} represents the number of expected Top (τ_{had}) and Top ($\ell \rightarrow \tau_{\text{had}}$)

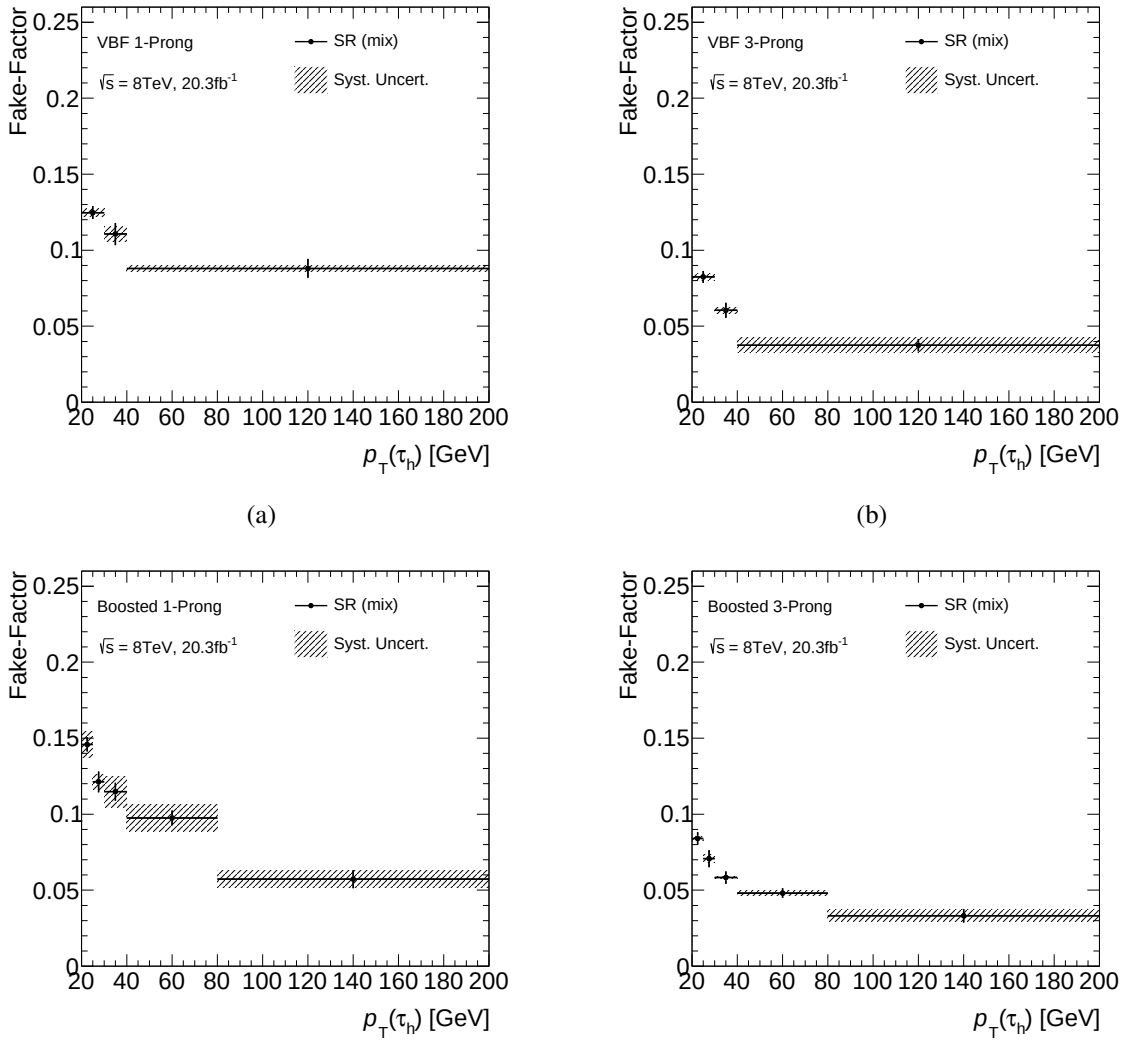

Fig. 4.12: Combined fake factors as a function of τ_{had} p_{T} for 1-prong (a,c) and 3-prong (b,d), for VBF (a,b) and boosted (c,d) categories in 8 TeV. The hatched bands show the systematic uncertainty.

events, and N_{other} represents the number of expected other background events. The obtained scale factors are listed in Table 4.6. Figure 4.14 shows transverse mass distributions in the top control regions of the VBF and Boosted categories, after applying the scale factors.

Category	8 TeV	7 TeV
VBF	0.84 ± 0.08	1.44 ± 0.36
Boosted	0.96 ± 0.04	1.12 ± 0.14

Table 4.6: Normalization scale factors for Top (τ_{had}) and Top $(\ell \rightarrow \tau_{\text{had}})$ events, for the VBF and Boosted categories in 8 TeV and 7 TeV analysis.

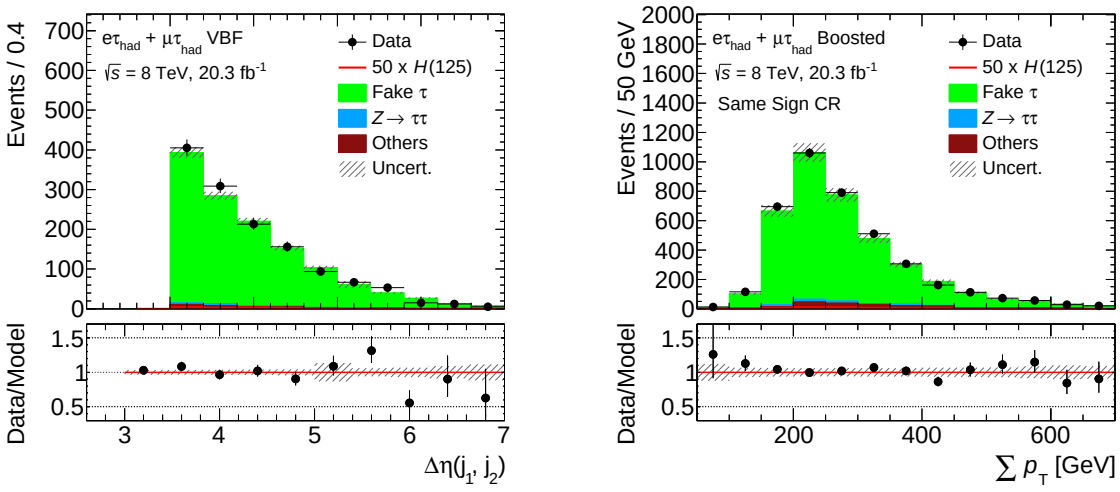

(a) (b)

Fig. 4.13: (a) The $\Delta\eta$ (jet1, jet2) distribution in the same sign control region of the VBF category, and (b) the $\sum p_{\mathrm{T}}$ distribution in the same sign control region of the Boosted category. The data distribution is shown as black dots, while the fake τ_{had} events predicted by the fake factor method are represented by the green filled histogram. The signal contribution shown as red line is negligible, where the normalization is 50 times from the expected number of events. The lower panel shows the ratio between data and the background model. The hatched band corresponds to the statistical and systematic uncertainties of the background estimation.

4.6.4 $Z \to \ell\ell$ and di-boson Background

The $Z \to \ell\ell$ (jet $\to \tau_{\mathrm{had}}$) events are estimated as a part of the fake τ_{had} background. The remaining $Z \to \ell\ell$ ($\ell \to \tau_{\mathrm{had}}$) events are estimated by simulation samples, normalized by the predicted cross sections. The di-boson events are also modeled by simulation samples. The simulation samples are corrected by all scale factors, such as trigger, reconstruction and identification scale factors. While the di-boson events contain several decay process including a misidentified τ_{had} from a jet, they are estimated together as one background process due to their smaller cross sections than the other backgrounds, as described in Section 4.3.2.

4.6.5 Comparison between Observed Data and Background Modeling

This section summarizes comparisons between the observed data and the estimated events with the background modeling described in above sections. Comparisons between the number of observed data events and the number of expected background events with their uncertainties are shown in Table 4.7 and Table 4.8, for the VBF and boosted categories in 8 TeV and 7 TeV analyses. The quoted uncertainties include both statistical and systematic uncertainties. Main background processes are the $Z \to \tau\tau$ and fake τ_{had} background events for the both VBF and Boosted categories, while fractions of these contributions are different between them. For example, the fake τ_{had} and the $Z \to \tau\tau$ background has 59.7% and 32.9% contributions in 8 TeV VBF category, while 42.5% and 49.4% contributions in the 8 TeV Boosted

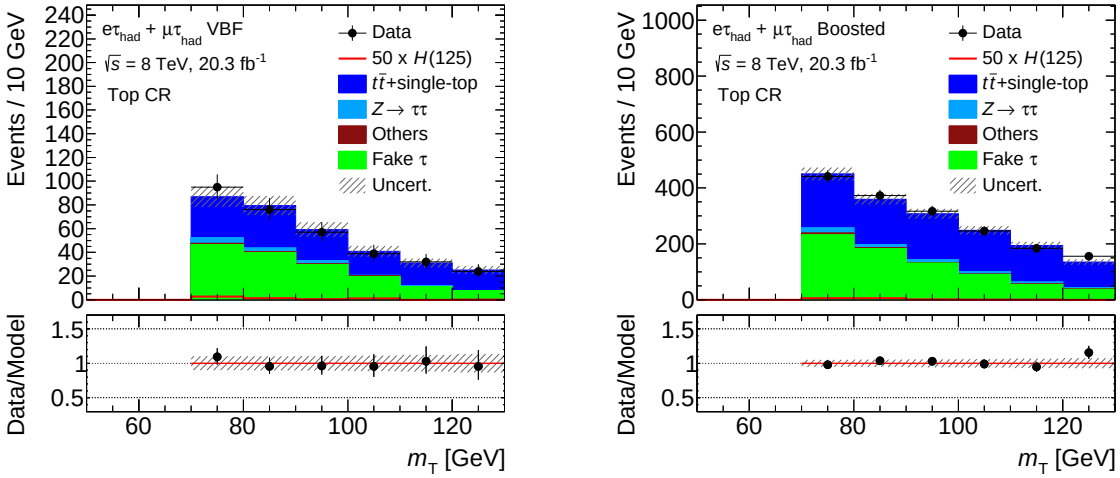

(a) (b)

Fig. 4.14: Transverse mass distributions in the top control regions for (a) the VBF and (b) Boosted categories. The data distribution is shown as black dots, while the Top (τ_{had}) and Top ($\ell \to \tau_{\text{had}}$) events are represented by blue filled histograms, where the normalization is the expected number of events times the scale factors. The fake τ_{had} background mainly from Top (jet $\to \tau_{\text{had}}$) events are shown as green histograms. The signal distribution shown as a red line is negligible, where the normalization is 50 times from its expected number of events. The lower panel shows the ratio between data and the total background model. The hatched band corresponds to the statistical and systematic uncertainties of the background estimation.

category, respectively. The comparison is also performed in dedicated control regions, and each background modeling agrees with the observed data within their uncertainties. Figure 4.15 and 4.16 shows mT, $\Delta R(\ell, \tau_{\text{had}})$ and $m_{\tau\tau}$ distributions for the signal, W+jets control, and $Z \to \tau\tau$ control regions, for the VBF and Boosted categories. The number of expected signal events are very small compared to the number of total background events in the signal region. In order to enhance a signal over background ratio, further background suppression and signal extraction procedure are needed

Process	8 TeV VBF category	8 TeV boosted category
Fake τ_{had}	$1637 \pm 13 \pm 72$	$5426 \pm 26^{+337}_{-335}$
$Z \to \tau\tau$	$900 \pm 17^{+61}_{-60}$	$6320 \pm 60 \pm 280$
Top (τ_{had})	$79 \pm 5 \pm 10$	$360 \pm 10 \pm 30$
$Z \to \ell\ell$ ($\ell \to \tau_{\text{had}}$)	$34.1 \pm 2.8^{+21.3}_{-19.5}$	$210 \pm 11^{+56}_{-57}$
Di-boson	$64 \pm 5 \pm 13$	$420 \pm 12 \pm 48$
ggF ($m_H = 125$ GeV)	$12.2 \pm 0.5^{+5.4}_{-5.0}$	$40.3 \pm 0.7^{+12.8}_{-10.2}$
VBF	$22.1 \pm 0.17^{+2.58}_{-2.64}$	$11.39 \pm 0.12^{+0.93}_{-0.92}$
WH	$0.231 \pm 0.023^{+0.111}_{-0.099}$	$6.43 \pm 0.12^{+0.69}_{-0.70}$
ZH	$0.115 \pm 0.013^{+0.033}_{-0.025}$	$3.2 \pm 0.07 \pm 0.32$
Total Background	$2714 \pm 23^{+98}_{-97}$	$12736 \pm 60^{+450}_{-440}$
Total Signal	$34.6 \pm 0.5^{+6.0}_{-5.7}$	$51.3 \pm 0.8^{+12.9}_{-10.3}$
Data	2830	12952

Table 4.7: Predicted event yields for VBF and boosted categories in 8 TeV. Uncertainties correspond to the statistical and systematic uncertainties, respectively.

Process	7 TeV VBF category	7 TeV boosted Category
Fake τ_{had}	$197 \pm 3^{+50.7}_{-51.7}$	$829 \pm 7^{+167}_{-203}$
$Z \to \tau\tau$	$136 \pm 7^{+21}_{-22}$	$1228 \pm 25^{+144}_{-142}$
Top (τ_{had})	$9.8 \pm 0.9^{+2.2}_{-2.1}$	$50.7 \pm 1.8^{+4.2}_{-4.1}$
$Z \to \ell\ell$ ($\ell \to \tau_{\text{had}}$)	$4.6 \pm 0.7^{+1.7}_{-0.9}$	$30.1 \pm 3^{+6.8}_{-6.1}$
Di-boson	$6.5 \pm 0.4^{+1.3}_{-1.5}$	$40.2 \pm 1.1^{+4.7}_{-4.9}$
ggF ($m_H = 125$ GeV)	$1.51 \pm 0.09^{+0.66}_{-0.62}$	$6.44 \pm 0.15^{+2.09}_{-1.69}$
VBF	$3.35 \pm 0.07 \pm 0.41$	$2.12 \pm 0.05^{+0.19}_{-0.2}$
WH	$0.034 \pm 0.01^{+0.41}_{-0.31}$	$1.00 \pm 0.05 \pm 0.12$
ZH	$0.016 \pm 0.005^{+0.014}_{-0.020}$	$0.514 \pm 0.028^{+0.069}_{-0.06}$
Total Background	$354 \pm 8^{+55}_{-56}$	$2178 \pm 26^{+221}_{-248}$
Total Signal	$4.91 \pm 0.11^{+0.78}_{-0.74}$	$10.07 \pm 0.17^{+2.10}_{-1.71}$
Data	349	2199

Table 4.8: Predicted event yields for VBF and boosted categories in 7 TeV. Uncertainties correspond to the statistical and systematic uncertainties, respectively.

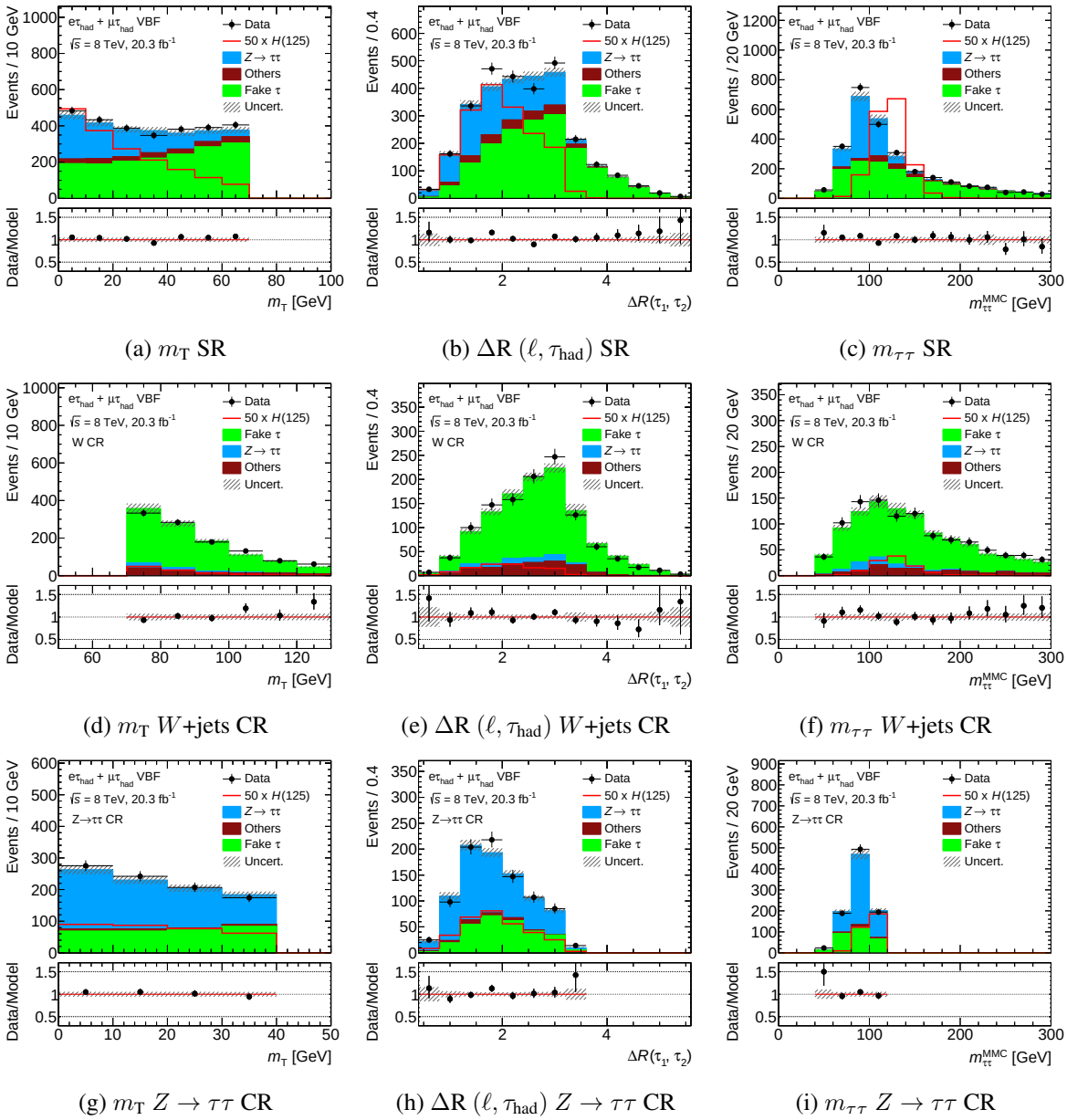

(a) m_{T} SR (b) $\Delta\mathrm{R}\,(\ell, \tau_{\mathrm{had}})$ SR (c) $m_{\tau\tau}$ SR

(d) m_{T} W+jets CR (e) $\Delta\mathrm{R}\,(\ell, \tau_{\mathrm{had}})$ W+jets CR (f) $m_{\tau\tau}$ W+jets CR

(g) m_{T} $Z \to \tau\tau$ CR (h) $\Delta\mathrm{R}\,(\ell, \tau_{\mathrm{had}})$ $Z \to \tau\tau$ CR (i) $m_{\tau\tau}$ $Z \to \tau\tau$ CR

Fig. 4.15: The m_{T}, $\Delta\mathrm{R}\,(\ell, \tau_{\mathrm{had}})$, and $m_{\tau\tau}$ distributions for (a,b,c) the signal region, (d,e,f) the W+jets control region and (g,h,i) the $Z \to \tau\tau$ control region of the VBF category. The data distribution is shown as black dot. The signal distribution is shown as red line, where the normalization is 50 times from the expected number of events. Color filled histograms represent each background contribution. The lower panel shows the ratio between data and the background model. The hatched band corresponds to the statistical and systematic uncertainties of the background estimation.

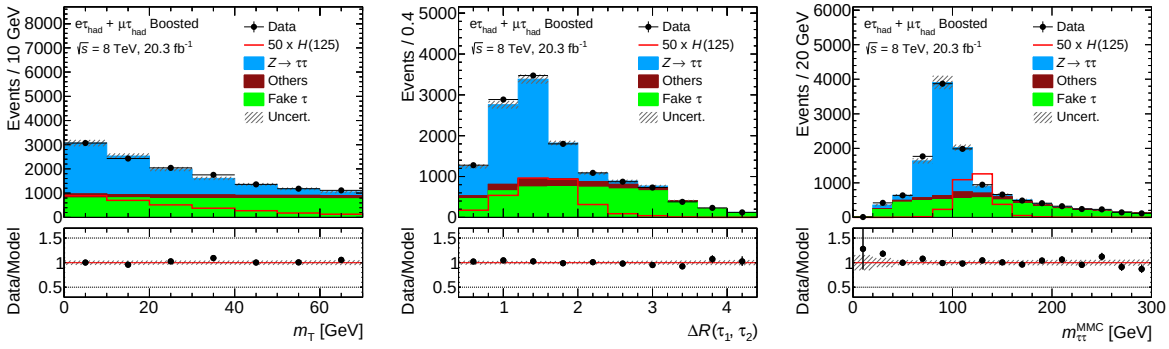

(a) m_{T} SR (b) $\Delta\mathrm{R}\,(\ell, \tau_{\mathrm{had}})$ SR (c) $m_{\tau\tau}$ SR

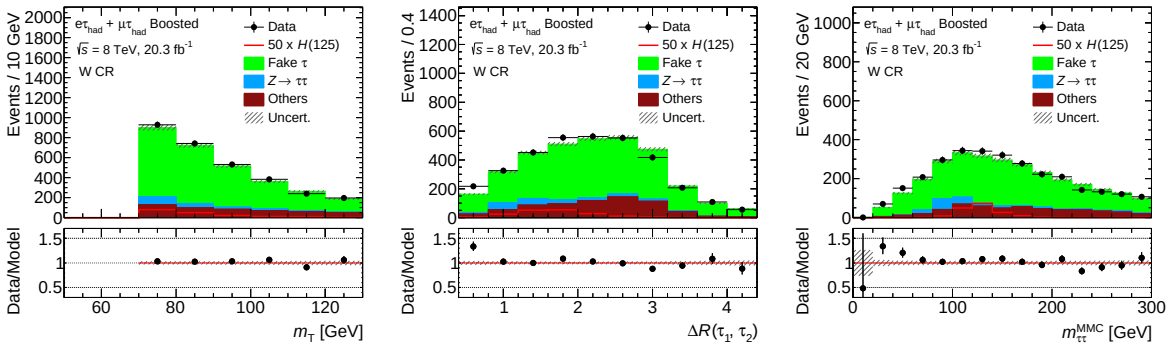

(d) m_{T} W+jets CR (e) $\Delta\mathrm{R}\,(\ell, \tau_{\mathrm{had}})$ W+jets CR (f) $m_{\tau\tau}$ W+jets CR

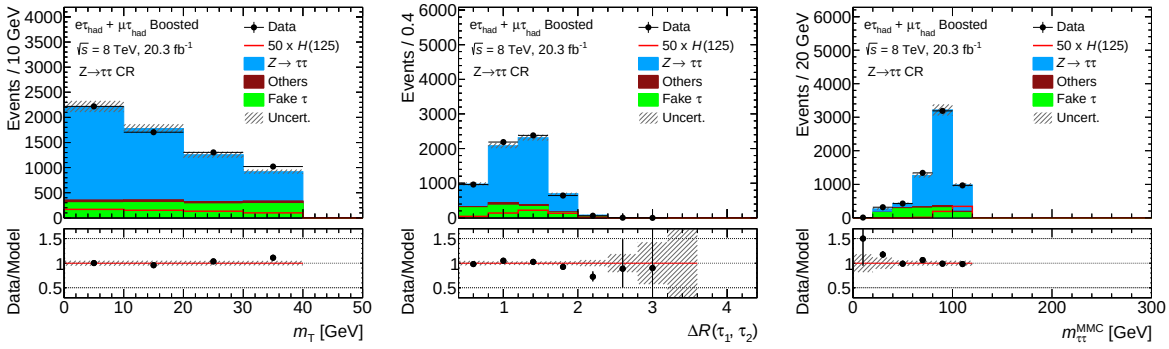

(g) m_{T} $Z \to \tau\tau$ CR (h) $\Delta\mathrm{R}\,(\ell, \tau_{\mathrm{had}})$ $Z \to \tau\tau$ CR (i) $m_{\tau\tau}$ $Z \to \tau\tau$ CR

Fig. 4.16: The m_{T}, $\Delta\mathrm{R}\,(\ell, \tau_{\mathrm{had}})$, and $m_{\tau\tau}$ distributions for (a,b,c) the signal region, (d,e,f) the W+jets control region and (g,h,i) the $Z \to \tau\tau$ control region of the Boosted category. The data distribution is shown as black dot. The signal distribution is shown as red line, where the normalization is 50 times from the expected number of events. Color filled histograms represent each background contribution. The lower panel shows the ratio between data and the background model. The hatched band corresponds to the statistical and systematic uncertainties of the background estimation.

4.7 Multivariate Analysis

The preselection and categorization described in Section 4.4 are intended a minimal selection. The multivariate technique with the Boosted Decision Tree (BDT) as classifier is applied for main background suppression in this analysis. In Section 4.7.1, the basic algorithm of the BDT is introduced, and then an optimization procedure of the BDT is detailed in Section 4.7.2. Finally, BDT output score distributions for signal region and each control region are shown in Section 4.7.3.

4.7.1 Boosted Decision Tree (BDT)

A background suppression method is divided in general into a cut-based approach and a multivariate analysis (MVA) approach. The cut based approach is the method to cut out a signal dominant region using characteristic variables. Although this approach is possible to visualize and understand easily, the ability of the background suppression is generally lower than the MVA approach, since the MVA approach uses characteristic variables including their complex correlations. The MVA outputs signal or background likeness as numerical values, which are determined according to a classifier algorithm in the MVA. This classifier is generally expressed by $F(\mathbf{x}) = \hat{y}$, where $\mathbf{x}$ and $\hat{y}$ represent input variables and output values from the algorithm F. The classifier requires "training", using events that true categories (signal or background) are known. The classifier is optimized by considering the correlations between input variables in this training procedure. The application of the optimized classifier to events is referred to as "testing". The BDT discrimination performance is generally evaluated by the testing using test samples, which are not used to train the BDT.

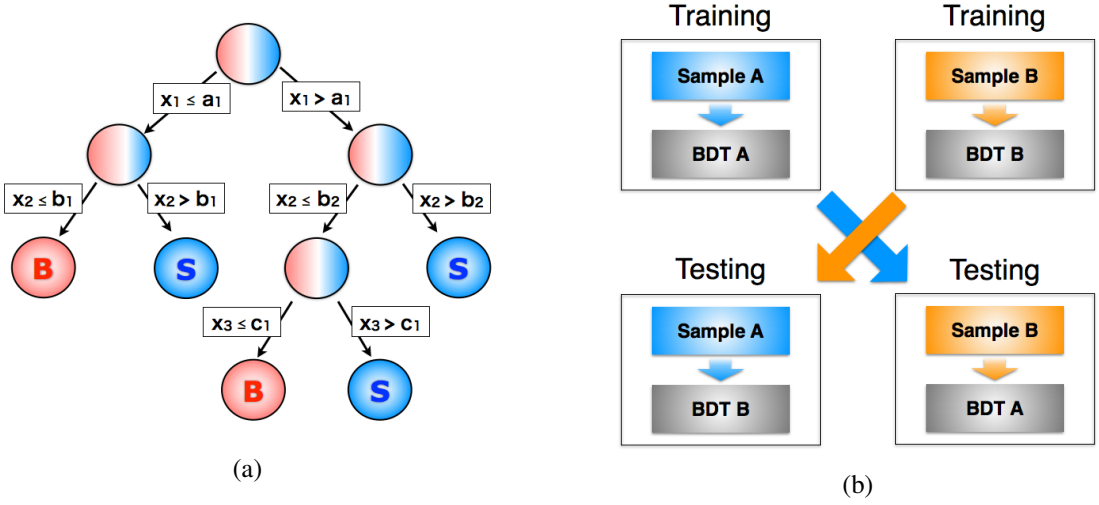

(a) (b)

Fig. 4.17: (a) Schematic view of a single decision tree and (b) concept of the cross-evaluation.

The BDT [53] is used as the classifier in this analysis. A concept of the BDT algorithm starts from a single decision tree, which can be expressed by a simple tree structure as shown in Fig. 4.17 (a). The decision tree performs a decision whether signal or background on one single variable (leaf node), and

the decision is repeated for each variable from a start (root node) to a stop condition (stop node). The stop node has one numerical value corresponding to a signal or background likeness, and the BDT outputs the likeness as a discrimination score. In principle, the decision tree can continue to split leaf nodes until each leaf node contains exactly 1 training event. However, this excessive splitting makes statistical fluctuation in each leaf node, and thereby the performance of the decision tree becomes unstable. The excessive splitting is referred to as "overtraining". In order to avoid the overtraining, the stop condition is defined by two parameters: a maximum tree depth (*MaxDepth*) and a minimum node size (*MinNodeSize*). The *MaxDepth* is the limit number of the splitting, and the *MinNodeSize* is the minimum number of training events in one node. Although the overtraining is avoided by two parameters, the performance may become unstable by not enough statistics of the training events. This instability is overcome by creating additional decision trees and making a decision of a majority vote of them. This procedure is referred to as "boosting". The number of trees (*Ntrees*) is one of the optimized parameters of the boosting. All decision trees are derived from the same training sample, while the weight in the majority vote is slightly modified. The weight is increased, in case that the decision tree classifies events into the true category. The procedure of the boosting can be expressed by:

$$\hat{y} = \sum_{m=0}^{M} w_m F_m(\mathbf{x}), \tag{4.15}$$

where M is the number of trees and w_m is a weight of a decision tree m. The output value from the BDT, $\hat{y}$, is defined as the weighted sum of outputs from all decision trees. The w_m is determined to minimize a "loss function", $L(F(\mathbf{x}), y)$, which is a deviation between a decision tree output $\hat{y}$ and the true category y. Thus, the performance of the boosting algorithm depends on the loss function form. An adoptive boost (AdaBoost) [118] is the most popular boosting algorithm, and it uses an exponential loss function, $L(F(\mathbf{x}), y) = e^{-yF(\mathbf{x})}$ However, the AdaBoost has a weakness that a lack of stability to outliers of the $F(\mathbf{x})$. Instead of the AdaBoost, a different boosting algorithm is used in this analysis, so-called GradientBoost [119]. The loss function form of the GradientBoost is a binomial log-likelihood formula,

$$L(F, y) = \ln\bigl(1 + e^{-2yF(\mathbf{x})}\bigr). \tag{4.16}$$

The GradientBoost uses a gradient descent method to minimize the loss function. For each decision tree, the gradient of the loss function is calculated, and then a weight of a next decision tree is determined by taking a steepest descent value towards a minimum of the loss function. This procedure is iterated until the loss function takes the minimum value. The stability of BDT output is enhanced by a large number of iterations of the gradient calculation. The number of iterations (learning rate) is controlled by multiplying the w_m by a *shrinkage* parameter. The small number shrinkage (0.0-1.0) increases the number of iterations and improves the performance of the BDT. The BDT performance is improved by setting *shrinkage* parameter within the range of (0.0,1.0).

4.7.2 BDT Optimization

This analysis uses the BDT with the GradientBoost method implemented in the Toolkit for MultiVariate Data Analysis (TMVA) package [120]. Two BDTs are prepared and optimized for the VBF and the Boosted categories, using different input variables and BDT parameters. Only VBF signal process is used in the training procedure for the VBF category, while all signal production processes are considered for the Boosted category, where the Higgs boson mass is set to $m_H = 125$ GeV for both categories.

BDT Training Sample

The BDT training requires samples, which have large statistics and physics processes are known. In order to maximize statistics of the training samples, the $m_{\mathrm{T}} < 70$ GeV requirement and the $\Delta\eta\,(\mathrm{jet1}, \mathrm{jet2}) < 3.0$ requirement are removed. In addition, different background modelings for the $Z \to \tau\tau$ and the fake τ_{had} background events are used from the modelings described in Section 4.6. The $Z \to \tau\tau$ background is modeled by simulation samples (see Section 4.3.1) instead of the embedding sample. A different data-driven estimation is applied for the fake τ_{had} background, referred to as OS-SS method [121, 122]. Furthermore, a cross-evaluation technique [123] is performed in the training procedure. A concept of the technique is shown in Fig. 4.17 (b). Events are spitted into *sample A* and *sample B* with a random bias, and then two independent BDTs denoted by *BDT A* and *BDT B* are trained using *sample A* and *sample B*, respectively. Based on the fact that the *sample A* is statistically independent from *sample B*, *BDT A* is tested with *sample B* and *BDT B* is tested with *sample A*. Finally, the BDT score distribution as the result of the cross-evaluation is constructed by the sum of *BDT A* and *BDT B* distributions. By applying the cross-evaluation technique, statistics of training samples becomes twice for signal and background events estimated by simulation samples.

Input Variables and BDT Parameters

Although the number of input variables are not limited in the BDT algorithm, it is difficult to understand and model the correlations of a large number of input variables, so that the number and kind of input variables must be optimized according to the BDT performance. The performance is evaluated using the discrimination significance expressed by:

$$\text{Significance} = \frac{< S > + < B >}{\sqrt{\sigma_S^2 + \sigma_B^2}}, \tag{4.17}$$

where $< S >$ and $< B >$ denote means of BDT output distribution for signal and background, and σ_S and σ_B denote root-mean-square (RMS). At first, a large number of input variables are tested to train the BDT, and then a variable which has the lowest importance is discarded. The importance of each input variable is quantified by determining the number of times used in a node splitting of the BDT training. This optimization procedure is repeated until the discrimination significance is maximized. Table 4.9

lists input variables for the VBF and the Boosted category after the optimization. The definitions of the input variables and their importances are also shown in the table.

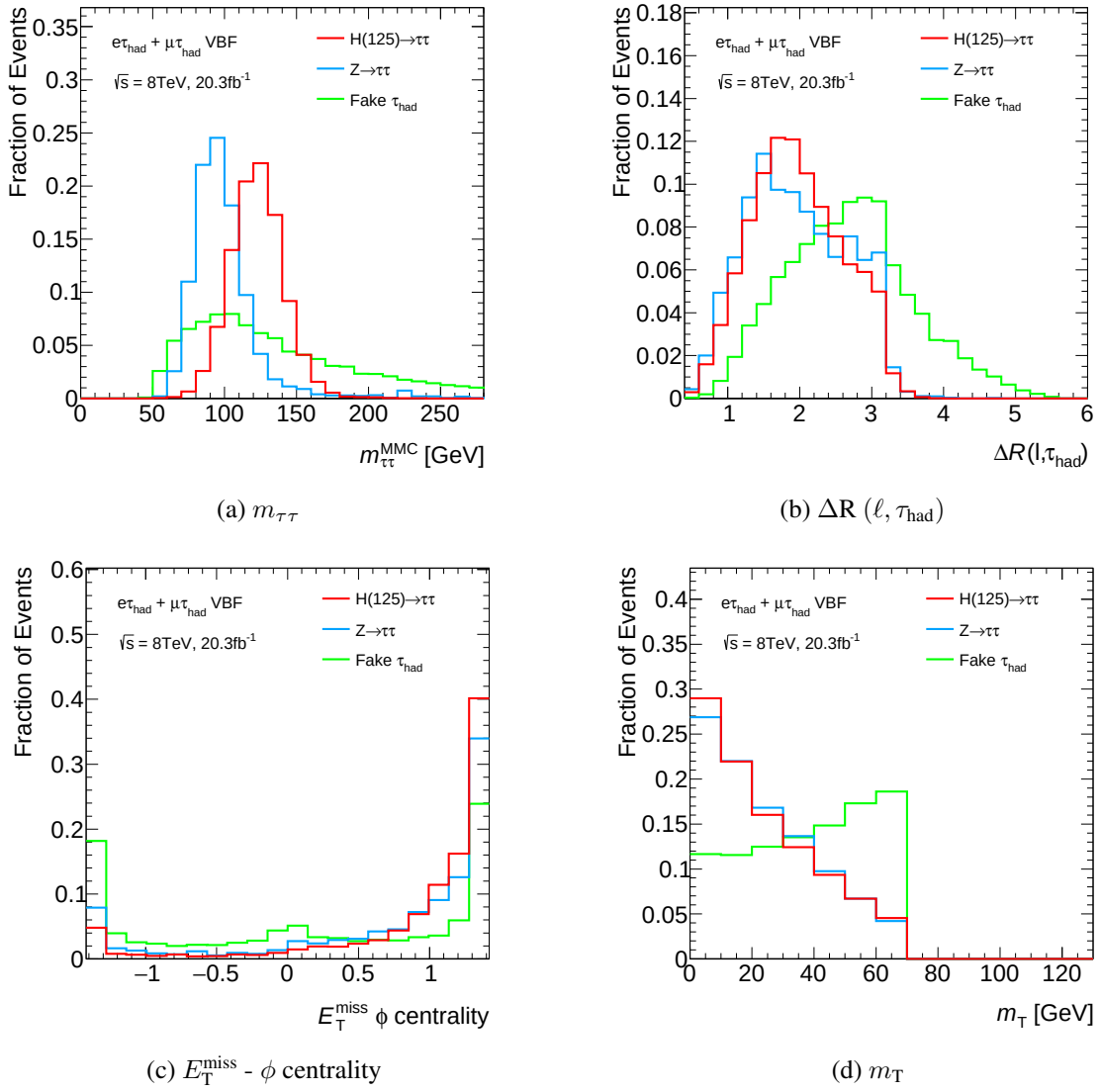

(a) $m_{\tau\tau}$

(b) ΔR $(\ell, \tau_{\text{had}})$

(c) $E_{\text{T}}^{\text{miss}}$ - ϕ centrality

(d) m_{T}

Fig. 4.18: Input variable disctributions of $m_{\tau\tau}$,ΔR $(\ell, \tau_{\text{had}})$, $E_{\text{T}}^{\text{miss}}$ - ϕ centrality, and m_{T} in the VBF category, for the signal (red), the $Z \to \tau\tau$ background (blue) and the fake τ_{had} background (green). The signal represents only the VBF signal process.

The input variables of $m_{\tau\tau}$,ΔR $(\ell, \tau_{\text{had}})$ and $E_{\text{T}}^{\text{miss}}$ - ϕ centrality represent a feature of the reconstructed $H \to \tau_{\ell}\tau_{\text{had}}$ final state. They are commonly used for the VBF and the Boosted category. Figure 4.18 and 4.19 shows their distributions for the VBF and Boosted category, respectively. The $m_{\tau\tau}$ and ΔR $(\ell, \tau_{\text{had}})$ variables, which include the information of the invariant mass difference between the Higgs and the Z boson, are useful to distinguish the $Z \to \tau\tau$ background events from the signal events. The $E_{\text{T}}^{\text{miss}}$ - ϕ centrality has a relatively complex definition compared with other variables. This variable quantifies the relative angular position of the $E_{\text{T}}^{\text{miss}}$ with respect to the lepton and the τ_{had} in the transverse

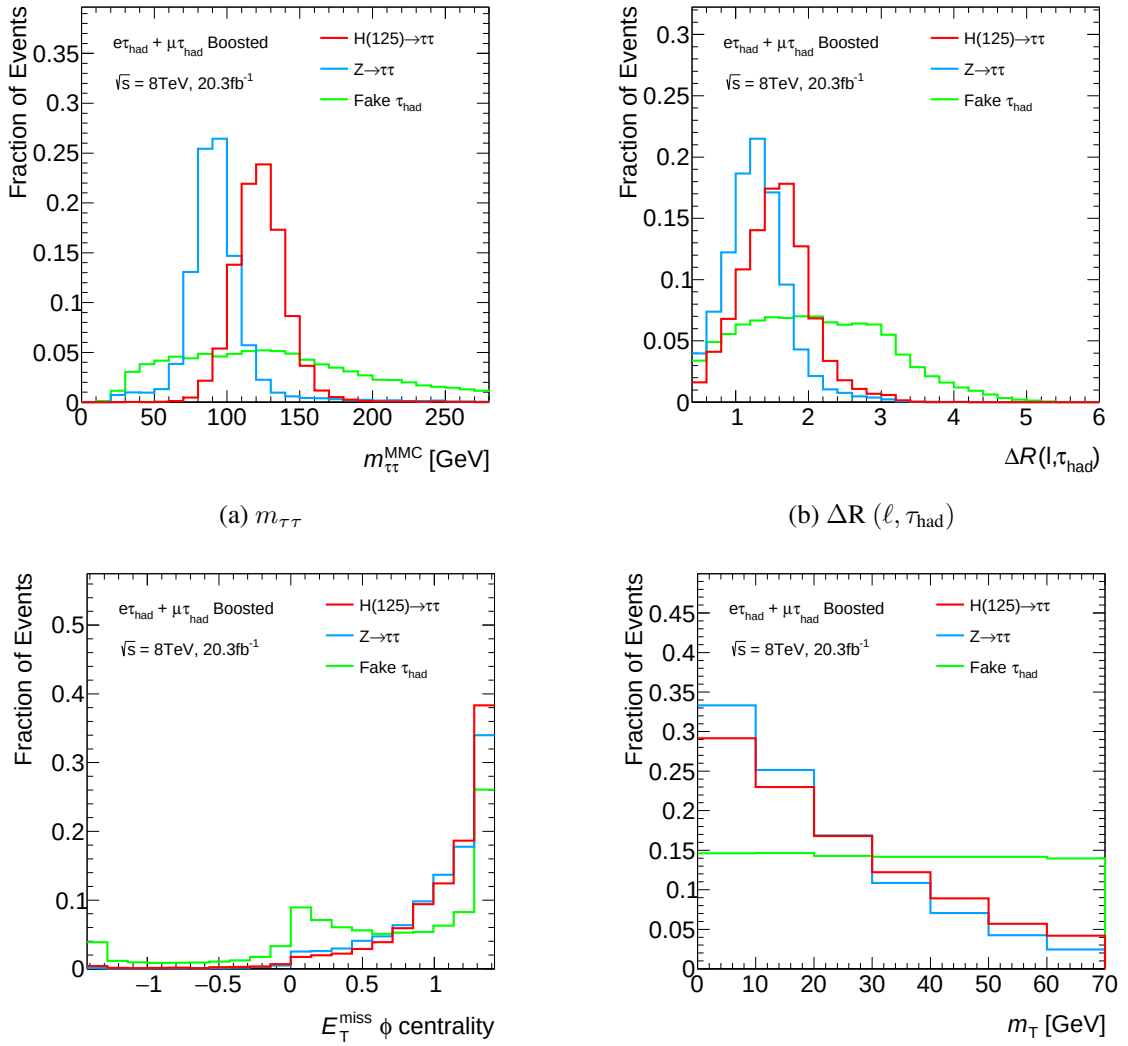

(a) $m_{\tau\tau}$

(b) ΔR $(\ell, \tau_{\text{had}})$

(c) $E_{\text{T}}^{\text{miss}}$ - ϕ centrality

(d) m_{T}

Fig. 4.19: Input variable disctributions of $m_{\tau\tau}$,ΔR $(\ell, \tau_{\text{had}})$, $E_{\text{T}}^{\text{miss}}$ - ϕ centrality, and m_{T} in the Boosted category, for the signal (red), the $Z \to \tau\tau$ background (blue) and the fake τ_{had} background (green). The signal represents the sum of all signal processes.

plane, expressed by:

$$E_{\text{T}}^{\text{miss}} \text{ - } \phi \text{ centrality} = \frac{A+B}{\sqrt{A^2+B^2}},$$
$$A = \frac{\sin(\phi_{E_{\text{T}}^{\text{miss}}} - \phi_{\ell})}{\sin(\phi_{\tau_{\text{had}}} - \phi_{\ell})}\ ,\ B = \frac{\sin(\phi_{E_{\text{T}}^{\text{miss}}} - \phi_{\tau_{\text{had}}})}{\sin(\phi_{\ell} - \phi_{\tau_{\text{had}}})}. \tag{4.18}$$

It takes a value $\sqrt{2}$ in case that the $E_{\text{T}}^{\text{miss}}$ vector is perfectly center between the lepton and the τ_{had}, while it takes less than 1 in case that the $E_{\text{T}}^{\text{miss}}$ vector is not between them. The m_{T} is used to distinguish the fake τ_{had} background, especially the W+jets background. While a dominant phase space of the W+jets

background is already rejected by a requirement of $m_{\mathrm{T}} < 70$ GeV in the signal region, the remaining events are still present as one of the dominant background. The m_{T} is still meaningful as input variable using a shape difference between the signal and the W+jets background.

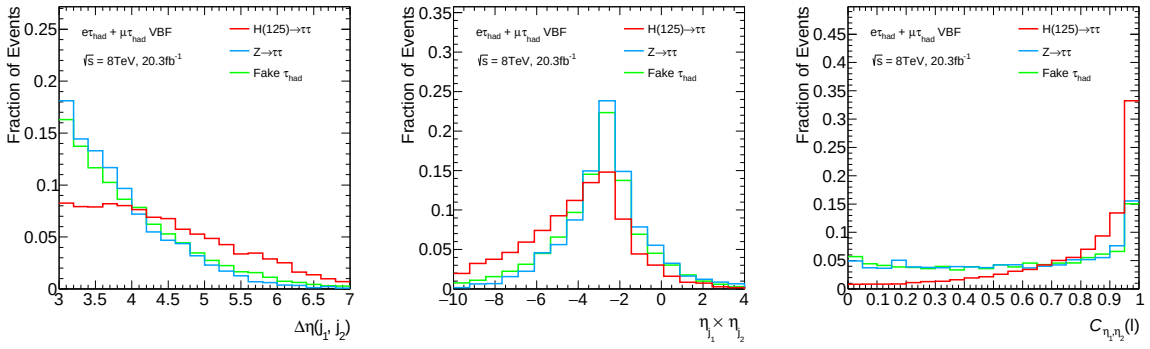

(a) $\Delta\eta$ (jet1, jet2) (b) $\eta_{\mathrm{jet1}} \times \eta_{\mathrm{jet2}}$ (c) ℓ - η centrality

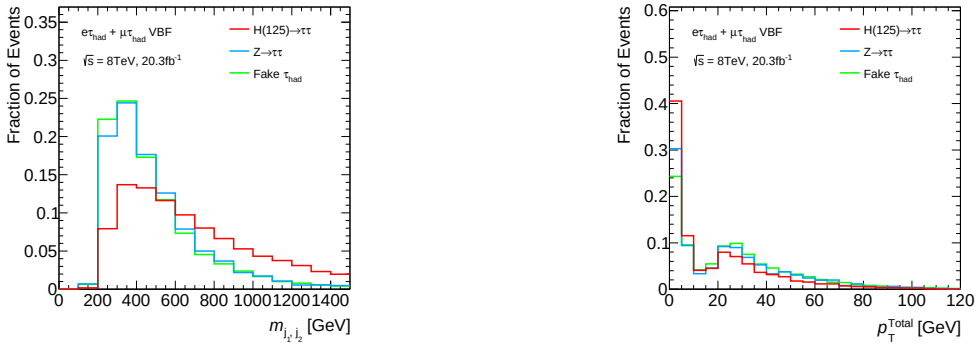

(d) $m_{\mathrm{j1,j2}}$ (e) $p_{\mathrm{T}}^{\mathrm{total}}$

Fig. 4.20: Input variable disctributions used in the VBF category for the signal (red), the $Z \to \tau\tau$ background (blue) and the fake τ_{had} background (green). The signal represents only the VBF signal process.

For the VBF category, variables using two high momentum jets with a large pseudo-rapidity gap are input to the training. Figure 4.20 shows the input variable distributions which are used in only the VBF category. Both the $\Delta\eta$ (jet1, jet2) and the $\eta_{\mathrm{jet1}} \times \eta_{\mathrm{jet2}}$ contain an angular separation of two jets in η. The VBF signal provides higher $\Delta\eta$ (jet1, jet2) values and a long negative tail shape in $\eta_{\mathrm{jet1}} \times \eta_{\mathrm{jet2}}$, compared with the backgrounds. The $m_{\mathrm{j1,j2}}$ is a variable including a combined information of two jet momenta and their angular separation, and the VBF signal provides higher $m_{\mathrm{j1,j2}}$ values than the backgrounds. The ℓ - η centrality variable quantifies the η position of the lepton with respect to the two jets in the pseudo-rapidity plane, expressed by:

$$\ell \text{ - } \eta \text{ centrality} = \exp\Big[\frac{-1}{(\eta_{\mathrm{jet1}} - \eta_{\mathrm{jet2}})^2}\Big(\eta_\ell - \frac{\eta_{\mathrm{jet1}} + \eta_{\mathrm{jet2}}}{2}\Big)\Big]. \tag{4.19}$$

It takes a value of 1 in case that the lepton is perfectly center between two jets, while it takes less than a value of $1/e$ in case that the lepton is outside of jets. The $p_{\mathrm{T}}^{\mathrm{total}}$ is a vector sum of transverse momenta of objects in the VBF signal process: a lepton, a τ_{had}, two jets and an $E_{\mathrm{T}}^{\mathrm{miss}}$. This variable represents an additional activity other than the VBF objects.

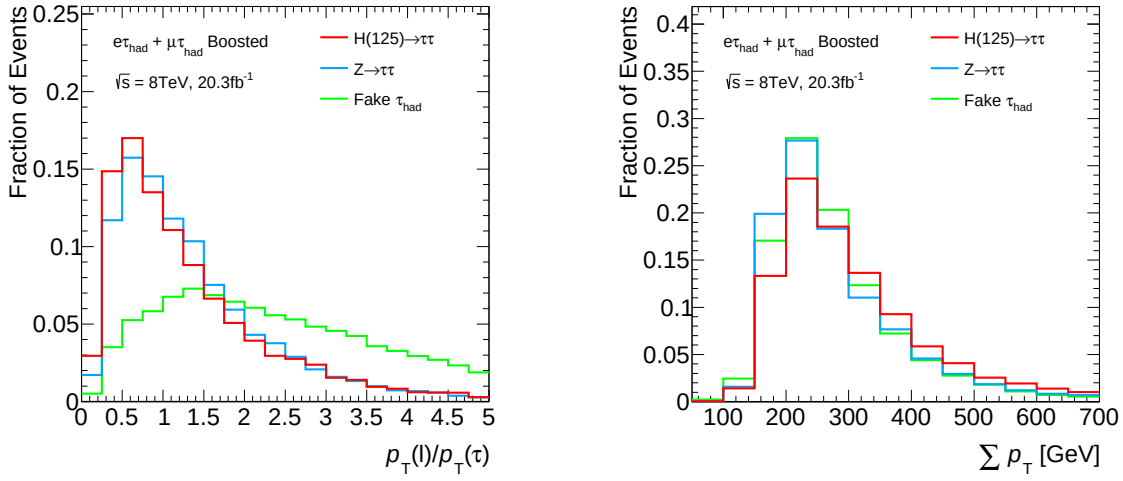

(a) $p_{\mathrm{T}}^{\ell}/p_{\mathrm{T}}^{\tau_{\mathrm{had}}}$ (b) $\sum p_{\mathrm{T}}$

Fig. 4.21: Input variable disctributions used in the Boosted category for the signal (red), the $Z \to \tau\tau$ background (blue) and the fake τ_{had} background (green). The signal represents the sum of all signal processes.

For the Boosted category, two additional variables representing a feature of the boosted topology are used. The $\sum p_{\mathrm{T}}$ represents a total activity in an event, and the signal provide much higher $\sum p_{\mathrm{T}}$ values than the backgrounds. The $p_{\mathrm{T}}^{\ell}/p_{\mathrm{T}}^{\tau_{\mathrm{had}}}$ is especially useful to discriminate the fake τ_{had} background, based on an asymmetry between p_{T}^{ℓ} and $p_{\mathrm{T}}^{\tau_{\mathrm{had}}}$ due to a difference of the number of neutrinos from τdecays. As a result, the signal provides lower $p_{\mathrm{T}}^{\ell}/p_{\mathrm{T}}^{\tau_{\mathrm{had}}}$ values than the fake τ_{had} background. Figure 4.21 shows the $\sum p_{\mathrm{T}}$ and the $p_{\mathrm{T}}^{\ell}/p_{\mathrm{T}}^{\tau_{\mathrm{had}}}$ distributions.

The BDT with GradientBoost requires to optimize some parameters to maximize its performance. The parameters are *MaxDepth*, *MinNodeSize*, *Ntrees* and *Shrinkage*, as described in Section 4.7.1. The *MaxDepth* and the *MinNodeSize* control how much grow each decision tree, while the *Ntrees* and the *Shrinkage* determine the boosting algorithm. A two-dimensional scan of *MaxDepth* and *Ntrees* are performed to maximize the significance of the BDT output, and then the remaining parameters are optimized by step-by-step scanning. This optimization procedure is separately performed for the VBF and Boosted categories. The parameter values are summarized in Table 4.10.

4.7.3 Validation of BDT Output Distributions

Before comparing data and the background modeling in actual BDT output distributions, the validation of all input variables is important to ensure the background modeling is accurate in data. All input variables

Variable	Definition	Ranking	
		VBF	Boosted
$m_{\tau\tau}$	Di-τ invariant mass reconstructed by the MMC method	2	1
ΔR $(\ell, \tau_{\text{had}})$	Separation of τ_{had} and isolated lepton	7	2
m_{T}	Transverse mass of ℓ and $E_{\text{T}}^{\text{miss}}$	3	5
$E_{\text{T}}^{\text{miss}}$ - ϕ centrality	$E_{\text{T}}^{\text{miss}}$ centrality† between ℓ and τ_{had} in ϕ direction	4	4
$\sum p_{\text{T}}$	Sum p_{T} of τ, ℓ, and jets	-	6
$p_{\text{T}}^{\ell}/p_{\text{T}}^{\tau_{\text{had}}}$	p_{T} ratio of ℓ and τ_{had}.	-	3
$m_{\text{j1,j2}}$	Invariant mass of two leading jets	6	-
$\eta_{\text{jet1}} \times \eta_{\text{jet2}}$	Product of pseudo-rapidities of two leading jets	9	-
$\Delta\eta$ (jet1, jet2)	Pseudo-rapidity difference between two leading jets	1	-
ℓ - η centrality	lepton centrality† between two leading jets in η direction	8	-
$p_{\text{T}}^{\text{total}}$	$\lvert\vec{p}_{\text{T}}^{\ell} + \vec{p}_{\text{T}}^{\tau_h} + \vec{p}_{\text{T}}^{\text{jet1}} + \vec{p}_{\text{T}}^{\text{jet2}} + \vec{E}_{\text{T}}^{\text{miss}}\rvert$	5	-

Table 4.9: Input variables used for VBF and Boosted categories with ranking of variable importance in the training. ($\dagger$: see text for the detail definition)

Parameter	VBF	Boosted
MaxDepth	5	4
MinNodeSize	0.1%	0.17%
Ntrees	400	600
Shrinkage	0.2	0.1

Table 4.10: Summary of training parameters with their optimized values for the VBF and Boosted categories.

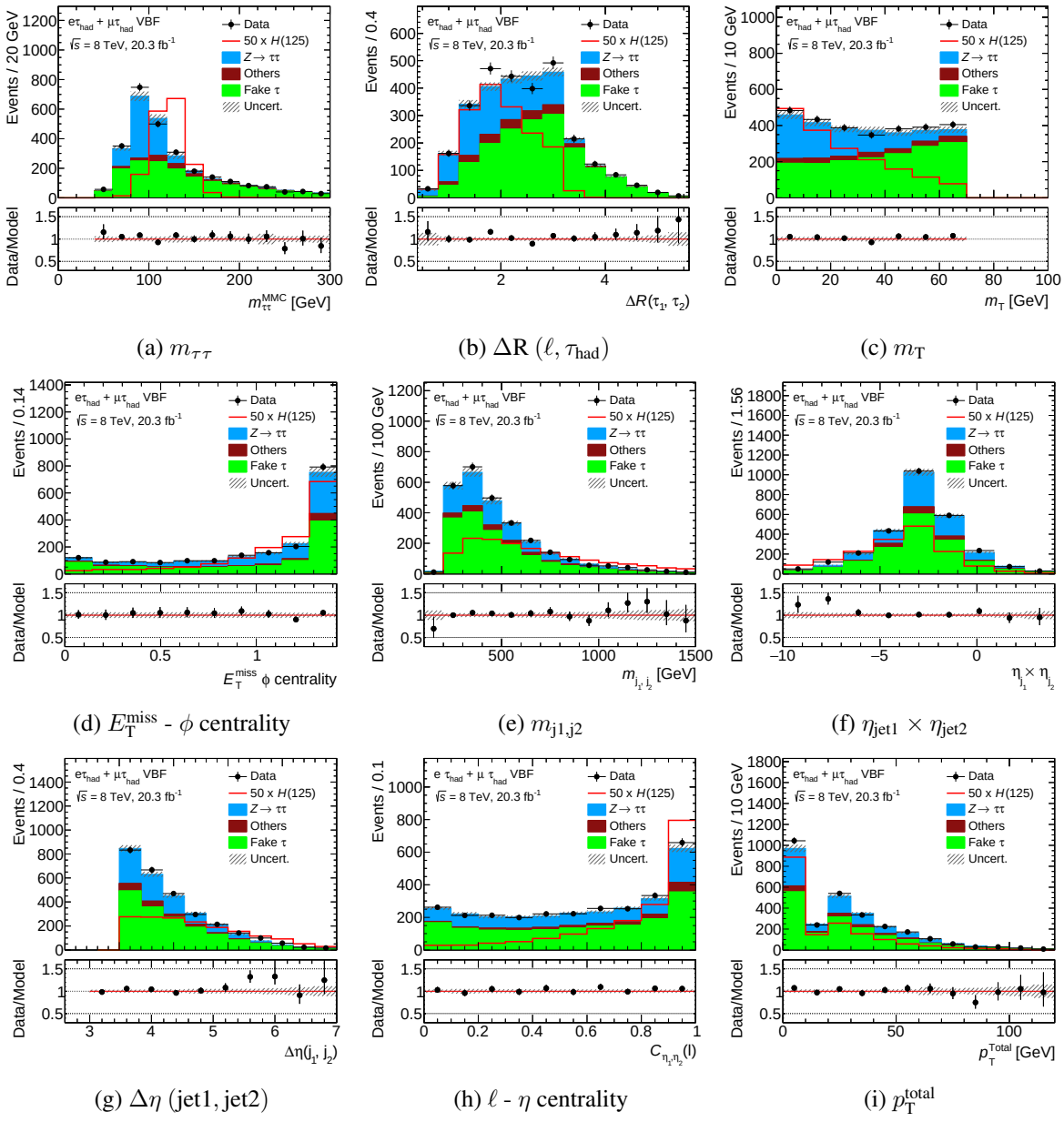

(a) $m_{\tau\tau}$ (b) ΔR $(\ell, \tau_{\text{had}})$ (c) m_{T}

(d) $E_{\text{T}}^{\text{miss}}$ - ϕ centrality (e) $m_{\text{j1,j2}}$ (f) $\eta_{\text{jet1}} \times \eta_{\text{jet2}}$

(g) $\Delta\eta$ (jet1, jet2) (h) ℓ - η centrality (i) $p_{\text{T}}^{\text{total}}$

Fig. 4.22: Input variable distributions for the VBF category in the 8 TeV analysis. The data and the signal are shown as black dot and red line, respectively. The signal is normalized to 50 times from the expected number of events. Color filled histograms represent estimated backgrounds. The lower panel shows the ratio between data and the background model, while the hatched band corresponds to the statistical and systematic uncertainties of the background estimation.

comparing data and the background modeling in 8 TeV are shown in Fig. 4.22 and Figure 4.23 for the VBF and the Boosted categories, respectively. The validation for each background component is also performed using each dedicated control regions, shown in Section A.1. Basically, all of data distributions are well described by the background modeling within uncertainties.

The BDT performs the discrimination using the correlation of each input variable, so that the validation of the correlation is also important. The variation is performed by comparing data and the background

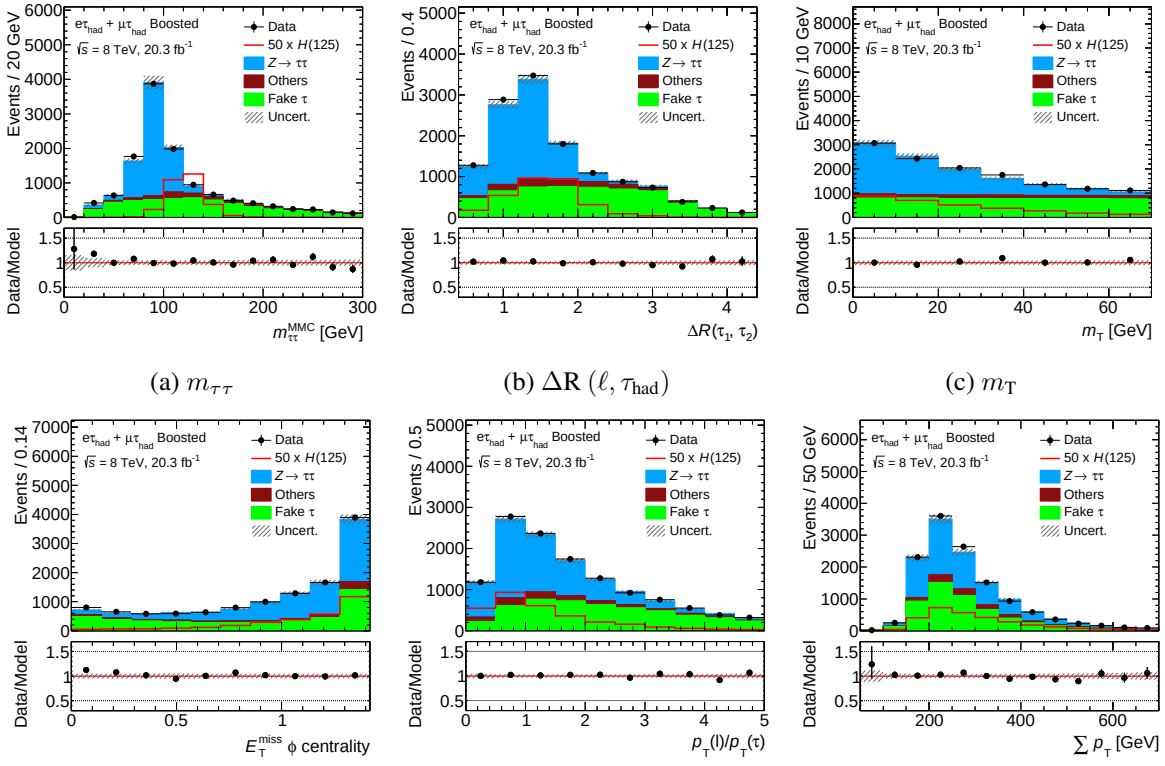

(a) $m_{\tau\tau}$ (b) ΔR $(\ell, \tau_{\text{had}})$ (c) m_{T}

(d) $E_{\text{T}}^{\text{miss}}$ - ϕ centrality (e) $p_{\text{T}}^{\ell}/p_{\text{T}}^{\tau_{\text{had}}}$ (f) $\sum p_{\text{T}}$

Fig. 4.23: Input variable distributions for the Boosted category in the 8 TeV analysis. The data and the signal are shown as black dot and red line, respectively. The signal is normalized to 50 times from the expected number of events. Color filled histograms represent estimated backgrounds. The lower panel shows the ratio between data and the background model, while the hatched band corresponds to the statistical and systematic uncertainties of the background estimation.

modeling in z_i v.s. $< z_j >$ distributions, where $z_{i,j}$ represents any two input variables. Correlations of all input variable pairs are well modeled for the VBF and Boosted categories. Figure 4.24 shows example distributions of z_i v.s. $< z_j >$, $m_{\tau\tau}$ v.s. $< \Delta\text{R}\ (\ell, \tau_{\text{had}}) >$ for the VBF and Boosted categories, $m_{\text{j1,j2}}$ v.s. $< \Delta\eta\ (\text{jet1}, \text{jet2}) >$ for the VBF category and $p_{\text{T}}^{\ell}/p_{\text{T}}^{\tau_{\text{had}}}$ v.s. $< \sum p_{\text{T}} >$ for the Boosted category. Other distributions are shown in Fig. A.9 and Fig. A.10 for the VBF and Boosted categories, respectively.

Moreover, the validation of the actual BDT output distribution is crucial because the distribution is used as the final discriminant. The validation is performed for each background component using each dedicated control region. Figure 4.25 and Figure 4.26 show the BDT output distributions of each background control region for the VBF and the Boosted categories, respectively. The background modeling also well agrees with data on the BDT output distributions within uncertainties, so that there is no significant mis-modeling.

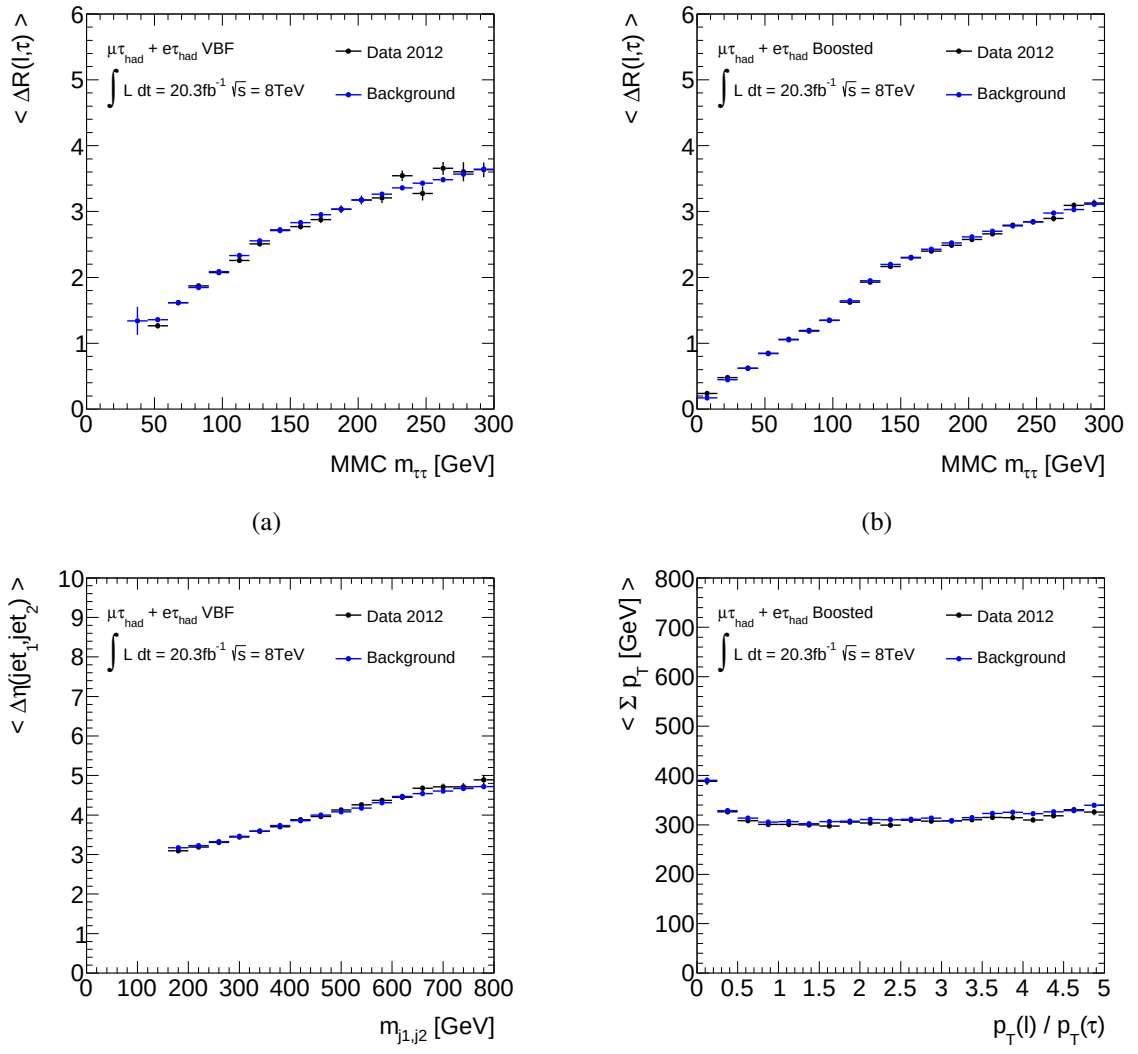

Fig. 4.24: Example distributions of z_i v.s. $< z_j >$ in the 8 TeV analysis, $m_{\tau\tau}$ v.s. $< \Delta\mathrm{R}\,(\ell, \tau_{\mathrm{had}}) >$ for the (a) VBF and (b) Boosted categories, (c) $m_{\mathrm{j1,j2}}$ v.s. $< \Delta\eta\,(\mathrm{jet1}, \mathrm{jet2}) >$ for the VBF category and (d) $p_{\mathrm{T}}^{\ell}/p_{\mathrm{T}}^{\tau_{\mathrm{had}}}$ v.s. $< \sum p_{\mathrm{T}} >$ for the Boosted category. The data and the background distributions are shown as black and blue dots, respectively. The displayed uncertainties represents the statistical uncertainty on each mean value.

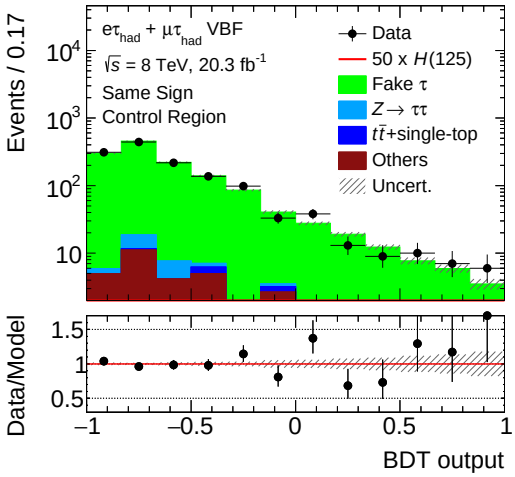

(a) Same Sign Control Region

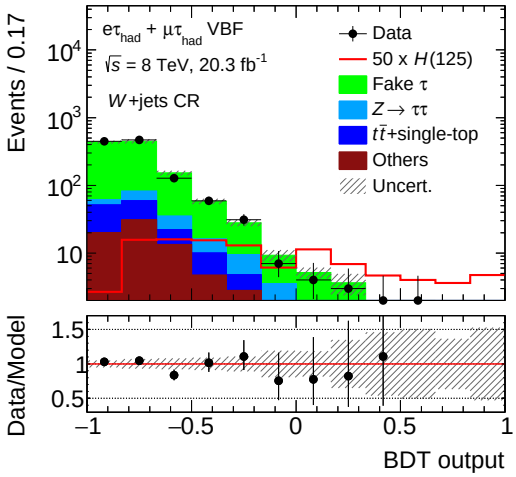

(b) W+jets Control Region

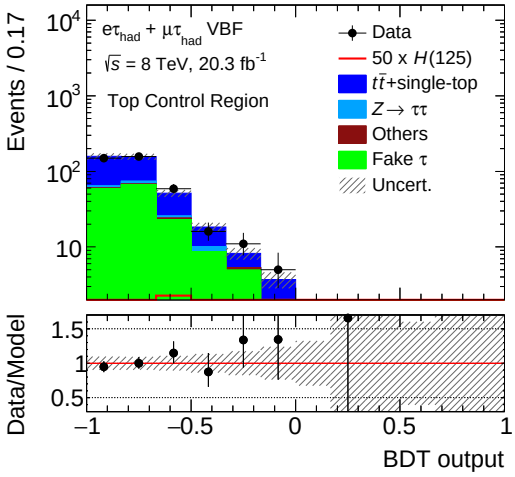

(c) Top Control Region

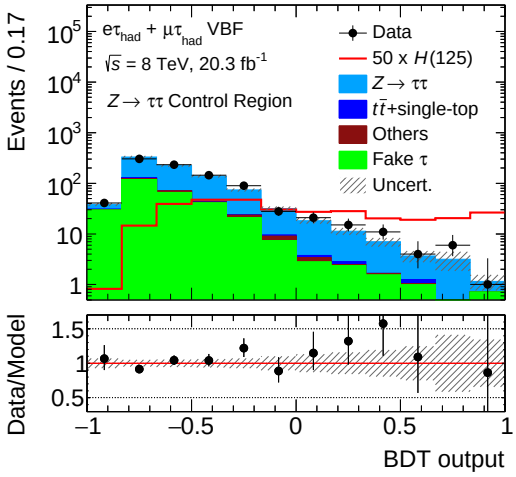

(d) $Z \to \tau\tau$ Control Region

Fig. 4.25: BDT output distributions of each dedicated control region for the VBF category in the 8 TeV analysis. The data distribution is shown as black dot. The signal is shown as red line, where a normalization of the signal is the expected number of events times 50. The backgrounds are shown as colored histograms, $Z \to \tau\tau$ (blue), the fake τ_{had} (green), and other backgrounds (brown).

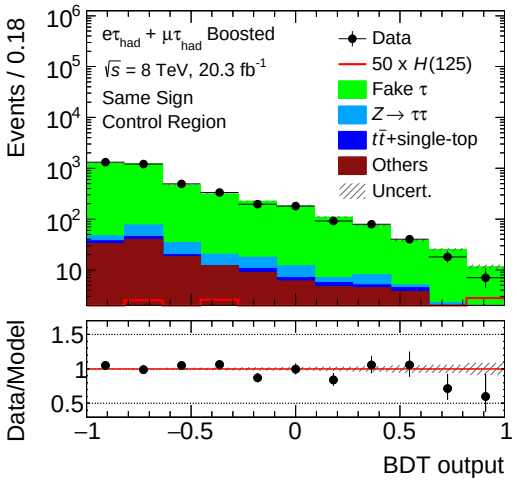

(a) Same Sign Control Region

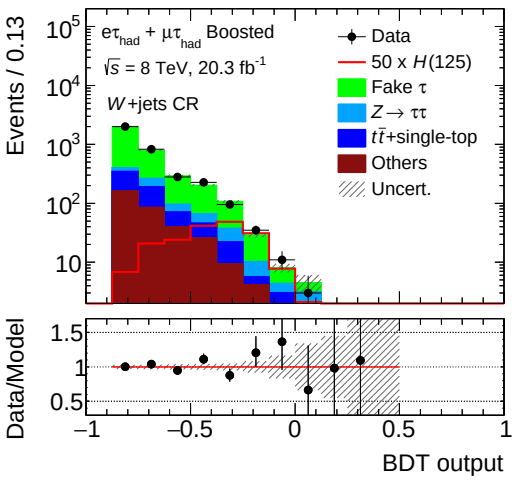

(b) W+jets Control Region

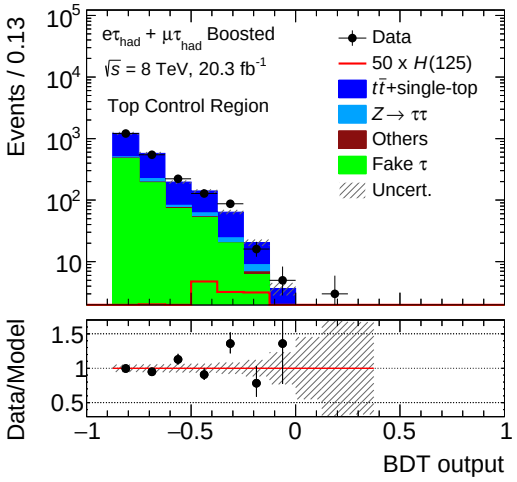

(c) Top Control Region

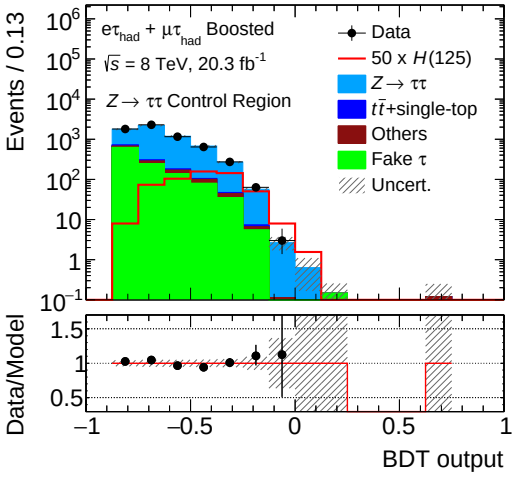

(d) $Z \to \tau\tau$ Control Region

Fig. 4.26: BDT output distributions of each dedicated control region for the Boosted category in the 8 TeV analysis. The data distribution is shown as black dot. The signal is shown as red line, where a normalization of the signal is the expected number of events times 50. The backgrounds are shown as colored histograms, $Z \to \tau\tau$ (blue), the fake τ_{had} (green), and other backgrounds (brown).

4.8 Systematic Uncertainties

Systematic uncertainties are evaluated for both the expected number of events and shape differences of BDT output distributions. The source of the uncertainties is grouped into theoretical, experimental uncertainties and uncertainties on the background modeling, detailed in Section 4.8.1, 4.8.2 and 4.8.3, respectively.

4.8.1 Theoretical Systematic Uncertainties

Several theoretical uncertainties are assigned for all signal and background processes estimated by simulation samples. The $Z \to \tau\tau$ and the fake τ_{had} backgrounds are not affected by theoretical uncertainties because data-driven techniques are applied for both backgrounds. For signal processes, following theoretical uncertainties are considered.

QCD Scale Uncertainties

The uncertainties due to missing higher order QCD correction in a cross section calculation, referred to as QCD scale uncertainty, are evaluated based on simulation samples. For the VBF, WH and ZH processes, the uncertainty is evaluated by varying factorization and renormalization scales ($\mu_{\text{D}} = \mu_{\text{R}} = m_W$) from half to twice. In this evaluation, the VBF and Boosted categories are defined by applying corresponding selection to parton level information, where parton level jets are built using the anti-k_t algorithm. The result of the uncertainties are $(2\% \sim 4\%)$ depending on the process and the category. In addition for the VBF process, a 2% uncertainty is assigned for the NLO EW correction [88].

For the ggF process, the QCD scale uncertainty is relatively larger than other processes because additional jets are not present at LO level. The evaluation procedure is the same as other processes, while factorization and normalization scales are defined by $\mu_{\text{D}} = \mu_{\text{R}} = \sqrt{m_H^2 + p_{T,H}^2}$ (see Section 4.3.2). This uncertainty on the ggF process is considered separately for the VBF and Boosted categories, because the categorization of this analysis is defined exclusively. For the Boosted category, an inclusive cross section uncertainty of events which pass the Boosted category selection is assigned. For the VBF category, an uncertainty of events which pass selections of both the VBF and Boosted categories is considered. The two uncertainties are considered as anti-correlation to take into account a category migration effect, following the procedure of Ref. [124]. The results of this uncertainties are $\pm 23\%$ and $\pm 24\%$ for the VBF and Boosted categories, respectively.

The QCD scale uncertainties also affects the shape of BDT output distributions, especially the uncertainty of the ggF process in the VBF category. While the definition of the VBF category does not include an explicit jet veto, input variables related to jet activity (e.g., $p_{\text{T}}^{\text{total}}$) are used in the BDT. Thereby, events with a third jet are indirectly reduced in a high BDT output region. This introduces the large shape uncertainty because the cross section of events with a third jet from ggF process is only predicted at LO precision. The uncertainty is evaluated by a parton-level simulation program, so-called MCFM program [125].

UE and PS Uncertainties

An uncertainties on underlying events (UE) and parton showers (PS) are evaluated by the acceptance difference between POWHEG+PYTHIA and POWHEG+HERWIG . The results of this uncertainties are $(4\% \sim 8\%)$ depending on the process and the category.

PDF Uncertainties

An inclusive cross section uncertainty due to the PDF is estimated by the LHC Higgs Cross Section Working Group [88, 126]. The additional uncertainties on the choice of PDF set is evaluated using different PDF sets and varying parameters of the default CT10 PDF set. The CT10 is reweighted to the MSTW2008NLO [127], NNPDF [128] and the CT10 eigen-tunes parameterisation, and then the largest variation among them are taken into account as the PDF uncertainty. The result of total PDF uncertainties are $(3\% \sim 9\%)$ depending on the process and the category. The choice of PDF set changes the acceptance and the shape of BDT output distributions, and therefore the shape uncertainty due to the PDF is also considered.

Uncertainties on the choice of event generators

An acceptance difference from the choice of the event generator is assigned as an additional systematic uncertainty. For the ggF process in the Boosted category, a $\pm 1.9\%$ uncertainty is found and assigned by comparing between the default POWHEG+HERWIG and MC@NLO+HERWIG/JIMMY [129] simulations. For the VBF process in the VBF category, this uncertainty is evaluated by the same method as Ref. [130], and $\pm 4.2\%$ uncertainty is assigned by comparing between the default POWHEG+HERWIG and aMC@NLO+HERWIG/JIMMY [131] simulations.

Uncertainty on the $H \to \tau\tau$ Branching Ratio

An uncertainty on the $H \to \tau\tau$ branching ratio for signal processes is estimated by the LHC Higgs Cross Section Working Group [88, 126], and the result of 5.7% uncertainty is assigned to all signal processes and categories.

The summary of assigned theoretical uncertainties for signal processes is shown in Table 4.11. The theoretical uncertainties for background processes are also evaluated by the same procedures as used for signal processes.

4.8.2 Experimental Systematic Uncertainties

Luminosity Uncertainties

The systematic uncertainty on the integrated luminosity is assigned $\pm 2.8\%$ for 8 TeV and $\pm 1.8\%$ for 7 TeV, which are evaluated from beam-separation scans performed in 2011 and 2012 [132].

Source	VBF category			Boosted category		
	ggF	VBF	W/ZH	ggF	VBF	W/ZH
QCD scale	$^{+21\%}_{-29\%}$	$\pm 2.1\%$	$\pm 0.2\%$	$^{+29.2\%}_{-22.2\%}$	$\pm 1.4\%$	$\pm 4.0\%$
PDF	$\pm 9.2\%$	$\pm 3.2\%$	$\pm 0.2\%$	$\pm 9.9\%$	$\pm 3.2\%$	$\pm 3.2\%$
UE and PS	$\pm 8.0\%$	$\pm 4.0\%$	$< 0.1\%$	$\pm 4.0\%$	$\pm 6.0\%$	$\pm 6.0\%$
Generator	-	$\pm 4.2\%$	-	$\pm 1.9\%$	-	-
$H \to \tau\tau$ B.R.	$\pm 5.7\%$	$\pm 5.7\%$	$\pm 5.7\%$	$\pm 5.7\%$	$\pm 5.7\%$	$\pm 5.7\%$

Table 4.11: Summary of the theoretical uncertainties for each signal process.

Electron and Muon Uncertainties

The acceptances of simulation samples for signal and background processes are corrected by applying scale factors of the single lepton trigger and the lepton identification efficiency. The scale factors are measured using $Z/\gamma^* \to ee/\mu\mu$ tag-and-probe techniques, and its systematic uncertainties are assigned. While the uncertainties depends on the transverse momentum and pseudo-rapidity of a reconstructed lepton, they are relatively small uncertainties of $(1\% \sim 2\%)$ [45, 50].

The electron energy and muon momentum scales are determined by comparing shape difference between data and simulation samples in $Z/\gamma^* \to$ ee $/\mu\mu$events, and their systematic uncertainties are less than 0.5%.

Hadronic Tau Uncertainties

The scale factor of the τ_{had} identification efficiency is also applied to simulation samples, which is measured using the $Z \to \tau\tau \to \mu\tau_{\text{had}}$ tag-and-probe method (see Section 3.4). The systematic uncertainties on the scale factor are $(2\% \sim 3\%)$ for 1-prong and $(3\% \sim 5\%)$ for 3-prong, depending on the number of tracks, the transverse momentum and the pseudo-rapidity.

The electron misidentification efficiency and its scale factor is measured using $Z \to$ ee $(e \to \tau_{\text{had}})$ events. The systematic uncertainties on the scale factor is evaluated depending on the τ_{had} transverse momentum and pseudo-rapidity, and they are $(8\% \sim 30\%)$. In addition, a conservative 15% uncertainty is assigned to simulated events with misidentified τ_{had}s from muons by comparing data and simulated events in the $Z \to \mu\mu(\mu \to \tau_{\text{had}})$ control region.

The TES is determined from a fit to the m_{vis} distribution in $Z \to \tau\tau \to \mu\tau_{\text{had}}$ events. The systematic uncertainties are treated separately for real τ_{had} and fake τ_{had} as uncorrelated uncertainties, and they are $(2\% \sim 4\%)$.

Jet Uncertainties

The uncertainty on the selection efficiency of the JVF is assigned to simulation samples, and it is evaluated by varying the number of bunch crossing using data $Z \rightarrow$ ee +jets events. The systematic uncertainties depending on the jet transverse momentum and pseudo-rapidity are less than 1%.

The uncertainties on the b-tagging efficiency and the mis-tag rate of a light-flavour jet are considered because the b-jet veto is included in the definitions of the VBF and Boosted categories, and the b-jet requirement is applied in the top control region. They are evaluated from data using di-leptonic $t\bar{t}$ events as described in Section 3.5, and the combined uncertainty is assigned by taking a diagonalization of the covariant matrix constructed from total 26 uncorrelated uncertainty components. The combined uncertainties depending on the b-jet transverse momentum are $(1\% \sim 2\%)$ [55].

The JES uncertainty is classified into several components as summarized in Section 3.5. Total eleven uncertainty components are considered as uncorrelated uncertainties. The combined uncertainties are within the range of $(1\% \sim 2\%)$ for central jets, and the range of $(3\% \sim 7\%)$ for forward jets.

Missing Transverse Energy Uncertainties

The uncertainty on the $E_{\mathrm{T}}^{\mathrm{miss}}$ depends on energy and momentum scales of each object, as mentioned in Section 3.6. Their uncertainties are propagated to the $E_{\mathrm{T}}^{\mathrm{miss}}$ reconstruction. Additionally, uncertainties on the energy scale and resolution of the soft term are considered as the $E_{\mathrm{T}}^{\mathrm{miss}}$ characteristic uncertainty. The uncertainties are $(5\% \sim 8\%)$ depending on the $E_{\mathrm{T}}^{\mathrm{miss}}$.

4.8.3 Systematic Uncertainties on the Background Modeling

Embedding Method Uncertainties

Two uncorrelated components of systematic uncertainties are assigned, the isolation requirement of the muon selection and the muon energy subtraction procedure. The isolation uncertainties are $(1 \sim 4\%)$, which is evaluated by varying isolation requirement from nominal ($I(p_{\mathrm{T}}, 0.4) < 0.2$) to a *tight* isolation requirement ($I(p_{\mathrm{T}}, 0.4) < 0.06$ and $I(E_{\mathrm{T}}, 0.2) < 0.04$) or removing the isolation requirement. The subtraction uncertainty is obtained by varying the expected muon energy deposition in the calorimeter by $20\%(30\%)$ for 8 TeV$(7$ TeV$)$ [114].

Fake Factor Method Uncertainties

The systematic uncertainty on the Fake Factor method is grouped into a background composition and a statistical uncertainty of fake factors, where two uncertainties are considered as uncorrelated components. The statistical uncertainty is due to the data statistics of control regions used in the fake factor measurement (see Section 4.6.2). The impact on the expected number of fake τ_{had} events is $\sim 5\%(\sim 20\%)$ for 8 TeV$(7$ TeV$)$ analysis. The background composition uncertainty is assigned for the ambiguity of the R_i

because they are obtained from the simulation based method. To evaluate this uncertainty, each R_i value is varied in the range [$R_i/2$,$R_i \times 2$], and a maximum difference of the number of expected events is taken as the uncertainty value. The impact of this uncertainty is $\sim 5\%(\sim 15\%)$ for 8 TeV$(7$ TeV$)$ analysis. As the cross check of this uncertainty evaluation, an another evaluation is performed by varying the m_{T} and $p_{\mathrm{T}}(\tau_{\mathrm{had}})$ requirement in the W+jets control region used for the R_W estimation. While the R_W value is changed within the range of $(25 \sim 40\%)$, the final impact on the expected number of events is at the same order. Additional uncertainties of data and simulation difference and a modeling in the same sign control region are considered, while they have a negligible impact on the number of expected events.

All systematic uncertainties are summarized in Table 4.12. The quoted numbers are uncertainties on the sum of the signal yields and on the sum of the background yields in the 8 TeV analysis, which are shown in Table 4.7.

Syst. Source	VBF		Boosted	
	S	B	S	B
Experimental Uncertainties				
Luminosity	$\pm 2.8\%$	$\pm 0.1\%$	$\pm 2.8\%$	$\pm 0.1\%$
Tau ID	$\pm 3.3\%$	$\pm 1.2\%$	$\pm 3.3\%$	$\pm 1.8\%$
e/μ ID and trig.	$\pm 1.8\%$	$\pm 0.5\%$	$\pm 1.8\%$	$\pm 0.8\%$
b-tagging	$< 0.1\%$	$\pm 0.2\%$	$\pm 0.4\%$	$\pm 0.2\%$
TES	$\pm 2.4\%$	$\pm 1.3\%$	$\pm 2.4\%$	$\pm 0.9\%$
JES	$^{+9.5}_{-8.7}\%$	$\pm 1.0\%$	$\pm 3.9\%$	$\pm 0.4\%$
$E_{\mathrm{T}}^{\mathrm{miss}}$ soft term	$^{+0.8}_{-0.3}\%$	$\pm 0.2\%$	$\pm 0.4\%$	$< 0.1\%$
Background Modeling Uncertainties				
Embedding	-	$\pm 2.6\%$	-	$\pm 2.6\%$
Fake Factor	-	$\pm 1.5\%$	-	$\pm 1.2\%$
Theoretical Uncertainties				
QCD Scale	$^{+9.7}_{-7.6}\%$	$\pm 0.2\%$	$^{+19.3}_{-14.7}\%$	$\pm 0.2\%$
PDF	$^{+3.9}_{-3.6}\%$	$\pm 0.2\%$	$^{+6.6}_{-6.1}$	$\pm 0.2\%$
UE and PS	$\pm 3.8\%$	$< 0.1\%$	$\pm 2.8\%$	$< 0.1\%$
Generator	$\pm 1.3\%$	$< 0.1\%$	$\pm 2.8\%$	$< 0.1\%$
$H \to \tau\tau$ B.R.	$\pm 5.7\%$	-	$\pm 5.7\%$	-

Table 4.12: Summary of systematic uncertainties on the sum of all signals and on the sum of all backgrounds for the VBF and Boosted categories for the 8 TeV analysis.

4.9 Results of the Search for the Higgs Boson

This section describes the result of the $H \to \tau_\ell \tau_{\text{had}}$ search, and the combined result of three channels of the $H \to \tau\tau$ search. The signal events are extracted by a maximum likelihood fit on the BDT output distributions. The statistical model is describe in Section 4.9.1, and then the $H \to \tau_\ell \tau_{\text{had}}$ search result is summarized in Section 4.9.2. Finally, the $H \to \tau\tau$ combined result is described in Section 4.9.3 as the final result of this chapter.

4.9.1 Signal Extraction Procedure

The results of this analysis are obtained by the evaluation of the agreement of the observed data with either the *signal+background* or the *background only* hypotheses. Therefore, an appropriate statistical model of the observed data is necessary including the expected signal and background events with their systematic uncertainties. This model is based on several parameters, corresponding to normalization factors of signal and background events, and statistical and systematic uncertainties. Among these parameters, the parameter of interest (PoI) is the signal strength μ, expressed by

$$\mu = \frac{(\sigma \times \text{B.R.}(H \to \tau\tau)_{\text{obs.}})}{(\sigma \times \text{B.R.}(H \to \tau\tau)_{\text{SM}})}, \tag{4.20}$$

where σ and B.R.$(H \to \tau\tau)$ are the Higgs boson production cross section and the $H \to \tau\tau$ branching ratio, respectively. The case of $\mu = 1$ represents a perfect agreement between the measured signal and the SM prediction. The other parameters are referred to as Nuisance Parameters (NPs).

The parameters are determined by performing a binned maximum likelihood fit on the BDT output distributions, where probability density functions are obtained from the expected signal and background distributions. As the simplest example, the likelihood function is expressed by;

$$L(\mu) = \prod_{x}^{\text{N}_{\text{bin}}} \frac{e^{\nu_x(\mu|x)} \nu_x(\mu|x)^{\text{N}_{\text{obs.(x)}}}}{\text{N}_{\text{obs.}(x)}!}, \tag{4.21}$$

$$\nu(\mu|x) = \mu \sum_{s}^{\text{N}_{\text{sig}}} n_s \cdot p_s(x) + \sum_{b}^{\text{N}_{\text{bkg}}} n_b \cdot p_b(x), \tag{4.22}$$

where N_{bin} is the number of bins of probability density functions p, and $\text{N}_{\text{obs.}(x)}$ represents the observed data in given bin x, and $n_{s,b}$ represents the expected number of events of each signal and background process. As seen in the equation (4.21), the likelihood is expressed by the product of the Poisson distribution to the observed data for each bin, where expected value $\nu(\mu|x)$ is the total number of expected events of signal and background processes. The number of expected events of each signal process is normalized by the signal strength μ. The signal and background predictions depend on several parameters, such as their normalization factor, statistical and systematic uncertainties. The likelihood function is expanded including their effects. The NPs (θ) are constrained by their estimated variation (σ_θ) in the fit using the Gaussian functions $G(\theta, \sigma_\theta)$.

In this analysis, a simultaneous fit is performed to the signal and top control regions for the VBF and Boosted categories, for the 8 TeV and 7 TeV analysis, in order to estimate all parameters of the signal and background processes. The fit on the top control region provides a handle on the normalization factors for top background events, where one bin histogram is used as the probability density function in order to focus on only normalization factors of Top (τ_{had}) and Top ($\ell \rightarrow \tau_{\text{had}}$) events. Therefore, the final likelihood function is expanded as following:

$$L(\nu|\theta) = \Big(\prod_{y}^{\text{N}_{\text{year}}} \prod_{c}^{\text{N}_{\text{categ.}}} \prod_{r}^{\text{N}_{\text{region}}} \prod_{x}^{\text{N}_{\text{bin}}} \frac{e^{\nu(\mu|y,c,r,x)}\nu(\mu|c,y,x)^{\text{N}_{\text{obs.}}(y,c,r,x)}}{\text{N}_{\text{obs.}}(y,c,r,x)!}\Big) \times \prod_{\theta}^{\text{N}_{\theta}} G(\theta,\sigma_{\theta}), \tag{4.23}$$

where year corresponds to the 8 TeV and 7 TeV analysis, categ. corresponds to the VBF and Boosted categories, and region corresponds to the signal and top control regions. Total 185 NPs are considered and fitted by the likelihood.

Based on the likelihood function, the signal strength μ is tested by a profile likelihood ratio with the following test statistic (q_{μ}):

$$q_{\mu} = -2\ln(\lambda(\mu)) = -2\ln\Big(\frac{L(\mu|\hat{\theta_{\mu}})}{L(\hat{\mu}|\hat{\theta})}\Big), \tag{4.24}$$

where $\hat{\mu}$ and $\hat{\theta_{\mu}}$ are the parameters that maximize the likelihood L, and $\hat{\theta_{\mu}}$ represents nuisance parameters that maximize the likelihood for a given μ. The signal strength is evaluated by this test statistics obtained from the a maximum likelihood fit. A level of disagreement between data and *signal+background* hypothesis is represents by the p-value, defined as

$$p_{\mu} = \int_{q_{\mu}^{\text{obs.}}}^{\infty} f(q_{\mu}|\mu)dq_{\mu}, \tag{4.25}$$

where $q_{\mu}^{\text{obs.}}$ is the test statistic observed in data, and $f(q_{\mu}|\mu)$ is the probability density function for a certain signal strength. Based on this p-value, the signal significance is quantified by p_0, where its definition is the same as the equation (4.25) with $\mu = 0$. The p_0 represents the probability that the observed data can be explained by *background only* hypothesis.

4.9.2 Results of the $H \rightarrow \tau_{\ell}\tau_{\textbf{had}}$ Search

The signal strength μ is determined by combined likelihood fit to data distributions. Figure 4.27 shows the BDT output distributions after the fit.

The combination of the VBF and Boosted categories in 7 TeV and 8 TeV analyses gives the best-fit signal strength at $m_H = 125$ GeV of

$$\mu = 0.98^{+0.35}_{-0.33}(\text{stat.})\ ^{+0.36}_{-0.30}(\text{syst.})\ \pm 0.06(\text{theory syst.}), \tag{4.26}$$

where the systematic uncertainties are separately shown for the sum of experimental and theoretical

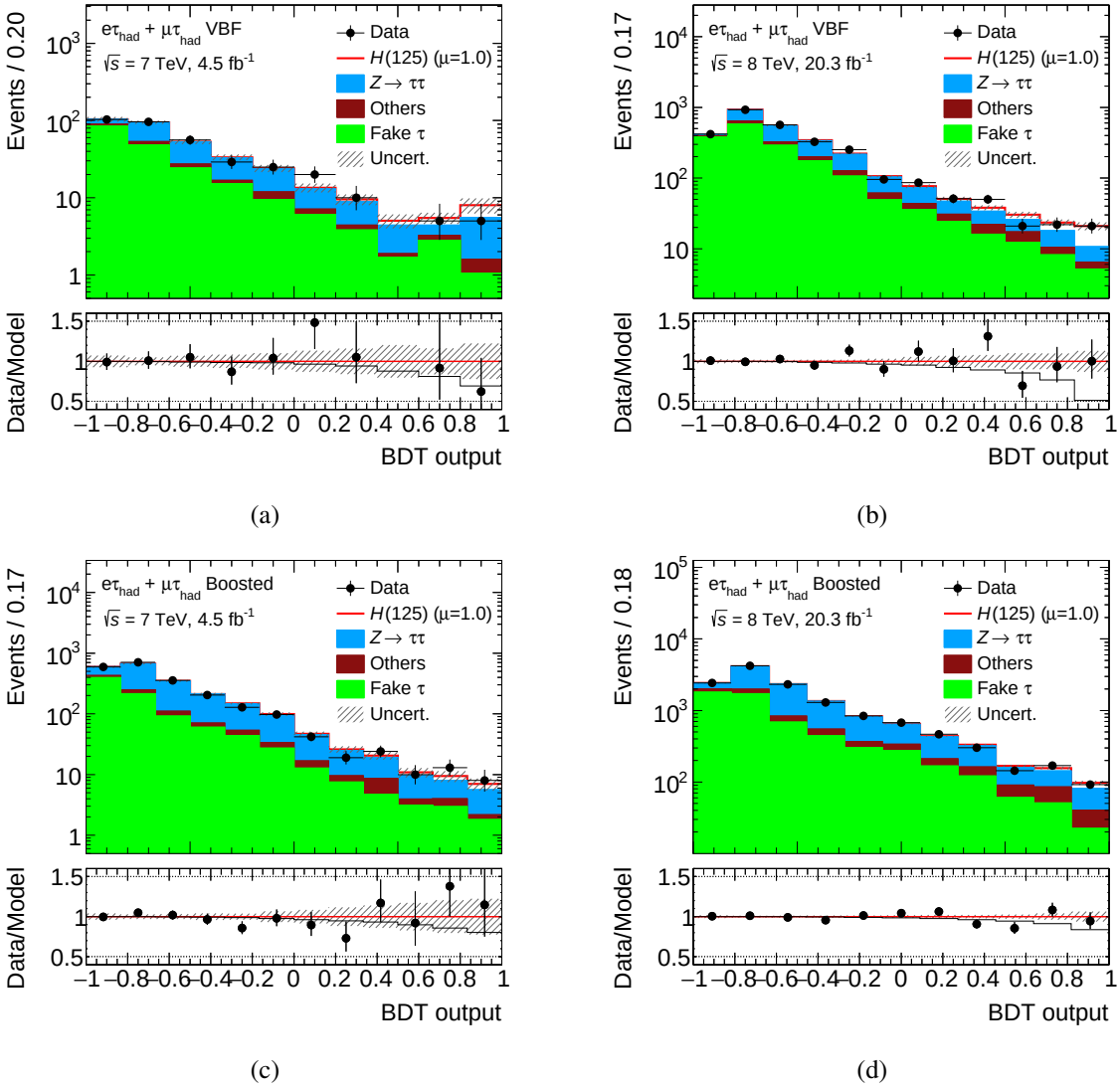

Fig. 4.27: BDT output distributions of the VBF (a,b) and Boosted (c,d) categories for 7 TeV (a,c) and 8 TeV (b,d) analysis after the maximum likelihood fit. The bottom panels show both the ratio of data and *signal+background* model, and the ratio of data and *background only* model, with statistical and systematic uncertainties.

uncertainties. The signal strength is consistent with the SM prediction within uncertainties.

Figure 4.28 (a) shows the $\log_{10}(S/B)$ distribution of signal and background events obtained from the fit with $\mu = 0.98$. The background distribution with $\mu = 0$ is also shown, which corresponds to the *background only* model. The distribution indicates a disagreement between the observed data and *background only* model, even including the effect of all systematic uncertainties.

The signal significance p_0 is also obtained from the fit. The results are $p_0 = 9.98 \times 10^{-3}$ and $p_0 = 9.09 \times 10^{-3}$ for observed data and expected *signal+background* Asimov [133] data, respectively. These p_0 values corresponds to an observed (expected) significance of 2.3σ (2.3σ) of the standard deviations.

Table 4.13 shows observed and expected signal significances and best-fit signal strengths at $m_H =$

125 GeV for individual years, categories and their combinations.

Year	Category	Observed (expected) significance	Signal strength
7 TeV	VBF	-0.44 (0.51)	$-0.77^{+1.73}_{-1.93}$
	Boosted	1.09 (0.42)	$2.73^{+2.77}_{-2.51}$
	Combined	-0.16 (0.65)	$-0.23^{+1.48}_{-1.44}$
8 TeV	VBF	2.48 (2.08)	$1.20^{+0.62}_{-0.52}$
	Boosted	0.66 (1.06)	$0.64^{+1.05}_{-0.96}$
	Combined	2.54 (2.35)	$1.10^{+0.54}_{-0.47}$
$7+8$ TeV	VBF	2.23 (2.11)	$1.02^{+0.56}_{-0.48}$
	Boosted	1.01 (1.11)	$0.92^{+1.00}_{-0.91}$
	Combined	2.33 (2.33)	$0.98^{+0.50}_{-0.48}$

Table 4.13: Observed and expected significances and best-fit signal strengths at $m_H = 125$ GeV for the VBF and Boosted categories in 7 TeV and 8 TeV analyses and their combinations.

In order to investigate an impact on $\hat{\mu}$ for individual uncertainties, $\Delta\hat{\mu}$ is evaluated for each NP by performing conditional maximum likelihood fits, where each NP value is fixed to its $\pm1\sigma$ obtained from nominal fit. The $\Delta\hat{\mu}$ for each NP is obtained by taking the $\hat{\mu}$ difference between nominal fit and NP fixed fit, referred to as post-fit $\Delta\hat{\mu}$. Then, all nuisance parameters are ranked by the size of the post-fit $\Delta\hat{\mu}$ in descending order, indicating their importance for the μ measurement. Moreover, $\Delta\hat{\mu}$ is also evaluated by another conditional fit, where each NP value is fixed to pre-estimated $\pm1\sigma$, referred to as pre-fit $\Delta\hat{\mu}$. The pre-fit $\Delta\hat{\mu}$ is used to evaluate the estimation of systematic uncertainties. Figure 4.29 shows the 25 highest ranked nuisance parameters. The post-fit $\Delta\hat{\mu}$, the pre-fit $\Delta\hat{\mu}$ and the difference of NP value between before and after fit $(\hat{\theta} - \theta_0)$ are shown for each NP. Text colors of the NP names represents the type of NP, which are statistical, experimental, theoretical uncertainties and normalization factors. The highest ranked nuisance parameter is statistical uncertainty on the highest BDT output bin in 8 TeV VBF category because this bin has the highest S/B ratio with smallest statistics. The uncertainty on the $H \to \tau\tau$ branching ratio has highest ranking in the theoretical uncertainties. The higher ranked (important) experimental uncertainties are the JES uncertainties and the uncertainty on the electron to τ_{had} misidentification efficiency. This indicates that precise reconstruction and systematic uncertainty estimation of jets and τ_{had} are crucial points of this analysis, and there is a room for the experimental improvement in addition to statistically and theoretically limited parameters. Other nuisance parameters are detailed in Section A.2.

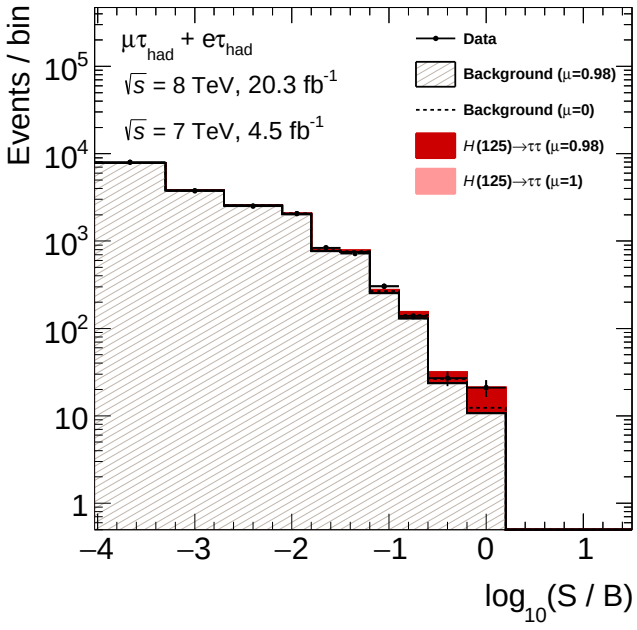

(a)

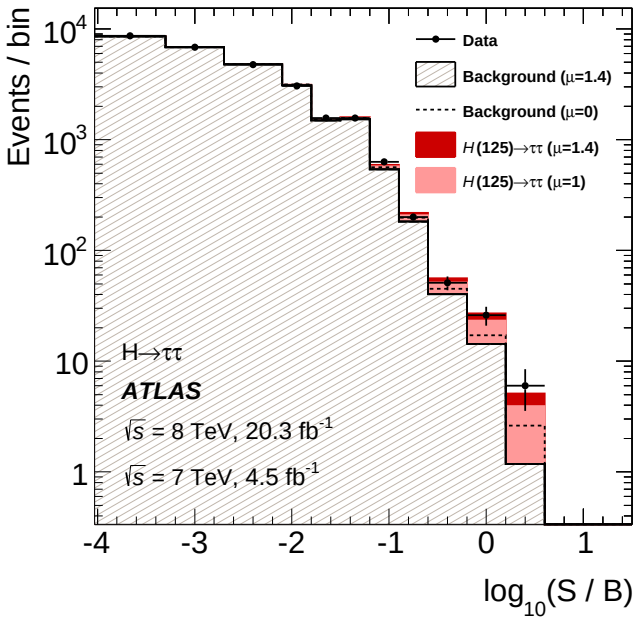

(b)

Fig. 4.28: Distributions of $\log_{10}(S/B)$ for the $H \to \tau_\ell\tau_{\text{had}}$ channel (a) and for the $H \to \tau\tau$ combination (b), where S and B are taken from the BDT output bin of each event, assuming a signal strength $\mu = 1.4$. The predicted background is obtained from the fit with best-fit μ value (hatch) and with $\mu = 0$ (dashed line). The signal yields are shown for $m_H = 125$ GeV at $\mu = 1$ and the best-fit value (0.98 for $H \to \tau_\ell\tau_{\text{had}}$ channel and 1.4 for $H \to \tau\tau$ combination).

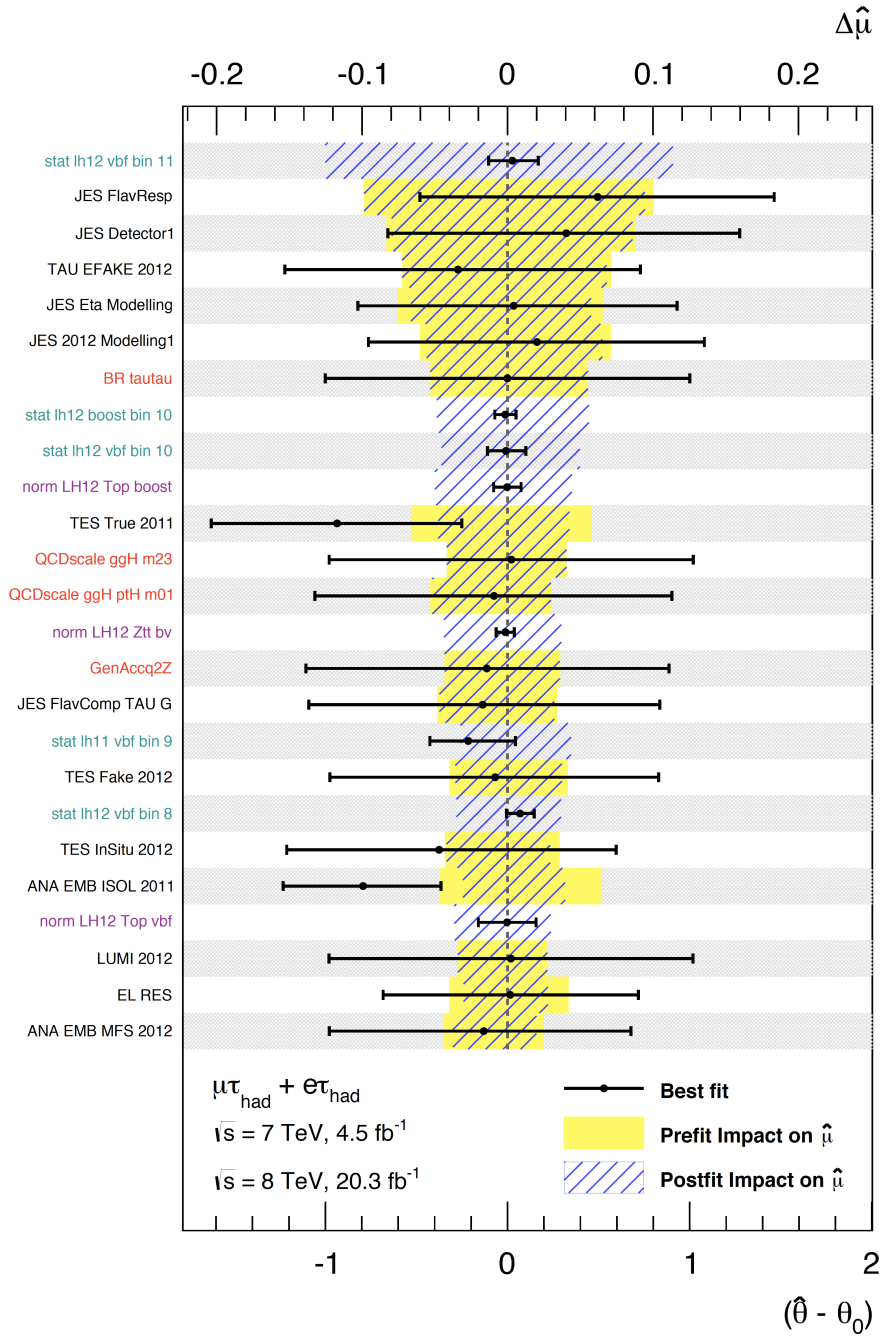

Fig. 4.29: The 25 nuisance parameters which have the largest impact on the signal strength, with post-fit $\Delta\hat{\mu}$ (blue hatch), the pre-fit $\Delta\hat{\mu}$ (yellow band) and $\hat{\theta} - \theta_0$ (black dot), detailed in the text.

4.9.3 Combination Results of the $H \to \tau\tau$ Search

In the above section, the results of the $H \to \tau_\ell \tau_{\text{had}}$ search are presented. In addition, $H \to \tau_\ell \tau_\ell$ and $H \to \tau_{\text{had}} \tau_{\text{had}}$ searches are also performed in the ATLAS experiment [123]. These two searches are applied basically the same analysis strategy as the $H \to \tau_\ell \tau_{\text{had}}$ analysis such as category definition,

background suppression using BDTs, systematic uncertainty estimations. However, the event selection in the three channels is fully orthogonal, and therefore statistical combination of these individual results can be performed. Based on the same statistical model described in Section 4.9.1, the likelihood function is obtained by multiplying the individual likelihood functions. The common systematic uncertainties, such as object related uncertainties and theoretical uncertainties, are included as correlated nuisance parameters.

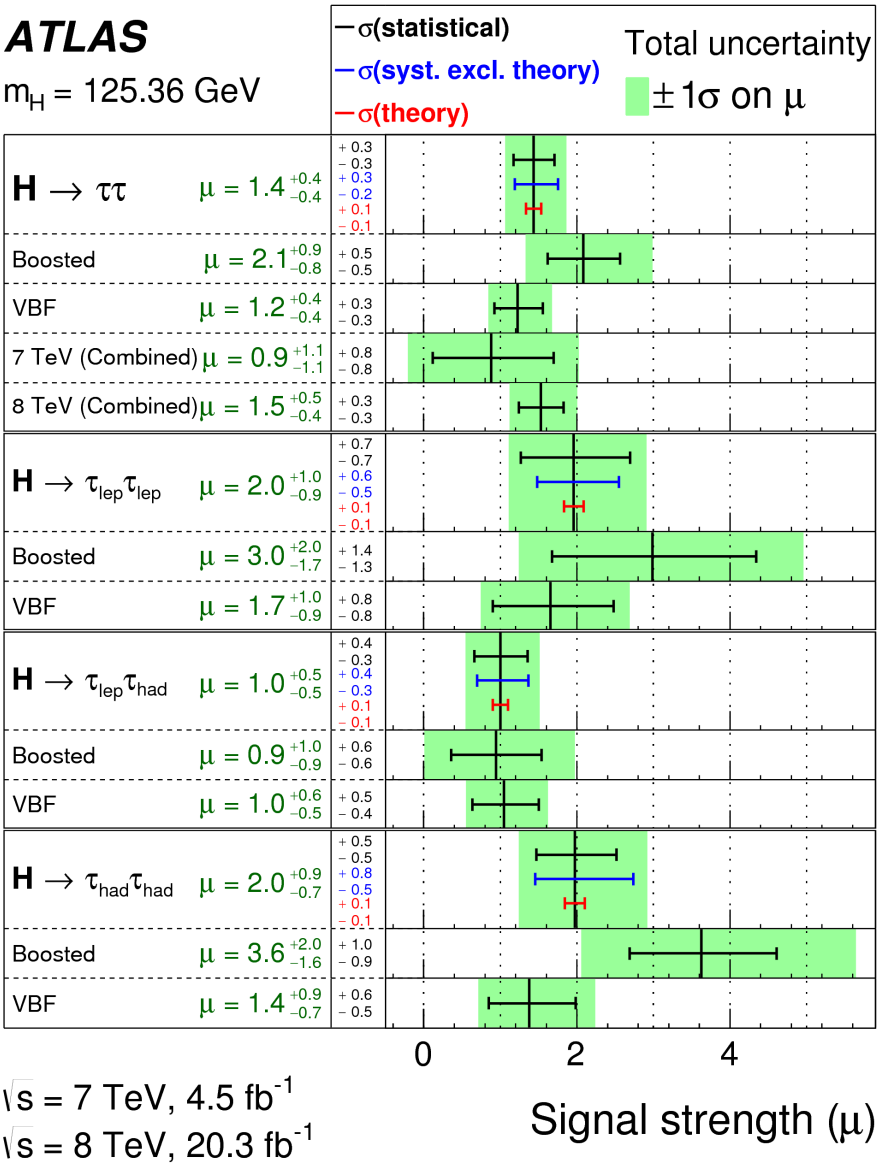

Fig. 4.30: The best-fit value for the signal strength μ for the individual channels and their combination. The total $\pm 1\sigma$ is represented by the green band, with the statistical uncertainty (black), the experimental uncertainty (blue) and the theory uncertainty (red).

The best-fit value of the signal strength at $m_H = 125$ GeV is

$$\mu = 1.43^{+0.27}_{-0.26}(\text{stat.})\ ^{+0.32}_{-0.25}(\text{syst.})\ \pm 0.09(\text{theory syst.}). \tag{4.27}$$

The results for individual channels and for each category are shown in Fig. 4.30. The results are consistent with the SM prediction within uncertainties for both the combination and the individual channels.

The signal significance p_0 is also extracted from the combined fit. The observed p_0 value is 2.7×10^{-6}, which corresponds to a significance of 4.5σ of the standard deviation, while an expected significance is 3.4σ. This result indicates "evidence for the decay of the Higgs boson into tau leptons".

In order to visualize extract information of the Higgs boson mass from the fitted BDT output distribution, a weighted $m_{\tau\tau}$ distribution is shown in Fig. 4.31, where events are weighted by a factor of $\ln(1 + \text{S/B})$. This weight procedure enhances events compatible with *signal+background* model. The excess can be seen around $m_{\tau\tau} = 125$ GeV in the figure, which is consistent with the SM with $m_H = 125$ GeV.

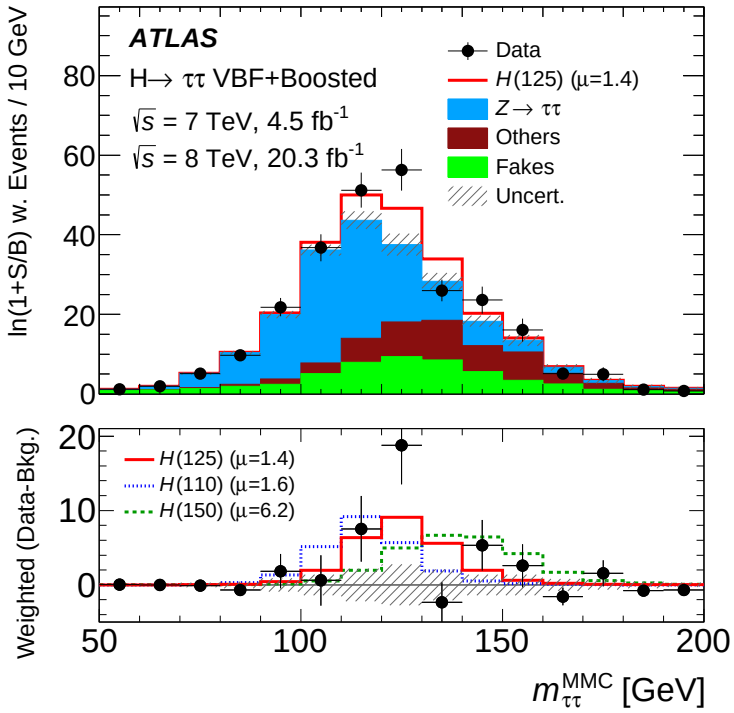

Fig. 4.31: The weighted $m_{\tau\tau}$ distribution, where events are weighted by $\ln(1 + S/B)$. These weights are determined by the signal (S) and background (B) predictions for each BDT bin. The background predictions are obtained from the fit with $m_H = 125$ GeV signal hypothesis (signal strength μ = 1.4). The lower panel shows weighted (data-background) distribution (black). The weighted signal distributions with $m_H = 125$ GeV (red), $m_H = 110$ GeV (blue) and $m_H = 150$ GeV (green) are also shown, normalizing by each best-fit μ value.

In order to evaluate each NPs, the same procedure described in Section 4.9.2 is performed. The absolute contributions of the most important uncertainties on the measured signal strength parameter are summarized in Table 4.14. The highest ranked nuisance parameter is statistical uncertainty of $^{+27}_{-26}\%$, the second

highest one is the uncertainty on the JES of 13%. The situation is the same as the $H \to \tau_\ell \tau_{\text{had}}$ search, and so-that an improvement of the JES leads to increase the future analysis of the $H \to \tau\tau$ search sensitivity. The possibility of the JES uncertainty improvement can be considered by an analysis specific JES measurement, such as the measurement using events which have the VBF or the Boosted topology.

Source of Uncertainty	Uncertainty on μ
Signal region statistics (data)	$^{+0.27}_{-0.26}$
Jet energy scale	$\pm$ 0.13
Tau energy scale	$\pm$ 0.07
Tau identification	$\pm$ 0.06
Background normalization	$\pm$ 0.12
Background estimate stat.	$\pm$ 0.10
BR ($H \to \tau\tau$)	$\pm$ 0.08
Parton shower/Underlying event	$\pm$ 0.04
PDF	$\pm$ 0.03
Total sys.	$^{+0.33}_{-0.26}$
Total	$^{+0.43}_{-0.37}$

Table 4.14: Important sources of uncertainties on the best-fit signal strength μ. The contributions are given as absolute uncertainties on the best-fit value of $\hat{\mu} = 1.43$.

CHAPTER 5

Study of CP Measurement in the $\tau\tau$ Final State

This chapter describes the sensitivity estimation of the measurement of CP properties of the Higgs boson in the $\tau\tau$ final state. As described in Section 4, evidence for the decay of the Higgs boson into tau leptons is found, and therefore the $H \to \tau\tau$ analysis is shifted from the observation stage to the property measurement stage.

In the $H \to \tau\tau$ analysis, the signal strength corresponding to the coupling constant and the Higgs boson mass has been measured and are so far consistent with the SM. On the other hand, information of the CP properties of the Higgs boson have not yet been measured in the $H \to \tau\tau$ analysis. Another main part of this thesis is development and sensitivity estimation of the CP measurement in the $\tau\tau$ final state.

The $H \to \tau_\ell\tau_{\text{had}}$ and $H \to \tau_{\text{had}}\tau_{\text{had}}$ channels used for this analysis are detailed in Chapter 4 and Section 5.1, respectively. The $H \to \tau_\ell\tau_\ell$ channel is not included because this channel has the lowest signal significance in the $H \to \tau\tau$ channels, and it is hard to precisely reconstruct CP observables due to the presence of four neutrinos in the final state. This analysis is performed only using the data sample collected in 2012 with $\sqrt{s} = 8$ TeV because the data sample collected in 2011 with $\sqrt{s} = 7$ TeV is statistically limited to reconstruct observables in a high sensitivity region (high BDT score bins).

The analysis strategies, such as analyzed samples, event selection, categorization, background suppression method and systematic uncertainties, are basically the same as the $H \to \tau_\ell\tau_{\text{had}}$ search. This chapter focuses on the different points from Chapter 4 as follows: the $H \to \tau_{\text{had}}\tau_{\text{had}}$ channel, CP observables, and the statistical model.

5.1 Overview of the $H \to \tau_{\text{had}}\tau_{\text{had}}$ Analysis

This analysis uses the $H \to \tau_{\text{had}}\tau_{\text{had}}$ channel in addition to the $H \to \tau_\ell\tau_{\text{had}}$ channel. This section describes a brief overview of the analysis of the $H \to \tau_{\text{had}}\tau_{\text{had}}$ channel, which is detailed in Ref. [123].

The branching ratio of the $H \to \tau_{\text{had}}\tau_{\text{had}}$ channel is $\sim 42\%$, which is the second largest next to the $H \to \tau_\ell\tau_{\text{had}}$ channel. This channel has slightly higher $m_{\tau\tau}$ resolution than the other channels since this channel includes the less number of neutrinos in the final state. The main backgrounds of this channel are events from $Z \to \tau\tau$ and multi-jet processes. The other events from electroweak process are few percent level in the total expected event yields.

The analyzed data is collected by the di-tau trigger with τ_{had} p_{T} thresholds of 29 GeV and 20 GeV (see Section 3.4). The amount of data is integrated luminosity of 20.3 fb^{-1} at $\sqrt{s} = 8$ TeV. The same simulation samples for 8 TeV analysis are used as summarized in Section 4.3.2.

Preselection
Di-tau Trigger
Lepton veto
Exactly two τ_{had}s
Leading τ_{had} $p_{\text{T}} > 35$ GeV
Sub-leading τ_{had} $p_{\text{T}} > 25$ GeV
Tight identification for leading τ_{had}
Medium identification for sub-leading τ_{had}
τ_{had} isolation
$E_{\text{T}}^{\text{miss}} > 20$ GeV
$E_{\text{T}}^{\text{miss}}$ direction between the two visible taus in ϕ, or within $\Delta\phi(\tau_{\text{had}}, E_{\text{T}}^{\text{miss}}) < \pi/4$
$0.8 < \Delta R(\tau_{\text{had}}, \tau_{\text{had}}) < 2.4$
$\lvert\Delta\eta(\tau_{\text{had}}, \tau_{\text{had}})\rvert < 1.5$
Physical MMC solution
VBF Category Definition
leading jet $p_{\text{T}} > 50$ GeV with $\lvert\eta\rvert < 4.5$
sub-leading jet $p_{\text{T}} > 35$ GeV with $2.4 < \lvert\eta\rvert < 4.5$
$\Delta\eta(\text{jet}_1, \text{jet}_2) > 2.0$
b-jet veto
Boosted Category Definition
Not VBF
$p_{\text{T}}^{H} > 100$ GeV

Table 5.1: Summary of the event selection and the event categorization for the $H \to \tau_{\text{had}}\tau_{\text{had}}$ channel.

While the object definitions are exactly the same as listed in Table 4.2, the preselection is different from the $H \to \tau_\ell \tau_{\text{had}}$ channel. Table 5.1 presents the preselection criteria in the $H \to \tau_{\text{had}}\tau_{\text{had}}$ analysis. Events with electron or muon candidates are rejected, while one *medium* τ_{had} candidate and one *tight* τ_{had} candidate with opposite charges are required. τ_{had} candidates with additional tracks in the region $0.2 < \Delta R < 0.6$ are removed. In addition, events are required to have $E_{\text{T}}^{\text{miss}} > 20$ GeV and its direction must either be between the two τ_{had} in a ϕ plane, or within $\Delta\phi(\tau_{\text{had}}, E_{\text{T}}^{\text{miss}}) < \pi/4$ of the nearest τ_{had}. In order to further reduce the background from multi-jet production, requirements of the $\Delta R(\tau_{\text{had}}, \tau_{\text{had}})$ and $\Delta\eta(\tau_{\text{had}}, \tau_{\text{had}})$ are applied. Each threshold of the preselection is determined to reduce background contamination with a minimal signal efficiency loss because the main background suppression is performed by the BDT. After applying the preselection, the final state of this channel is orthogonal to the $H \to \tau_\ell \tau_{\text{had}}$ channel.

The event categorization is performed with slightly different definitions from the $H \to \tau_\ell \tau_{\text{had}}$ channel. The threshold of $\Delta\eta(\text{jet}_1, \text{jet}_2) > 3.0$ cut in the VBF category is lowered to 2.0, and requirements of $m_{\tau\tau} > 40$ GeV and the b-jet veto are removed, due to a different background composition between two channels.

The $Z \to \tau\tau$ background events are modeled by the embedding sample, while the multi-jet background events are modeled by data events in the fake τ_{had} enriched control region. The control region is defined by reverting the τ_{had} isolation and opposite sign requirement, and the number of τ_{had} tracks requirement is not enforced. In order to determine the normalization of multi-jet backgrounds, a template fit on a $\Delta\eta(\tau_{\text{had}}1, \tau_{\text{had}}2)$ distribution are performed using a dedicated category, referred to as rest category. The rest category is defined by applying the preselection requirements but not passing the VBF or boosted category selections. The result of the template fit is shown in Fig. 5.1, demonstrating the agreement between data and background estimations with a negligible signal contamination. The other electroweak backgrounds are modeled with simulation samples.

The background suppression is performed based on BDTs trained separately for the VBF and Boosted categories. The input variables are basically synchronized with the $H \to \tau_\ell \tau_{\text{had}}$ channel, where lepton related variables are replaced to τ_{had}, i.e., ℓ - η centrality $\to$ τ_{had} - η centrality and $p_{\text{T}}^{\ell}/p_{\text{T}}^{\tau_{\text{had}}} \to p_{\text{T}}^{\tau_{\text{had}}1}/p_{\text{T}}^{\tau_{\text{had}}2}$. The m_{T} variable is removed because the W+jets background contribution is minor ($\sim 2\%$) after the preselection in the $H \to \tau_{\text{had}}\tau_{\text{had}}$ channel. In W+jet process, especially the $W \to \tau\nu_{\tau_{\text{had}}}(\text{jet} \to \tau_{\text{had}})$ process can be the background for the $H \to \tau_{\text{had}}\tau_{\text{had}}$ signal. However, the requirement of the $E_{\text{T}}^{\text{miss}}$ direction significantly reduces this background.

A maximum likelihood fit is performed on BDT output distributions, including the same systematic uncertainties described in Section 4.8. Figure 5.2 shows BDT output distributions in the $H \to \tau_{\text{had}}\tau_{\text{had}}$ channel for the VBF and Boosted categories. The statistic uncertainty on the highest BDT bin in the VBF category gives the most impact on the signal strength. The JES and TES uncertainties are the next important nuisance parameters. In the $H \to \tau_{\text{had}}\tau_{\text{had}}$ 8 TeV analysis, the best-fit value of the signal strength at $m_H = 125$ GeV is $\mu = 1.8\ ^{+0.9}_{-0.7}$, and the observed (expected) signal significance of this channel is $2.9\sigma(1.9\sigma)$.

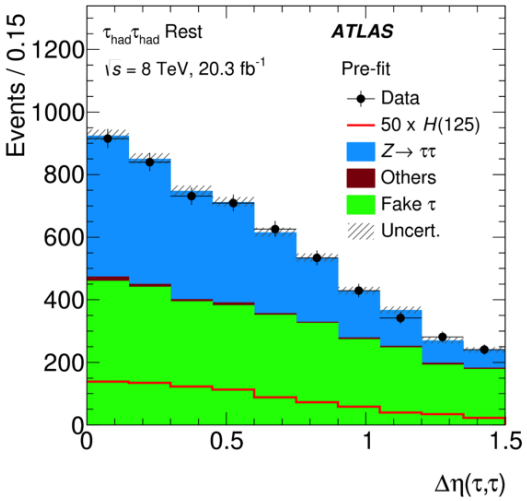

Fig. 5.1: The $\Delta\eta(\tau_{\text{had}}1, \tau_{\text{had}}2)$ distribution in the rest category. The expected signal contribution is multiplied by a factor 50.

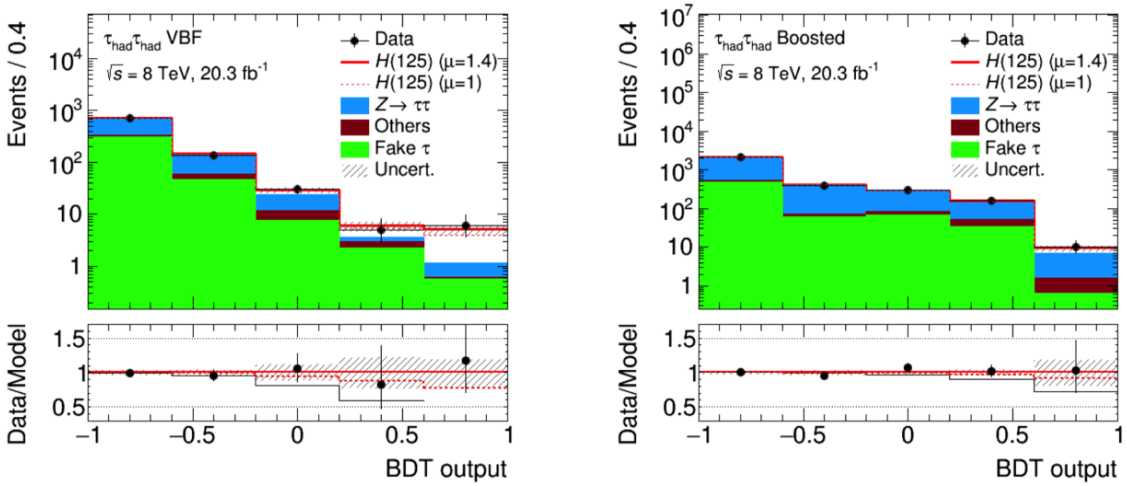

(a) (b)

Fig. 5.2: BDT output distributions of the VBF (a) and Boosted (b) categories after the maximum likelihood fit.

5.2 CP Observables in the $H \rightarrow \tau\tau$ analysis

In the $H \rightarrow \tau\tau$ decay process, the CP state of the Higgs boson can be distinguished by spin correlations of the di-τ lepton decay. The correlation is reflected in the angle between decay planes of the di-τ lepton. In this section, the reconstruction method of the angle is described.

For the generator-level investigation, the ggF and VBF samples with the CP-odd Higgs boson ($m_H = 125$ GeV) are generated using POWHEG event generator at NLO QCD [134], interfaced to PYTHIA for the parton shower, hadronization and underlying events. These samples are used to verify generator-level

distributions of CP sensitive observables, referred to as "truth" samples in this analysis.

5.2.1 Transverse Spin Correlations

A spin correlation of the di-τ pair has information of the CP state of the Higgs boson in the $H \to \tau\tau$ process [135]. Denoting the Higgs boson with a mixing CP state by H_{mix}, the spin dependence of the $H_{\text{mix}} \to \tau\tau$ decay probability is given by:

$$\Gamma(H_{\text{mix}} \to \tau^+\tau^-) \sim 1 - \boldsymbol{s}_{\parallel}^{\tau^+} \cdot \boldsymbol{s}_{\parallel}^{\tau^-} + \boldsymbol{s}_{\perp}^{\tau^+} \cdot R(\pi\alpha) \cdot \boldsymbol{s}_{\perp}^{\tau^-}, \tag{5.1}$$

$$R(\pi\alpha) = \begin{pmatrix} -\cos(\pi\alpha) & -\sin(\pi\alpha) \\ -\sin(\pi\alpha) & \cos(\pi\alpha) \end{pmatrix} = \begin{pmatrix} Rxx & Rxy \\ Ryx & Ryy \end{pmatrix}, \tag{5.2}$$

where $\boldsymbol{s}^{\tau^\pm}$ is spin polarization vectors of τ leptons, and $R(\pi\alpha)$ is a spin density matrix with a mixing angle $\pi\alpha$. The parallel and vertical component of $\boldsymbol{s}^{\tau^\pm}$ to the τ lepton direction are denoted by $\boldsymbol{s}_{\parallel}^{\tau^+}$ and $\boldsymbol{s}_{\perp}^{\tau^+}$, respectively. $Rxx = -1$ and $Ryy = +1$ represents the pure CP-even state Higgs boson (the SM Higgs boson H_0), while $Rxx = +1$ and $Ryy = -1$ represents the pure CP-odd Higgs boson (the BSM Higgs boson A_0). Schematic diagram of the relation of transverse spin vectors and the $\tau^\pm\tau^\mp \to \pi^\pm\pi^\mp$ decay for the CP-even and CP-odd Higgs boson is shown in Fig. 5.3. Observables which include the information of the transverse spin correlation between the di-τ leptons can be used to discriminate from the CP-even and CP-odd Higgs boson.

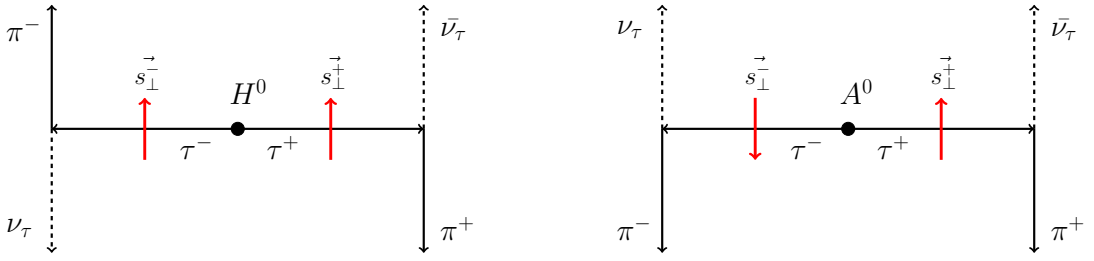

Fig. 5.3: Schematic diagram of the relation of transverse spin vectors of di-τ leptons and the $\tau^\pm\tau^\mp \to \pi^\pm\pi^\mp$ decay for the (a) CP-even and (b) CP-odd Higgs boson.

5.2.2 Acoplanarity Angle

One typical CP sensitive variable is proposed for reflecting the transverse spin correlation, referred to as "acoplanarity" angle [135]. In order to define this variable, an another coordinate system (x', y' and z' axis) is defined in the di-τ rest frame. The z' axis is defined as the τ lepton direction, while the x', y' axes are defined as horizontal and vertical axes in the transverse plane with respect to the z' axis, respectively.

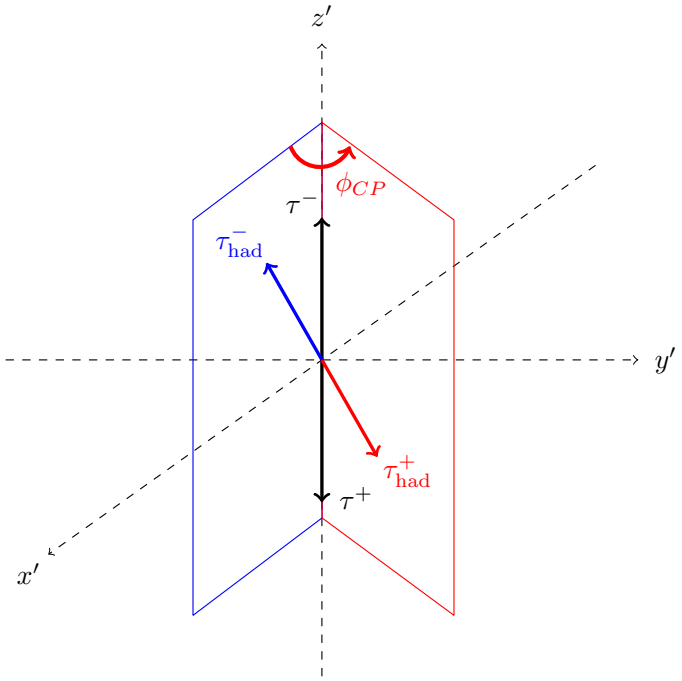

Fig. 5.4: Definition of the acoplanarity angle $\phi_{\rm CP}$. The z' axis is defined as the τ lepton direction in the di-τ rest frame. The x', y' axes are defined as horizontal and vertical axes in the transverse plane with respect to the z' axis, respectively. The $\phi_{\rm CP}$ is defined as the angle between the $\tau^+ \to \tau^+ \bar{\nu}_\tau$ decay plane and the $\tau^- \to \tau^- \nu_\tau$ decay plane.

The definition of the acoplanarity angle $\phi_{\rm CP}$ is illustrated in Fig. 5.4. The range of $\phi_{\rm CP}$ is $[0, 2\pi]$. In order to increase statistics of each bin in the $\phi_{\rm CP}$ distribution, the $\phi_{\rm CP}$ is modified as the following:

$$\phi_{\rm CP} = \begin{cases} \pi - \phi_{\rm CP} & (0 \leq \phi_{\rm CP} \leq \pi) \\ \phi_{\rm CP} - \pi & (\pi \leq \phi_{\rm CP} \leq 2\pi). \end{cases} \tag{5.3}$$

(5.4)

The $\phi_{\rm CP}$ distribution becomes the distribution that is folded into 2π around π by the modification. The range of the $\phi_{\rm CP}$ becomes $[0, \pi]$, and thus statistics of each bin is increased to 2 times.

Figure 5.5 shows acoplanarity distributions of the $H/A \to \tau\tau$ and $Z \to \tau\tau$ processes for $\pi^\pm\ \pi^\mp$, $\pi^\pm\ \rho^\mp$, $\rho^\pm\ \rho^\mp$ and $\ell^\pm\pi^\mp$ decays. The sensitivity on the CP state in the acoplanarity angle depends on the number of visible particles. In case of multi-$\pi^\pm$ and/or multi-π^0 decay modes, the decay plane cannot be properly reconstructed because the $\tau_{\rm had}$ direction is determined as the vector sum of these particles. The acoplanarity angle for the $\ell^\pm\pi^\mp$ decay has opposite distribution to other decays. In the $\tau^\pm\tau^\mp \to \ell^\pm\pi^\mp$ decay, the relation of the transverse spin vector and the lepton direction is inverted from the relation in Fig. 5.3 due to the presence of two neutrinos in the leptonic τ decay [136]. Acoplanarity distributions for other typical di-τ decays are summarized in Section B.

The acoplanarity angle requires information of neutrinos, and therefore the precise neutrino reconstruction or an alternative angle reconstructed by only information of visible decay products is necessary at

the analysis.

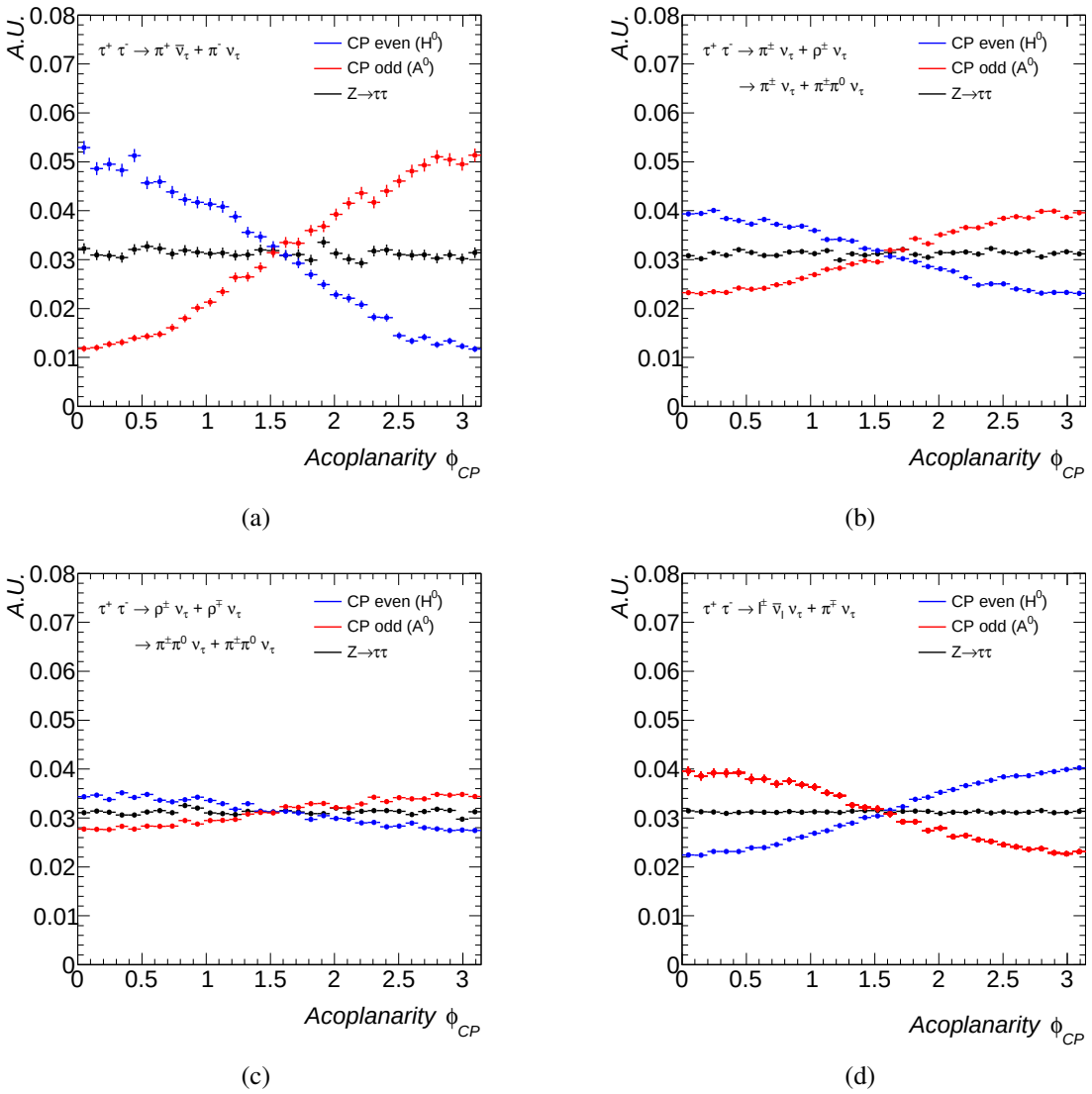

Fig. 5.5: Acoplanarity ϕ_{CP} distributions from truth samples, for the (a) $\pi^{\pm}\,\pi^{\mp}$, (b) $\pi^{\pm}\,\rho^{\mp}$, (c) $\rho^{\pm}\,\rho^{\mp}$ and (d) $\ell^{\pm}\pi^{\mp}$ decay modes from CP-even, CP-odd Higgs boson (red,blue) and the Z boson (black) production processes, where the Higgs boson production process is the ggF process, and the Higgs boson mass is set to 125 GeV.

5.2.3 CP Observables

The method of the precise neutrino reconstruction has not yet been established in the $H \to \tau\tau$ analysis, and therefore several alternative methods are proposed to reconstruct the acoplanarity angle according to the di-τ lepton decay mode [135–143]. This analysis uses two typical methods for the $\pi^{\pm}\,\pi^{\mp}$ and $\rho^{\pm}\,\rho^{\mp}$ decay modes, referred to as the impact parameter and the $\rho \to \pi^{\pm}\pi^{0}$ decay plane method, respectively.

Impact Parameter Method

The main target of the impact parameter method [135–138] is the $\tau^{\pm}\tau^{\mp} \to \pi^{\pm}\pi^{\mp}$ decay mode, which has 2.8% branching fraction in the $H \to \tau_{\text{had}}\tau_{\text{had}}$ channel. The method constructs three types of CP sensitive angles using pseudo planes of the $\tau^{\pm} \to \pi^{\pm}\nu_{\tau}$ decay, where neutrino directions are approximated from the primary vertex and impact parameter information. The reconstruction procedure of three angles is as follows:

The first angle $\phi_{\text{IP}}^{\text{lab}}$ is defined as:

$$\phi_{IP}^{lab.} = \arccos(\boldsymbol{n}_{\text{lab.}}^{+} \cdot \boldsymbol{n}_{\text{lab.}}^{-}), \tag{5.5}$$

where $\boldsymbol{n}_{\text{lab.}}^{\pm}$ are impact parameter vectors. The impact parameter vector is defined as the perpendicular vector to the $\pi^{\pm}$ vector from the primary vertex position, illustrated in Fig. 5.6.

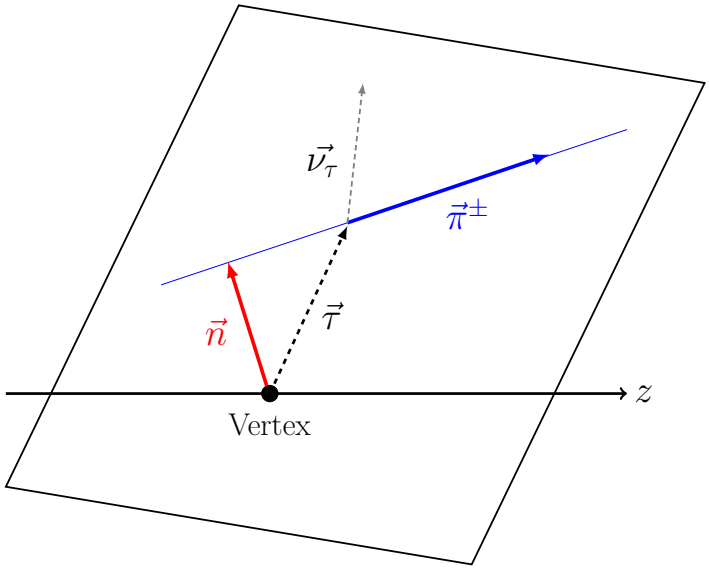

Fig. 5.6: Schematic diagram of the definition of the impact parameter vector $\boldsymbol{n}_{\text{lab.}}^{\pm}$, where the z axis is defined as the proton beam direction The impact parameter vector $\vec{n}$ is defined as the perpendicular vector from the primary vertex position to the $\pi^{\pm}$ vector.

The second angle is ϕ_{IP}, which is defined as:

$$\phi_{\text{IP}} = \arccos\left(\frac{\boldsymbol{n}_{\perp}^{+} \cdot \boldsymbol{n}_{\perp}^{-}}{|\boldsymbol{n}_{\perp}^{+}||\boldsymbol{n}_{\perp}^{-}|} \right), \tag{5.6}$$

where $\boldsymbol{n}_{\perp}^{\pm}$ are perpendicular components of impact parameter vectors in the $\pi^{+}\pi^{-}$ rest frame. The impact parameter vectors defined in laboratory frame are boosted into the rest frame using measured $\pi^{\pm}$ four-momenta ($\boldsymbol{n}_{\text{lab.}}^{\pm} \to \boldsymbol{n}^{\pm}$). Then, the $\boldsymbol{n}^{\pm}$ is decomposed into parallel ($\boldsymbol{n}_{\parallel}^{\pm}$) and perpendicular ($\boldsymbol{n}_{\perp}^{\pm}$)

components to each $\boldsymbol{p}^{\pm}$, expressed by:

$$\boldsymbol{n}^{\pm} = r_{\perp} \cdot \boldsymbol{n}_{\perp}^{\pm} + r_{\parallel} \cdot \boldsymbol{n}_{\parallel}^{\pm}, \tag{5.7}$$

where $r_{\parallel}$ and $r_{\perp}$ are fractions of parallel and perpendicular components, respectively. The $\boldsymbol{n}_{\parallel}^{\pm}$ and $\boldsymbol{n}_{\perp}^{\pm}$ are unit vectors.

The third angle is ψ_{IP}, which is defined as:

$$\psi_{\text{IP}} = \arccos(\boldsymbol{p}^{-} \cdot (\boldsymbol{n}_{\perp}^{+} \times \boldsymbol{n}_{\perp}^{-})), \tag{5.8}$$

where $\boldsymbol{p}^{-}$ represents the unit vector of the π^{-} direction. The ψ_{IP} variable is especially sensitive to the CP mixing state of the Higgs boson because it includes CP-odd and T-odd triple correlations [135].

Figure 5.7 shows the $\phi_{\text{IP}}^{\text{lab}}$ and ϕ_{IP} distributions for the $\tau^{\pm}\tau^{\mp} \to \pi^{\pm}\pi^{\mp}$ and the $\tau^{\pm}\tau^{\mp} \to \ell^{\pm}\pi^{\mp}$ decay from the ggF $H \to \tau\tau$ process. The impact parameter method focuses on the $\tau^{\pm}\tau^{\mp} \to \pi^{\pm}\pi^{\mp}$ decay mode, while these angles can be also reconstructed in the $\tau^{\pm}\tau^{\mp} \to \ell^{\pm}\pi^{\mp}$ decay mode by replacing the $\pi^{\pm}$ vector with the $\ell^{\pm}$ vector. The $\phi_{\text{IP}}^{\text{lab}}$ distributions of the Z boson in Fig. 5.7 (a) and (c) have the tendency to be close to the distribution of the CP-even Higgs boson. This is due to the spin correlation of $Z \to \tau\tau$ process as the following: The spin directions of di-τ leptons are the same due to the Z boson spin of 1. In the $\tau^{\pm}\tau^{\mp} \to \pi^{\pm}\pi^{\mp}$ decay, pions are emitted in the τ spin direction because of the left-handed nature of the neutrino. Hence, the impact parameter vectors tend to have the opposite directions i.e. $\phi_{\text{IP}}^{\text{lab}}$ tends to be a large angle. On the other hand, in the $\ell^{\pm}\pi^{\mp}$ decay, the tendency is opposite due to the presence of two neutrinos in the leptonic decay. The ϕ_{IP} gives more sensitivity than the $\phi_{\text{IP}}^{\text{lab}}$ and the flat distribution of the Z boson thanks to moving from the laboratory frame to the π^{+} π^{-} rest frame. In order to discriminate the CP-even and CP-odd Higgs boson, the ϕ_{IP} variable is mainly used in this analysis. The ψ_{IP} is dedicated to distinguish the CP mixing Higgs boson as shown in Fig. 5.11 (see Section 5.3.1), so that this variable is useful to a CP mixing measurement in future analysis.

$\tau^{\pm}\tau^{\mp} \to \rho^{\pm}\rho^{\mp}$ decay plane Method

The main target of this method [139–142] is the $\tau^{\pm}\tau^{\mp} \to \rho^{\pm}\rho^{\mp}$ decay mode, which has 16.0% branching fraction in the $H \to \tau_{\text{had}}\tau_{\text{had}}$ channel. In this decay mode, the neutrino has relatively small momentum compared with other decay modes due to the ρ meson mass of $\sim$ 770 MeV. Therefore, the ρ^{+} ρ^{-} rest frame is useful to approximate the τ^{+} τ^{-} rest frame. As discussed in Section 1.2.4, a ρ meson decays into detectable particles: one charged pion and one neutral pion. The approximated acoplanarity angle ϕ_{ρ} [139] is defined as an angle between the ρ^{+}-π^{+} plane and the ρ^{-}-π^{-} plane, expressed by:

$$\phi_{\rho} = \arccos\Big(\frac{\boldsymbol{n}^{+} \cdot \boldsymbol{n}^{-}}{|\boldsymbol{n}^{+}||\boldsymbol{n}^{-}|} \Big), \tag{5.9}$$

$$\boldsymbol{n}^{\pm} = \boldsymbol{p}_{\pi^{\pm}} \times \boldsymbol{p}_{\pi^{0}}, \tag{5.10}$$

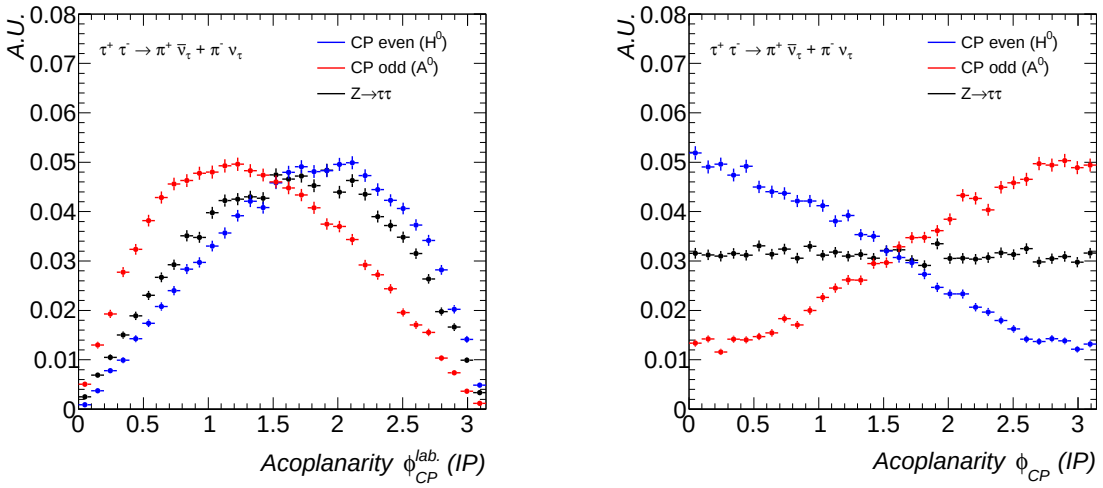

(a) (b)

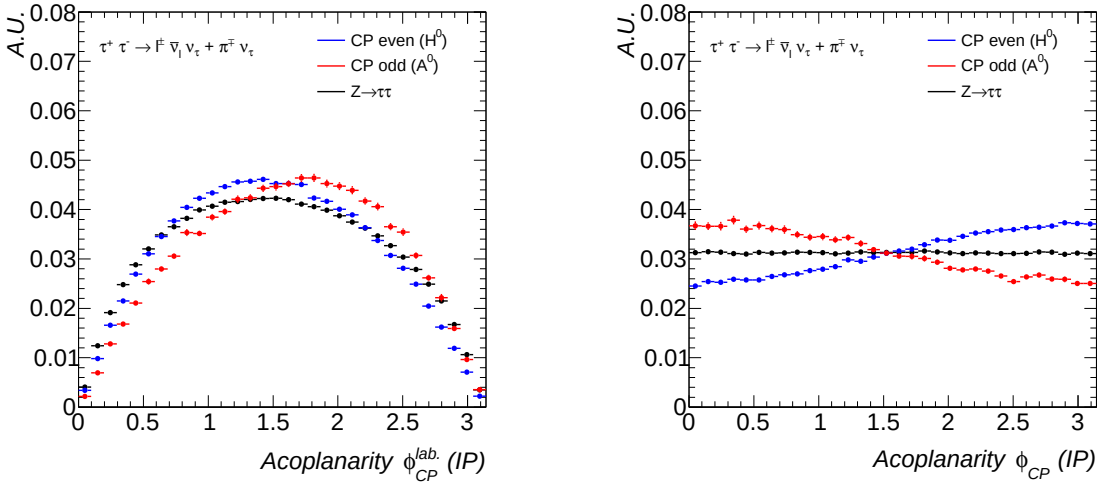

(c) (d)

Fig. 5.7: The $\phi_{\mathrm{IP}}^{\mathrm{lab}}$ and ϕ_{IP} angle distributions reconstructed by the impact parameter method, for the (a,b) $\tau^{\pm}\tau^{\mp} \to \pi^{\pm}\pi^{\mp}$ and the (c,d) $\tau^{\pm}\tau^{\mp} \to \ell^{\pm}\pi^{\mp}$ decay modes from the CP-even (blue), CP-odd (red) Higgs boson and the Z boson (black), where the Higgs boson is produced from the ggF process with a mass of 125 GeV.

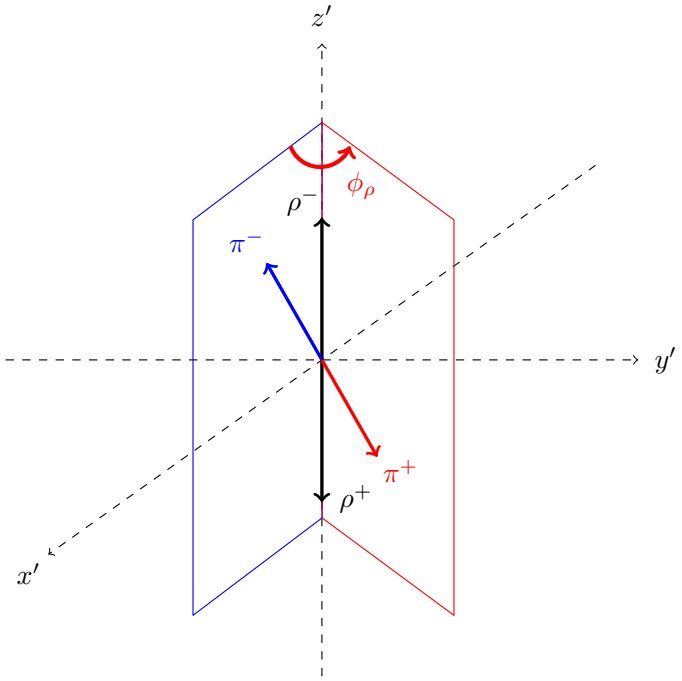

Fig. 5.8: Definition of the acoplanarity angle ϕ_ρ. The z' axis is defined as the ρ meson direction in the ρ^+-ρ^- rest frame, The x', y' axes are defined as horizontal and vertical axes in the transverse plane with respect to the z' axis, respectively. The ϕ_ρ is defined as the angle between the $\rho \to \pi^\pm\pi^0$ decay planes.

where $\boldsymbol{p}_{\pi^\pm}$ and $\boldsymbol{p}_{\pi^0}$ are momentum vectors of $\pi^\pm$ and π^0, respectively. The definition of ϕ_ρ is illustrated in Fig. 5.8, and it takes the range of $[0, 2\pi]$. The $\pi^\pm$ $\rho^\mp$ is also folded into 2π around π by the same procedure with the equation (5.3).

If a spin correlation in the $\tau^\pm \to \rho^\pm \left(\to \pi^\pm\pi^0\right) \nu_\tau$ decay is not taken into account, this variable has no sensitivity to the CP state of the Higgs boson. In order to cope with this, a charged energy asymmetry ($y^\pm$) variable, which reflects to the spin correlation, is defined as the following:

$$y^\pm = \frac{E_{\pi^\pm} - E_{\pi^0}}{E_{\pi^\pm} + E_{\pi^0}}, \tag{5.11}$$

where $E_{\pi^\pm}$ and E_{π^0} are energies of the $\pi^\pm$ and the π^0, respectively. According to a product of charged energy asymmetries ($y_1 \times y_2$), the ϕ_ρ distributions with $y_1 \times y_2 > 0$ and $y_1 \times y_2 < 0$ are shown as Figure 5.9 for the $\tau^\pm\tau^\mp \to \rho^\pm\rho^\mp$ decay mode from the CP-even and CP-odd Higgs boson and the Z boson. In order to deal with the effect, the ϕ_ρ angle is re-defined as the following:

$$\phi_\rho = \begin{cases} \phi_\rho & (y^+ \times y^- > 0) \\ \pi - \phi_\rho - \pi & (y^+ \times y^- < 0). \end{cases} \tag{5.12}$$

(5.13)

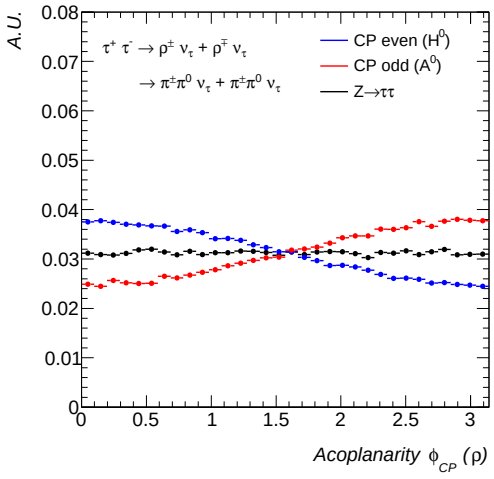

(a) ϕ_ρ angle ($y_1 \times y_2 > 0$)

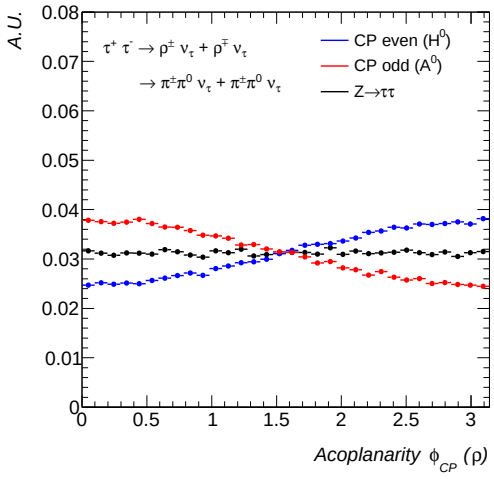

(b) ϕ_ρ angle ($y_1 \times y_2 < 0$)

Fig. 5.9: The ϕ_ρ angle distributions with $y_1 \times y_2 > 0$ (a) and with $y_1 \times y_2 < 0$ (b) for the $\tau^\pm\tau^\mp \to \rho^\pm\rho^\mp$ decay mode from the CP-even (blue) and CP-odd (red) Higgs boson and the Z boson (black), where the Higgs boson is produced from the ggF process with a mass of 125 GeV.

Mixture Method

In order to cover one of the remaining decay mode of $\tau^\pm\tau^\mp \to \pi^\pm\rho^\mp$, which has non-negligible branching fraction of 13.6% in the $H \to \tau_{\text{had}}\tau_{\text{had}}$ channel, an another acoplanarity angle $\phi_{\text{IP-}\rho}$ is reconstructed by mixing the impact parameter method and the $\rho \to \pi^\pm\pi^0$ decay plane method. The definition is expressed by:

$$\phi_\rho = \arccos\left(\frac{\boldsymbol{n}_{\text{IP}} \cdot \boldsymbol{n}_\rho}{|\boldsymbol{n}_{\text{IP}}||\boldsymbol{n}_\rho|} \right), \tag{5.14}$$

where $\boldsymbol{n}_{\text{IP}}$ is the cross product vector of the impact parameter vector and the $\pi^\pm$ momentum vector, and $\boldsymbol{n}_\rho$ is the cross product vector of $\pi^\pm$ and π^0 momentum vectors. The $\phi_{\text{IP-}\rho}$ is also folded into 2π around π by the same procedure with the equation (5.3).

This method also needs to take into account the effect of the spin correlation of the $\tau^\pm \to \rho^\pm \left(\to \pi^\pm\pi^0\right) \nu_\tau$ decay, and the acoplanarity angle is classified corresponding to the sign of the charge asymmetry y as the following:

$$\phi_{\text{IP-}\rho} = \begin{cases} \phi_{\text{IP-}\rho} & (y < 0) \\ \pi - \phi_{\text{IP-}\rho} & (y > 0) \end{cases} \qquad y = \frac{E_{\pi^\pm} - E_{\pi^0}}{E_{\pi^\pm} - E_{\pi^0}}. \tag{5.15}$$

Figure 5.10 shows the $\phi_{\text{IP-}\rho}$ distributions with $y > 0$ and $y < 0$ for the $\tau^\pm\tau^\mp \to \pi^\pm\rho^\mp$ decay mode from

the CP-even, CP-odd Higgs boson and the Z boson.

The approximated acoplanarity angles are used as discriminant variables in this analysis, according to the di-τ lepton decay mode. The separation ability of the impact parameter method is equivalent to Fig. 5.5 because the method indirectly uses the same neutrino information using the impact parameter vector. The separation ability of the $\rho \to \pi^{\pm}\pi^{0}$ decay plane and the mixture methods are inferior to the impact parameter method because these methods ignore neutrinos in the reconstruction of the $\tau^{\pm} \to \rho^{\pm}\left(\to \pi^{\pm}\pi^{0}\right)\nu_{\tau}$ decay plane. The reconstruction method for each decay mode with its branching ratio is summarized in Table 5.2.

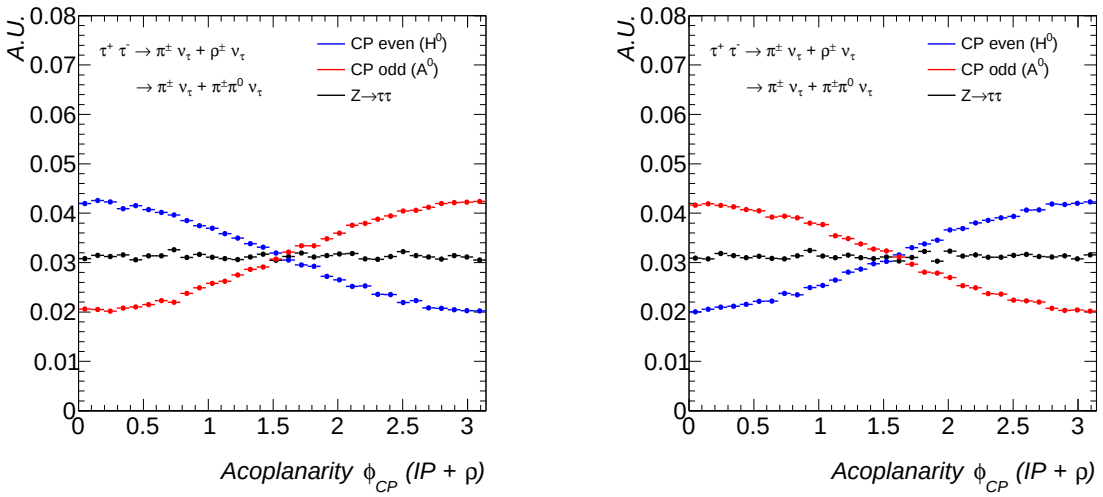

(a) $\phi_{\text{IP-}\rho}$ angle ($y < 0$) (b) $\phi_{\text{IP-}\rho}$ angle ($y > 0$)

Fig. 5.10: The $\phi_{\text{IP-}\rho}$ angle distributions with $y < 0$ (a) and with $y > 0$ (b) or the $\tau^{\pm}\tau^{\mp} \to \pi^{\pm}\rho^{\mp}$ decay mode from the CP-even (blue) and CP-odd (red) Higgs boson and the Z boson (black), where the Higgs boson is produced from the ggF process with a mass of 125 GeV.

Decay	Method	B.R.
$H \to \tau_{\text{had}}\tau_{\text{had}}$		42.0%
$\tau^{\pm}\tau^{\mp} \to \pi^{\pm}\pi^{\mp}$	Impact Parameter	1.2%
$\tau^{\pm}\tau^{\mp} \to \rho^{\pm}\rho^{\mp}$	$\rho \to \pi^{\pm}\pi^{0}$ decay plane	6.5%
$\tau^{\pm}\tau^{\mp} \to \pi^{\pm}\rho^{\mp}$	Mixture	5.5%
$H \to \tau_{\ell}\tau_{\text{had}}$		45.6%
$\tau^{\pm}\tau^{\mp} \to \ell^{\pm}\pi^{\mp}$	Impact Parameter	7.6%

Table 5.2: Summary of the reconstruction method for each decay mode with its branching ratio.

5.3 Event Selection and Observable Reconstruction

The CP state of the Higgs boson can be clearly classified by acoplanarity angles using the generator information. However, these angles are smeared after the ATLAS detector simulation due to resolutions of objects, the primary vertex and impact parameters. This section describes reconstruction procedures of approximated acoplanarity angles.

5.3.1 Simulation of the CB-odd Higgs Boson Sample

The CP-odd Higgs samples after the ATLAS detector simulation are prepared by the SM (CP-even) Higgs samples, which are used in the $H \to \tau\tau$ search, with `TauSpinner` program [144, 145]. The `TauSpinner` program is able to modify τ spin effects in a process that an intermediate state decays into final states including τ leptons. The generator information of τ lepton kinematics in the CP-even Higgs samples is necessary to reconstruct the information of τ lepton polarizations and spin correlations in this program. This program provides event-by-event weights corresponding to required spin effects based on the input information, and it allows to model spin correlations of the pseudo-scalar or mixing state Higgs boson by changing the mixing angle α. The CP-even and CP-odd Higgs boson correspond to $\alpha = 0.0$ and $\alpha = 1.0$, respectively. Figure 5.11 shows the ϕ_{IP} and ψ_{IP} distributions for the Z boson and the weighted CP-even sample modified the mixing angle from 0.0 to 1.0.

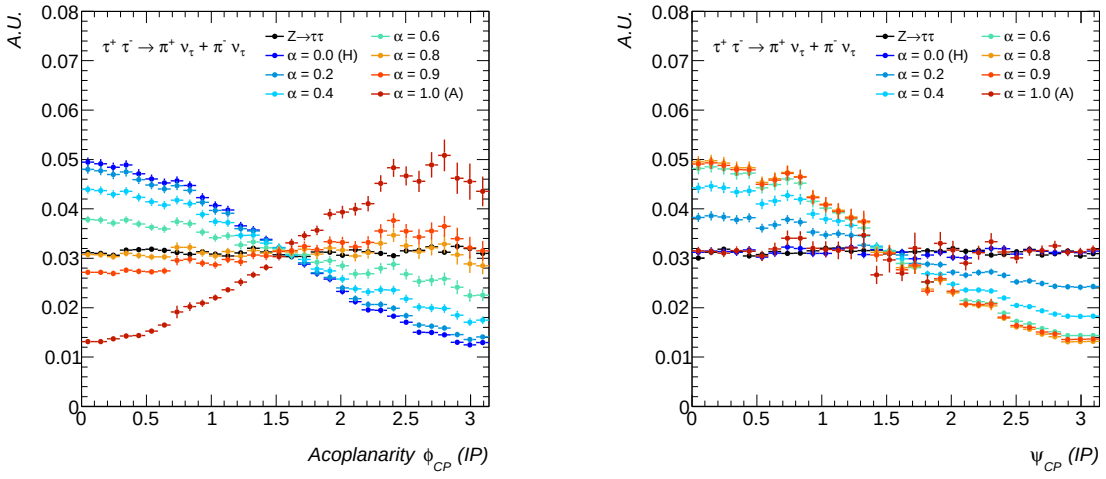

(a) ϕ_{IP} angle

(b) ψ_{IP} angle

Fig. 5.11: The ϕ_{IP} (a) and ψ_{IP} (b) distributions from the Z boson (black dot) and the weighted Higgs boson (colored dots) samples for the $\tau^{\pm}\tau^{\mp} \to \pi^{\pm}\pi^{\mp}$ decay mode, where the Higgs boson is produced from the ggF process with a mass of 125 GeV. The mixing angle is modified from 0.0 to 1.0, and the CP-even (-odd) Higgs boson corresponds to $\alpha = 0.0(1.0)$.

The important advantage of this weighting method is that a desired sample can be prepared without the ATLAS detector simulation which generally consumes a large amount of time. Figure 5.12 shows a

comparison on acoplanarity angles between truth samples and weighted samples, demonstrating a correct performance of the weighting method. A relatively large statistical uncertainty around $\phi_{\mathrm{CP}} \sim \pi$ is due to small statistics with relatively large weights. The `TauSpinner` weighted SM Higgs boson samples are used as the CP-odd Higgs boson samples in this analysis.

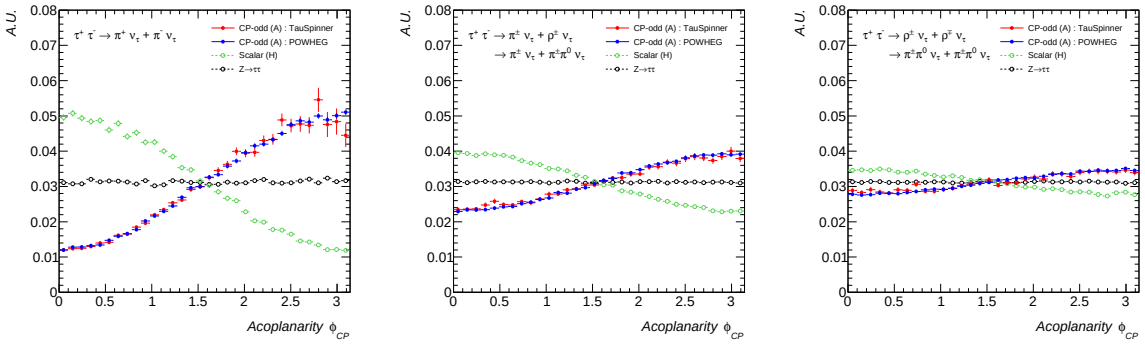

(a) (b) (c)

Fig. 5.12: Comparison between the truth (blue dot) and `TauSpinner` weighed (red dot) CP-odd Higgs boson samples on the ϕ_{CP} distribution for the $\pi^{\pm}\,\pi^{\mp}$ (a), $\pi^{\pm}\,\rho^{\mp}$ (b) and $\rho^{\pm}\,\rho^{\mp}$ (c) decay modes, where the Higgs boson is produced from the ggF process with a mass of 125 GeV. Distributions from the CP-even Higgs boson (green circle) and the Z boson (black circle) are also shown.

5.3.2 Event Selection and Categorization

The event selection and categorization are summarized in Section 4.4 and Section 5.1 for the $H \to \tau_{\ell}\tau_{\mathrm{had}}$ and $H \to \tau_{\mathrm{had}}\tau_{\mathrm{had}}$ channels, respectively. In addition, the τ_{had} decay classification based on the π^0 reconstruction is performed because the acoplanarity angle is reconstructed for each τ lepton decay modes. As described in Section 3.4, the π^0 reconstruction [54] is used in the BDTs of the τ_{had} identification. Events are classified into $N_{\pi^0} = 0$ or 1 or ≥ 2 using two dedicated BDTs, and it allows to classify 1-prong τ_{had} into the $\pi^{\pm}\,\pi^{\mp}$, $\pi^{\pm}\,\rho^{\mp}$ and $\rho^{\pm}\,\rho^{\mp}$ decay modes. Figure 5.13 shows the number of π^0 distribution of 1-prong τ_{had}s and jets, and identification and misidentification efficiencies of the N_{π^0} reconstruction in the form of a matrix. Although the π^0 reconstruction has a high performance for the discrimination between $N_{\pi^0} = 0$ and $N_{\pi^0} > 0$, the large migration between $N_{\pi^0} = 1$ and $N_{\pi^0} = 2$ can be seen in the matrix. A significant loss of the true decay mode of $N_{\pi^0} = 1$ can be expected due to the migration, so that the τ_{had} decay is classify into $N_{\pi^0} = 0$ and $N_{\pi^0} > 0$ in this analysis.

Total four decay channels are defined as $\pi^{\pm}\,\pi^{\mp}$, $\pi^{\pm}\,\rho^{\mp}$,$\rho^{\pm}\,\rho^{\mp}$ and $\ell^{\pm}\tau_{\mathrm{had}}^{\mp}$ channels, where the $\ell^{\pm}\tau_{\mathrm{had}}^{\mp}$ channel is treated as one decay mode. Events with 3-prong τ_{had}s are discarded because they have no discrimination abilities in their acoplanarity angles. The π^0 four-momentum is determined from the cluster information in the π^0 reconstruction algorithm (see Section 3.4) with a mass value of 134.98 MeV, while the $\pi^{\pm}$ four-momentum and its impact parameters are obtained from τ_{had} associated tracks with a mass value of 139.57 MeV [15]. The primary vertex is determined by requiring to have largest $\sum(p_{\mathrm{T}}^{\mathrm{track}})^2$.

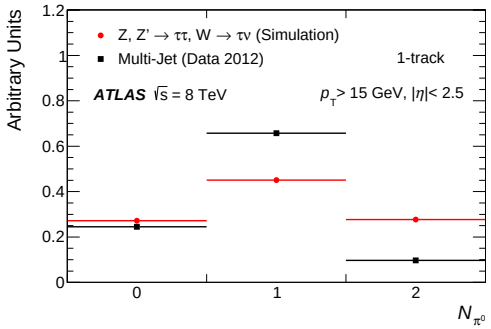

(a)

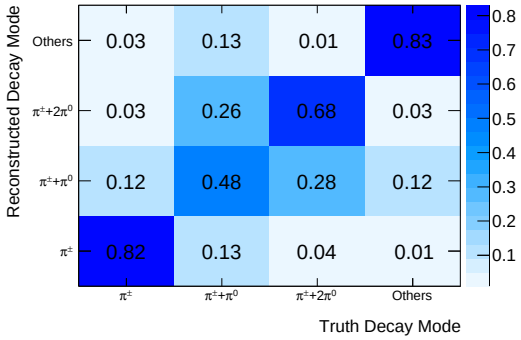

(b)

Fig. 5.13: The number of π^0 distribution (a) for signal (red) and background (black) events, where a reconstructed τ_{had} candidate is required to have 1-prong, $p_{\text{T}} > 15$ GeV and $|\eta| < 2.5$. The signal of a τ lepton is obtained from simulated $Z/Z^{'} \rightarrow \tau\tau$ and $W \rightarrow \tau\nu_{\tau}$ events, while the background of a jet is from the data sample collected by jet triggers. Probability matrix (b) of true and reconstructed decay modes of τ leptons with $p_{\text{T}} > 15$ GeV and $|\eta| < 2.5$, which are obtained from simulated $Z \rightarrow \tau\tau$ events.

Moreover, an additional selection, that events are required to be in three highest bins of the BDT output distribution, is applied for both the VBF and Boosted categories in order to enhance the signal over background ratio and to keep reasonable statistics.

After the event selection and categorization, the background estimation is performed for each decay channel. Table 5.3 and 5.4 show predicted event yields in the four decay channels for the VBF and Boosted categories. For signal, the number of events is estimated by SM (CP-even) Higgs signal samples, then the number is scaled by the measured signal strength of $\mu = 1.4$ (see Section 4.9.3). Normalizations of the CP-even and CP-odd signal events are adjusted with the quoted numbers in the table. The number of events used in this analysis is quite limited due to additional selections of τ_{had} decay classification and the cut on the BDT distribution, while the signal over background ratio is significantly increased from the preselection. The acoplanarity angles are reconstructed as discriminant variables based on the decay channels and the yields.

Process/Channel	$\pi^{\pm}\,\pi^{\mp}$	$\pi^{\pm}\,\rho^{\mp}$	$\rho^{\pm}\,\rho^{\mp}$	$\ell^{\pm}\tau_{\text{had}}^{\mp}$
Fake τ_{had}	< 0.1	2.1 ± 0.24	1.9 ± 0.22	1.1 ± 0.12
$Z \to \tau\tau$	1.9 ± 0.15	3.7 ± 0.46	5.4 ± 0.67	6.8 ± 0.81
Others	0.12 ± 0.04	1.3 ± 0.06	2.8 ± 0.14	3.7 ± 3.0
ggF ($m_H = 125$ GeV)	0.36 ± 0.12	0.97 ± 0.35	0.93 ± 0.34	0.75 ± 0.3
VBF	0.73 ± 0.18	2.1 ± 0.54	2.2 ± 0.56	1.7 ± 0.41
WH	< 0.1	< 0.1	< 0.1	< 0.1
ZH	< 0.1	< 0.1	< 0.1	< 0.1
Total background	2.0 ± 1.6	7.1 ± 2.9	10.1 ± 3.1	11.6 ± 3.7
Total signal	1.1 ± 1.0	3.1 ± 2.0	3.1 ± 1.9	2.5 ± 1.9

Table 5.3: Predicted event yields for VBF category in the $\pi^{\pm}\,\pi^{\mp}$, $\pi^{\pm}\,\rho^{\mp}$, $\rho^{\pm}\,\rho^{\mp}$ and $\ell^{\pm}\tau_{\text{had}}^{\mp}$ channels, assuming the data in 8 TeV with an integrated luminosity of 20.3 fb^{-1}. For signal, the quoted numbers are estimated by CP-even Higgs signal events with the measured signal strength of $\mu = 1.4$. The quoted uncertainties on the individual background and signal components represent only systematic uncertainties, while the total background and the total signal represent full statistical and systematic uncertainties.

Process/Channel	$\pi^{\pm}\,\pi^{\mp}$	$\pi^{\pm}\,\rho^{\mp}$	$\rho^{\pm}\,\rho^{\mp}$	$\ell^{\pm}\tau_{\text{had}}^{\mp}$
Fake τ_{had}	8.3 ± 0.1	17.1 ± 2.0	24.1 ± 2.8	3.8 ± 0.4
$Z \to \tau\tau$	39.2 ± 4.9	61.3 ± 7.7	110.0 ± 14.1	45.3 ± 3.6
Others	< 0.1	< 0.1	< 0.10	26.0 ± 9.1
ggF ($m_H = 125$ GeV)	1.4 ± 0.52	3.9 ± 1.4	4.5 ± 1.6	2.7 ± 0.96
VBF	0.43 ± 0.11	1.3 ± 0.33	1.4 ± 0.36	1.4 ± 0.36
WH	0.30 ± 0.08	0.87 ± 0.23	0.84 ± 0.22	0.73 ± 0.22
ZH	0.18 ± 0.05	0.45 ± 0.12	0.55 ± 0.15	0.34 ± 0.09
Total background	47.5 ± 7.6	78.4 ± 11.3	134.1 ± 42.7	75.1 ± 24.1
Total signal	2.3 ± 2.2	6.5 ± 2.8	7.3 ± 3.4	5.2 ± 2.6

Table 5.4: Predicted event yields for Boosted category in the $\pi^{\pm}\,\pi^{\mp}$, $\pi^{\pm}\,\rho^{\mp}$, $\rho^{\pm}\,\rho^{\mp}$ and $\ell^{\pm}\tau_{\text{had}}^{\mp}$ channels, assuming the data in 8 TeV with an integrated luminosity of 20.3 fb^{-1}. For signal, the quoted numbers are estimated by CP-even Higgs signal events with the measured signal strength of $\mu = 1.4$. The quoted uncertainties on the individual background and signal components represent only systematic uncertainties, while the total background and the total signal represent full statistical and systematic uncertainties.

5.3.3 Observable Reconstruction

The three different methods described in Section 5.2 are applied to reconstruct acoplanarity angles according to the decay channels. The impact parameter method is applied for the $\pi^{\pm}$ $\pi^{\mp}$ and $\ell^{\pm}\tau^{\mp}_{\text{had}}$ channels, while the $\rho \to \pi^{\pm}\pi^{0}$ decay plane method and the mixture method are applied for $\rho^{\pm}$ $\rho^{\mp}$ and $\pi^{\pm}$ $\rho^{\mp}$ channels, respectively. Figure 5.14 shows reconstructed and truth acoplanarity distributions for each decay channel, where events are required to pass the preselection. In the remainder of this analysis, the preselection is the event selection before the categorization, listed in 5.1 and 4.3 for the $H \to \tau_{\text{had}}\tau_{\text{had}}$ and the $H \to \tau_{\ell}\tau_{\text{had}}$ analysis, respectively. Significant decreases of the discrimination ability of reconstructed distributions can be seen for all categories compared to truth distributions.

For the impact parameter method, the reason of this behavior is resolutions of the primary vertex position and impact parameters. Figure 5.15 shows the resolution of the primary vertex position, indicating the most significant source is the resolution of z position with its RMS of ~ 0.2 mm. The z_0 resolution gives more effects to the acoplanarity angle than the d_0 resolution. For the $\rho \to \pi^{\pm}\pi^{0}$ decay plane method, the smearing source is the migration between $N_{\pi^0} = 1$ and $N_{\pi^0} > 1$. While the dedicate π^0 reconstruction algorithm is applied, the $\rho^{\pm}$ $\rho^{\mp}$ decay channel contains both events with $N_{\pi^0} = 1$ and $N_{\pi^0} > 1$. The π^0 four-momentum is defined as the vector sum of all π^0s in case of events with $N_{\pi^0} > 1$, which is not perfectly matched with the assumption of the $\rho \to \pi^{\pm}\pi^{0}$ decay plane method. For the mixture method, the smearing comes from the convolution of both sources.

Although the acoplanarity angles are smeared after the reconstruction, they still have an ability to distinguish the CP-even from CP-odd Higgs boson. Figure 5.16 and Figure 5.17 shows acoplanarity distributions for the CP-even and CP-odd signals and all background processes after event selections and categorizations, which are final discriminates of the analysis. The distributions are divided into two bins considering the statistics.

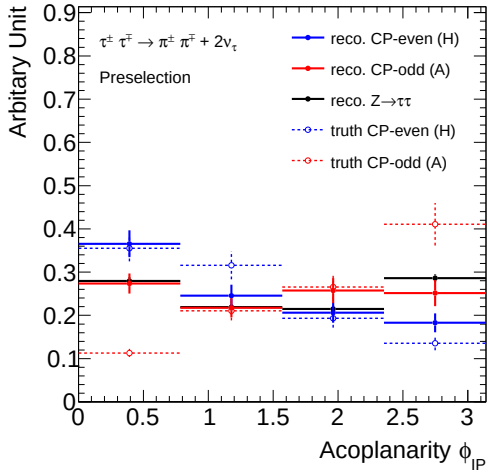

(a) $\pi^{\pm}\,\pi^{\mp}$

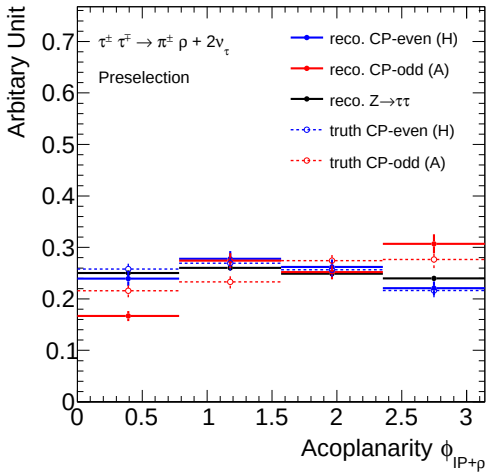

(b) $\pi^{\pm}\,\rho^{\mp}$

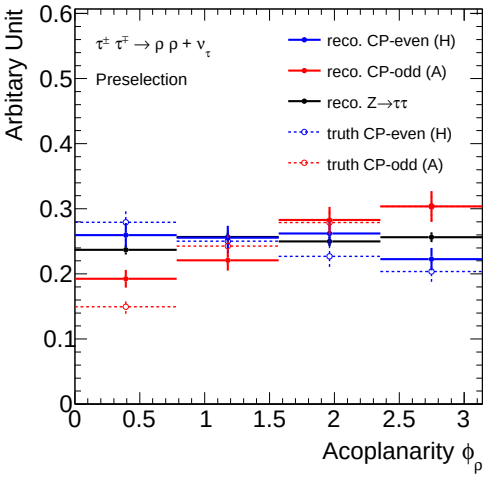

(c) $\rho^{\pm}\,\rho^{\mp}$

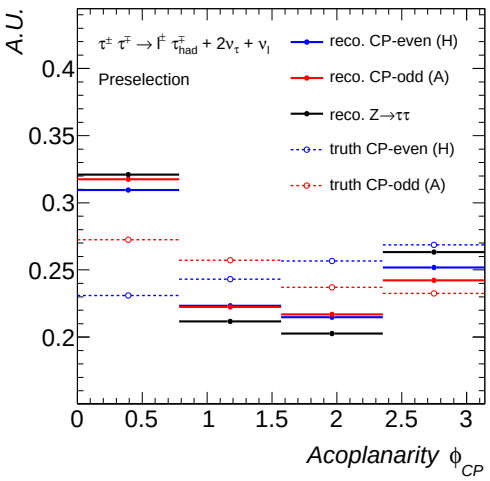

(d) $\ell^{\pm}\tau^{\mp}_{\text{had}}$

Fig. 5.14: Reconstructed acoplanarity ϕ_{CP} distributions after the preselection for the (a) $\pi^{\pm}\,\pi^{\mp}$, (b) $\pi^{\pm}\,\rho^{\mp}$, (c) $\rho^{\pm}\,\rho^{\mp}$ and (d) $\ell^{\pm}\tau^{\mp}_{\text{had}}$ decay modes from CP-even, CP-odd Higgs boson (red,blue) and the Z boson (black) production processes. Truth distributions for the CP-even and CP-odd Higgs boson after the preselection are also shown as dashed line. The Higgs boson production process is the ggF process, and the Higgs boson mass is set to 125 GeV.

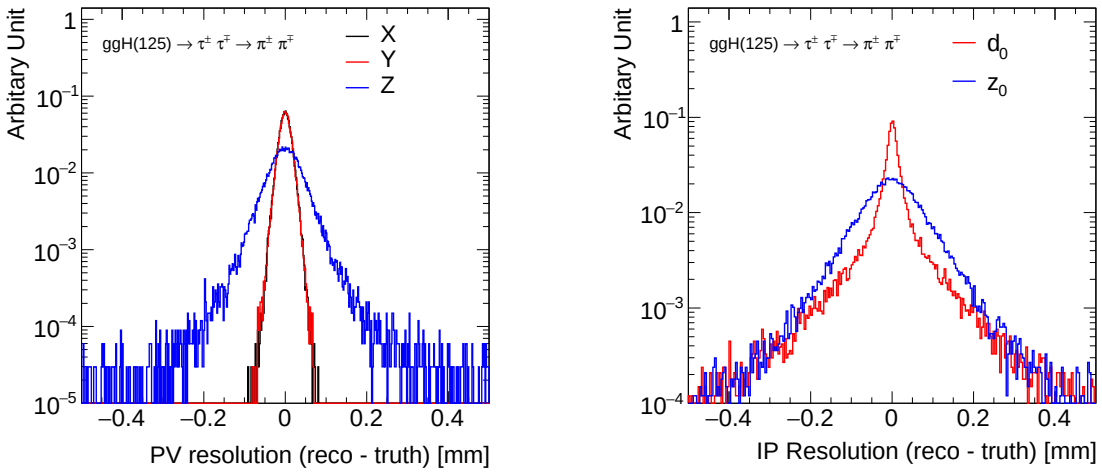

(a) primary vertex

(b) impact parameters

Fig. 5.15: The resolution of the reconstructed primary vertex position (a) for x (black), y (red) and z (blue) coordinates, and the resolution of $\pi^{\pm}$ track impact parameters (b) for d_0 (red) and z_0 (blue), for simulated $H \to \tau_{\text{had}}\tau_{\text{had}}$ events with the Higgs boson mass of 125 GeV.

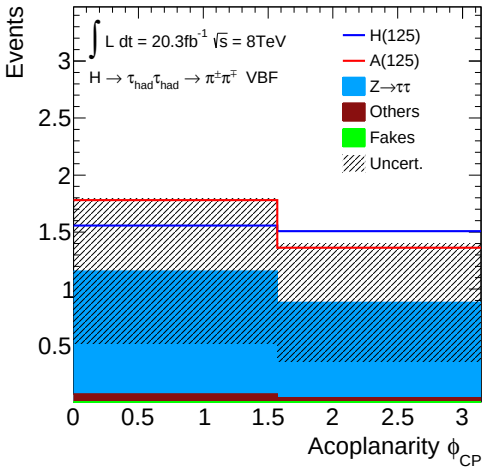

(a) $\pi^{\pm}\,\pi^{\mp}$

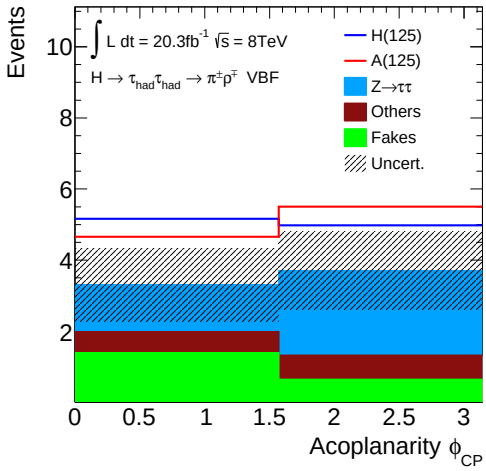

(b) $\pi^{\pm}\,\rho^{\mp}$

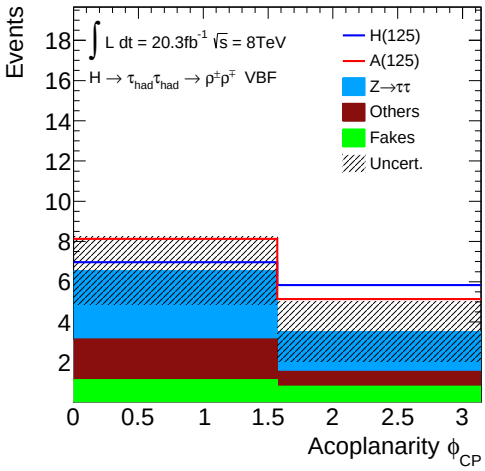

(c) $\rho^{\pm}\,\rho^{\mp}$

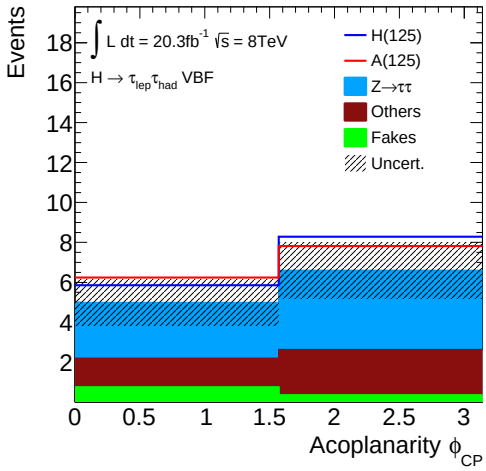

(d) $\ell^{\pm}\tau_{\mathrm{had}}^{\mp}$

Fig. 5.16: The acoplanarity distributions for $\pi^{\pm}\,\pi^{\mp}$ (a), $\pi^{\pm}\,\rho^{\mp}$ (b), $\rho^{\pm}\,\rho^{\mp}$ (c) and $\ell^{\pm}\tau_{\mathrm{had}}^{\mp}$ (d) classifications in the VBF category. The blue and red line shows CP-even and CP-odd Higgs distributions, respectively. The black line represents the $Z \to \tau\tau$ background distribution.

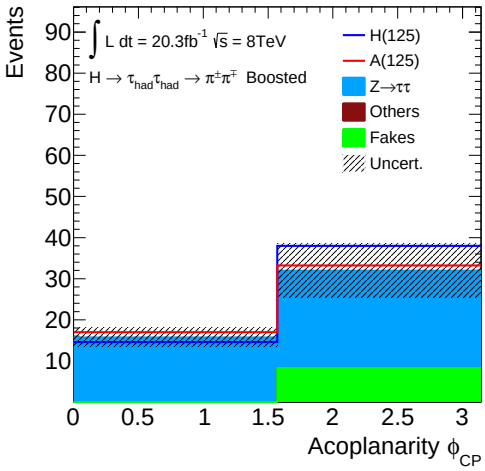

(a) $\pi^{\pm}\ \pi^{\mp}$

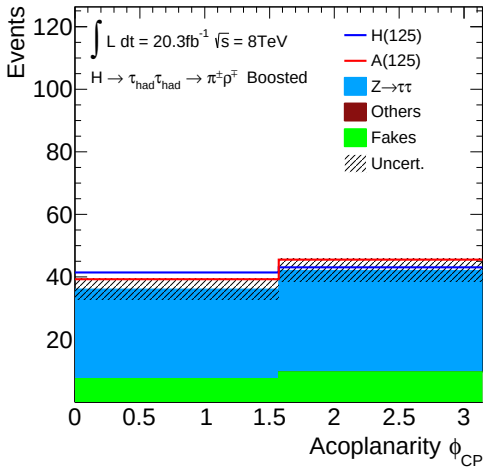

(b) $\pi^{\pm}\ \rho^{\mp}$

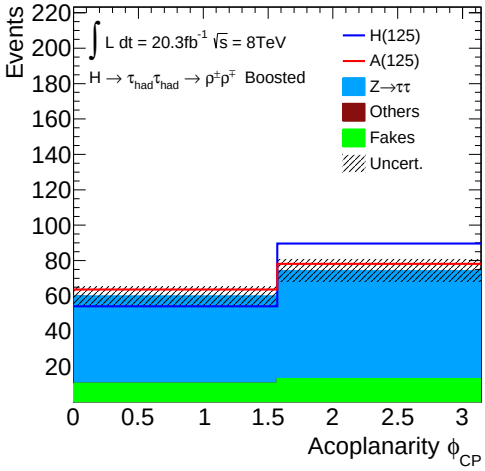

(c) $\rho^{\pm}\ \rho^{\mp}$

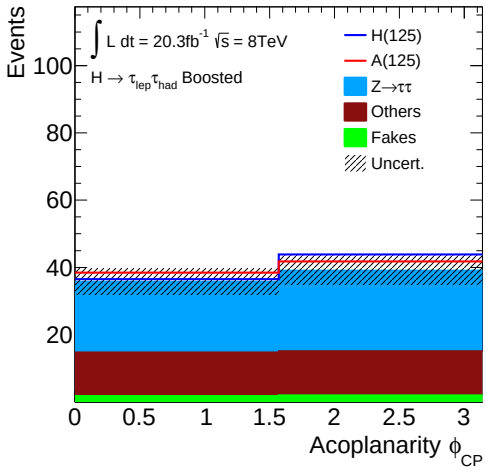

(d) $\ell^{\pm}\tau_{\text{had}}^{\mp}$

Fig. 5.17: The acoplanarity distributions for $\pi^{\pm}\ \pi^{\mp}$ (a), $\pi^{\pm}\ \rho^{\mp}$ (b), $\rho^{\pm}\ \rho^{\mp}$ (c) and $\ell^{\pm}\tau_{\text{had}}^{\mp}$ (d) classifications in the Boosted category. The blue and red line shows CP-even and CP-odd Higgs distributions, respectively. The black line represents the $Z \to \tau\tau$ background distribution.

5.4 Systematic Uncertainties

The systematic uncertainties for the $H \to \tau_\ell \tau_{\text{had}}$ channel are already summarized in the Section 4.8. For the $H \to \tau_{\text{had}} \tau_{\text{had}}$ channel, the sources of the systematic uncertainties are basically the same as the $H \to \tau_\ell \tau_{\text{had}}$ channel, while the uncertainty related to electron and muon are not needed and the uncertainty on the di-tau trigger is assigned, which is the order of $(8 \sim 9\%)$. In addition, the Fake Factor uncertainty is replaced to the uncertainty on the template fit for the multi-jet event estimation. The uncertainty is evaluated by the template fit with alternative template derived from a sample where the τ_{had} candidates fail just the opposite-sign charge requirement. The alternative template gives a different set of yields from the default template, and they are assigned as the systematic uncertainty. Table 5.5 shows the summary of the systematic uncertainties on the sum of the signal yields and on the sum of the background yields for the $H \to \tau_{\text{had}} \tau_{\text{had}}$ analysis.

Syst. Source	VBF		Boosted	
	S	B	S	B
Experimental Uncertainties				
Luminosity	$\pm 2.8\%$	$\pm 0.1\%$	$\pm 2.8\%$	$\pm 0.1\%$
Tau trig.	$^{+7.7}_{-8.8}\%$	$< 0.1\%$	$^{+7.8}_{-8.9}\%$	$< 0.1\%$
Tau ID	$\pm 6.6\%$	$\pm 3.8\%$	$\pm 6.6\%$	$\pm 5.1\%$
TES	$\pm 2.9\%$	$\pm 2.5\%$	$\pm 2.9\%$	$\pm 2.5\%$
JES	$^{+10.1}_{-8.0}\%$	$\pm 0.3\%$	$\pm 5.1\%$	$\pm 0.2\%$
$E_{\text{T}}^{\text{miss}}$ soft term	$\pm 0.5\%$	$\pm 0.2\%$	$\pm 0.1\%$	$< 0.1\%$
Background Modeling Uncertainties				
Embedding	-	$\pm 5.2\%$	-	$\pm 0.6\%$
Fake Est.	-	$\pm 2.2\%$	-	$\pm 3.3\%$
Theoretical Uncertainties				
QCD Scale	$^{+9.7}_{-7.6}\%$	$\pm 0.2\%$	$^{+19.3}_{-14.7}\%$	$\pm 0.2\%$
PDF	$^{+3.9}_{-3.6}\%$	$\pm 0.2\%$	$^{+6.6}_{-6.1}$	$\pm 0.2\%$
UE and PS	$\pm 3.8\%$	$< 0.1\%$	$\pm 2.8\%$	$< 0.1\%$
Generator	$\pm 1.3\%$	$< 0.1\%$	$\pm 2.8\%$	$< 0.1\%$
$H \to \tau\tau$ B.R.	$\pm 5.7\%$	-	$\pm 5.7\%$	-

Table 5.5: Summary of systematic uncertainties on the sum of signal and background yields for the VBF and Boosted categories in the $H \to \tau_{\text{had}} \tau_{\text{had}}$ channel.

5.5 Results of the CP Measurement

5.5.1 Statistical Model

The number of events in the signal region is not enough to measure the mixing angle α of the CP state of the Higgs boson, so that an expected exclusion limit on the pure CP-odd Higgs production is derived, without using the observed data. In order to archive this, the statistical model described in Section 4.9.1 is slightly modified with *pure CP-even* and *pure CP-odd* hypotheses based on Ref. [146]. The POI is the fraction of CP-odd Higgs boson (f_{odd}) on the total Higgs boson production. Here, the fraction of CP-even Higgs boson (f_{even}) is constrained by a condition of $f_{\text{even}} = 1 - f_{\text{odd}}$. Therefore, the equation (4.22) is modified as

$$\nu(f_{\text{odd}}|x) = \hat{\mu} \sum_{s}^{\text{N}_{\text{sig}}} n_{\text{sig}} \left[f_{\text{odd}} \cdot p_{\text{odd}}(x) + (1 - f_{\text{odd}}) \cdot p_{\text{even}}(x) \right] + \sum_{b}^{\text{N}_{\text{bkg}}} n_b \cdot f_b(x), \tag{5.16}$$

where $p(x)$ denotes the distribution of the acoplanarity angles normalized to unit, which is used as probability density functions. The signal strength $\hat{\mu}$ in the Asimov dataset is fixed to the measured best-fit value $\mu = 1.43$. The likelihood function itself is the same as the equation (4.23).

The exclusion limit is derived by performing a binned maximum likelihood fit on the Asimov dataset with $f_{\text{odd}} = 0$. The value of f_{odd} is evaluated with the test statistics $q_{f_{\text{odd}}} = -2\ln(\lambda(f_{\text{odd}}))$. The level of disagreement of the Asimov dataset is quantified with the p-value $p_{f_{\text{odd}}}$ defined as the equation 4.24. In order to obtain the exclusion limit, the frequent statistical method, referred to as CL_s method, is used [133, 147].

$$CL_s = \frac{p_{f_{\text{odd}}}}{1 - p_1} \tag{5.17}$$

5.5.2 Results

The maximum likelihood fit is performed on the Asimov dataset to estimate expected CL_s exclusion limit of the CP-odd Higgs boson production. Figure 5.18 (a) shows the test statistics q distributions for the pure CP-even ($f_{\text{even}} = 1$) and CP-odd ($f_{\text{even}} = 0$) Higgs boson combining the $H \to \tau_{\ell}\tau_{\text{had}}$ and $H \to \tau_{\text{had}}\tau_{\text{had}}$ channels. Based on the q distribution, the result of the confidence level for exclusion is 56%, corresponding to the exclusion significance of 0.78σ. The same NP evaluation method as described in Section 4.9.2 is performed. The most important NPs are dominated by statistical uncertainties on the bins of the acoplanarity, indicating this analysis is limited by the statistics rather than systematic uncertainty.

Furthermore, the prospect study is performed for the LHC Run-2 experiment. The LHC operation is restarted from June, 2015 with $\sqrt{s} = 13$ TeV after two years of shout down time, and it is planned to collect the data amount of integrated luminosity of 100 fb^{-1} until 2018. The signal and background cross sections are scaled from $\sqrt{s} = 8$ TeV to $\sqrt{s} = 13$ TeV [88, 126]. However, the analysis procedures, such

as event selection, categorization, BDT approach and acoplanarity reconstruction, are not modified from the 8 TeV analysis, and exactly the same systematic uncertainties are assigned. The maximum likelihood fit is performed assuming integrated luminosity of 20 fb^{-1}, 50 fb^{-1} and 100 fb^{-1}. The confidence level of the expected CP-odd Higgs boson exclusion limit at $\sqrt{s} = 13$ TeV for each integrated luminosity is shown in Fig. 5.18 (b). The expected limit with 100 fb^{-1} is 96% confidence level, indicating that the 95% CL_s exclusion is promising at least within 100 fb^{-1}, i.e., full data amount of the LHC Run-2 experiment. This prospect study uses the most conservative approach because any analysis improvement is not taken into account. Several improvements for the LHC Run-2 experiment have been studied, such as the primary vertex re-fitting without τ_{had} associated tracks, additional discrimination variables, specific BDT for the CP analysis and so on. These improvements would enhance the sensitivity of the measurement, and therefore the expected 95% CL_s exclusion limit will be achieved with a smaller data amount than 100 fb^{-1}.

An additional important point of this analysis is that exactly the same measurement methodology can be applied for any particles which decay into the $\tau\tau$ final state, regardless of the particle mass. The search for the BSM Higgs boson in the $\tau\tau$ final state is in progress at the LHC Run-2 experiment, assuming the MSSM theory model. In case of a discovery of a new particle with a high mass, the CP measurement of the discovered particle is important to examine its theory model. As the summary of the analysis, it can be said that a door to the CP measurement of the SM/BSM Higgs boson in the $\tau^+\tau^-$ final state is opened for overall mass range.

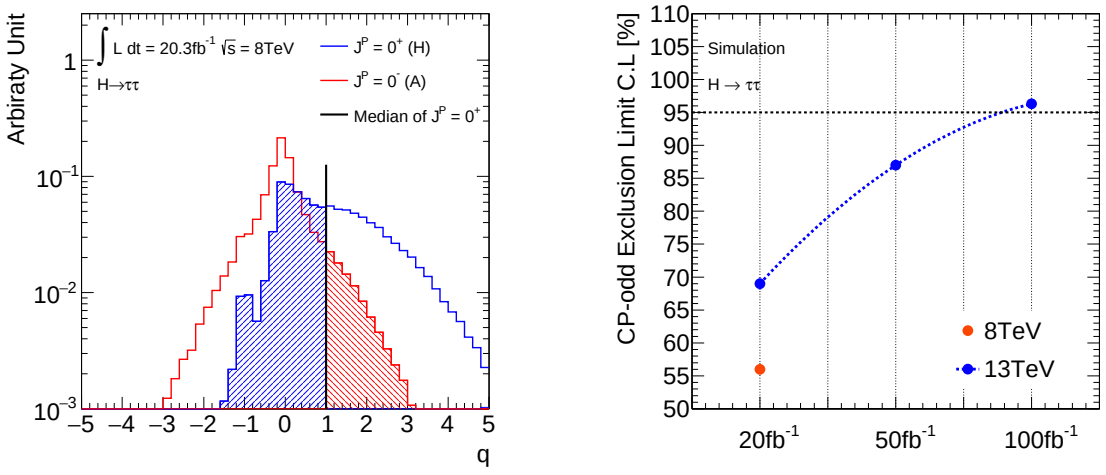

(a) (b)

Fig. 5.18: Example of the distribution of the test statistics $q_{f_{\text{odd}}}$ (a). The CP-even and CP-odd Higgs boson (H and A) are represented by blue and red lines, while the shade areas correspond to the integrals of the expected distributions used to compute the p-value for the CP-odd Higgs boson exclusion. Expected confidence level of the CP-odd Higgs boson exclusion as a function of an expected integrated luminosity (b). The red marker represents the result of $\sqrt{s} = 8$ TeV with an integrated luminosity of 20 fb^{-1}, while the blue markers represent the results of $\sqrt{s} = 13$ TeV with 20 fb^{-1}, 50 fb^{-1} and 100 fb^{-1}.

CHAPTER 6

Conclusions and Prospects

The Higgs mechanism, which is responsible for the mass generation via spontaneous symmetry breaking, plays an important role in the SM. The W and Z boson masses are generated by the gauge couplings with a predicted scalar particle, the Higgs boson. The mechanism also predicts fermion masses via the couplings between the Higgs boson and fermions, so-called Yukawa couplings. In order to verify the Higgs mechanism, an experimental discovery of the Higgs boson was one of the most important motivation of the LHC programme.

In July 2012, the ATLAS and CMS experiments reported a discovery of the Higgs boson with a mass of ~ 125 GeV with di-boson final states. With full dataset in 2011-2012, corresponding to an integrated luminosity of up to 25 fb^{-1}, the measurement of spin and parity quantum numbers of the discovered Higgs boson is performed by both experiments, and the result is consistent with the $J^P = 0^+$ predicted by the SM. Taking the discovery and the measurement with di-boson final state, the recent major focus of physics analysis at the LHC is the direct observation of the Yukawa coupling. For the Higgs boson with ~ 125 GeV, the most sensitive fermionic search channels at the LHC is the $H \to \tau\tau$ channel.

This thesis presents a search for the Higgs boson and a study of its CP measurement in the $\tau\tau$ final state with the ATLAS detector. The first main part is the search for the Higgs boson in the $\tau\tau$ final state, based on data corresponding to an integrated luminosity of 4.5 fb^{-1} of $\sqrt{s} = 7$ TeV and 20.3 fb^{-1} of $\sqrt{s} = 8$ TeV collected in 2011 and 2012, respectively. The $H \to \tau\tau$ decay can be subdivided into three search channels corresponding to τ lepton decays, i.e., lepton-hadron, fully hadronic, fully leptonic channels. The analysis presented in this thesis focuses on the lepton-hadron channel, while the statistical combination of three channels is performed. Event selections and categorizations are optimized corresponding to main production processes of the ggF and the VBF. Several background processes contribute to the selected signal region. Dedicated data-driven estimation methods are applied to main background events of $Z \to \tau\tau$, W+jets and QCD processes. In order to efficiently discriminate signal events from background events, a multi-variate technique, Boosted Decision Tree (BDT) as classifier, is used with various input variables. A maximum likelihood fit is performed to data with the expected signal and background on the BDT output distribution in order to measure the signal strength μ, which is defined as the ratio of cross section times branching ratio in data to that in theoretical prediction.

An excess of data over the expected background from other SM processes is observed in the high BDT score region. The measured signal strength at $m_H = 125$ GeV in the lepton-hadron channel is:

$$\mu = 0.98^{+0.35}_{-0.33}(\text{stat.})\ ^{+0.36}_{-0.30}(\text{syst.})\ \pm 0.06(\text{theory syst.}). \tag{6.1}$$

The observed (expected) significance of the excess is 2.3σ (2.3σ). The statistical combination of three

search channels is performed, and the measured signal strength at $m_H = 125$ GeV is:

$$\mu = 1.43^{+0.27}_{-0.26}(\text{stat.})\ ^{+0.32}_{-0.25}(\text{syst.})\ \pm 0.09(\text{theory syst.}). \tag{6.2}$$

The corresponding observed (expected) significance is 4.5σ (3.4σ). The result presents that "evidence for the decay of the Higgs boson into leptons", and also "first evidence for the Yukawa coupling to down-type fermions".

The LHC Run-2 experiment at $\sqrt{s} = 13$ TeV already started from June 2015, and data of ~ 100 fb^{-1} is collected in 2015-2018. Higgs signal events with ~ 11 times higher statistics are expected in the data, taking into account an increase of the cross section from 8 TeV to 13 TeV. Therefore, a discovery for the $H \to \tau\tau$ is promising and precise measurements of the coupling constant, mass and CP will be performed. Furthermore, it might be interesting to search other production processes (e.g., $VH, t\bar{t}H \to \tau\tau$) for better understanding of Yukawa couplings, and to search for the BSM Higgs boson predicted in the MSSM with the $\tau\tau$ final state.

The second main part is the CP measurement of the Higgs boson in the $\tau\tau$ final state. The analysis is performed with the lepton-hadron and the fully hadronic channels, based on data corresponding to an integrated luminosity of 20.3 fb^{-1} of $\sqrt{s} = 8$ TeV collected in 2012. The CP state of the Higgs boson reflects the transverse spin correlation of τ leptons in the final state. The dedicated variable named acoplanarity angle is defined, which is an angle between $\tau^{\pm} \to \tau^{\pm}_{\text{had}}\nu_{\tau}$ decay planes. Instead of the precise neutrino reconstruction, alternative reconstruction methods are applied according to τ lepton decays. Event selections and categorizations are basically the same as the search analysis, while the τ_{had} classification and the cut on the BDT score are applied for the CP analysis as additional selections.

A maximum likelihood fit on the acoplanarity angle is performed to obtain the expected exclusion limit of the CP-odd Higgs hypothesis. The fit on the observed data is not performed due to limited statistics. The expected exclusion limit is 56% confidence level assuming the data of 20.3 fb^{-1} at $\sqrt{s} = 8$ TeV. The prospect study at $\sqrt{s} = 13$ TeV is also performed by scaling cross sections and an integrated luminosity. The confidence level for exclusion with 100 fb^{-1} corresponding to expected full data amount of the LHC Run-2 experiment is 96%, indicating that the 95% confidence level exclusion is promising at the Run-2 experiment. Several analysis improvement is under development in the Run-2, so that an earlier exclusion is expected. Also it might be interesting to continue the CP analysis to measure the mixing angle of the CP state, with an assumption of a mixing state of the CP-even and CP-odd Higgs boson. Moreover, in case of a discovery of the BSM Higgs boson in the $\tau\tau$ final state, its CP state can be measured by using the analysis strategy presented in this thesis.

APPENDIX A

Additions for Chapter 4

A.1 Background Modeling

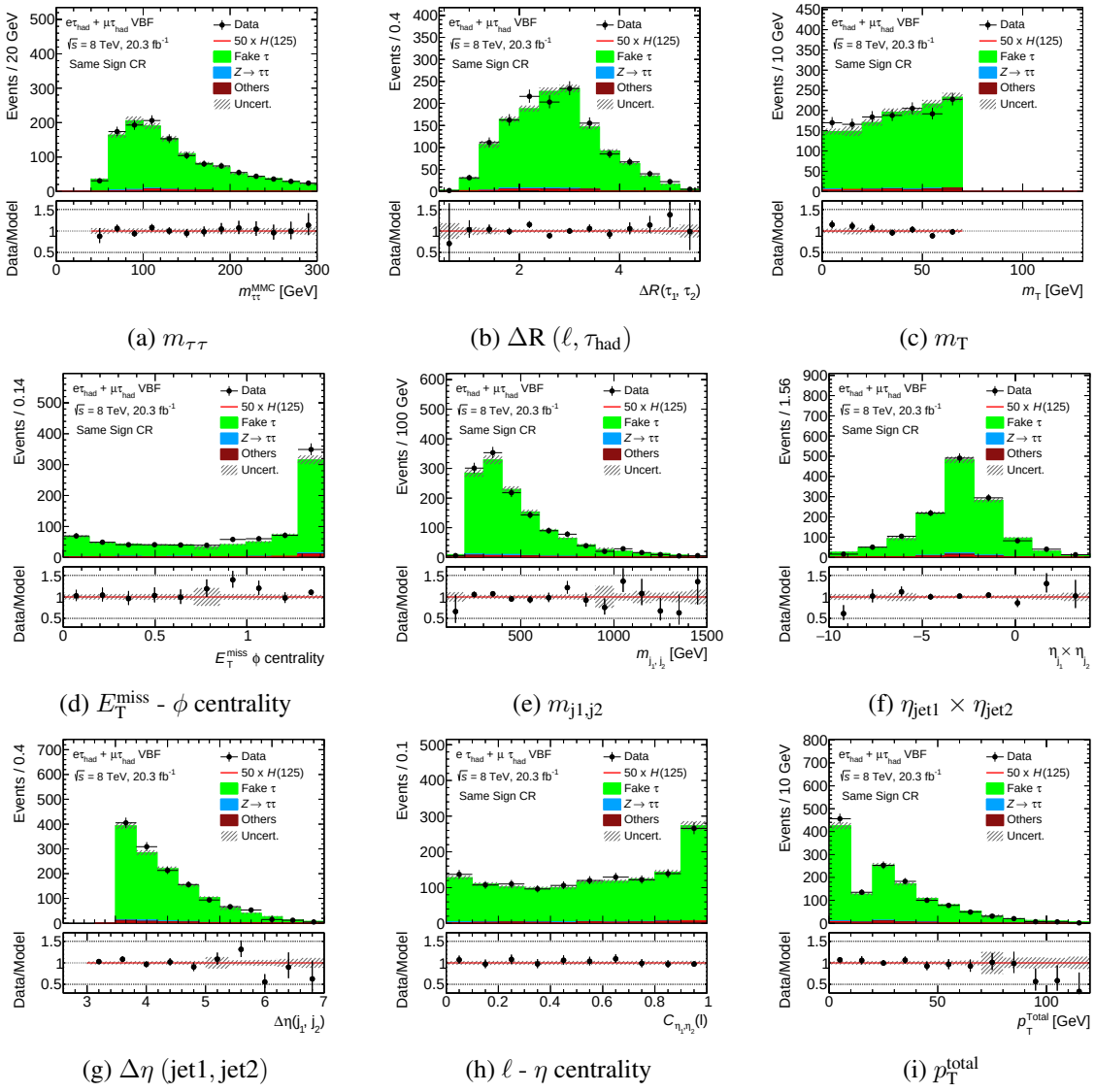

(a) $m_{\tau\tau}$ (b) ΔR $(\ell, \tau_{\text{had}})$ (c) m_{T}

(d) $E_{\text{T}}^{\text{miss}}$ - ϕ centrality (e) $m_{\text{j1,j2}}$ (f) $\eta_{\text{jet1}} \times \eta_{\text{jet2}}$

(g) $\Delta\eta$ (jet1, jet2) (h) ℓ - η centrality (i) $p_{\text{T}}^{\text{total}}$

Fig. A.1: Input variable distributions for the same sign control region of the 8 TeV VBF category.

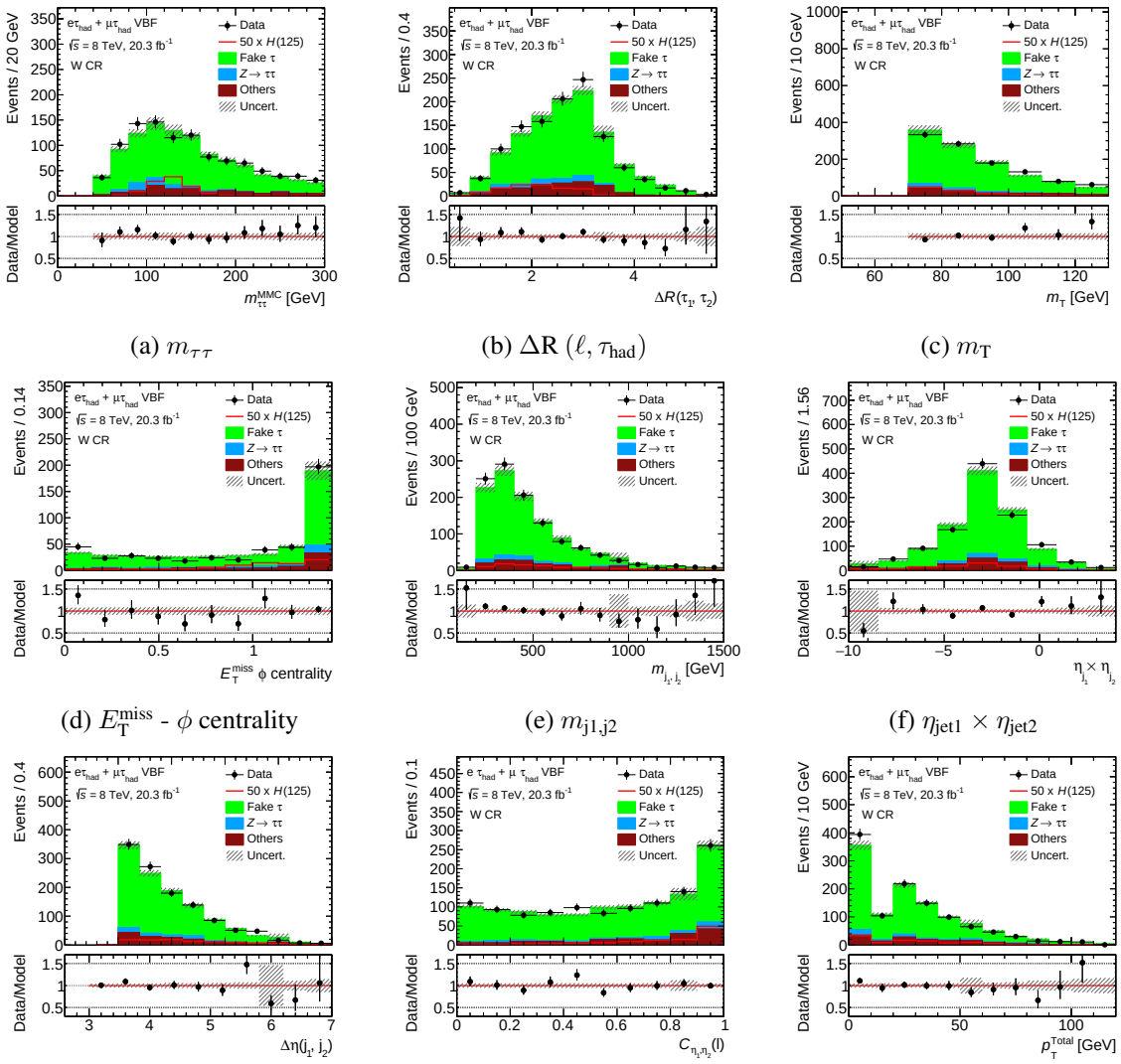

(a) $m_{\tau\tau}$ (b) ΔR $(\ell, \tau_{\text{had}})$ (c) m_{T}

(d) $E_{\text{T}}^{\text{miss}}$ - ϕ centrality (e) $m_{\text{j1,j2}}$ (f) $\eta_{\text{jet1}} \times \eta_{\text{jet2}}$

(g) $\Delta\eta$ (jet1, jet2) (h) ℓ - η centrality (i) $p_{\text{T}}^{\text{total}}$

Fig. A.2: Input variable distributions for the W+jets control region of the 8 TeV VBF category.

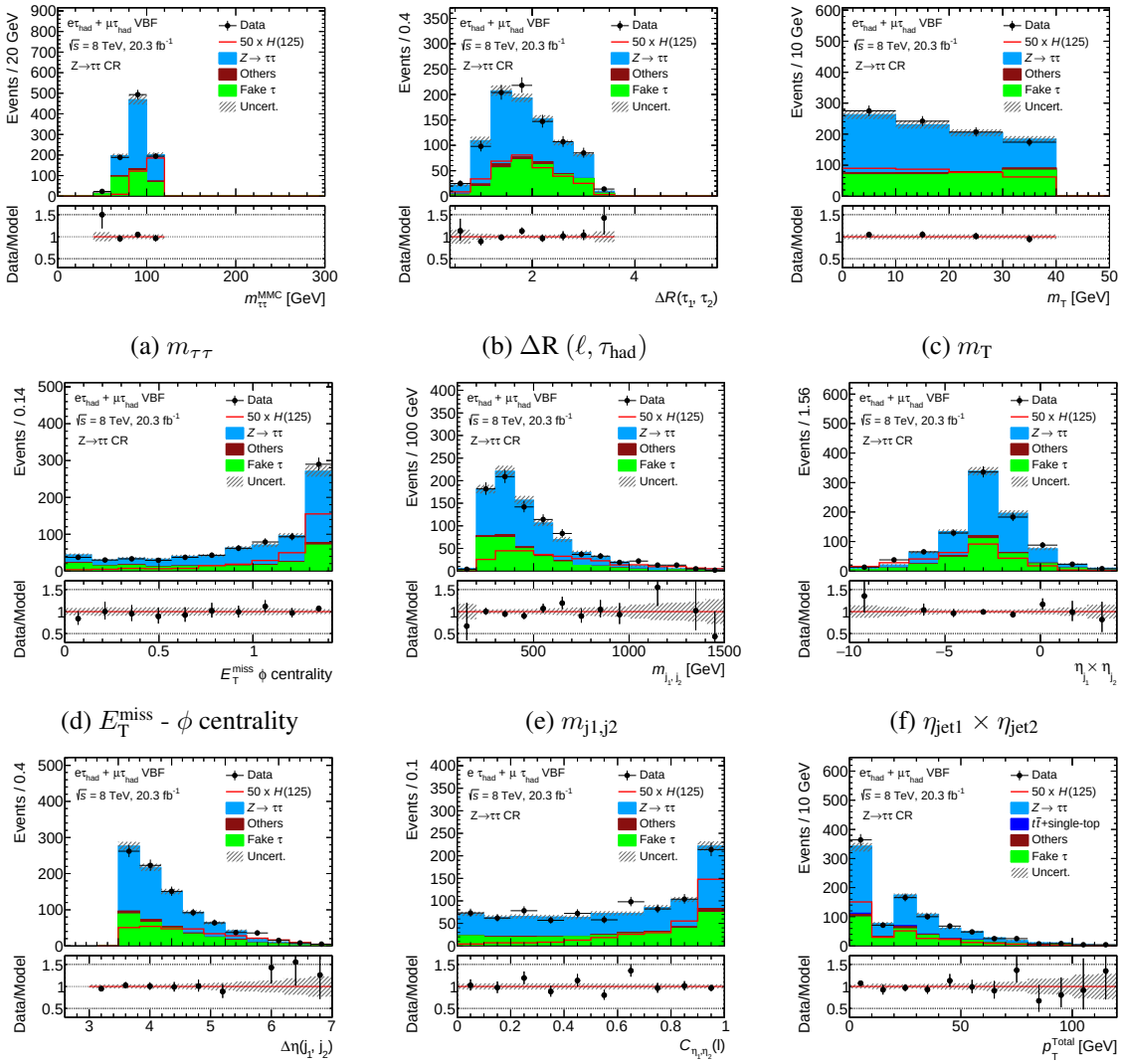

(a) $m_{\tau\tau}$ (b) ΔR $(\ell, \tau_{\text{had}})$ (c) m_{T}

(d) $E_{\text{T}}^{\text{miss}}$ - ϕ centrality (e) $m_{\text{j1,j2}}$ (f) $\eta_{\text{jet1}} \times \eta_{\text{jet2}}$

(g) $\Delta\eta$ (jet1, jet2) (h) ℓ - η centrality (i) $p_{\text{T}}^{\text{total}}$

Fig. A.3: Input variable distributions for the $Z \to \tau\tau$ control region of the 8 TeV VBF category.

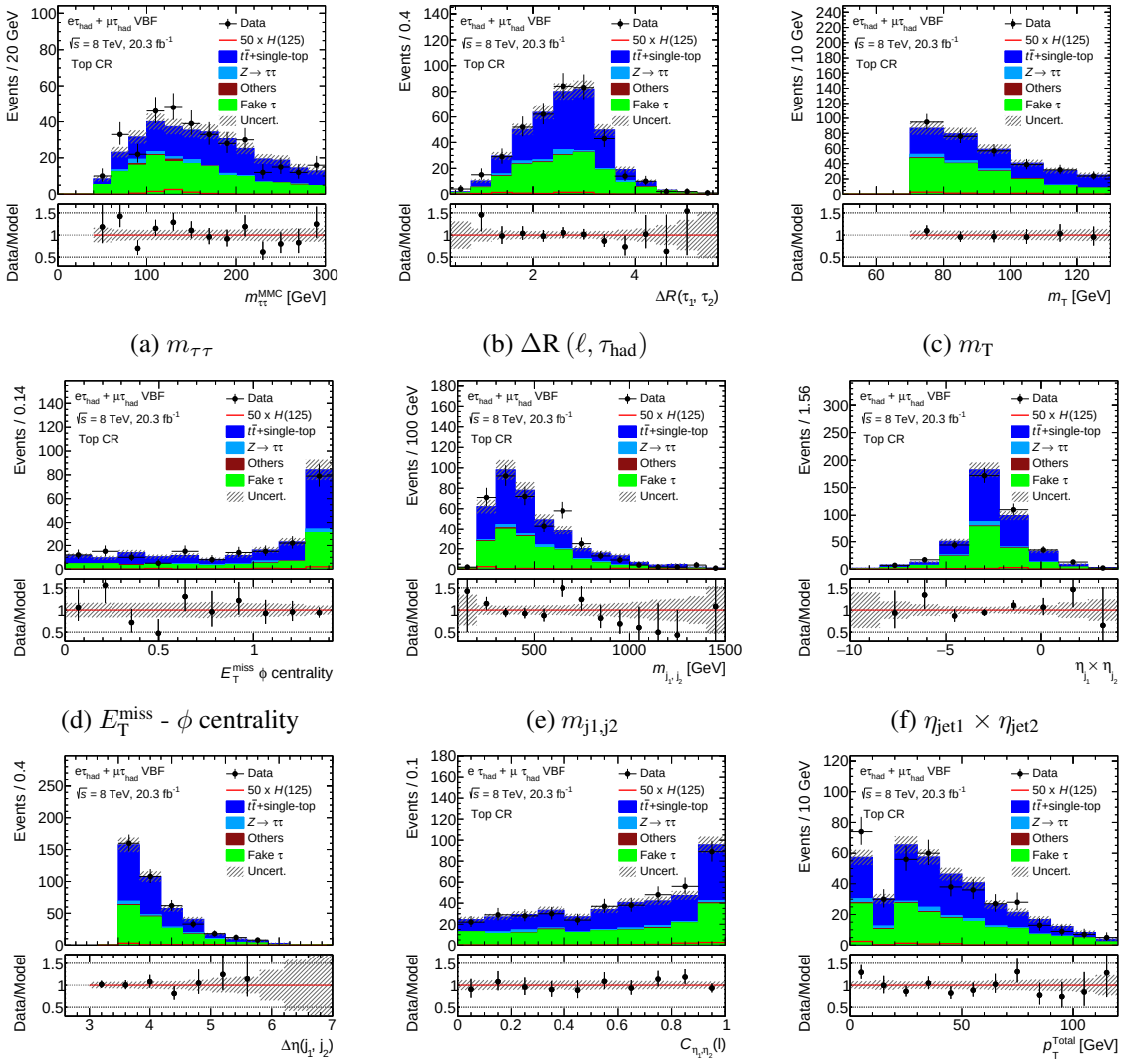

(a) $m_{\tau\tau}$ (b) ΔR $(\ell, \tau_{\text{had}})$ (c) m_{T}

(d) $E_{\text{T}}^{\text{miss}}$ - ϕ centrality (e) $m_{\text{j1,j2}}$ (f) $\eta_{\text{jet1}} \times \eta_{\text{jet2}}$

(g) $\Delta\eta$ (jet1, jet2) (h) ℓ - η centrality (i) $p_{\text{T}}^{\text{total}}$

Fig. A.4: Input variable distributions of the Top (τ_{had}) control region in the 8 TeV VBF category.

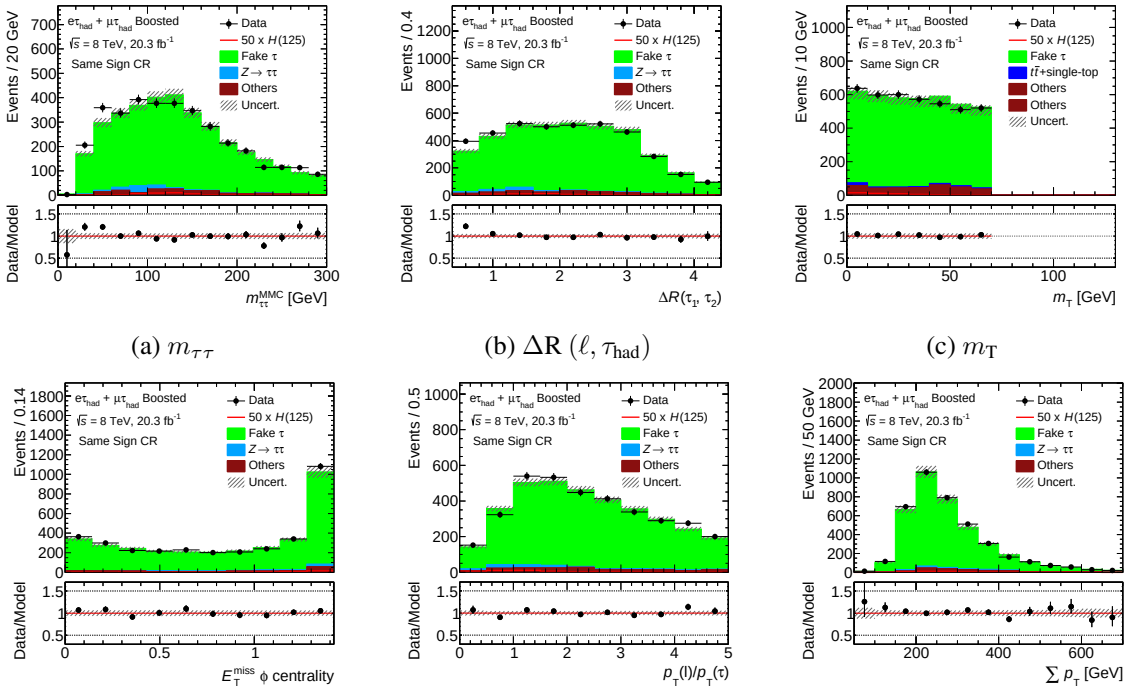

(a) $m_{\tau\tau}$ (b) ΔR $(\ell, \tau_{\text{had}})$ (c) m_{T}

(d) $E_{\text{T}}^{\text{miss}}$ - ϕ centrality (e) $p_{\text{T}}^{\ell}/p_{\text{T}}^{\tau_{\text{had}}}$ (f) $\sum p_{\text{T}}$

Fig. A.5: Input variable distributions for the same sign control region of the 8 TeV Boosted category.

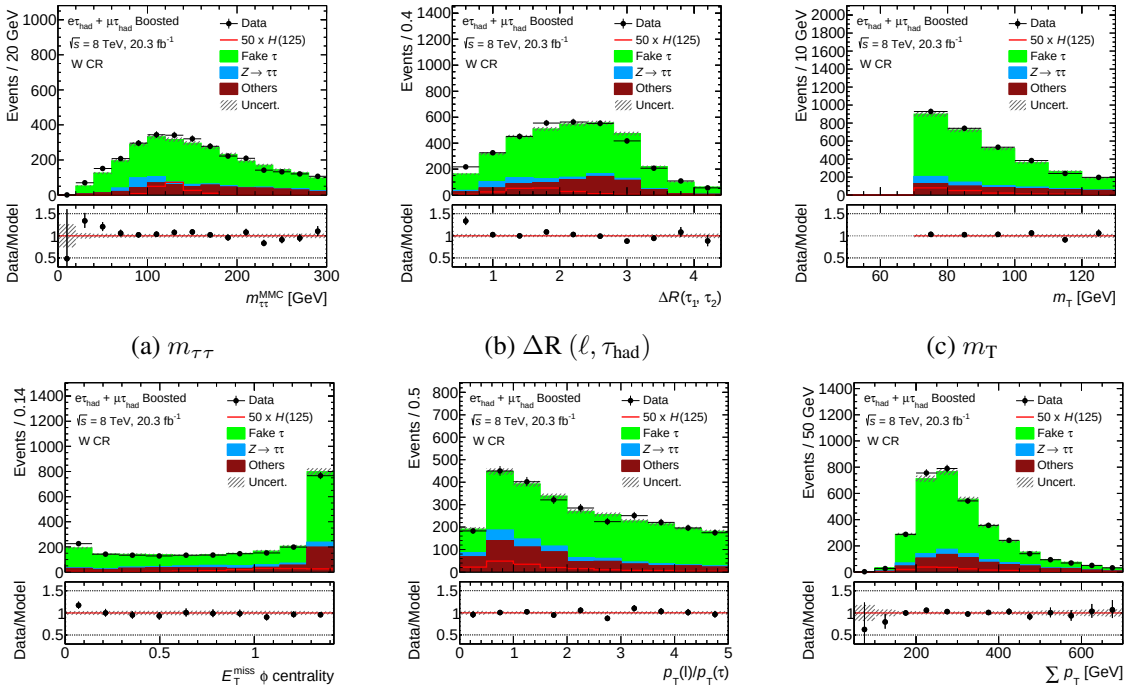

(a) $m_{\tau\tau}$ (b) ΔR $(\ell, \tau_{\text{had}})$ (c) m_{T}

(d) $E_{\text{T}}^{\text{miss}}$ - ϕ centrality (e) $p_{\text{T}}^{\ell}/p_{\text{T}}^{\tau_{\text{had}}}$ (f) $\sum p_{\text{T}}$

Fig. A.6: Input variable distributions for the W+jets control region of the 8 TeV Boosted category.

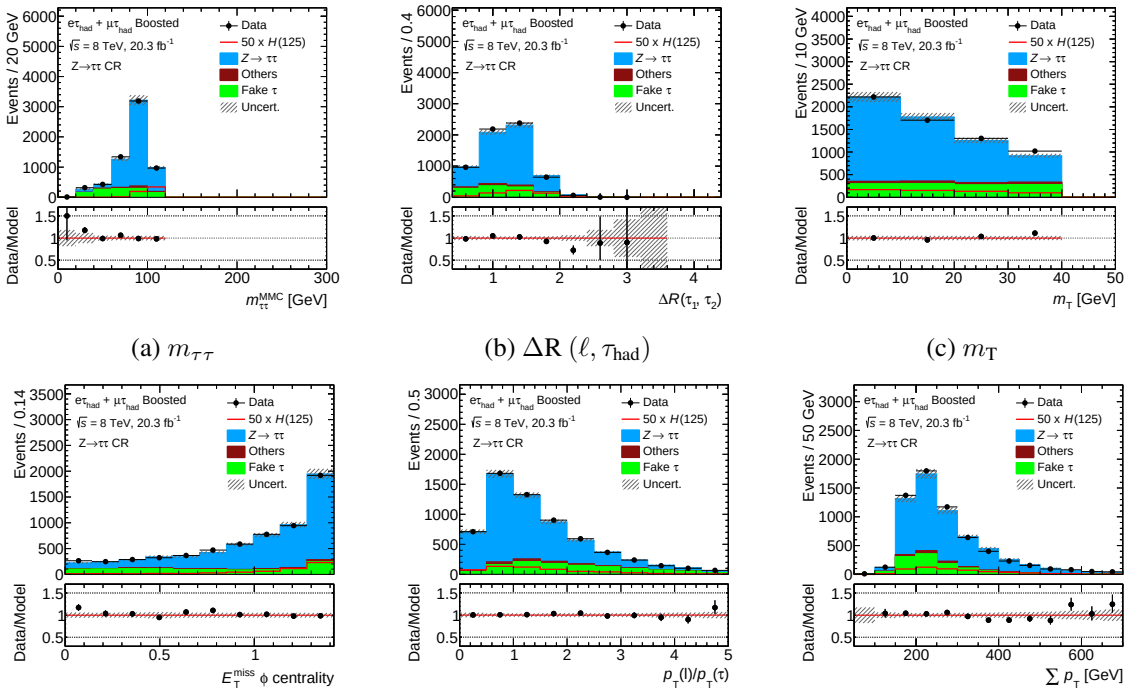

(a) $m_{\tau\tau}$ (b) ΔR $(\ell, \tau_{\text{had}})$ (c) m_{T}

(d) $E_{\text{T}}^{\text{miss}}$ - ϕ centrality (e) $p_{\text{T}}^{\ell}/p_{\text{T}}^{\tau_{\text{had}}}$ (f) $\sum p_{\text{T}}$

Fig. A.7: Input variable distributions for the $Z \rightarrow \tau\tau$ control region of the 8 TeV Boosted category.

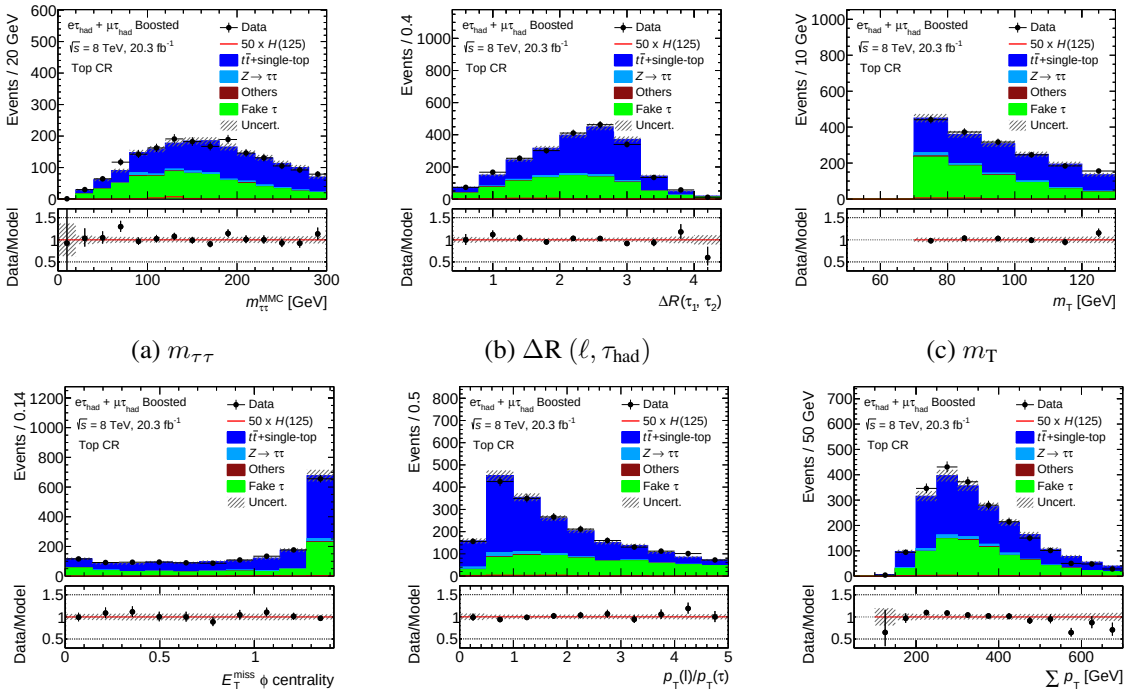

(a) $m_{\tau\tau}$ (b) ΔR $(\ell, \tau_{\text{had}})$ (c) m_{T}

(d) $E_{\text{T}}^{\text{miss}}$ - ϕ centrality (e) $p_{\text{T}}^{\ell}/p_{\text{T}}^{\tau_{\text{had}}}$ (f) $\sum p_{\text{T}}$

Fig. A.8: Input variable distributions for the Top (τ_{had}) control region of the 8 TeV Boosted category.

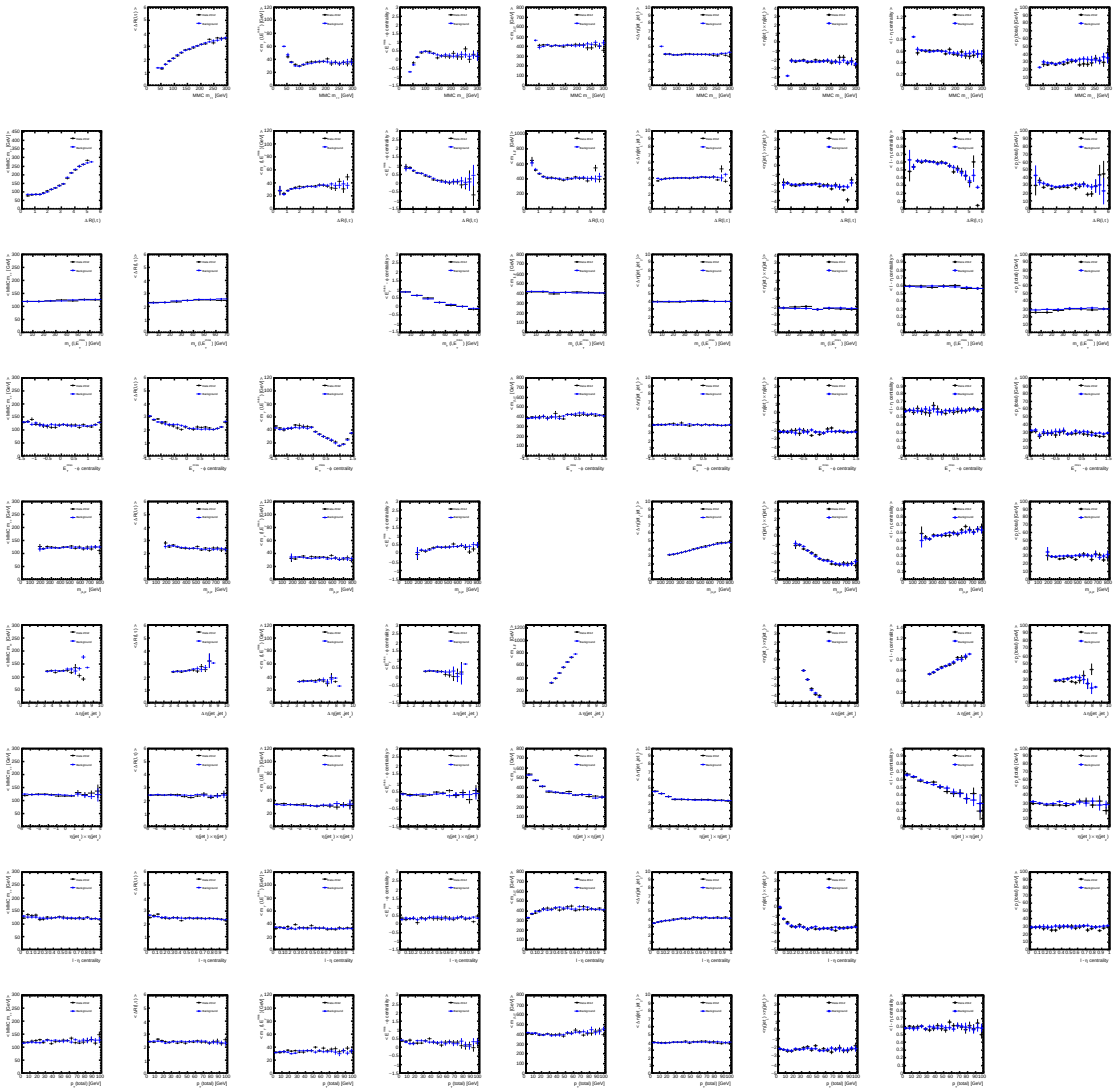

Fig. A.9: Correlation distributions of input variables, z_i v.s. $< z_j >$, for the VBF category in 8 TeV analysis. The $z_{i,j}$ represents any two input variables, and $< z_j >$ represents the mean value of z_j. The data and the background distributions are shown as black and blue dots, respectively. The displayed uncertainties represents the statistical uncertainty on each mean value.

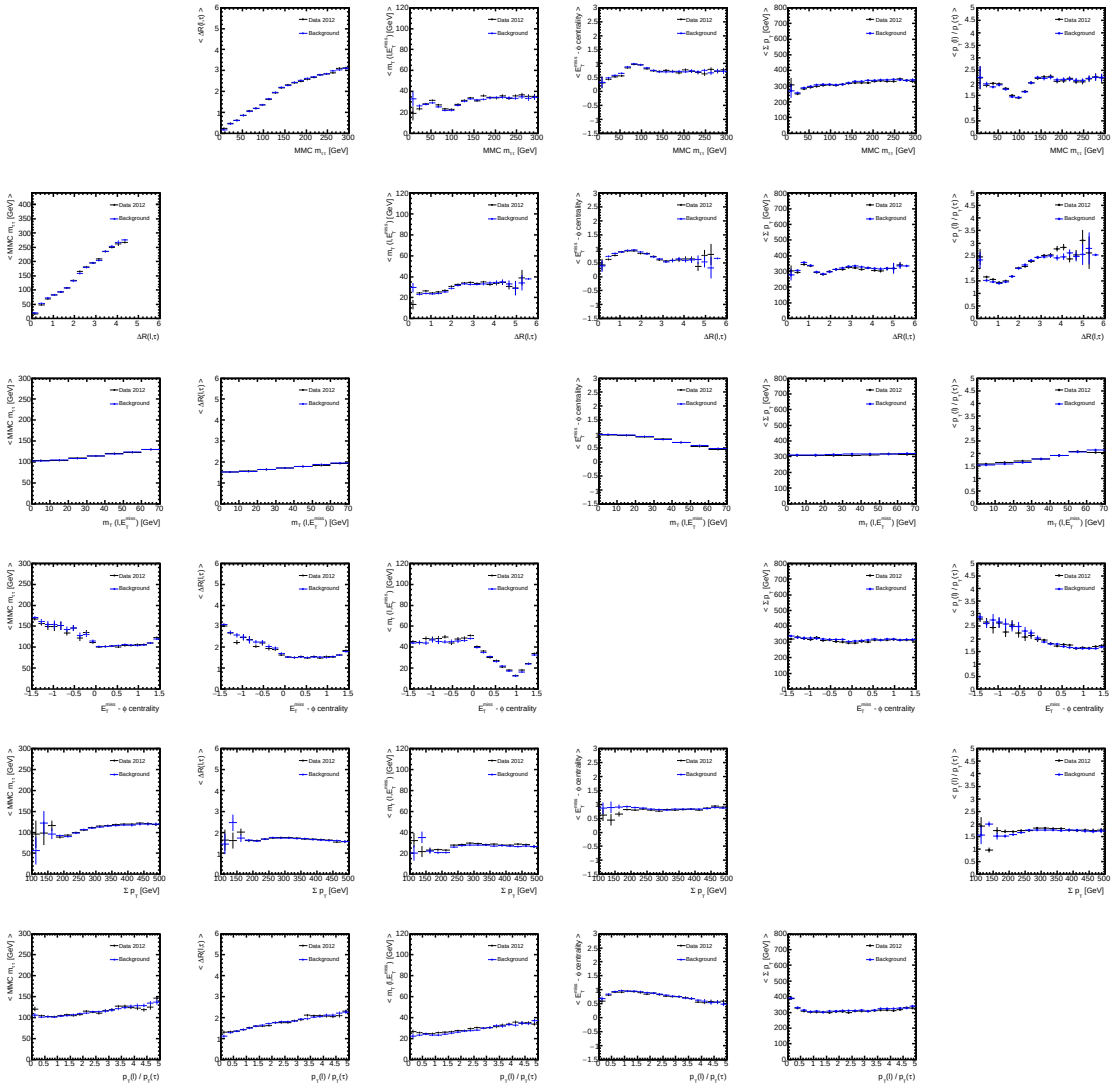

Fig. A.10: Correlation distributions of Input variables, z_i v.s. $< z_j >$, for the Boosted category in 8 TeV analysis. The $z_{i,j}$ represents any two input variables, and $< z_j >$ represents the mean value of z_j. The data and the background distributions are shown as black and blue dots, respectively. The displayed uncertainties represents the statistical uncertainty on each mean value.

A.2 Nuisance Parameters

The 25 nuisance parameters which have the largest impact on the signal strength are summarized in Fig. 4.29. The meaning of each nuisance parameter is the following:

stat lh12 vbf bin11
Statistical uncertainty on 11th (highest score) bin of the BDT output score distribution for the 8 TeV VBF category.

JES FlavResp
Flavour composition and response uncertainties for the JES difference between quark and gluon initiated jets.

JES Detector1
Systematic uncertainty on the JES related to detector responses.

TAU EFAKE2012
Systematic uncertainty on electron to τ_{had} fake probability measured using $Z \rightarrow$ ee (e $\rightarrow \tau_{\text{had}}$) tag-and-probe method.

JES EtaModeling
Systematic uncertainty on the JES, related to the η-intercalibration.

JES 2012 Modeling1
Systematic uncertainty on the JES in the 8 TeV analysis, related to modeling and theoretical uncertainties in the JES measurement procedure.

BR tautau
Uncertainty on the $H \rightarrow \tau\tau$ branching ratio.

stat lh12 boost bin10
Statistical uncertainty on the 10th (highest score) bin of the BDT output score distribution for the 8 TeV Boosted category.

stat lh12 vbf bin10
Statistical uncertainty on the 10th (second highest score) bin of the BDT output score distribution for the 8 TeV VBF category.

norm LH12 Top boost
Normalization factor for Top (τ_{had}) and Top ($\ell \rightarrow \tau_{\text{had}}$) backgrounds in the Boosted category, which is free parameter in the maximum likelihood fit.

TES True 2011
Systematic uncertainty on the TES in the 7 TeV analysis.

QCDscale ggH m23
QCD scale uncertainty on $H+ \geq 2$ jets signal events from the ggF production process.

QCDscale ggH ptH m01

QCD scale uncertainty on $H+ < 2$ jets signal events from the ggF production process.

norm LH12 Ztt bv

Normalization factor for the $Z \to \tau\tau$ background, which is free parameter in the maximum likelihood fit and the same value is used for the VBF and Boosted categories.

GenAcc2Z

Uncertainty on the choice of event generators for the $Z \to \ell\ell$ ($\ell \to \tau_{\text{had}}$) background.

JES FlavComp TAU G

Systematic uncertainty on the JES for events with gluon or τ initiated jets.

stat lh11 vbf bin9

Statistical uncertainty on the 9th (highest score) bin of the BDT output score distribution for the 7 TeV VBF category.

TES Fake 2012

Systematic uncertainty on the TES for events with misidentified τ_{had}s in the 8 TeV analysis.

stat lh12 vbf bin8

Statistical uncertainty on the 8th (fourth highest score) bin of the BDT output score distribution for the 8 TeV VBF category.

TES InSitu 2012

Systematic uncertainty related to the *in-situ* based TES measurement in the 8 TeV analysis.

ANA EMB ISOL 2011

Isolation uncertainty for the embedding sample in the 7 TeV analysis.

norm LH12 Top vbf

Normalization factor for Top (τ_{had}) and Top ($\ell \to \tau_{\text{had}}$) backgrounds in the VBF category, which is free parameter in the maximum likelihood fit.

LUMI 2012

Systematic uncertainty on the integrated luminosity in the 8 TeV analysis.

EL RES

Systematic uncertainty of the electron energy resolution.

ANA EMB MFS 2012

Subtraction uncertainty for the embedding sample in the 8 TeV analysis.

APPENDIX B

Additions For Chapter 5

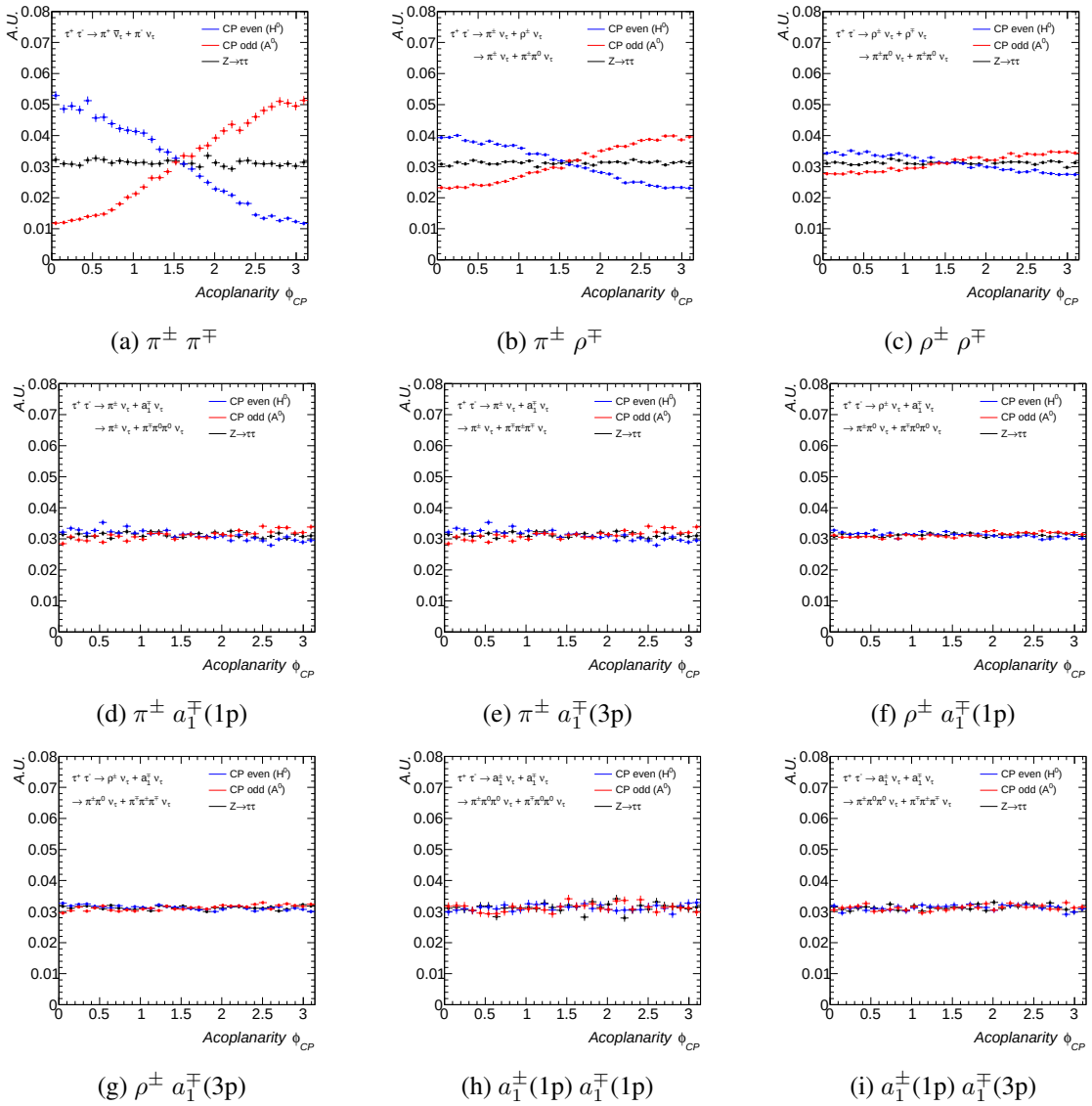

(a) $\pi^{\pm}\,\pi^{\mp}$ (b) $\pi^{\pm}\,\rho^{\mp}$ (c) $\rho^{\pm}\,\rho^{\mp}$

(d) $\pi^{\pm}\,a_1^{\mp}(1p)$ (e) $\pi^{\pm}\,a_1^{\mp}(3p)$ (f) $\rho^{\pm}\,a_1^{\mp}(1p)$

(g) $\rho^{\pm}\,a_1^{\mp}(3p)$ (h) $a_1^{\pm}(1p)\,a_1^{\mp}(1p)$ (i) $a_1^{\pm}(1p)\,a_1^{\mp}(3p)$

Fig. B.1: Truth acoplanarity distributions of the CP-even (blue), CP-odd (red) Higgs boson and the Z boson (black) for each $\tau^+\tau^-$ → hadron-hadron decay.

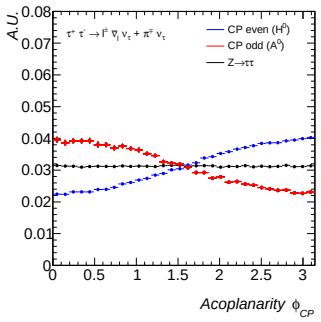

(a) $\ell^{\pm}\pi^{\mp}$

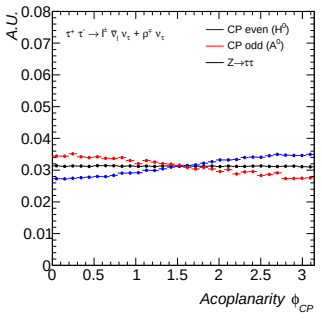

(b) $\ell^{\pm}\rho^{\mp}$

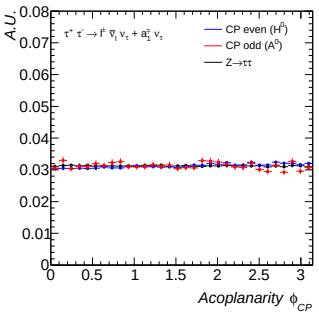

(c) $\ell^{\pm}a_1^{\mp}$(1p)

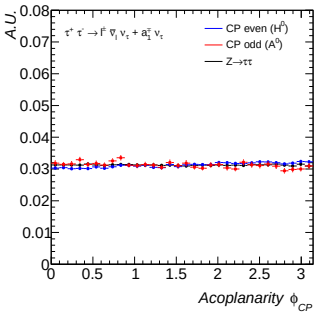

(d) $\ell^{\pm}a_1^{\mp}$(3p)

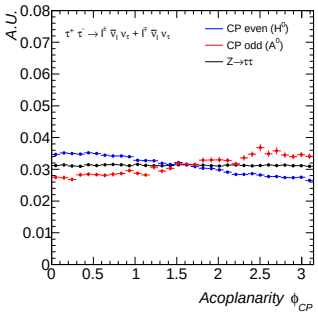

(e) $\ell^{\pm}\ell^{\mp}$

Fig. B.2: Truth acoplanarity distributions of the CP-even (blue), CP-odd (red) Higgs boson and the Z boson (black) for each $\tau^{+}\tau^{-} \rightarrow$ lepton-hadron (a,b,c,d) and lepton-lepton (e) decay.

Bibliography

[1] S.L. Glashow. Partial Symmetries of Weak Interactions. *Nucl.Phys.*, 22:579–588, 1961.

[2] F. Englert and R. Brout. Broken Symmetry and the Mass of Gauge Vector Mesons. *Phys. Rev. Lett.*, 13:321–323, Aug 1964.

[3] Peter W. Higgs. Spontaneous Symmetry Breakdown without Massless Bosons. *Phys.Rev.*, 145:1156–1163, 1966.

[4] Peter W. Higgs. Broken Symmetries and the Masses of Gauge Bosons. *Phys. Rev. Lett.*, 13:508–509, Oct 1964.

[5] F. Halzen and A. D. Martin. *Quarks and Leptons: An Introductory Course in Modern Particle Physics*. 1984.

[6] Sandra Leone. Electroweak and top physics at the Tevatron and indirect Higgs limits. In *SUSY 2007 proceedings, 15th International Conference on Supersymmetry and Unification of Fundamental Interactions, July 26 - August 1, 2007, Karlsruhe, Germany*, 2007.

[7] LEP Collaboration. LEP Design Report: Vol.2. The LEP Main Ring. Technical report, CERN, 1984.

[8] The ALEPH, DELPHI, L3, OPAL Collaborations, the LEP Electroweak Working Group. Electroweak Measurements in Electron-Positron Collisions at W-Boson-Pair Energies at LEP. *Phys. Rept.*, 532:119, 2013.

[9] R. Barate et al. Search for the standard model Higgs boson at LEP. *Phys. Lett.*, B565:61–75, 2003.

[10] T. Aaltonen et al. Higgs Boson Studies at the Tevatron. *Phys.Rev.*, D88(5):052014, 2013.

[11] T. Aaltonen et al. Search for a low mass Standard Model Higgs boson in the τ-τ decay channel in $p\bar{p}$ collisions at $\sqrt{s} = 1.96$ TeV. *Phys. Rev. Lett.*, 108:181804, 2012.

[12] Georges Aad et al. Observation of a new particle in the search for the Standard Model Higgs boson with the ATLAS detector at the LHC. *Phys. Lett.*, B716:1–29, 2012.

[13] Serguei Chatrchyan et al. Observation of a new boson at a mass of 125 GeV with the CMS experiment at the LHC. *Phys. Lett.*, B716:30–61, 2012.

[14] Georges Aad et al. Study of the spin and parity of the Higgs boson in diboson decays with the ATLAS detector. `arXiv:1506.05669` (2015).

[15] K.A. Olive et al. Review of Particle Physics. *Chin.Phys.*, C38:090001, 2014.

[16] G.C. Branco, P.M. Ferreira, L. Lavoura, M.N. Rebelo, Marc Sher, et al. Theory and phenomenology of two-Higgs-doublet models. *Phys.Rept.*, 516:1–102, 2012.

[17] A. Barroso, P. M. Ferreira, Rui Santos, Marc Sher, and Joao P. Silva. 2HDM at the LHC - the story so far. In *1st Toyama International Workshop on Higgs as a Probe of New Physics 2013 (HPNP2013) Toyama, Japan, February 13-16, 2013*, 2013.

[18] Pierre Fayet. Supersymmetry and Weak, Electromagnetic and Strong Interactions. *Phys.Lett.*, B64:159, 1976.

[19] Pierre Fayet. Spontaneously Broken Supersymmetric Theories of Weak, Electromagnetic and Strong Interactions. *Phys.Lett.*, B69:489, 1977.

[20] Glennys R. Farrar and Pierre Fayet. Phenomenology of the Production, Decay, and Detection of New Hadronic States Associated with Supersymmetry. *Phys.Lett.*, B76:575–579, 1978.

[21] Pierre Fayet. Relations Between the Masses of the Superpartners of Leptons and Quarks, the Goldstino Couplings and the Neutral Currents. *Phys.Lett.*, B84:416, 1979.

[22] Jihn E. Kim. Light Pseudoscalars, Particle Physics and Cosmology. *Phys.Rept.*, 150:1–177, 1987.

[23] Michael Joyce, Tomislav Prokopec, and Neil Turok. Nonlocal electroweak baryogenesis. Part 2: The Classical regime. *Phys.Rev.*, D53:2958–2980, 1996.

[24] Vardan Khachatryan et al. Constraints on the spin-parity and anomalous HVV couplings of the Higgs boson in proton collisions at 7 and 8 TeV. *Phys. Rev.*, D92(1):012004, 2015.

[25] Lyndon Evans and Philip Bryant. LHC Machine. *JINST*, 3:S08001, 2008.

[26] TE-EPS-LPC in LHC. http://teepclpc.web.cern.ch/teepclpc/machines/pagesources/Cern-AcceleratorComplex.jpg. Access at Mar 2015.

[27] ATLAS Collaboration. ATLAS twiki: LuminosityPublicResults. https://twiki.cern.ch/twiki/bin/view/AtlasPublic/LuminosityPublicResults. Access at Jun 2015.

[28] G. Aad et al. The ATLAS Experiment at the CERN Large Hadron Collider. *JINST*, 3:S08003, 2008.

[29] A. Airapetian et al. ATLAS: Detector and physics performance technical design report. Volume 1. 1999. CERN-LHCC-99-14, ATLAS-TDR-14.

[30] A. Airapetian et al. ATLAS: Detector and physics performance technical design report. Volume 2. 1999. CERN-LHCC-99-15, ATLAS-TDR-15.

[31] ATLAS collaboration. ATLAS inner detector: Technical Design Report 1. 1997. CERN-LHCC-97-016, ATLAS-TDR-4.

[32] ATLAS collaboration. ATLAS inner detector: Technical Design Report 2. 1997. CERN-LHCC-97-017,ATLAS-TDR-5.

[33] G. Aad, M. Ackers, F.A. Alberti, M. Aleppo, G. Alimonti, et al. ATLAS pixel detector electronics and sensors. *JINST*, 3:P07007, 2008.

[34] ATLAS collaboration. ATLAS pixel detector: Technical Design Report. 1998. CERN-LHCC-98-013,ATLAS-TDR-11.

[35] A. Ahmad, Z. Albrechtskirchinger, P.P. Allport, J. Alonso, L. Andricek, et al. The Silicon microstrip sensors of the ATLAS semiconductor tracker. *Nucl.Instrum.Meth.*, A578:98–118, 2007.

[36] A. Abdesselam, T. Akimoto, P.P. Allport, J. Alonso, B. Anderson, et al. The barrel modules of the ATLAS semiconductor tracker. *Nucl.Instrum.Meth.*, A568:642–671, 2006.

[37] A. Abdesselam et al. The ATLAS semiconductor tracker end-cap module. *Nucl.Instrum.Meth.*, A575:353–389, 2007.

[38] E. Abat et al. The ATLAS Transition Radiation Tracker (TRT) proportional drift tube: Design and performance. *JINST*, 3:P02013, 2008.

[39] E. Abat et al. The ATLAS TRT barrel detector. *JINST*, 3:P02014, 2008.

[40] E. Abat, E. Arik, M. Arik, N. Becerici, O.B. Dogan, et al. The ATLAS TRT end-cap detectors. *JINST*, 3:P10003, 2008.

[41] ATLAS Collaboration. Measurements of the photon identification efficiency with the ATLAS detector using 4.9 fb^{-1} of pp collision data collected in 2011. Technical Report ATLAS-CONF-2012-123, CERN, Geneva, Aug 2012.

[42] ATLAS Collaboration. Performance of primary vertex reconstruction in proton-proton collisions at $\sqrt{s} = 7$ TeV in the ATLAS experiment. Technical Report ATLAS-CONF-2010-069, CERN, Geneva, Jul 2010.

[43] ATLAS Collaboration. Performance of the ATLAS Inner Detector Track and Vertex Reconstruction in the High Pile-Up LHC Environment. Technical Report ATLAS-CONF-2012-042, CERN, Geneva, Mar 2012.

[44] Georges Aad et al. Electron performance measurements with the ATLAS detector using the 2010 LHC proton-proton collision data. *Eur.Phys.J.*, C72:1909, 2012.

[45] ATLAS Collaboration. Electron reconstruction and identification efficiency measurements with the ATLAS detector using the 2011 LHC proton-proton collision data. *Eur. Phys. J.*, C 74:2941, 2014.

[46] M Wielers, R Mantifel, A Tricoli, and P Bell. Single Electron Trigger Performance Plots. Technical Report ATL-COM-DAQ-2012-146, CERN, Geneva, Jun 2012.

[47] ATLAS Collaboration. Improved electron reconstruction in ATLAS using the Gaussian Sum Filter-based model for bremsstrahlung. Technical Report ATLAS-CONF-2012-047, CERN, Geneva, May 2012.

[48] Georges Aad et al. Electron and photon energy calibration with the ATLAS detector using LHC Run 1 data. *Eur.Phys.J.*, C74(10):3071, 2014.

[49] ATLAS Collaboration. Performance of the ATLAS muon trigger in 2011. Technical Report ATLAS-CONF-2012-099, CERN, Geneva, Jul 2012.

[50] ATLAS Collaboration. Measurement of the muon reconstruction performance of the ATLAS detector using 2011 and 2012 LHC proton-proton collision data. *Eur. Phys. J.*, C 74:3130, 2014.

[51] Georges Aad et al. Measurement of the muon reconstruction performance of the ATLAS detector using 2011 and 2012 LHC protonproton collision data. *Eur. Phys. J.*, C74(11):3130, 2014.

[52] ATLAS Collaboration. ATLAS twiki: Muon Trigger Public Result. https://twiki.cern.ch/twiki/bin/view/AtlasPublic/MuonTriggerPublicResults. Access at Jun 2015.

[53] L. Breiman, J. Friedman, R. Olshen, and C. Stone. *Classification and Regression Trees*. Chapman & Hall, New York, 1984.

[54] Georges Aad et al. Identification and energy calibration of hadronically decaying tau leptons with the ATLAS experiment in pp collisions at $\sqrt{s} = 8$ TeV. 2014.

[55] Georges Aad et al. Jet energy measurement and its systematic uncertainty in proton-proton collisions at $\sqrt{s} = 7$ TeV with the ATLAS detector. *Eur.Phys.J.*, C75(1):17, 2015.

[56] JoAnne L. Hewett and Thomas G. Rizzo. Low-Energy Phenomenology of Superstring Inspired E(6) Models. *Phys. Rept.*, 183:193, 1989.

[57] Mirjam Cvetic and Stephen Godfrey. Discovery and identification of extra gauge bosons. `hep-ph:9504216` (1995).

[58] A. Leike. The Phenomenology of extra neutral gauge bosons. *Phys. Rept.*, 317:143–250, 1999.

[59] Thomas G. Rizzo. Z' phenomenology and the LHC. In *Proceedings of Theoretical Advanced Study Institute in Elementary Particle Physics : Exploring New Frontiers Using Colliders and Neutrinos (TASI 2006)*, pages 537–575, 2006.

[60] Ross Diener, Stephen Godfrey, and Travis A. W. Martin. Unravelling an Extra Neutral Gauge Boson at the LHC using Third Generation Fermions. *Phys. Rev.*, D83:115008, 2011.

[61] Paul Langacker. The Physics of Heavy Z' Gauge Bosons. *Rev. Mod. Phys.*, 81:1199–1228, 2009.

[62] Matteo Cacciari, Gavin P. Salam, and Gregory Soyez. The Anti-k(t) jet clustering algorithm. *JHEP*, 0804:063, 2008.

[63] Gavin P. Salam. Towards Jetography. *Eur.Phys.J.*, C67:637–686, 2010.

[64] ATLAS Collaboration. ATLAS twiki: JetEtmiss Public Result. https://twiki.cern.ch/twiki/bin/view/AtlasPublic/JetEtmissApproved2013JESUncertainty. Access at Jun 2015.

[65] ATLAS Collaboration. Calibration of the performance of b-tagging for c and light-flavour jets in the 2012 ATLAS data. Technical Report ATLAS-CONF-2014-046, CERN, Geneva, Jul 2014.

[66] ATLAS Collaboration. Calibration of b-tagging using dileptonic top pair events in a combinatorial likelihood approach with the ATLAS experiment. Technical Report ATLAS-CONF-2014-004, CERN, Geneva, Feb 2014.

[67] ATLAS Collaboration. Performance of Impact Parameter-Based b-tagging Algorithms with the ATLAS Detector using Proton-Proton Collisions at $\sqrt{s} = 7$ TeV. Technical Report ATLAS-CONF-2010-091, CERN, Geneva, Oct 2010.

[68] ATLAS Collaboration. Performance of the ATLAS Secondary Vertex b-tagging Algorithm in 7 TeV Collision Data. Technical Report ATLAS-CONF-2010-042, CERN, Geneva, Jul 2010.

[69] ATLAS Collaboration. Performance of Missing Transverse Momentum Reconstruction in ATLAS studied in Proton-Proton Collisions recorded in 2012 at 8 TeV. Technical Report ATLAS-CONF-2013-082, CERN, Geneva, Aug 2013.

[70] Paolo Nason. A New method for combining NLO QCD with shower Monte Carlo algorithms. *JHEP*, 0411:040, 2004.

[71] Stefano Frixione, Paolo Nason, and Carlo Oleari. Matching NLO QCD computations with Parton Shower simulations: the POWHEG method. *JHEP*, 0711:070, 2007.

[72] Simone Alioli, Paolo Nason, Carlo Oleari, and Emanuele Re. NLO Higgs boson production via gluon fusion matched with shower in POWHEG. *JHEP*, 0904:002, 2009.

[73] Torbjorn Sjostrand, Stephen Mrenna, and Peter Z. Skands. A Brief Introduction to PYTHIA 8.1. *Comput.Phys.Commun.*, 178:852–867, 2008.

[74] Hung-Liang Lai, Marco Guzzi, Joey Huston, Zhao Li, Pavel M. Nadolsky, et al. New parton distributions for collider physics. *Phys.Rev.*, D82:074024, 2010.

[75] A. Djouadi, M. Spira, and P.M. Zerwas. Production of Higgs bosons in proton colliders: QCD corrections. *Phys. Lett.*, B 264:440, 1991.

[76] S. Dawson. Radiative corrections to Higgs boson production. *Nucl. Phys.*, B 359:283, 1991.

[77] M. Spira et al. Higgs boson production at the LHC. *Nucl. Phys.*, B 453:17, 1995.

[78] Robert V. Harlander and William B. Kilgore. Next-to-next-to-leading order Higgs production at hadron colliders. *Phys. Rev. Lett.*, 88:201801, 2002.

[79] Charalampos Anastasiou and Kirill Melnikov. Higgs boson production at hadron colliders in NNLO QCD. *Nucl. Phys.*, B 646:220, 2002.

[80] V. Ravindran, J. Smith, and W. L. van Neerven. NNLO corrections to the total cross-section for Higgs boson production in hadron hadron collisions. *Nucl. Phys.*, B 665:325, 2003.

[81] Stefano Catani, Daniel de Florian, Massimiliano Grazzini, and Paolo Nason. Soft gluon resummation for Higgs boson production at hadron colliders. *JHEP*, 07:028, 2003.

[82] U. Aglietti et al. Two loop light fermion contribution to Higgs production and decays. *Phys. Lett.*, B 595:432, 2004.

[83] Stefano Actis et al. NLO electroweak corrections to Higgs boson production at hadron colliders. *Phys. Lett.*, B 670:12, 2008.

[84] Massimiliano Grazzini and Hayk Sargsyan. Heavy-quark mass effects in Higgs boson production at the LHC. *JHEP*, 09:129, 2013.

[85] D. de Florian et al. Higgs boson production at the LHC: transverse momentum resummation effects in the $H \to 2\gamma, H \to WW \to \ell\nu\ell\nu$ and $H \to ZZ \to 4\ell$ decay modes. *JHEP*, 06:132, 2012.

[86] John M. Campbell, R. Keith Ellis, and Giulia Zanderighi. Next-to-Leading order Higgs + 2 jet production via gluon fusion. *JHEP*, 0610:028, 2006.

[87] Paolo Nason and Carlo Oleari. NLO Higgs boson production via vector-boson fusion matched with shower in POWHEG. *JHEP*, 1002:037, 2010.

[88] S. Dittmaier et al. (LHC Higgs Cross Section Working Group). Handbook of LHC Higgs Cross Sections: 2. Differential Distributions. `arXiv:1201.3084` (2012).

[89] M. Ciccolini, Ansgar Denner, and S. Dittmaier. Strong and electroweak corrections to the production of Higgs + 2jets via weak interactions at the LHC. *Phys.Rev.Lett.*, 99:161803, 2007.

[90] Mariano Ciccolini, Ansgar Denner, and Stefan Dittmaier. Electroweak and QCD corrections to Higgs production via vector-boson fusion at the LHC. *Phys.Rev.*, D77:013002, 2008.

[91] J. Pumplin, D.R. Stump, J. Huston, H.L. Lai, Pavel M. Nadolsky, et al. New generation of parton distributions with uncertainties from global QCD analysis. *JHEP*, 0207:012, 2002.

[92] Ansgar Denner, Stefan Dittmaier, Stefan Kallweit, and Alexander Muck. Electroweak corrections to Higgs-strahlung off W/Z bosons at the Tevatron and the LHC with HAWK. *JHEP*, 1203:075, 2012.

[93] M. Mangano et al. ALPGEN, a generator for hard multiparton processes in hadronic collisions. *JHEP*, 07:001, 2003.

[94] G. Corcella et al. HERWIG 6.5 release note. `hep-ph/0210213` (2002).

[95] J.M. Butterworth, Jeffrey R. Forshaw, and M.H. Seymour. Multiparton interactions in photoproduction at HERA. *Z.Phys.*, C72:637–646, 1996.

[96] M. Mangano et al. Multijet matrix elements and shower evolution in hadronic collisions: $Wb\bar{b}$ + n jets as a case study. *Nucl. Phys.*, B 632:343, 2002.

[97] T. Gleisberg et al. Event generation with SHERPA 1.1. *JHEP*, 02:007, 2009.

[98] Borut Paul Kersevan and Elzbieta Richter-Was. The Monte Carlo event generator AcerMC versions 2.0 to 3.8 with interfaces to PYTHIA 6.4, HERWIG 6.5 and ARIADNE 4.1. *Comput.Phys.Commun.*, 184:919–985, 2013.

[99] Matteo Cacciari et al. Top-pair production at hadron colliders with next-to-next-to-leading logarithmic soft-gluon resummation. *Phys. Lett.*, B 710:612, 2012.

[100] Brnreuther, Peter, Czakon, Michal, and Mitov, Alexander. Percent Level Precision Physics at the Tevatron: First Genuine NNLO QCD Corrections to $q\bar{q} \to t\bar{t} + X$. *Phys. Rev. Lett.*, 109:132001, 2012.

[101] M. Czakon and A. Mitov. NNLO corrections to top-pair production at hadron colliders: the all-fermionic scattering channels. *JHEP*, 12:054, 2012.

[102] M. Czakon and A. Mitov. NNLO corrections to top pair production at hadron colliders: the quark-gluon reaction. *JHEP*, 01:080, 2013.

[103] M. Czakon, P. Fiedler, A. Mitov. The total top quark pair production cross-section at hadron colliders through $\mathcal{O}(\alpha_S^4)$. *Phys. Rev. Lett.*, 110:252004, 2013.

[104] M. Czakon and A. Mitov. Top++: A Program for the Calculation of the Top-Pair Cross-Section at Hadron Colliders. *Comput. Phys. Commun.*, 185:2930, 2014.

[105] Nikolaos Kidonakis. Next-to-next-to-leading-order collinear and soft gluon corrections for t-channel single top quark production. *Phys.Rev.*, D83:091503, 2011.

[106] Nikolaos Kidonakis. NNLL resummation for s-channel single top quark production. *Phys.Rev.*, D81:054028, 2010.

[107] Nikolaos Kidonakis. Two-loop soft anomalous dimensions for single top quark associated production with a W^- or H^-. *Phys.Rev.*, D82:054018, 2010.

[108] T. Binoth, M. Ciccolini, N. Kauer, and M. Kramer. Gluon-induced W-boson pair production at the LHC. *JHEP*, 0612:046, 2006.

[109] Stefano Catani et al. Vector boson production at hadron colliders: A fully exclusive QCD calculation at next-to-next-to-leading order. *Phys. Rev. Lett.*, 103:082001, 2009.

[110] S. Agostinelli et al. GEANT4 Collaboration. Geant4– A Simulation toolkit. *Nucl. Instrum. Meth.*, A 506:250, 2003.

[111] G. Aad et al. The ATLAS Simulation Infrastructure. *Eur. Phys. J.*, C70:823–874, 2010.

[112] R.K. Ellis et al. Higgs decay to $\tau^+\tau^-$: A possible signature of intermediate mass Higgs bosons at high energy hadron colliders. *Nucl. Phys.*, 297:221, 1988.

[113] A. Elagin et al. A new mass reconstruction technique for resonances decaying to di-tau. *Nucl. Instrum. Meth.*, A 654:481, 2011.

[114] Georges Aad et al. Modelling $Z \to \tau\tau$ processes in ATLAS with τ-embedded $Z \to \mu\mu$ data. `arXiv:1506.05623` (2015).

[115] Z. Was. TAUOLA the library for tau lepton decay, and KKMC / KORALB / KORALZ /... status report. *Nucl.Phys.Proc.Suppl.*, 98:96–102, 2001.

[116] N. Davidson, T. Przedzinski, and Z. Was. PHOTOS Interface in C++: Technical and Physics Documentation. `arXiv:1011.0937` (2010).

[117] *ATLAS Computing: technical design report*. Technical Design Report ATLAS. CERN, Geneva, 2005.

[118] Yoav Freund and Robert E. Schapire. A decision-theoretic generalization of on-line learning and an application to boosting. *J. Comput. Syst. Sci.*, 55:119, 1997.

[119] J. Friedman. Stochastic gradient boosting. *Comput. Stat. Data Anal.*, 38:367, 2002.

[120] Andreas Hocker, J. Stelzer, F. Tegenfeldt, H. Voss, K. Voss, et al. TMVA - Toolkit for Multivariate Data Analysis. *PoS*, ACAT:040, 2007.

[121] Georges Aad et al. Search for the Standard Model Higgs boson in the H to $\tau^+\tau^-$ decay mode in $\sqrt{s} = 7$ TeV pp collisions with ATLAS. *JHEP*, 1209:070, 2012.

[122] ATLAS Collaboration. Data-driven background estimation for the $H \to \tau\tau \to$lh search at 7 TeV with the ATLAS detector. Technical Report ATLAS-CONF-2010-096, CERN, Geneva, Oct 2010.

[123] Georges Aad et al. Evidence for the Higgs-boson Yukawa coupling to tau leptons with the ATLAS detector. *JHEP*, 1504:117, 2015.

[124] Iain W. Stewart and Frank J. Tackmann. Theory Uncertainties for Higgs and Other Searches Using Jet Bins. *Phys.Rev.*, D85:034011, 2012.

[125] John M. Campbell, R. Keith Ellis, and Ciaran Williams. Vector boson pair production at the LHC. *JHEP*, 1107:018, 2011.

[126] S. Dittmaier et al. (LHC Higgs Cross Section Working Group). Handbook of LHC Higgs Cross Sections: 1. Inclusive Observables. `arXiv:1101.0593` (2011).

[127] A.D. Martin, W.J. Stirling, R.S. Thorne, and G. Watt. Parton distributions for the LHC. *Eur.Phys.J.*, C63:189–285, 2009.

[128] Richard D. Ball, Valerio Bertone, Francesco Cerutti, Luigi Del Debbio, Stefano Forte, et al. Impact of Heavy Quark Masses on Parton Distributions and LHC Phenomenology. *Nucl.Phys.*, B849:296–363, 2011.

[129] Stefano Frixione and Bryan R. Webber. Matching NLO QCD computations and parton shower simulations. *JHEP*, 0206:029, 2002.

[130] ATLAS Collaboration. Measurements of the properties of the Higgs-like boson in the $WW^{(*)} \to \ell\nu\ell\nu$ decay channel with the ATLAS detector using $25ifb$ of proton-proton collision data. Technical Report ATLAS-CONF-2013-030, CERN, Geneva, Mar 2013.

[131] J. Alwall, R. Frederix, S. Frixione, V. Hirschi, F. Maltoni, et al. The automated computation of tree-level and next-to-leading order differential cross sections, and their matching to parton shower simulations. *JHEP*, 1407:079, 2014.

[132] Georges Aad et al. Improved luminosity determination in pp collisions at $\sqrt{s} = 7$ TeV using the ATLAS detector at the LHC. *Eur.Phys.J.*, C73(8):2518, 2013.

[133] Glen Cowan, Kyle Cranmer, Eilam Gross, and Ofer Vitells. Asymptotic formulae for likelihood-based tests of new physics. *Eur. Phys. J.*, C71:1554, 2011.

[134] E. Bagnaschi, G. Degrassi, P. Slavich, and A. Vicini. Higgs production via gluon fusion in the POWHEG approach in the SM and in the MSSM. *JHEP*, 1202:088, 2012.

[135] Stefan Berge and Werner Bernreuther. Determining the CP parity of Higgs bosons at the LHC in the tau to 1-prong decay channels. *Phys.Lett.*, B671:470–476, 2009.

[136] Stefan Berge, Werner Bernreuther, and Hubert Spiesberger. Higgs CP properties using the τ decay modes at the ILC. *Phys.Lett.*, B727:488–495, 2013.

[137] S. Berge, W. Bernreuther, B. Niepelt, and H. Spiesberger. How to pin down the CP quantum numbers of a Higgs boson in its tau decays at the LHC. *Phys.Rev.*, D84:116003, 2011.

[138] Stefan Berge, Werner Bernreuther, and Sebastian Kirchner. Determination of the Higgs CP-mixing angle in the tau decay channels at the LHC including the DrellYan background. *Eur.Phys.J.*, C74(11):3164, 2014.

[139] G.R. Bower, T. Pierzchala, Z. Was, and M. Worek. Measuring the Higgs boson's parity using $\tau \to \rho\, \nu^*$. *Phys.Lett.*, B543:227–234, 2002.

[140] K. Desch, Z. Was, and M. Worek. Measuring the Higgs boson parity at a linear collider using the tau impact parameter and $\tau \to \rho\, \nu^*$ decay. *Eur.Phys.J.*, C29:491–496, 2003.

[141] K. Desch, A. Imhof, Z. Was, and M. Worek. Probing the CP nature of the Higgs boson at linear colliders with tau spin correlations: The Case of mixed scalar - pseudoscalar couplings. *Phys.Lett.*, B579:157–164, 2004.

[142] Roni Harnik, Adam Martin, Takemichi Okui, Reinard Primulando, and Felix Yu. Measuring CP violation in $h \to \tau^+\tau^-$ at colliders. *Phys.Rev.*, D88(7):076009, 2013.

[143] Stefan Berge, Werner Bernreuther, and Jorg Ziethe. Determining the CP parity of Higgs bosons at the LHC in their tau decay channels. *Phys.Rev.Lett.*, 100:171605, 2008.

[144] Z. Czyczula, T. Przedzinski, and Z. Was. TauSpinner Program for Studies on Spin Effect in tau Production at the LHC. *Eur.Phys.J.*, C72:1988, 2012.

[145] T. Przedzinski, E. Richter-Was, and Z. Was. TauSpinner: a tool for simulating CP effects in $H \to \tau\tau$ decays at LHC. *Eur.Phys.J.*, C74(11):3177, 2014.

[146] ATLAS Collaboration. Study of the spin and parity of the Higgs boson in HVV decays with the ATLAS detector. Technical Report ATLAS-CONF-2015-008, CERN, Geneva, Mar 2015.

[147] A L Read. Presentation of search results: the CL s technique. *Journal of Physics G: Nuclear and Particle Physics*, 28(10):2693, 2002.

List of publications

Selected Publications

1. T. Aaltonen et. al., CDF Collaboration, Search for a low mass Standard Model Higgs boson in the $\tau^+\tau^-$ decay channel at CDF, *Phys. Rev. Lett.* 108, 181804 (2012)

2. T. Aaltonen et. al., CDF Collaboration, Combination of searches for the Higgs boson using the full CDF data set, *Phys. Rev.* D88 (2013) 052013

3. G. Aad et. al., ATLAS Collaboration, Evidence for the Higgs-boson Yukawa coupling to tau leptons with the ATLAS detector, *JHEP* 04 (2015) 117

4. G. Aad et. al.,ATLAS Collaboration, Identification and energy calibration of hadronically decaying tau leptons with the ATLAS experiment in pp collisions at $\sqrt{s} = 8$ TeV, *Eur.Phys.J.* C75 (2015) 7, 303

Other Publications

30 co-authored publications from the CDF Collaboration
162 co-authored publications from the ATLAS Collaboration

Selected Public Analysis Notes

1. T. Aaltonen et. al., CDF Collaboration, Search for the Standard Model Higgs boson in $\tau^+\tau^-$ + jets final state with 8.3 fb^{-1} of CDF data, CDF Note 10625 (2011)

2. G. Aad et. al., ATLAS Collaboration, Evidence for Higgs Boson Decays to the $\tau^+\tau^-$ Final State with the ATLAS Detector, ATLAS-CONF-2013-108 (2013)

3. G. Aad et. al., ATLAS Collaboration, Identification of Hadronic Decays of Tau Leptons in 2012 Data with the ATLAS Detector, ATLAS-CONF-2013-066 (2013)

Conference Proceedings

1. Y. Sakurai, ATLAS Collaboration, Search for the Standard Model Higgs Boson in the H to τ-τ to lepton-hadron and hadron-hadron Decay Modes with the ATLAS Detector, *Nuclear Physics B - Proceedings Supplements , The Twelfth International Workshop on Tau-Lepton Physics (TAU2012)* , Pages 226-227 (2014)

Talks at Conference

1. Standard Model Higgs Searches at Tevatron/CDF experiment, Lake Louise Winter Institute 2012, Alberta, Canada, Feb. 2012

2. Search for the Higgs boson in fermionic channels using the ATLAS detector, Phenomenology 2014 Symposium, Pittsburgh, USA, May 2014

Poster Presentations

1. Search for the Standard Model Higgs Boson in the H to $\tau^+\tau^-$ to lepton-hadron and hadron-hadron Decay Modes with the ATLAS Detector, The Twelfth International Workshop on Tau-Lepton Physics (TAU2012), Nagoya, Japan, Sep. 2012

2. The ATLAS Tau Trigger Performance during LHC Run1 and Prospects for Run2, Large Hadron Collier Physics (LHCP) 2014, New York, USA, Jun 2014

審査員（主査）　早稲田大学准教授　博士（理学）早稲田大学　寄田浩平

2015.10.1

（副査）　早稲田大学教授　工学博士（東京大学）　鷲尾方一

2015年10月7日

早稲田大学教授　博士（理学）広島大学　安倍博之

2015.10.7

東京大学准教授　博士（理学）東京大学　田中純一

2015.10.2